Spectroelectrochemical Characterization of Self-Assembled Monolayers on a Single Crystal Au Bead Electrode: the Influence of Surface Crystallography

by

Zhinan Yu

B.Sc., Nanjing University, 2010

A THESIS SUBMITTED IN PARTIAL FULFILLMENT OF
THE REQUIREMENTS FOR THE DEGREE OF

DOCTOR OF PHILOSOPHY

in

The Faculty of Graduate and Postdoctoral Studies

(Chemistry)

THE UNIVERSITY OF BRITISH COLUMBIA

(Vancouver)

January 2017

Abstract

Self-assembled monolayers (SAMs) are important structures commonly employed to functionalize metal surfaces. To optimize a metal-SAM construct, it is important to characterize the influence of the surface crystallography. In this thesis, a single crystal Au bead electrode was employed to investigate different types of SAMs, enabling studies on a variety of surfaces under identical conditions and avoiding laborious experimental replicates on a large number of crystal orientations.

The application of a single crystal Au bead electrode was demonstrated by investigating the reductive desorption process for two types of SAM: the alkanethiolate SAM and the α-aminoisobutyric acid (Aib) peptide thiolate SAM. Using in situ fluorescence imaging, the influence of surface crystallography on reductive desorption was observed, reflected as a correlation between the density of broken bonds of a surface and the reductive desorption potential of a SAM deposited on the surface. Besides the surface crystallography, intermolecular interactions also had a significant impact on determining the desorption potential.

Aib peptide thiolate SAMs on a Au(111) facet were further investigated. It was found that the low packing density Aib peptide thiolate SAMs exhibited a potential-modulated fluorescence response which was believed to be due to the orientational or structural change of the peptide molecules in response to the applied potential.

The potential-driven reorientation effect of the DNA SAMs has been intensively explored due to its application in biosensing. Characterization of the DNA SAMs with in situ fluorescence methods suggested that surface crystallography exerts an influence not only on the formation of the DNA SAMs but also on the efficiency of the potential-driven response. Moreover, a spectroelectrochemical technique that couples electrochemistry, fluorescence microscopy and harmonic analysis was developed to explore the non-linearity of the fluorescence response to an applied AC potential. This technique could be potentially applied to detect changes in DNA

hybridization state.

The experimental results demonstrate the convenience and wide applicability of using a single crystal Au bead electrode to investigate SAMs. On the other hand, applying existing and developing new spectroelectrochemical techniques give insights into creating SAMs with desirable properties.

Preface

All the experimental work presented in this thesis was performed by the author in Advanced Materials and Process Engineering Laboratory (AMPEL) at University of British Columbia (UBC). The experimental design and data analysis was performed in collaboration with Dr. Dan Bizzotto (the research supervisor).

Contents from two publications have been included in part of the thesis.

A journal article (Yu, Z. L.; Casanova-Moreno, J.; Guryanov, I.; Maran, F.; Bizzotto, D. "Influence of Surface Structure on Single or Mixed Component Self-Assembled Monolayers via in Situ Spectroelectrochemical Fluorescence Imaging of the Complete Stereographic Triangle on a Single Crystal Au Bead Electrode" *J. Am. Chem. Soc.* **2015**, 137, 276-288.) covers the contents presented in Chapter 4 and a portion of Chapter 6. The thesis author performed all the experiments in this publication and the majority of data analysis with the advice from Dr. Dan Bizzotto. Dr. Jannu Casanova-Moreno optimized the DNA SAM preparation procedures previously and these procedures were followed by the thesis author in this publication. Dr. Ivan Guryanov and Dr. Flavio Maran at University of Padova synthesized the BODIPY fluorophore labeled thiol-modified Aib peptide HS-Aib4-BODIPY. Dr. Dan Bizzotto structured the manuscript which was edited by the thesis author and Dr. Jannu Casanova-Moreno.

Part of a book chapter (Casanova-Moreno, J.; Yu, Z. L.; Massey-Allard, J.; Ditchburn, B.; Young, J. F.; Bizzotto, D. "In-situ Spectroelectrochemical Fluorescence Microscopy for Visualizing Interfacial Structure and Dynamics in Self-Assembled Monolayers" In *Luminescence in Electrochemistry: Applications in Analytical Chemistry, Physics and Biology*; Miomandre, F. and Audebert, P., Eds.; Springer International Publishing, 2017.) contains the content presented in Chapter 5. The thesis author was responsible for experiments, data analysis and manuscript composition for the section related to the Aib peptide thiolate SAMs, with advice and edits from Drs. Dan Bizzotto and Jannu Casanova-Moreno.

Three important contributions to the work presented in this thesis are worth highlighting.

Brian Ditchburn, the glassblower in Department of Chemistry, UBC made all the cells for electrochemical and spectroelectrochemical measurements.

Arnold Kell and Dr. Mark S. Workentin at University of Western Ontario synthesized the BODIPY fluorophore labeled alkanethiol, HS-C10-BODIPY, enabling the studies of the alkanthiol SAMs presented in Chapter 4.

Drs. Ivan Guryanov and Flavio Maran synthesized the HS-Aib4-BODIPY, enabling the studies of the Aib peptide SAMs presented in Chapter 4 and Chapter 5. Dr. Flavio Maran also gave valuable advice in these studies.

Table of Contents

Appendices

List of Tables

List of Figures

Nomenclature

α	angular semi-aperture
χ^M	metal surface potential induced by dipole
ε	the dielectric constant of a medium
ε_0	the permittivity of free space
Γ_i	surface excess of a species
γ	surface tension
$1/\kappa$	diffuse layer thickness, i.e., Debye length
λ	wavelength
$\bar{\mu}$	electrochemical potential
μ_i	chemical potential of a species
Φ	work function
ϕ_2	potential at OHP
ϕ_M	potential at the electrode surface
ϕ_S	potential at bulk solution
$\triangle\phi$	dipole barrier
σ	surface charge density
σ_D	total charge density of diffuse layer

σ_I	total charge density of inner layer
σ_M	excess charge density on a metal surface
σ_S	the excess charge density on the solution side of a metal-solution interface
θ	fractional surface coverage
θ_1	angle of incident
θ_2	angle of refraction
τ	measured lifetime of a fluorophore
τ_0	intrinsic lifetime of a fluorophore
Γ	surface packing density
A	electrode area
C	capacitance
C_D	diffuse layer capacitance
C_D	diffuse layer capacitance
C_H	inner layer capacitance
C_H	inner layer capacitance
C_{dl}	capacitance of the electric double layer
C_d	differential capacitance of surface described by the simple capacitor model
d	distance between a fluorophore and a metal surface
d	distance between the two plates of a capacitor
d_{bb}	density of broken bonds
d_{min}	depth of focus or axial resolving power

d_{min}	minimum resolved distance
E	FRET efficiency
E	electric potential
e	elementary charge
E_a	a positive potential at which a SAM is adsorbed
E_b	base potential in a potential stepping process
E_d	a negative potential at which a SAM is desorbed
E_f	final potential in a potential stepping process
$E_{H(2)min}$	potential at which the second harmonic intensity is minimum
E_i	initial potential in a potential stepping process
E_{rms}	rms amplitude of an AC potential wave
E_s	step potential in a potential stepping process
F	Faraday constant
f	aperture diameter
f	focal length
f	frequency of an AC perturbation
F_{Ebase}	fluorescence intensity extracted from the last image taken at the base potential immediately after the step potential
F_{Estep}	fluorescence intensity extracted from the last image taken at a step potential
h	Planck constant
$h\,k\,l$	Miller indices
i	cathodic current

i_{Im}	imaginary component of an AC current
i_{Re}	real component of an AC current
k	Boltzmann constant
$\mathbf{k}$	wavevector
k_r	emission rate constant
k_{nr}	non-radiactive decay rate constant
n	charge number
n	refraction index of a medium
n^0	number concentration of a z:z type of electrolyte
p	momentum
Q	total charge
R	distance between a FRET donor-acceptor pair
R_0	Förster Radius
R_S	solution resistance
R_S	solution resistance
S_0	electronic ground state
S_1	first singlet electronic excited state
T	absolute temperature
T_m	the temperature at which half of the DNA strands are in ssDNA state
V	voltage applied across the two plates of a capacitor
v	scan rate of a linear scan voltammetry measurement

x_1	distance betwen IHP and the metal surface
x_2	distance betwen OHP and the metal surface, i.e., inner layer thickness
AC	alternating current strictly, broadly referring to a signal that changes periodically with time
Aib	α-aminoisobutyric acid
BODIPY	the abbreviation of boron-dipyrromethene and the trade name for the series of fluorophores with the core structure of 4,4-difluoro-4-bora-3a,4a-diaza-s-indacene
CCD	charge-coupled device
CE	counter electrode
DAQ	data acquisition board
DC	direct current strictly, broadly referring to a signal that does not change periodically with time
DFT	density functional theory
dsDNA	double-stranded DNA
EC-AFM	electrochemical atomic force microscopy
EM gain	electron-multiplying gain
fcc	face-centered cubic
FLIM	fluorescence-lifetime imaging microscopy
FRET	fluorescence resonance energy transfer
hcp	hexagonal close packed
HPLC	high performance liquid chromatography
IHP	inner Helmholtz plane

IPE	ideal polarized (or ideally polarizable) electrode
LB film	Langmuir–Blodgett film
LEED	low-energy electron diffraction
MCH	6-mercaptohexan-1-ol
NA	numerical aperture
OHP	outer Helmholtz plane
PAGE	polyacrylamide gel electrophoresis
PCT	potential of conformation transition during a DNA reorientation process
PMT	photomultiplier tube
PZC	potential of zero charge
QY	quantum yield
RC circuit	resistor–capacitor circuit
RE	reference electrode
rms	root mean square
SAM	self-assembled monolayer
SCE	saturated calomel electrode
ssDNA	single-stranded DNA
STM	scanning tunneling microscropy
Tris	2-amino-2-(hydroxymethyl)propane-1,3-diol
UV	ultraviolet
WE	working electrode

Acknowledgements

My journey to Canada, to Vancouver and to University of British Columbia is a difficult but rewarding one. During this journey, so many people gave me helping hands, without whom this work cannot be presented here. I am sincerely expressing my acknowledgments to to all of them.

Dan, forgive me if I don't call you Dr. Bizzotto in a formal document. I am so glad that I have you as my supervisor. Your sense of responsibility, your scope of knowledge, your passion in research, your openness to diversity and your easily approachable personality, guide me through the difficulties and provide me with rewards during the journey.

All previous and present members or joint-members of Bizzotto lab that overlap with me: Dr. Amanda Musgrove, Dr. Jannu Casanova-Moreno, Dr. Tony Yang, Dr. Nidal Ashwawreh, Issac Martens, Santa Maria Gorbunova, Jonas Pfisterer, Kaylyn Leung, Elizabeth Fisher, Kamil Krawczyk, etc., I am very grateful to all of you for whatever helps you gave me. In particular, Amanda and Jannu, I enjoyed a lot when I was still a junior member of the group and you two help me so much, not only on work, but also out of work.

The contributions from the staffs in Department of Chemistry or AMPEL may not always be noticeable but are always invaluable. In particular, the glass blower in Department of Chemistry, Brian Ditchburn, fabricated all the electrochemical and spectrochemical cells of incomparable quality, making possible all the experiments presented here.

The valuable advice from experts in particular fields are highly appreciated: notably, Dr. Flavio Maran, who gave advice in Aib peptide, Dr. Hua-Zhong Yu and Dr. Thomas Doneux, who gave advice in DNA and Dr. Jeff Young and Jonathan Massey-Allard, who gave advice in metal-mediated fluorescence quenching.

Alumni from School of Chemistry and Chemical Engineering, Nanjing University, it is such an unforgettable experience for me to continue to study and work with you in Department of

Chemistry, UBC. Ru Li, Zhibo Liu, Zhengyu Cheng, Hui Yang, Cheng Qian and Sanjia Xu, how much difficulty I would have without you.

Zhaocheng Zeng, I have known you for almost twenty years and you are still one of my best friends. We both came to Canada to study and to work, albeit in different fields and in different cities, but any time when one of us had difficulty, the other one delivered the the psychological support immediately. I will cherish this friendship forever. Yiwei Li, you have also been a fiend of mine for almost twenty years. It is true that we lost contact for many years since you moved to Canada, but what a good luck I have to meet you again in Vancouver.

From a foreigner to a *de-facto* Vancouverite, this transition was indeed very smooth for me with such supports. Aunt Koi-Chi Chan and family members, although you are only distant relatives of me, you helped me settle down and often served me dinner, preventing me from feeling lonely. Two very friendly landlords, Eric Xu and Fluorence Tam, warmly hosted me, just as their family member, making me enjoy living in Vancouver and with Vancouverites.

The time I spent in the UBC Table Tennis Club was really beneficial to me. It was not just about relaxation and exercise. There, I not only made friends sharing the same hobby, but also made fiends from a variety of different fields. It might sound strange, but I am very grateful to those who broaden my understanding in math, physics, computer science, medical science, even history and music. What is more, about 60% of this thesis was written in the club office room, which was a very nice room.

Last but not least, my beloved parents and grandparents, you all have high expectations for me and uninterruptedly support me. I might not be able to satisfy all your expectations but I am sure your supports are not wasted. I am proud of having supports from you and I hope you will also be proud of me eventually.

Chapter 1

Introduction

1.1 Rationale

Self-assembled monolayers (SAMs) are organized surface structures formed when organic compounds are spontaneously adsorbed onto a solid substrate. Such structures can modify the properties of the solid substrate. Often the solid substrate is a metal (Au in this work) and the SAM-metal construct can be further developed into an electrochemical biosensor, because two fundamental elements of a biosensor, i.e., the bio-receptor and the transducer [1] can be conveniently incorporated. Therefore, investigating and engineering the SAM-metal construct has developed into an important research topic in an effort to construct biosensing interfaces with desirable performance [1–7]. There are many critical aspects of the SAM-metal construct in reaching the ultimate goal of optimizing the performance of biosensing interfaces, of which an important one is the influence of surface crystallography on SAMs [5]. Intuitively, surface crystallography determines a number of surface physical or chemical properties, e.g., atomic arrangement, surface roughness, and surface energy, which in turn influence the performance of the biosensing interface. The atomic arrangement can exert an impact on the structures and surface concentrations of the immobilized molecules, further affecting the binding specificity and sensitivity. Mixed-component SAMs are typically employed to control the density of bio-receptors and improve the accessibility to analytes. However, it has been proven that the local density of bio-receptors in these mixed-component SAMs depends on the surface crystallography [8]. Furthermore, the stability of a biosensing interface is greatly dependent on the adsorption strength, which in turn depends on surface energy [4, 5]. Thus the influence of surface crystallography on SAMs is profound and requires detailed exploration.

Studying the influence of surface crystallography on SAMs with single-crystal electrodes

has been established and widely exploited [9–12]. However, the conventional approach involves preparing a series of single crystal electrodes with designated crystallographic orientations and conducting copious experiments on these electrodes. On one hand the types of crystallographic orientations were mainly limited to low-index ones, and on the other hand the copious experiments required strict control of experimental conditions in order to achieve desirable reproducibility. Thus, in this thesis, a single crystal Au bead electrode with a family of crystallographic surfaces is employed as the substrate for the SAMs in an attempt to self-consistently investigate the influence from the crystallographic orientations within the stereographic triangle under identical conditions.

Electrochemistry is a natural tool to characterize the properties of a SAM-metal construct potentially as the platform for an electrochemical biosensor. However, conventional electrochemical methods only inform on the average response of an interface. Electrochemical methods can be coupled with various spectroscopy methods to achieve in situ spectroelectrochemical characterization with desirable resolution and to obtain information from different aspects [13]. Fluorescence microscopy, with a resolution down to the micrometer-to-submicrometer scale considering the Abbe resolution limit [14], is coupled with electrochemical methods to obtain such information as the lateral segregation of species on a surface and the longitudinal separation of species from a surface. In addition, the in situ fluorescence techniques enable the investigation of the potential-controlled properties of SAMs, which are essential for electrochemical biosensing interfaces.

1.2 Scope

The single crystal Au bead electrode will be employed as the substrate for the SAMs of interest throughout this thesis. Several different types of SAMs will be explored and different spectroelectrochemical techniques will be utilized to achieve a better understanding of these SAMs. Since this thesis covers many disciplines, it is necessary to briefly review the background theories behind these topics. The fundamental theoretical background combined with a general literature review will be presented in Chapter 2. Following the theoretical background, an overview of the general experimental methodology and instrumentation will be presented

in Chapter 3. In Chapter 4, a well-studied alkanethiolate SAM and a recently-developed α-aminoisobutyric acid (Aib) peptide thiolate SAM will be explored with an in situ fluorescence imaging technique to demonstrate the influence of the surface crystallography on the reductive desorption process and the convenience of using the single crystal Au bead electrode. SAMs formed with Aib peptides which have a special helical structure will be further explored and presented in Chapter 5. Chapter 6 will include studies of an alkanethiolate-spaced DNA SAM. This SAM will be first investigated with the imaging technique to demonstrate the influence of surface crystallography on DNA formation. In addition, a harmonic analysis technique of non-linear fluorescence will be developed to explore the potential-driven reorientation effect of the DNA SAM, which can be potentially applied in DNA sensing. Finally the results of Chapter 4 to 6 will be summarized in Chapter 7. In this chapter, the significance of using the single crystal Au bead electrode as the substrate will be discussed and future studies will be proposed.

Chapter 2

Theoretical background and literature review

In this chapter, a general review of theoretical background is presented in order to help understand the disciplines covered in the thesis. The single crystal Au bead electrode will be employed as the substrate for the SAMs of interest, so it is necessary to briefly discuss the surface crystallography of a face-centered cubic (fcc) single crystal. Fundamentals of SAMs are also presented, highlighting the structures of SAMs on Au crystalline surfaces. Coupled electrochemical methods and fluorescence techniques are the analytical tools used to investigate the systems. General principles of electrochemistry are reviewed, with the focus on depicting the interface between the SAM-modified Au surface and the electrolyte solution in electrochemical terms. A brief review of fluorescence near a metal surface is given in an attempt to intuitively describe the metal-mediated quenching effect. With the theoretical background reviewed, this chapter also aims at establishing a bridge between the systems studied and the methods employed.

2.1 Surface crystallography of a face-centered cubic single crystal

2.1.1 Overview

Crystallography is the study of the periodic atomic structures in crystalline solids. Traditionally, crystallography mainly focuses on the three-dimensional arrangements of the atoms in bulk crystals. As a consequence of the fast development of surface science and nano science where not all three dimensions have infinite atomic arrangements, surface crystallography becomes

an important branch of crystallography. In bulk crystals, usually, three-dimensional periodic geometric models simulate the systems with high accuracy. In surface crystallography, the systems are two-dimensional in a macroscopic scale and three-dimensional in a microscopic scale. For simplification, the truncated bulk crystal periodic models can be used to describe the ideal crystal surfaces. However, since the periodicity breaks in one dimension, there are some special structures and properties associated with the broken periodicity. Thus, some modifications of the models are necessary to describe the system more accurately [15]. In this section, what will be reviewed are the basic concepts of bulk crystals, the use of truncated bulk crystal models for description of the ideal crystal surfaces and the necessary modifications of the models for description of the real crystal surfaces. Au is the metal of interest in this thesis, and has a face-centered cubic (fcc) structure, so the review of fcc crystallography will be the main focus.

2.1.2 Basic concepts of bulk crystallography

The key characteristic of a crystal is its three-dimensional periodic repetition in atomic arrangement. To describe this periodicity, a lattice of infinite size is introduced. Based on the symmetry of the crystal, three non-unitary lattice vectors $\mathbf{a}$, $\mathbf{b}$ and $\mathbf{c}$ can be chosen to form the basis of the coordinate. Within the lattice, any lattice point resumes the same environment after the transitional operation of Equation 2.1 (u, v and w can be any integers).

$$\mathbf{r} = u\mathbf{a} + v\mathbf{b} + w\mathbf{c} \tag{2.1}$$

The smallest repeating unit of the lattice is the unit cell. The unit cell is a parallelepiped formed by varying u, v and w from 0 to 1. To describe a crystal more conveniently, usually there are atoms or molecules located in the vertexes of the parallelepiped. The relationship of the lengths of the edges, a, b and c and the angles between any of the two vectors α, β and γ, which signify the symmetry of the crystal, are called lattice parameters. Combining the crystallographic restriction theorem, i.e., in a crystal lattice, only 1-fold, 2-fold, 3-fold, 4-fold and 6-fold rotation axes and rotoinversion axes (1-fold rotoinversion operation is equivalent to inversion operation, 2-fold rotoinversion operation is equivalent to mirror operation) are allowed,
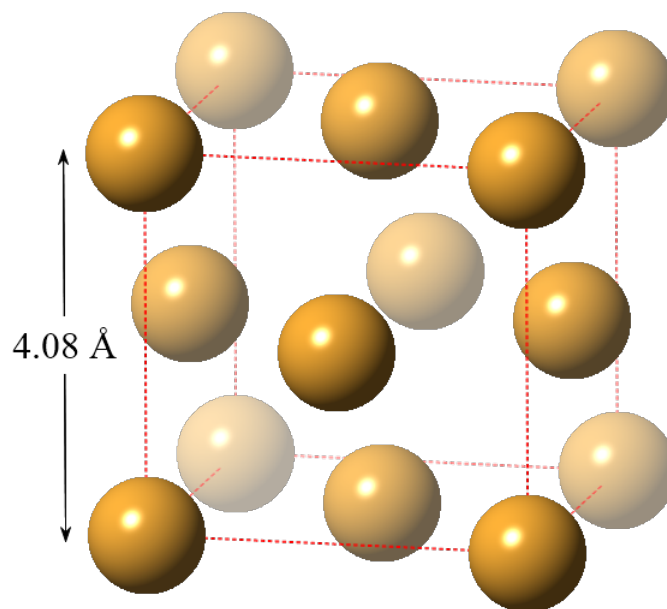
Figure 2.1: Unit cell of Au (created with CrystalMaker).

in 1850, French physicist Auguste Bravais derived the 14 lattices categorized into 7 crystal systems [16]. Thereafter, theses lattices are usually called Bravais lattices.

For the type of lattice of interest, the fcc lattice (also called Cubic-F), the lattice parameters follow: $a = b = c$, $\alpha = \beta = \gamma = 90°$, just as the other cubic lattices. The unit cell of Au is shown in Figure 2.1. As can be seen, the Au unit cell is the most fundamental type of fcc unit cell (as compared to: e.g., diamond). Each unit cell contains 4 Au atoms and the cell parameter a equals 4.08 Å. The fcc lattice is highly symmetric and the fact that each element point is a Au atom even enhances the degree of symmetry in space. The space group $F\frac{4}{m}\bar{3}\frac{2}{m}$ (usually simplified as $Fm\bar{3}m$) denotes the following symmetry elements: first direction - the 4-fold rotation axes along the cell edges and the mirror planes perpendicular to them; second direction - the 3-fold rotoinversion axes along the cell body diagonal direction; third direction - the 2-fold rotation axes along the cell face diagonal direction and the mirror planes perpendicular to them.

2.1.3   Basic concepts of surface crystallography

Surface crystallography can be derived from bulk crystallography. From Equation 2.1, a lattice can be described by the sum of spanning the three non-co-planar base vectors **a**, **b** and

c. Here, for example, if u is fixed, the three-dimensional vector **r** degenerates into a two-dimensional vector, which is used to describe a plane. Varying u results in a collection of parallel planes. This suggests a lattice can be viewed as a stack of parallel planes.

Miller indices (named after the Welsh mineralogist William Hallowes Miller) $h\,k\,l$ have been introduced to denote a plane in a crystal lattice. Still considering the three-dimensional coordinate with the three base vectors **a**, **b** and **c**, if a plane has intercepts r, s and t on the three directions, then the plane can be expressed as $\frac{u}{r} + \frac{v}{s} + \frac{w}{t} = 1$ and the group of parallel planes can be expressed as $\frac{u}{r} + \frac{v}{s} + \frac{w}{t} = C$. By multiplying both sides of the equation with a common multiple (this must be durable according to the Law of Rational Indexes [16]), the final expression can be written as Equation 2.2, where h, k, l, are all integers and called Miller indices.

$$hu + kv + lw = C \tag{2.2}$$

By convention, the greatest common divider of h, k, l is 1 since parallel planes experience the same environment in an infinite crystal.

Miller indices are usually quoted in brackets. Indices in different types of brackets have different physical meanings [15]. Indices in the round brackets (hkl) denote a particular plane where the indices can be negative. Indices in the curly brackets $\{hkl\}$ denote a family of equivalent planes based on the symmetry of the lattice. Indices in these two types of brackets, namely (hkl) and $\{hkl\}$ are used to denote crystallographic planes. The form of (hkl) is seen more often although strictly speaking in a lot of cases $\{hkl\}$ should be used. In this thesis, the form of (hkl) is used for the highly symmetric fcc crystal as a routine without interrogating the strict definition. Moreover, for a cubic lattice, because of the high order of symmetry, the sequence of h, k, l is highly flexible, which is not true for the other crystal systems. For example, the plane of (210) and the plane of (120) are symmetrically equivalent in a cubic lattice. Thus, hereafter, $h \geqslant k \geqslant l$ is also followed as a routine. Worth mentioning is that indices in the square brackets $[hkl]$ denote a particular direction based on the base vectors **a**, **b** and **c** where the indices can also be negative. Likewise, indices in the angle brackets $<hkl>$ denote a family of equivalent directions based on the symmetry of the lattice.
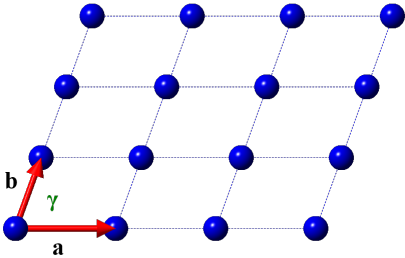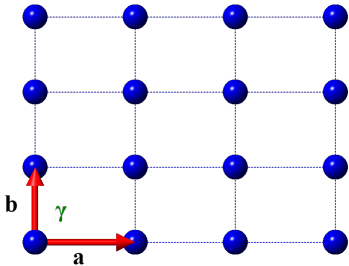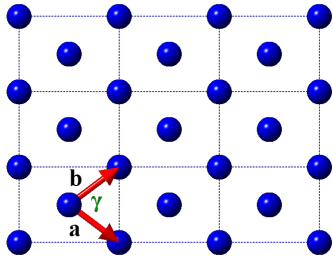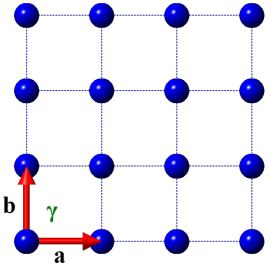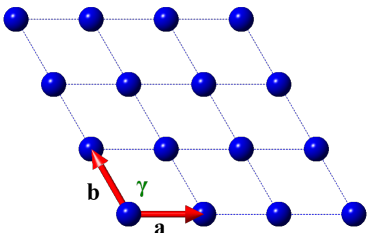
The crystallographic restriction theorem also applies to two-dimensional surfaces. As a result, there are only five types of two-dimensional Bravais lattices (Table 2.1): oblique, rectangular, centered rectangular, square and hexagonal.

The space group of Au, $F\frac{4}{m}\bar{3}\frac{2}{m}$ not only denotes the symmetry elements in three fundamental directions in space, but also denotes the type of two-dimensional lattice of an atomic monolayer of the three directions. The first direction is the normal direction of the (100) plane, which belongs to the square lattice. The second direction is the normal direction of the (111) plane, which belongs to the hexagonal lattice, and the 3-fold rotoinversion axis becomes a rotation axis if an atomic monolayer is considered. The third direction is the normal direction of the (110) plane, which belongs to the rectangular lattice.

2.1.4 The ideal fcc surface crystallography

An atomic monolayer is simply a conceptual understanding. The more reasonable model is an infinite three-dimensional lattice truncated at a particular direction. However, the three-dimensional model is not always easy to present. Therefore, a stereographic projection of the family of crystallographic planes onto a two dimensional map is frequently used. To construct such a map, first, a lattice is encapsulated into an auxiliary sphere which shares the same center with the lattice. From the center of the lattice, all the crystallographic plane normal vectors can find their intersections on the sphere surface (Figure 2.2a). If the lattice has a mirror plane, it is only necessary to project the planes above the mirror plane (usually a (100) plane that crosses the center for a cubic lattice) of the lattice onto a hemisphere. Connecting the pole of the blank hemisphere, and the plane intersections on the opposite hemisphere results in the intersections on the equator plane (Figure 2.2b). These intersections on the equator planes make the stereographic projection map of the crystallographic planes (Figure 2.3a). Since the cubic lattice is highly symmetric, the circular stereographic projection map can be further simplified into a stereographic triangle with the three low-index planes (100), (111) and (110) as the vertexes. The stereographic projection can be extended to any parallel plane with respect to the equator plane, as shown in Figure 2.4a. The points on the hemisphere representing crystallographic surfaces are sometimes perpendicularly projected onto this parallel plane (Figure

Table 2.1: The five types of two-dimensional Bravais lattices and their Lattice parameter relationship

Two-dimensional Bravais lattice	Lattice parameter relationship
	$a \neq b$; $\gamma \neq 90°$, $60°\,or\,120°$
	$a \neq b$; $\gamma = 90°$
	$a = b$; $\gamma \neq 90°$, $60°\,or\,120°$
	$a = b$; $\gamma = 90°$
	$a = b$; $\gamma = 120°$
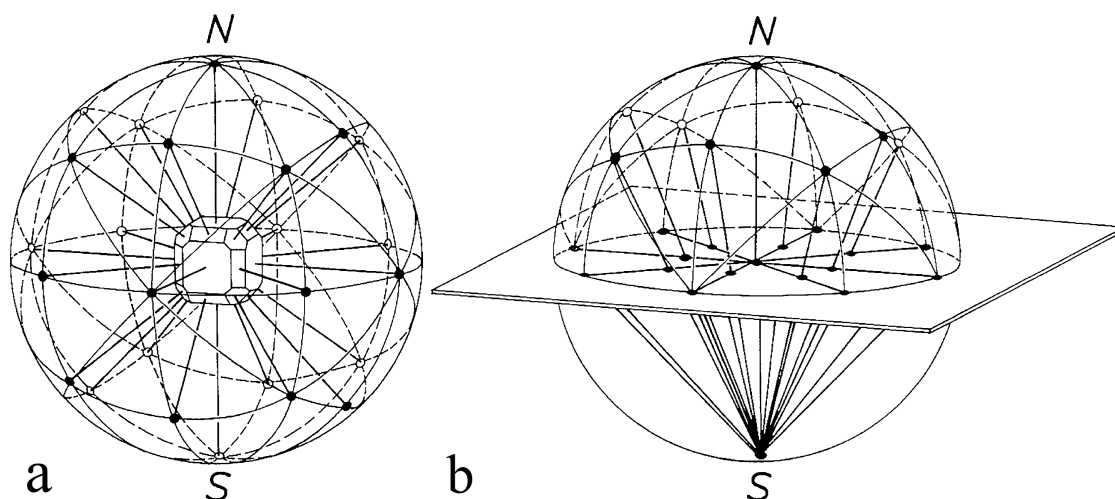
Figure 2.2: Constructing the stereographic projection of the crystallographic planes by: (a) vectorial projection of the crystallographic planes onto a sphere and (b) stereographically projection from the sphere onto the equator plane. Adapted from [17] with permission from Springer Berlin Heidelberg.

2.4b), because practically this is the projection realized during imaging. The stereographic triangle shown in Figure 2.3b is created by this perpendicular projection. Strictly speaking, it should not be called a stereographic triangle any more, but this term has been widely used to describe the crystallographic planes on a cubic crystal surface without specifying the projection used.

For the low-index planes such as (111) and (100), the atoms adopt the closest packing and the second closest packing in two-dimension, so the exposure of the underlying layers of atoms is relatively small. However, for other crystallographic planes, even the third low-index plane (110), there are significant "gaps" between close-packing rows of atoms. Thus, surface crystallography is dealing with three-dimensional systems where the z-axis is atomic scale.

Herein (511) is used as an example to demonstrate the morphology of high-index planes. Figure 2.5a shows the top view of a lattice truncated at (511) direction. The red plane is the conceptual (511) plane with parallel rows of atoms above it and the rest below it. The gaps between parallel rows of close-packing atoms of the same height are relatively big so the lower rows of close-packing atoms are exposed. Viewed from the side (Figure 2.5b) the crystallographic plane looks like steps. Therefore, this type of surfaces are called stepped surfaces composed of wide terraces and narrow steps. In the case of (511), the terrace plane is the

Figure 2.3: (a) A circular stereographic projection map (created with WinWulff) and (b) the steoreographic triangle of the cubic lattice created by perpendicular projection.
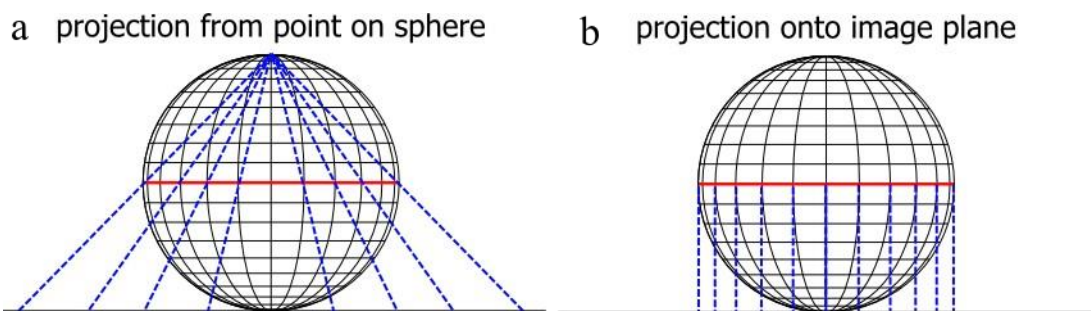
Figure 2.4: Comparison of (a) stereographic projection and (b) perpendicular projection. Adapted from [8] with permission from American Chemical Society.

(100) plane (indicated with the square in 2.5a) and the step plane is the (111) plane (indicated with the triangles in 2.5b). The terrace plane is usually one of the low-index planes with close packing. The step width is usually one atom for an ideal macroscopic two-dimensional crystallographic plane simply because forming multi-atomic steps requires removing atoms below the conceptual plane by non-ideal truncation of the lattice. For a plane (hkl) ($h \geqslant k \geqslant l$, excluding (111) and (100)), if $h = k$ or $k = l$, or if $h \cdot k \cdot l = 0$, the plane is a stepped plane. Stepped planes are located on the sides of the steoreographic triangle. (110) is sometimes viewed as a stepped plane composed of equal width of (111) terrace and (111) step.
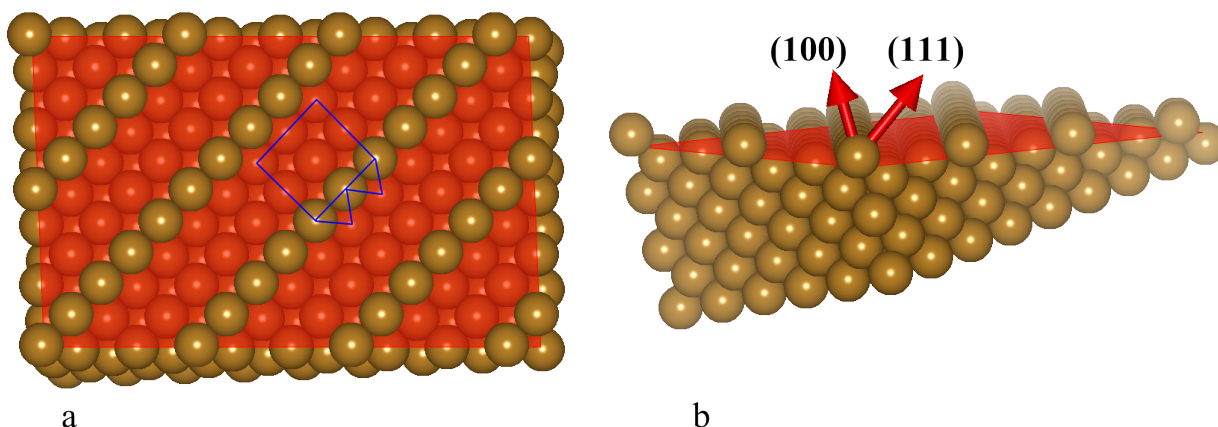
Figure 2.5: (a) Top view and (b) side view of a lattice truncated at (511) direction.

A plane like (931) (Figure 2.6a) adopts a more complicated morphology. The step edges themselves are stepped. This type of surfaces are called kinked surfaces. The terrace plane is still one of the low-index planes with close packing. However, the step plane is one of the stepped surfaces described above. In the case of (931), the terrace plane is the (100) plane

(indicated with the square in Figure 2.6a) and the step plane is the (331) plane. For a plane (hkl), if $h \neq k \neq l$ and $h \cdot k \cdot l \neq 0$, the plane is a kinked plane. Kinked planes are located in the interior of the stereographic triangle. A kinked surface does not have a mirror plane. Consequently, changing the sequence of any two of the three indices h, k, l effectively yields the mirror image crystallographic plane. As is shown in Figure 2.6, the (931) plane and the (913) planes are mirror images of each other. Therefore, a kinked surface is chiral. Chiral surfaces are potentially useful in chirality recognition or separation [18–20]. However, this thesis does not focus on chiral systems. Therefore, the mirror image crystallographic planes are not specifically differentiated and (hkl) in which $h \geqslant k \geqslant l$ is also used to represent the group of kinked surfaces regardless of their chirality.

a b
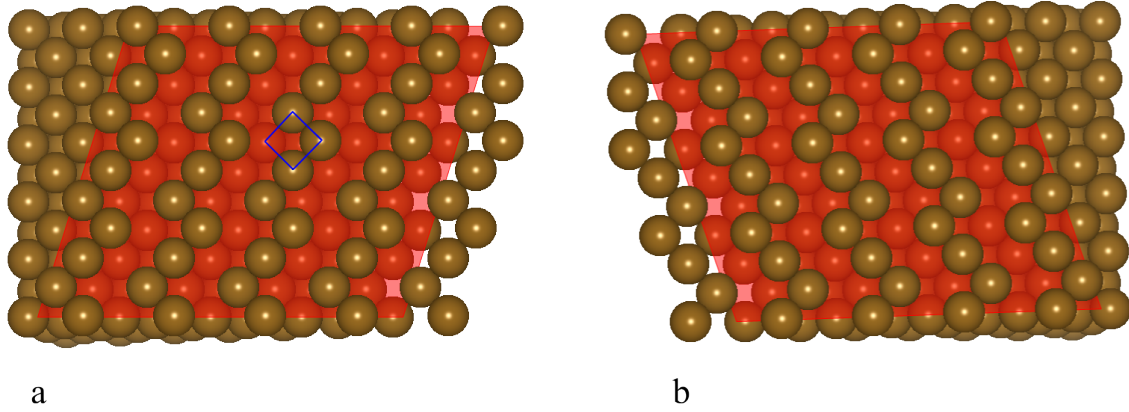
Figure 2.6: Top views of lattices truncated at a. (931) direction and b. (913) direction.

To describe the morphology of stepped and kinked surfaces, Somorjai proposed the step notation [21, 22]. The Miller indices of a stepped surface can be decomposed into the combination of the terrace plane Miller indices and the step plane Miller indices, expressed in Equation 2.3.

$$(hkl) = n_t(h_t k_t l_t) + n_s(h_s k_s l_s) \tag{2.3}$$

This is also called the additivity theorem which can be proved using the reciprocal lattice vector calculations [15]. Note that the Miller indices here can be negative. The step notation is usually written in the form of Equation 2.4.

$$(hkl) \equiv (n_t + 1)(h_t k_t l_t) \times n_s(h_s k_s l_s) \qquad (2.4)$$

The coefficients $(n_t + 1)$ and n_s have clear physical meanings: $(n_t + 1)$ is the width of the terrace plane and n_s is the width of the step plane. It can be seen from Figure 2.5b that the (511) plane is composed of the 3 atom wide (100) terrace and the 1 atom wide (111) step (the atom shared with the terrace and the step is usually assigned to the terrace), thus the step notation of (511) is $3(100) \times (111)$.

Worth mentioning is that the selection of terrace and step planes might not be unique. Taking (221) shown in Figure 2.7a as an example, (111) is the terrace plane, but either (110) (indicated with the rectangle in 2.7a) or (111) (indicated with the triangle in 2.7a) can be viewed as the step plane and the terrace width is dependent on the step plane chosen. Therefore, the step notation of (221) is either $3(111) \times (110)$ or $4(111) \times (111)$ (strictly speaking, the step plane here should be written as $(11-1)$ or $(11\bar{1})$). Since (110) itself is stepped and composed of equal widths of (111) planes, it is more natural to view (111) as the step when the long side of the (110) rectangle is the step of (221). However, another plane (310) shown in Figure 2.7b does not have (111) as the step plane, because the short side of the (110) rectangle is the step of (310) (indicated with the rectangle in 2.7b). Therefore, the step notation of (310) can be only written as $3(100) \times (110)$.

a   b
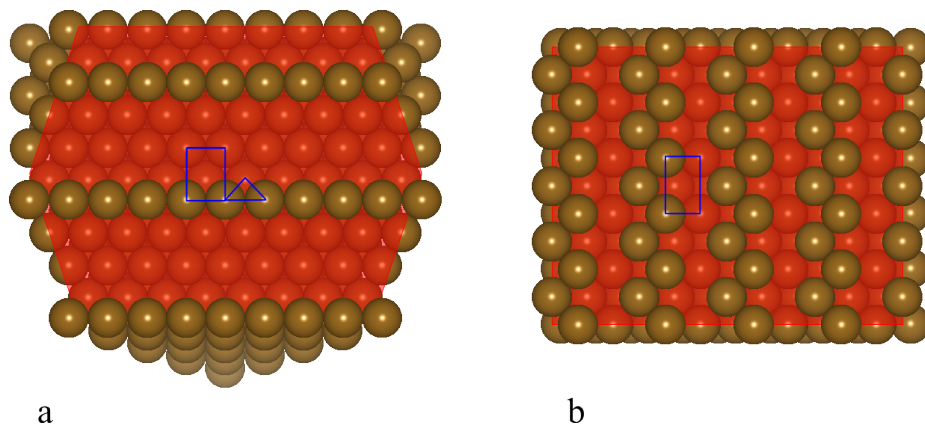
Figure 2.7: Top views of a lattice truncated at (a) (221) direction and (b) (310) direction.

Table 2.2 shows the step notations for the major crystallographic planes within the three

side zones from (111) to (100), from (100) to (110) and from (110) to (111) in the stereographic triangle. The general trends are as below. The terrace plane is the closest low-index plane and the step plane is the far end low-index plane of the same zone. (311), (210) and (331) are three "turning point" planes of the three zones where the two low-index planes of at the end of the zone can be viewed as either the terrace plane or the step plane. The group of ($n+2$, $n+2$, n) planes each has two step notations depending on the step plane chosen, the reason of which was given in the last paragraph.
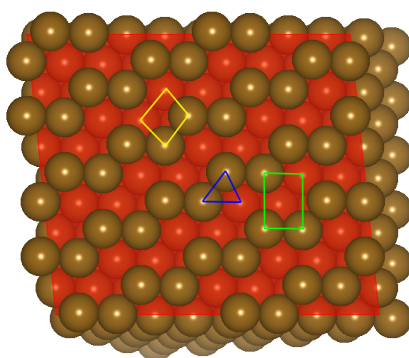
Figure 2.8: Top view of a lattice truncated at (531) direction.

The kinked surfaces are more complicated surfaces. The step notation cannot express the the kinked surfaces completely and unambiguously. Somorjai also proposed the microfacet notation which also decomposes the kinked step into low-index planes [22]. The microfacet notation is not discussed here. For a general understanding, similar to a step surface, a kinked surface that is close to a low-index plane has this low-index plane as the terrace plane. Using the additivity theorem, the kinked step plane can be found. From the stereographic triangle (Figure 2.3b), the kinked surfaces can be understood more intuitively. As the example, from (111) to (210) which is the turning point plane from (100) to (110), there exist a series of kinked planes. The kinked planes close to (111) should have (111) as the terrace plane and (210) and the step plane until a turning point after which (210) should conceptually become the terrace plane. Since (210) is stepped, so the terrace plane now becomes either (100) or (110). The same should apply to the series of kinked planes from (100) to (331) and from (110) to (311). This three kinked plane zones intersect at (531) (Figure 2.8), which would be the turning point plane of the three zones. From another aspect, in (531), the (100) terrace (indicated with a

15

Table 2.2: Step notations for the major crystallographic planes within the three side zones of the stereographic triangle (cited from and derived based on [22]).

Miller indices	Step notations	Miller indices	Step notations
(111)		(100)	
(322)	$5(111) \times (100)$	(510)	$5(100) \times (110)$
(533)	$4(111) \times (100)$	(410)	$4(100) \times (110)$
(211)	$3(111) \times (100)$	(310)	$3(100) \times (110)$
(311)	$2(111) \times (100)$	(210)	$2(100) \times (110)$
$(n{+}2, n, n)$	$(n+1)(111) \times (100)$	$(n{+}1, 1, 0)$	$(n+1)(100) \times (110)$
$(2n{+}1, 1, 1)$	$(n+1)(100) \times (111)$	$(n{+}1, n, 0)$	$(n+1)(110) \times (100)$
(311)	$2(100) \times (111)$	(210)	$2(110) \times (100)$
(511)	$3(100) \times (111)$	(320)	$3(110) \times (100)$
(711)	$4(100) \times (111)$	(430)	$4(110) \times (100)$
(911)	$5(100) \times (111)$	(540)	$5(110) \times (100)$
(100)		(110)	

Miller indices	Step notations
(110)	$2(111) \times (111)$
(991)	$5(110) \times (111)$
(771)	$4(110) \times (111)$
(551)	$3(110) \times (111)$
(331)	$2(110) \times (111)$
$(2n{+}1, 2n{+}1, 1)$	$(n+1)(110) \times (111)$
$(n{+}2, n{+}2, n)$	$(n+1)(111) \times (110)$ or $(n+2)(111) \times (111)$
(331)	$2(111) \times (110)$ or $3(111) \times (111)$
(221)	$3(111) \times (110)$ or $4(111) \times (111)$
(553)	$4(111) \times (110)$ or $5(111) \times (111)$
(332)	$5(111) \times (110)$ or $6(111) \times (111)$
(111)	

yellow quadrilateral), (111) terrace (indicated with a blue triangle) and (110) terrace (indicated with a green quadrilateral) can be found.

2.1.5 The real fcc surface crystallography

The model of an infinite three-dimensional lattice truncated at a particular direction assumes the atoms on the surface stay at the same positions as they were in the bulk. However, for a real crystal surface, this is not a reliable assumption because the atoms on the surface experience uneven forces from the two sides as soon as the crystal is truncated. To account for this environment change, typically, the atoms on the surface undergo necessary and ordered rearrangement to lower the surface energy.

The top layers of the atoms are usually not located at the assigned positions as those in the bulk crystal. A widely observed phenomenon is the top layers as a whole shift, typically vertically either closer to or farther away from the bulk crystal. This effect is defined as surface relaxation. The shift towards the bulk crystal is defined as inward relaxation, and the opposite way is defined as outward relaxation. The surface relaxation of a number of metals has been experimentally measured with low-energy electron diffraction (LEED) or theoretically calculated [23–32]. The results are not always compatible among each other. The experiment conditions and the calculation assumptions can always affect the results.

The surface relaxation of the metal of interest, Au, is not easy to measure or calculate accurately, because it is usually complicated by another surface effect: surface reconstruction. Surface reconstruction can occur at many exposed crystallographic surfaces. The reconstruction occurring on the three low-index crystallographic surfaces of Au has been well known and studied [33–43]. However, for Au, little or no reconstruction was observed on most (with some exception) stepped crystallographic surfaces with scanning tunneling microscropy (STM) [44, 45]. There is a lack of study on reconstruction on kinked crystallographic surfaces. Therefore, the basic concepts are introduced and reconstructions of the three low-index crystallographic surfaces of Au, (111), (100) and (110) will be reviewed.

Surfacial atoms can reconstruct into a different structure as compared to the bulk structure. Surface reconstruction primarily occurs on the topmost layer of a truncated lattice. After sur-

face reconstruction, this topmost layer resumes a structure with periodicity different from the layers beneath it. The reconstructed layer and the unreconstructed layers (viewed as the ideally truncated lattice) can be described with the Wood notation [46]:

$$S(hkl) - i(\frac{b_1}{a_1} \times \frac{b_2}{a_2})R\alpha - \eta A \qquad (2.5)$$

The wood notation treats the unreconstructed layers as the substrate S with the Miller indices (hkl) and the reconstructed layer as the adsorbate A. For a crystal with a single type of atom, the Wood notation is typically simplified as

$$S(hkl) - i(\frac{b_1}{a_1} \times \frac{b_2}{a_2})R\alpha \qquad (2.6)$$

The symmetry of the reconstructed layer is indicated with i, which is either "p" (usually omitted) for "primitive" or "c" for "centered". The reconstructed layer has a different two-dimensional Bravais lattice from the layers beneath. The unit cell base vectors are $\mathbf{b}_1$, $\mathbf{b}_2$ for the reconstructed layer and $\mathbf{a}_1$, $\mathbf{a}_2$ for the unreconstructed layers. If the unit cell for the reconstructed layer is rotated with respect to the unit cell for the unreconstructed layers, the angle need to be noted in α (R simply means rotation).

The reconstruction of the Au(111) surface was discovered with LEED [33]. It was generally accepted as a $(22 \times \sqrt{3})$ reconstruction [34] before detailed location of the atoms on the reconstructed layer by STM [37, 38]. Thereafter, the reconstruction of the Au(111) surface has been also written as $(23 \times \sqrt{3})$. The schematic of the reconstructed Au(111) surface is shown in Figure 2.9. The mismatch of the top layer atoms and the second layer atoms is a result of contraction of the top layer in the surface normal direction in order to reduce the surface tension. Because of this surface contraction, the Au atoms at the two proximal positions to the second layer, C and A end up in two different types of close-packing structure hollows: C is the fcc type of packing, similar to the packing scheme in the bulk and A is the hexagonal close-packed (hcp) type of packing. It takes 23 atoms to finish one period along the direction of the long side of the reconstructed unit cell (the $[11\bar{1}]$ direction), which lines up with 22 atoms along the same direction on the second layer. This model is a local structure, the actual surface has more complicated long range periodicity [38].
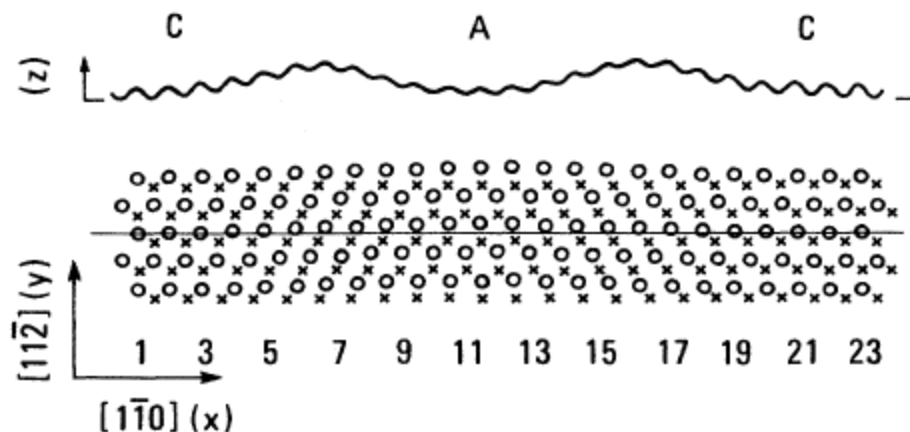
Figure 2.9: Schematic of the reconstructed Au(111) surface. The open circles denote the top layer of atoms and the crosses denote the second layer of atoms. Reprinted from [37] with permission from the American Association for the Advancement of Science.

The reconstruction of the Au(100) surface is more complex. When it was studied with LEED in the early stage, depending on the resolution of the measurements, a variety of reconstructed unit cells were found: (1×5), (20×5), (34×5), (26×48), (26×48) [34, 36]. The simplified scheme of the reconstruction is the (1×5) reconstruction shown in Figure 2.10. Before the reconstruction, the two directions of the unit cell are symmetrically equivalent. The reconstruction involves the contraction in one direction (the $[\bar{1}10]$ direction in Figure 2.10) and translation of atoms in the other direction (the $[110]$ direction in Figure 2.10), which as a consequence, resumes quasi-hexagonal symmetry [43]. The actual reconstruction of the unit cell in either direction is more subtle, also the reconstruction is dependent on the temperature [40], so there exists a variety of reconstructed unit cells.

The (1×2) reconstruction of Au(110) has been determined with a number of techniques [35, 39, 41, 42]. The schematic is shown in Figure 2.11. The intuitive way of understanding this reconstructed unit cell is the every other "missing row" of atoms along the direction of the long side of the (110) unit cell (the $[100]$ direction in Figure 2.11). The ideal (110) surface can be viewed as a stepped surface with (111) terrace and (111) step of equal widths. An ideal surface only allows one-atom steps. This reconstructed surface still has a (111) terrace and a (111) step of equal widths, but the step is a three atom step.
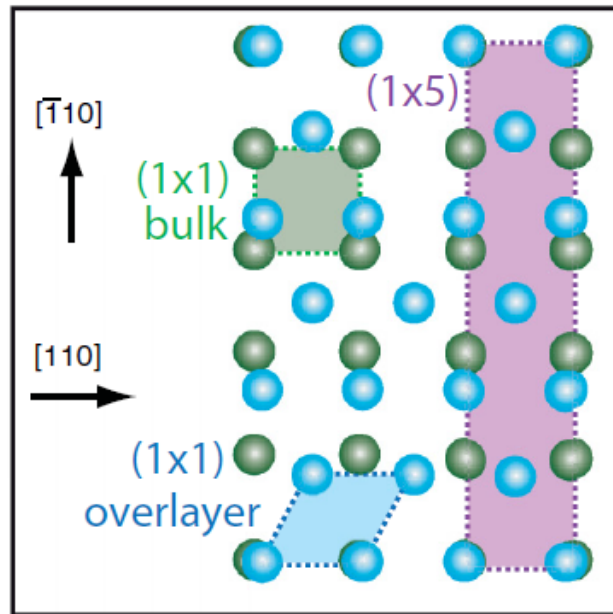
Figure 2.10: Schematic of the (1×5) reconstructed Au(100) surface. The blue circles denote the top layer of atoms and the green circles denote the second layer of atoms. Adapted from [43] with permission from American Physical Society.
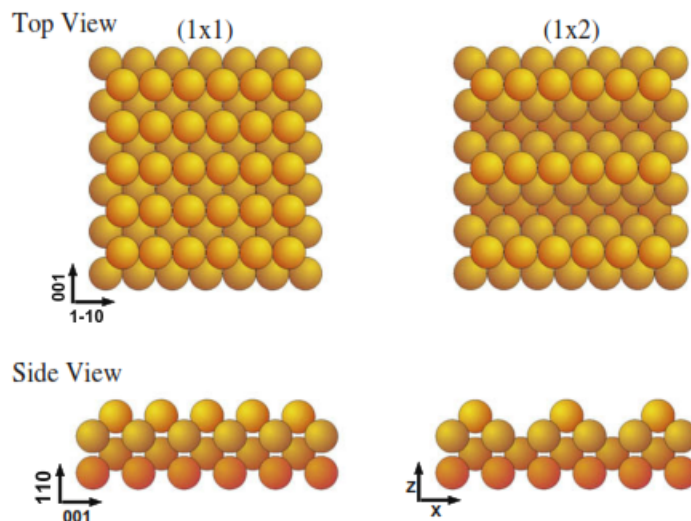
Figure 2.11: Schematic of the (1×2) reconstructed Au(110) surface. Reprinted from [42] with permission from Elsevier.

2.2 Fundamentals of self-assembled monolayers

2.2.1 Overview

An interface is the boundary between two immiscible phases, and typically if one phase is the gas phase, the interface can be called a surface. As a routine, the term "surface" is frequently used in scientific documents without strictly referring to its definition, so it is also employed here to describe an interface. Surface chemistry has become an intensely studied domain in material science as a result of the fast development of nano materials where surfaces are dominant compared to large scale materials.

The most evident characteristic of a surface is the large gradients due to the different compositions and properties of the two bulk phases between which the interface is formed. Thus it is proposed by some researchers that surfaces be viewed as a fourth state of matter [4]. Moreover, the atoms or molecules located at the surfaces are experiencing unequal forces, so they are more chemically active compared with those in the bulk phases. For instance, surfaces of some metals can spontaneously adsorb certain organic species. This forms the basis of self-assembled monolayers (SAMs). For SAMs, organic species adsorbed on the surfaces of substrates from a gas phase or a solution phase tend to organize into crystalline structures and assemble into arrays based on the arrangements of surface atoms, which in turn lower the surface energy and stabilize the surface atoms.

Figure 2.12 is a schematic diagram of an ideal SAM structure. Usually the adsorbates have head groups which chemically bind to the surface with considerable stability. A widely used head group is thiolate because it has a high affinity to a number of metals and semiconductors. The other ends of the organic adsorbates are the terminal groups that can be further linked to other structures to achieve future functionality. The head groups and terminal groups are usually connected by repeated units defined as spacers. By adjusting the length of the spacers, the thickness and other monolayer characteristics can be tuned. Therefore, the physical and chemical properties of surfaces modified with organic species are altered, or defined by the adsorbates, and this promotes surface functionalizations for designated purposes. In a sense, SAMs can act as platforms for surface process investigations. As an example, when the terminal functional groups are linked to bioreceptors, such as enzymes, nucleic acids
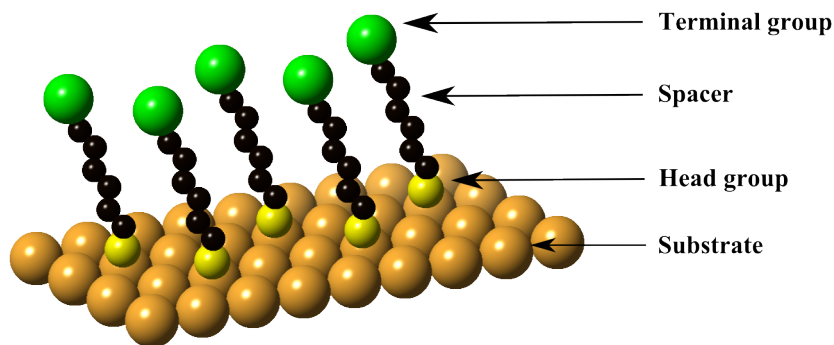
Figure 2.12: Schematic diagram of an ideal SAM structure.

or antibodies, the SAMs can be employed in biosensor applications [1]. A number of biosensors have been devised through the anchoring of different bioreceptors on the SAM platform. Among these, glucose sensors [47–51], DNA sensors [52–57] and immunosensors [58–64] have been extensively studied.

2.2.2 SAMs based on Au-S interactions

SAMs based on Au-S interactions with Au as the metal substrate and thiolate as the headgroup are a class of SAMs widely studied and applied to many fields. The main advantage of Au-S interactions is its high stability (~200 kJ/mol [4]) which accounts for SAMs of good quality and high order. In addition, Au of different forms, such as colloids, thin films, polycrystals and single crystals are available to meet different needs. Furthermore, as a noble metal, Au is relatively inert and not subject to oxidation under common conditions (e.g., being exposed in air at room temperature). Because of all the features above, SAMs based on Au-S interactions have become a primary choice for surface science studies. Among all SAMs based on Au-S interactions, SAMs formed by depositing alkanethiols on Au(111) surfaces, the most stable Au crystallographic surface, are the most intensively studied [4, 65, 66].

Assembling SAMs on substrates is usually performed in the gas phase or via the solution phase. Although the mechanism of assembly from gas phase is better understood theoretically, assembly from solution phase is practically speaking more convenient because not all thiols have an appreciable vapor pressure. This method simply requires immersion of substrates into adsorbate solutions for a certain period of time [4].

The mechanism of alkanethiol adsorption onto a gold surface is complex and sometimes controversial. There is evidence to show a two-step mechanism [66–68]. The first step is a physisorption process during which the alkanethiol molecules form a highly disordered state on the surface (Equation 2.7). The second step is a chemisorption during which the Au-S bond is formed and the H atom is released. It is generally believed that the second step follows either of the two routes below (Equation 2.8 and Equation 2.9, [O] in Equation 2 represents O_2 or other types of oxidizing agents present in the surroundings). It is also debatable what happens to the H atom [4, 66, 69–72]. Note that these proposed steps have been based on studies of alkanethiols on Au(111), but to date there is a lack of literature on whether they are generic to any SAMs based on the Au-S interaction.

$$RSH + Au_{(surface)} \rightarrow RSH_{(phys)}Au \qquad (2.7)$$

$$2RSH_{(phys)}Au \rightarrow 2RS-Au_{(SAM)} + H_{2(g)} \qquad (2.8)$$

$$2RSH_{(phys)} + [O] \rightarrow 2RS-Au_{(SAM)} + H_2O \qquad (2.9)$$
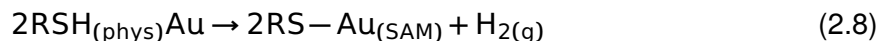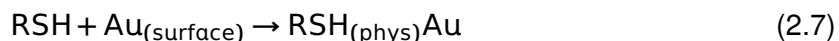
In theory, the formation of SAMs is a process driven by stabilization of active substrate surfaces. In Section 2.1.5, the reconstruction of a crystallographic surface was discussed. The reconstruction is also a process to lower the surface energy. Therefore, upon adsorption of a SAM, the surface tension is relaxed and the surface reconstruction is lifted. The process of lifting the reconstructed Au(111) surface by alkanethiol adsorbates has been observed experimentally [68, 73]. It is generally believed that highly dense alkanethiol SAMs with the relatively electronegative thiolate head group should withdraw the excess negative charge on the reconstructed surface and revert the reconstructed surface back to its (1×1) symmetry (also termed de-reconstruction) [74]. However, lifting the reconstructed surface does not result in a topmost layer becoming identical to the underlying layers. Take Au(111) as an example, the $(23 \times \sqrt{3})$ reconstruction results in a more dense surface with one additional atom per $(23 \times \sqrt{3})$ unit cell. Upon adsorption of thiol molecules, the reconstructed surface is relaxed and some atoms

are lifted on top of the top layer so that the density can be lowered to be similar to the bulk. This process leads to adatoms and vacancies. The adatoms tend to aggregate into big islands, and at the same time the vacancies also grow. As a whole, the surface becomes rough and defective [75].

When an adsorbate molecule is immobilized onto a surface, the alkyl chain orients at a particular direction. This orientation can be described using three angles (Figure 2.13): α is the tilt angle with reference to the surface normal; β is the angle between the plane of all-trans chains and the plane defined by surface normal vector and chain axis vector i.e., the angle of rotation; and χ is the angle of precession which defines the tilt direction with reference to the plane defined by surface normal vector and unit cell base vector [65, 66, 76]. For alkanethiolate SAMs on Au surfaces, these angles are dependent on the chain length of the adsorbate and the substrate crystal structure. On Au(111) surface, the tilt angle α is close to 30° [4, 77, 78] whereas for the Au(100) surface, it is only around half of that for the Au(111) surface [4, 77]. The value of β is usually close to 45° for the Au(111) surface and 70° for the Au(100) surface [4, 77]. The general trend for χ is that χ decreases as the chain becomes longer. Chain lengths of $n \leqslant 14$ and $n \geqslant 16$ fall into two different domains: $13° \leqslant \chi \leqslant 18°$ and $4° \leqslant \chi \leqslant 10°$, respectively [78].

The arrangement of adsorbed thiolates greatly depends on the exposed crystalline surfaces. The Wood notation (2.5) is also used to describe the periodicity of the adsorbates. The widely accepted pattern of alkanethiolates on Au(111) surface is the $(\sqrt{3} \times \sqrt{3})$R30° structure [4, 79]. Despite this well-established pattern, the adsorption site for the S atom is still under intense debate and not yet resolved. There is evidence from both experiments and calculations demonstrating that the S atom is located at the 3-fold hollow of the gold lattice (Figure 2.14, a = 2.88 Å) [4, 80–83]. Disagreement arises with density functional theory (DFT) studies predicting the adsorption of the S atoms on the bridge site [84–87], but these studies have been focused on the adsorption of CH_3SH or dissociated CH_3SSCH_3. Some recent experimental studies have also shown the atop adsorption site preference [88–90]. Furthermore, from the dynamic aspect, two types of adsorption sites or adsorption states may co-exist as a result of disulfide formation [91], progressing through different adsorption stages [67], or reorganization driven by two competing forces [92]. The $(\sqrt{3} \times \sqrt{3})$R30° unit cell only takes into account the
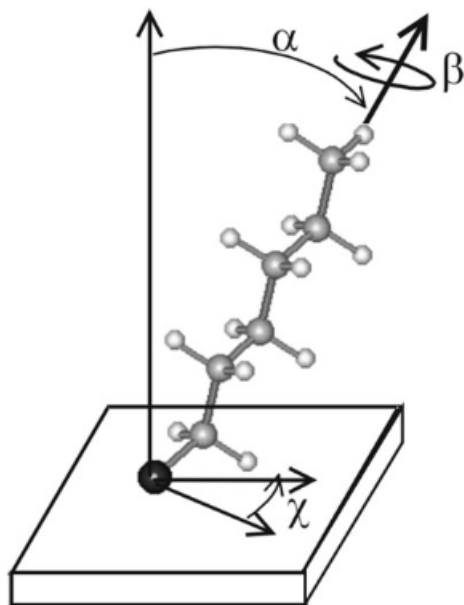
Figure 2.13: Schematic of an alkanethiol molecule immobilized on a Au surface with the three angles describing the orientation. Reprinted from [65] with permission from Royal Society of Chemistry.

position of the S atoms. If the orientation of the alkane chain is also considered, the adsorbates adopt a $(2\sqrt{3} \times 3)$ structure (Figure 2.14). An equivalent unit cell denoted as $c(4 \times 2)$ super-lattice is often used in early literature [4, 76, 93–95]. Although it is commonly accepted that the superlattice is a consequence of alkane chains of two different orientations (i.e., different χ), some evidence also implies the position of the S atoms also plays a role in the superlattice [76]. Apart from the Au(111) surface, there is a lack of systematic investigation of alkanethiol SAMs deposited on other gold surfaces. Alkanethiolate SAMs deposited on Au(100) have been studied, but the results are with much less agreement. Vapor-deposited methanethiol SAMs seem to prefer a $c(2 \times 2)$ structure [4, 77], and medium to long chain alkanethiol SAMs seem to prefer a $c(2 \times 8)$ structure with (1×4) Au missing row [96, 97], whereas alkanethiol SAMs prepared from solution phase can adopt a distribution of different structures, presumably due to different chain lengths [98–102]. These differences do not seem to be resolved yet. DFT studies have also predicted the favorable adsorption sites for a variety of surfaces, however they are not always in agreement with each other [83, 87].

In theory, the formation of SAMs is a process driven by stabilization of active surfaces, so SAMs tend to reorganize into structures patterned by exposed crystalline structures with
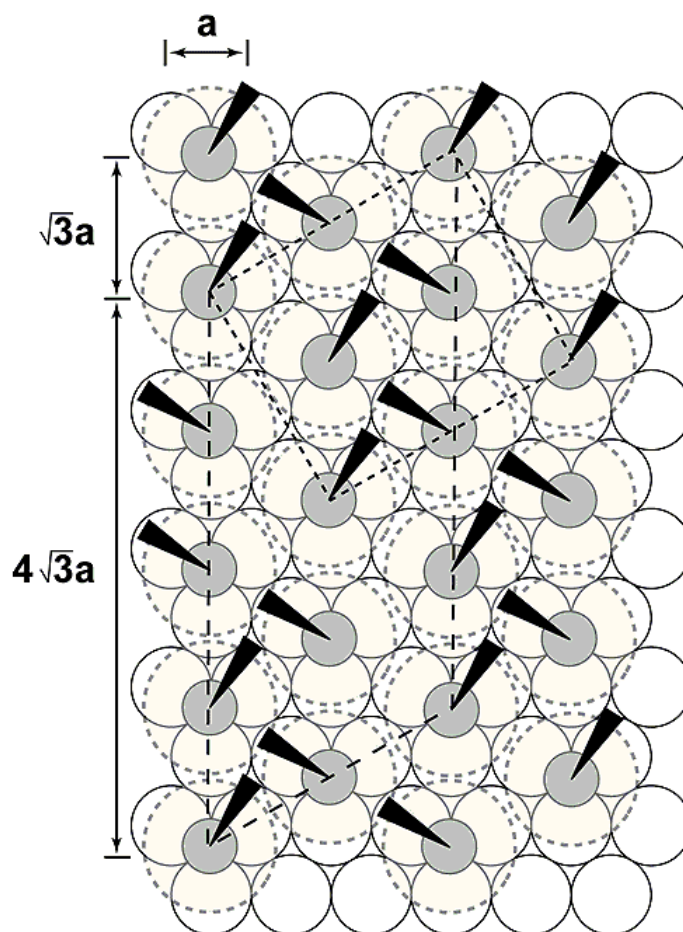
Figure 2.14: Schematic diagram of arrangement of alkanethiol SAMs on Au(111) surface with the S atoms located at the 3-fold fcc hollows. The $(2\sqrt{3} \times 3)$ unit cell is marked by short dashed lines and the $c(4 \times 2)$ unit cell is marked by the long dashed lines. Reprinted from [4] with permission from American Chemical Society.

high order and few defects. However, in practice, SAMs still possess large numbers of defects due to any non-ideal conditions involved in the processes of assembling SAMs. If the SAMs are further applied as building blocks for functionalization, the defects are inevitably affecting the performance. Although to achieve a perfect defectless SAM is almost impossible, the number of defects can be minimized by realizing the sources of defects [4, 65, 66]. Figure 2.15 depicts the possible sources of defects in a SAM formed on a polycrystalline Au surface. Take assembling SAMs from solution phase as an example: there might be some impurities either in the solution or on the substrate, which subsequently lead to defects in SAMs. Also the substrate surfaces are far from ideally depicted crystalline faces of high order, so defects
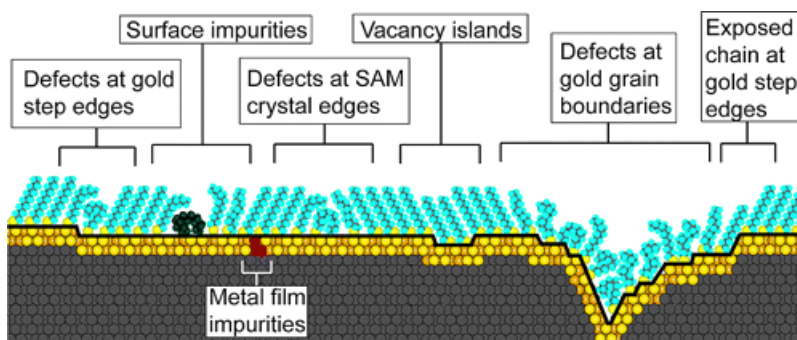
Figure 2.15: Schematic of possible sources of defects in a SAM formed on a polycrstalline Au surface. Reprinted from [4] with permission from American Chemical Society.

like vacancy islands, step edges or grain boundaries on the surfaces would eventually be inherited by SAMs adsorbed on them. Even if the substrate is a carefully fabricated crystalline surface with well-defined structure (e.g., Au(111)), a considerate number of defects can still be observed [65, 66]. One important type of defects is related to the intermolecular interactions between the adsorbate molecules. For alkanethiolate SAMs, the main intermolecular interactions is the van der Waals forces between chains. A large number of pinholes or pinstripes featuring missing molecules exist on short-chain (R ⩽ C6) alkanethiolate SAMs due to weak intermolecular interactions. [103, 104], resulting in a disordered liquid-like state [105]. On the contrary, long chain alkanethiolate SAMs (R ⩾ C16) appear to be less defective, approaching a crystalline-like state [104, 105]. However, even long chain alkanethiol SAMs tend to be in a dynamic gel-like state below the temperature of order-disorder (gel-liquid) transition. Even though typically the transition temperature for alkanethiol SAMs on planar substrates is above room temperature, the annealing and organizing process is usually too long to finish, so the gel-like state has a high motional gradient along the chain [106]. Consequently, alkanethiolate SAMs can undergo various phase transitions on substrate surfaces. For example, an unsaturated decanethiol monolayer assembled on Au(111) surface can undergo transitions between as many as six phases depending on the surface coverage [107]. Thus explains why alkanethiolate SAMs tend to be defective even on ordered crystalline surfaces.

Forming mixed-component SAMs via the thiol-exchange mechanism (i.e., partially displacing a surface-bound adsorbate with another) has become important in recent years, especially in SAM-based biosensing interfaces (e.g., DNA SAMs) where a molecular diluent is typically

used to prevent the non-specific adsorption and control the density of the bioactive adsorbate [108–111]. The presence of defects on a SAM indeed facilitates this process, because the displacement of the adsorbed molecules occurs rapidly on defective regions and slowly on ordered ones [112–115]. Moreover, the thiol-exchange efficiency is dependent on the intermolecular interactions between adsorbate molecules. In general, an adsorbate with weak interactions can be easily displaced by another one with strong interactions. For alkanethiols, since the chain length mostly determines the extent interactions, a mixed-component alkanethiolate SAM can be formed by displacing a short alkanethiol with a long one [4, 116].

In most cases, SAMs can be removed from the substrates to regenerate unmodified surfaces. This can be achieved by conventional thermal treatments, mechanical polishing and chemical oxidation methods. But these methods may not only remove the layers, but also damage the substrates as well. For thiolate SAMs deposited on Au, one alternative method is through photo-oxidation by exposing the SAMs to ultraviolet (UV) light to oxidize thiolate groups to sulfonate groups [4, 117]. Another widely studied method of removing SAMs is the reductive desorption, which is based on the reduction reaction below (Equation 2.10) [118]. Thus when a sufficiently negative potential is applied to a modified surface, the adsorbed thiolate layer can be removed from the substrate. Note that the reductive desorption process is reversible, so re-adsorption via oxidation can take place if the applied potential is less negative [12, 119]. Reductive desorption is an important process which can be used to quantify the adsorbate density or study the adsorbate-substrate interaction. This will be further reviewed and investigated in Chapter 4.

$$RS\text{-}Au + e^- \rightarrow RS^- + Au(0) \tag{2.10}$$

2.3 Electrochemistry

2.3.1 Overview

Electrochemistry is a branch of chemistry employed to study the interface between a metal phase and a solution phase. SAMs are structures concerning modified solid surfaces, so elec-
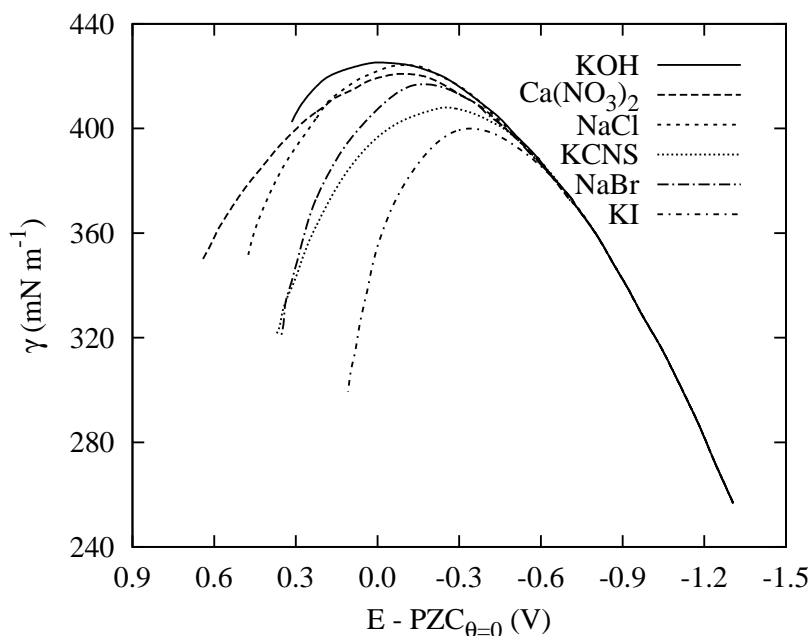
Figure 2.16: Experimental electrocapillary curves for Hg in various electrolyte solutions. Reproduced from [120] with permission from American Chemical Society.

trochemical methods are valuable tools to investigate this type of system. In this section, basic concepts and the electric double layer model to describe the metal (unmodified or modified) | solution interface will be reviewed. Based on the electric double layer model, the system of SAMs can be characterized. However, for the actual SAMs deposited on a substrate with certain crystal structure, the crystal structure inevitably influences the electrochemical properties of the SAMs. This will also be reviewed in this section.

2.3.2 Basic concepts

The invention of Hg dropping electrode opened the field of detailed electrochemical studies on an interface. Hg is the only liquid metal at room temperature and its surface tension can be easily measured. Using the dropping mercury electrode, the surface tension of the Hg drop in contact with an electrolyte solution at various electrochemical potentials was measured. The curve of surface tension as a function of potential is called the electrocapillary curve. Figure 2.16 shows the electrocapillary curves obtained in various electrolyte solutions [120]. The similarity of these curves is that they resemble the shape of a parabola with a maximum surface tension at a particular potential.

The electrocapillary curve is the experimental expression of the electrocapillary equation shown in Equation 2.11 [13, 120, 121]. In the electrocapillary equation, γ is the surface tension, σ_M is the excess charge density on the metal surface, E is the electric potential, Γ_i is the surface excess of a species, which measures the amount of the species from phase A (the solution) partitioning into phase B (the metal surface) and μ_i is the chemical potential of the species.

$$-\,\mathrm{d}\gamma = \sigma_M \mathrm{d}E + \sum \Gamma_i \mathrm{d}\mu_i \tag{2.11}$$

The electrocapillary curves converge at negative potential and diverge at positive potential. This is can be rationalized with the electrocapillary equation. At negative potential, the cations are non-specifically attracted onto the metal surface purely due to electrostatic interaction and the surface excess Γ_i for all cations is similar; at positive potential, some anions can be specifically adsorbed onto the metal surface through chemical interaction and the surface excess Γ_i for different cations varies.

From the electrocapillary equation, it is clear that the slope of the electrocapillary curve is the excess charge density on the metal surface (Equation 2.12).

$$\sigma_M = -(\frac{\partial \gamma}{\partial E})_{\mu_i} \tag{2.12}$$

When the surface tension reaches the maximum, the excess charge density on the metal surface σ_M equals zero. The potential at which this occurs is called the potential of zero charge (PZC) of the metal. Deviating from PZC, there is excess amount of charge on the surface, which induces repulsion. This repulsion counterbalances the trend of shrinking the Hg drop by surface tension and thus decreases the surface tension. Although the PZC is discovered from experiments with Hg electrodes, it is a generic parameter for any conductor in contact with electrolytes.

2.3.3 Electric double layer model of an electrode | solution interface

In many electrode | solution interfaces, species at the interfaces are relatively redox inactive, either thermodynamically or kinetically, with no electron transfer through the interface over a

range of potential. An electrode of this type is called an ideal polarized (or ideally polarizable) electrode (IPE) [13]. The Hg electrode, which is used widely, behaves similarly to an IPE over a potential range of nearly 2 V. Electrodes modified with SAMs can be viewed as a class of IPEs. However, the range of potentials at which they are stable and considered as IPEs may be restricted because they undergo reduction at negative potentials, oxidation at positive potentials and sometimes potential-induced structural transformation before being reduced or oxidized.

An IPE resembles a capacitor of which the most common form is two parallel metal plates separated by dielectric media, since both systems do not allow charge transfer through the interfaces within certain potential ranges. Thus, an IPE can be described with a simple capacitor model devised by Helmholtz [13]. In this Helmholtz Model, an IPE is modeled as a parallel-plate capacitor described by Equation 2.13 where σ is the surface charge density, V is the voltage applied across the two plates, ε is the dielectric constant of the medium, ε_0 ($\approx 8.854 \times 10^{-12}$F m^{-1}) is the permittivity of free space, and d is the distance between the two plates.

$$\sigma = \frac{\varepsilon \varepsilon_0}{d} V \tag{2.13}$$

Consequently, the charge stored in the capacitor is linearly proportional to the potential and the coefficient is the differential capacitance C_d (Equation 2.14).

$$C_d = \frac{d\sigma}{dV} = \frac{\varepsilon \varepsilon_0}{d} \tag{2.14}$$

This simple model suggests that C_d is constant and independent of potential V, which is contradictory to experimental results on IPE systems. Figure 2.17 shows the experimental results of the differential capacitance of a Hg electrode as a function of potential in various concentrations of NaF solutions [120]. An important feature is that at low electrolyte concentrations, a minimum capacitance value can be observed at PZC. Therefore, a more complex model was proposed by Gouy and Chapman independently and later extended by Stern. This Gouy-Chapman-Stern model is detailed in [13] and summarized here.

In the Gouy-Chapman-Stern model (Figure 2.18), the electrode has an excess amount of
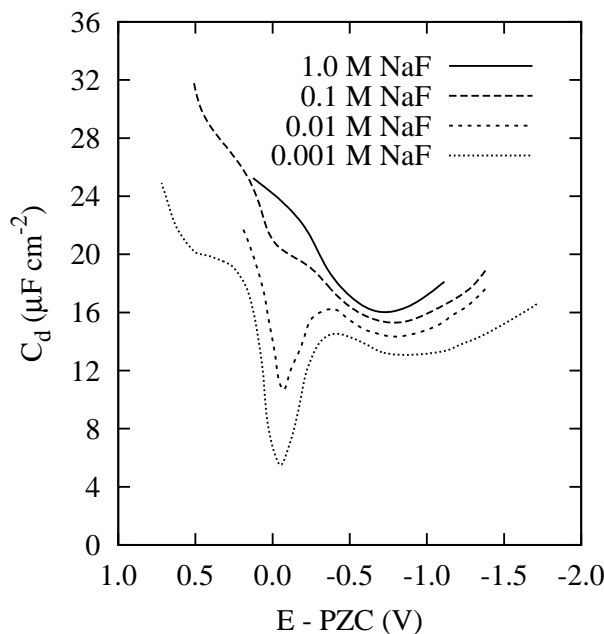
Figure 2.17: The differential capacitance-potential curves of a Hg electrode in various concentrations of NaF solution. Reproduced from [120] with permission from American Chemical Society.

charge with a density σ_M, while the solution side with the total excess charge density of σ_S, is modeled as consisting of two theoretical layers made up of ions in the solution to compensate for the excess charge. The layer closest to the electrode surface is the inner layer, sometimes also called compact, Helmholtz or Stern layer, with the total charge density σ_I. The inner layer mainly contains solvent molecules and sometimes some specifically adsorbed species with the electrical centers located at a distance of x_1 away from electrode surface at inner Helmholtz plane (IHP). The smallest distance to which solvated non-specifically adsorbed ions can approach the electrode is defined as x_2, the distance of outer Helmholtz plane (OHP) from the electrode surface. Non-specifically adsorbed ions are not concentrated close to the surface, instead, they are distributed from OHP to bulk solution in the layer called diffuse layer with the total charge density σ_D. In this model, the charge densities of the two layers follow the relation of Equation 2.15 at equilibrium.

$$\sigma_S = \sigma_I + \sigma_D = -\sigma_M \tag{2.15}$$

The main goals of this model are to derive the potential profile from ϕ_M at the electrode
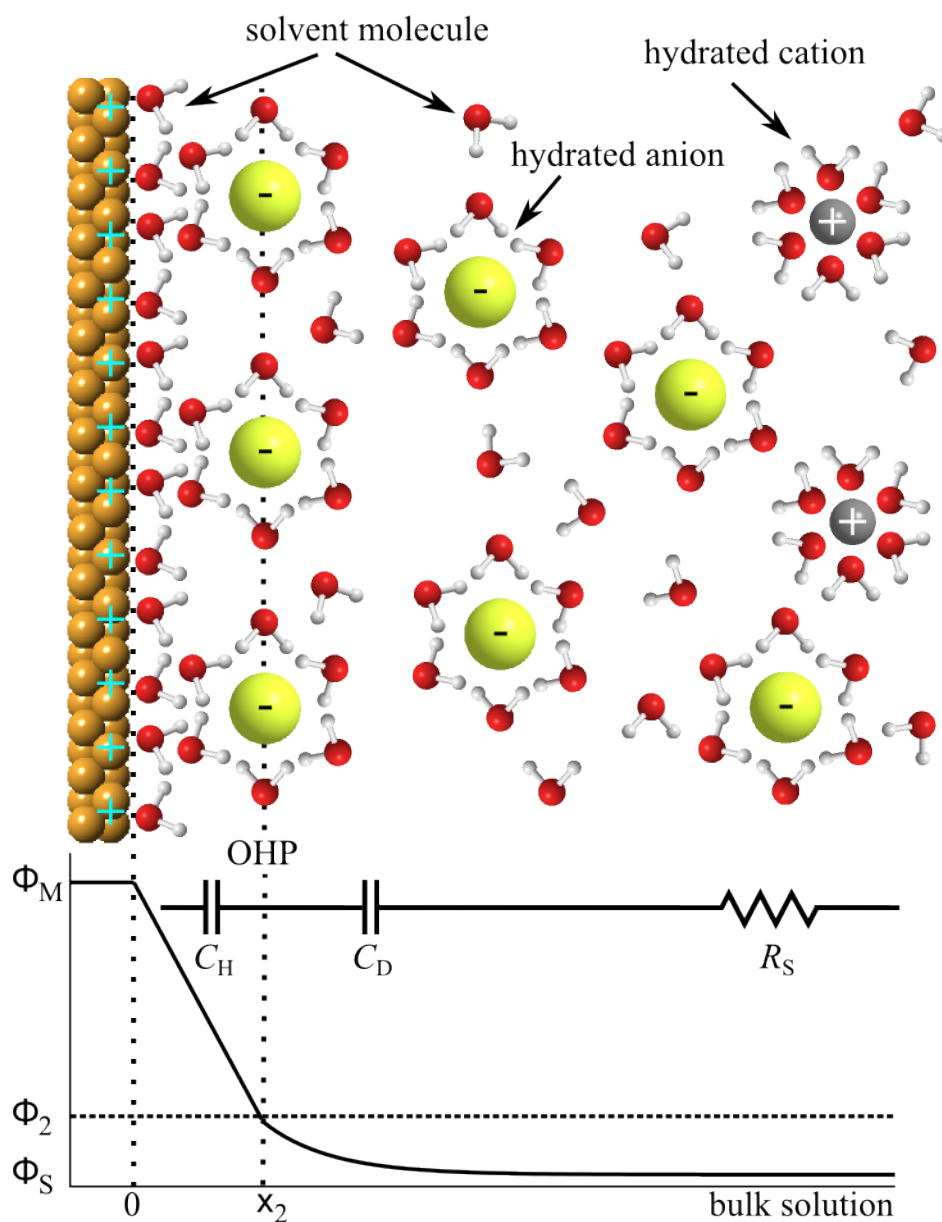
Figure 2.18: Schematic of the Gouy-Chapman-Stern model of the electric double layer near a metal surface with excess positive charge and the profile of the potential from the metal surface to the bulk solution. C_H is the inner layer capacitance and C_D is the diffuse layer capacitance. Note that the electric double layer eventually merges with the bulk solution which is represented by the solution resistance .

surface to ϕ_S at the bulk solution and the capacitance of the electric double layer C_{dl}. It is not attempted here but some of the most important points are highlighted in order to help describe the electrode | solution interface.

The potential at the electrode | solution interface decays from ϕ_M to ϕ_S following the profile depicted by Figure 2.18 if only non-specifically adsorbed ions are considered. To be specific, in the inner layer, the potential decays linearly from ϕ_M on electrode surface to ϕ_2 at OHP whereas in the diffuse layer, the potential decays non-linearly from ϕ_2 at OHP to ϕ_S in the bulk solution. The potential decays non-linearly following Equation 2.16 and Equation 2.17 in the diffuse layer for $z : z$ type of electrolyte, where e is the elementary charge, k is the Boltzmann constant, T is the temperature and n^0 is the concentration of the electrolyte.

$$\frac{\tanh(ze\phi/4kT)}{\tanh(ze\phi_2/4kT)} = \exp(-\kappa(x-x_2)) \tag{2.16}$$

$$\kappa = \sqrt{\left(\frac{2n^0 z^2 e^2}{\varepsilon\varepsilon_0 kT}\right)} \tag{2.17}$$

Two parameters are worth emphasizing here: x_2 is the inner layer thickness and $1/\kappa$ can be viewed as the diffuse layer thickness (also termed Debye length). The inner layer thickness, in ångström scale, is usually 1.5 to 2.0 times the thickness of a monolayer of solvent molecule [122]. While it is independent of the solid surface, the inner layer thickness becomes smaller with an increase of electrolyte concentration [123]. The diffuse layer thickness is strongly influenced by the electrolyte concentration as can be seen from Equation 2.17. With a high electrolyte concentration, the diffuse layer can reach single molecular layer thick while with a low electrolyte concentration, the diffuse layer can extend to hundreds of nanometers thick [13, 122]. The roughness of the metal surface also has a strong impact on the diffuse layer thickness. Generally, the diffuse layer thickness decreases with increasing roughness [124, 125].

The capacitance of the electric double layer in this model can be calculated with Equation 2.18.

$$\frac{1}{C_{dl}} = \frac{x_2}{\varepsilon\varepsilon_0} + \frac{1}{(2\varepsilon\varepsilon_0 z^2 e^2 n^0/kT)^{1/2}\cosh(ze\phi_2/2kT)} \tag{2.18}$$

The capacitance of the electric double layer C_{dl} can be interpreted as the expression of the total capacitance of two capacitors in series depicted in Equation 2.19 where C_H corresponds to the inner layer capacitance and C_D corresponds to the diffuse layer capacitance.

$$\frac{1}{C_{dl}} = \frac{1}{C_H} + \frac{1}{C_D} \tag{2.19}$$

The double layer capacitance C_{dl} is dominated by the layer with the lowest capacitance. The diffuse layer capacitance, C_D is dependent on ϕ_2 which is in turn dependent on the excess charge held on the electrode σ_M. In a dilute electrolyte solution, the concentration of counter ions in the diffuse layer is very low, so C_D is very low as well. C_{dl} reaches the minimum at the electrode's PZC where σ_M equals zero and consequently ϕ_2 equals zero. In this condition, there is no excess charge at the electrode surface which requires no excess charge in the diffuse layer, so C_D is a minimum. As a result, C_{dl} also reaches a minimum because it mainly depends on the low C_D. Changing potential from the PZC in either direction leads to an increase in C_{dl}. This matches the experimental results shown in Figure 2.17. However, in a concentrated electrolyte solution, the effect of diffuse layer capacitance becomes less evident due to the increase in C_D. The inner layer capacitor behaves similarly to a conventional parallel-plate electric capacitor. Its capacitance, C_H, is a function of the dielectric constant of the medium ε and the thickness of the inner layer, i.e., x_2, but not dependent on potential. The value of C_H can be calculated with Equation 2.14 in which d is replaced by x_2. However, the experimental result shown in Figure 2.17 suggests even at high electrolyte concentrations where the contribution from the diffuse layer capacitor is negligible, the double layer capacitance C_{dl}, mainly contributed from the inner layer capacitance, is still a function of potential. Further development of the electric double layer model involves the introduction of the dipole moment of the solvent molecules in the inner layer [126–128]. The orientation of the solvent molecules is influenced by the potential via dipole-charge interaction, which in turn influences the dielectric constant.

For an electrode surface modified with a SAM, the electric double layer model can still be applied to describe the electrode | solution interface. However, since the inner layer is now occupied by an organic layer instead of solvent molecules, some important changes of the pa-

rameters in Equation 2.18 need to be considered. First, ε of the organic layer is much lower than the solvent. For an alkanethiol, ε is typically less than 7 as compared to 78 for H_2O at room temperature, and it decreases as the carbon chain becomes longer [129]. Second, x_2 for an organic layer covered surface is much higher than that for a solvent covered surface. The thickness of an alkanethiolate layer can be estimated using 1.3 Å per CH_2 assuming vertical orientation [105]. Thus for a long alkanethiolate layer covered surface, x_2 should be on a nanometer scale, which is about one order of magnitude greater than that of a solvent covered surface. Considering the two contributions, the inner layer capacitance C_H of the SAM modified electrode is sufficiently small. Therefore, it is reasonable that the total capacitance of double layer capacitance C_{dl} is dominated by the inner layer capacitance C_H for SAM modified electrodes and the contribution from diffuse layer capacitance C_D is further reduced in high concentration electrolyte solution. Experimental results showed that the reciprocal of double layer capacitance $1/C_{dl}$ for an alkanethiol coated Au electrode is linearly related to the number of CH_2 units for long chain (no less than 10 CH_2 units) alkanethiol layers where ε is small enough (the layer is even impermeable to adsorbing anions) and the change of ε as a result of chain length change is negligible [105]. In this case, the Gouy-Chapman-Stern model is approximated into the Helmholtz capacitor model where Equation 2.14 can be used to calculate the capacitance of the electrode | solution interface. Worth mentioning is that the Helmholtz capacitor model is applicable only within the potential range in which the organic layer is stable and devoid of any redox reactions.

The capacitance of a SAM modified electrode can be used to calculate the fractional coverage of the SAM, which, in turn informs on the quality of the SAM. Since an ideally packed monolayer results in the lowest capacitance, $C_{dl(\theta=1)}$, the number defects in the SAMs inevitably lead to an increase in capacitance. Assuming the covered portion of the surface is ideally packed with a capacitance of $C_{dl(\theta=1)}$ and the defects are covered with solvent with a capacitance of $C_{dl(\theta=0)}$. Thus based on this simple model, the fractional surface coverage, θ, can be calculated based on Equation 2.20 [130, 131].

$$C_{dl} = \theta C_{dl(\theta=1)} + (1-\theta)C_{dl(\theta=0)} \qquad (2.20)$$

2.3.4 Electrochemistry on crystalline substrates

The electric double layer model was established mostly based on experimental results with Hg electrodes, where isotropic performance on a Hg drop surface would be expected. However, for a solid electrode with multiple crystallographic surfaces exposed, anisotropic electrochemical responses can be observed from different surfaces.

The electrons near a metal (any metal, not exclusively in solid state) surface become loosely bound because of the missing atoms on one side and tend to spread out of the crystal towards the vacuum. A jellium model is used to describe this spillover of electrons near the metal surface [132]. The jellium model assumes the positively charged ions resume their position based on the surface crystallography, therefore, the positive charge is bounded. If the position of this plane is referred to as zero, the positive charge only appears less than zero and treated as a uniform background. The spillover of electrons results in an excess amount of negative charge just outside the crystal and an excess amount of positive charge just inside the crystal. The electron density profile near the surface is represented in Figure 2.19. Because of the separation of the positive and negative charges, a dipole is formed near the metal surface. Therefore, to bring an electron out from the bulk, this dipole needs to be overcome. The work function Φ is the physical parameter to measure the minimum energy required to bring an electron from the bulk to a position just outside (a position where the electrostatic interaction with the crystal approaches zero) [132, 133]. It can be calculated with Equation 2.21, where $\bar{\mu}$ is the electrochemical potential and $\triangle\phi$ is the dipole barrier. The electrochemical potential $\bar{\mu}$ measures the energy of the electron in the bulk with the reference to vacuum, so it is not related to the electron density profile near the surface. However, the dipole barrier $\triangle\phi$, as its name suggests, measures the barrier created by the spillover of electrons near the surface, which is dependent on the surface crystallography.

$$\Phi = -\bar{\mu} + \triangle\phi \tag{2.21}$$

The jellium model discussed above is a one-dimensional model applicable to an ideally flat surface. For a rough two-dimensional surface, an intuitive model proposed by Smoluchowski demonstrates two effects which contribute to the electron density near the surface, represented
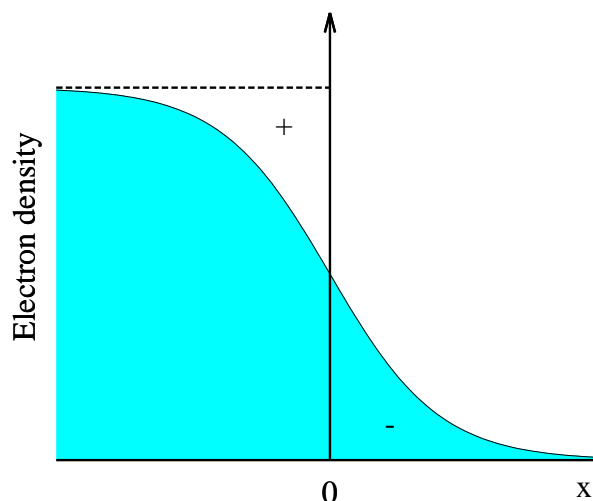
Figure 2.19: Schematic of the electron density profile near a metal surface based on jellium model.

in Figure 2.20 [134]. The first effect is suggested by the jellium model, the electrons spread out towards the vacuum due to the weak binding to the bulk. This effect results in a dipole (directed from negative to positive) which points to the bulk. This dipole impedes the movement of an electron from crossing the surface. The electron spillover is accompanied by the other effect near a rough surface. The electron density tend to smooth out to avoid the sharp edges of high energy instead of following the surface morphology. The sharp edges with positive charge are now exposed which form a layer of positive charge above the smoothed electron layer. The net result is a dipole which points away from the bulk. This dipole promotes an electron crossing the surface. Due to the density smoothing effect, the rougher is the surface, the stronger is the dipole resulted from smoothing and thus the smaller is the work function Φ. The conclusion drawn from here is that there is anisotropy in electrochemistry performed on crystalline electrodes because the work function depends on the atomic roughness of crystallographic planes exposed.

The work functions of the three low-index crystallographic planes of Au are listed in Table 2.3. As can be seen, the work function follows the order of $\Phi(111) > \Phi(100) > \Phi(110)$, which is consistent with the order of increasing atomic roughness of these three crystallographic planes.

The use of work function is more convenient if the metal is in vacuum. In an electrochemical system, the metal is in a solution, and what is typically measured is the PZC. The linear
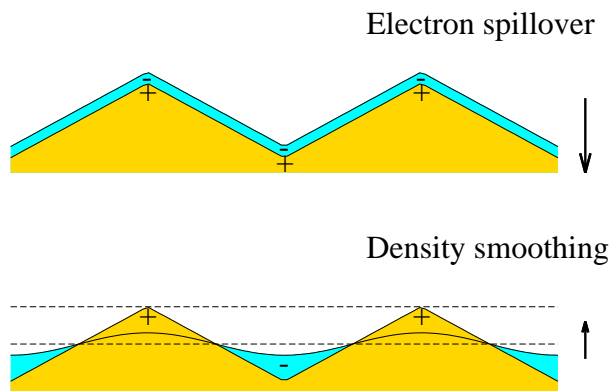
Figure 2.20: Schematic of the electron spill over and density smoothing effects near the metal surface.

Table 2.3: Work function and potential of zero charge for the three low-index crystallographic planes of Au

Crystallographic plane	Φ / eV	PZC / V vs. SCE***
(111)	5.26±0.04* [135], 5.15** [32]	0.23[†], 0.32[††] [136]
(100)	5.22±0.04* [135], 5.10** [32]	0.08[†],0.30[††] [136]
(110)	5.20±0.04* [135], 5.04** [32]	−0.02[†], −0.04[††] [136]

*Measured with angle-resolved photoemission spetroscopy.

**Calculated based on density functional theory.

***Measured in 0.01 M $HClO_4$.

[†]Unreconstructed.

[††]Reconstructed.

correlation between the two parameters was detailed in [137] and summarized here.

Equation 2.21 shows the correlation between work function Φ and dipole barrier $\triangle\phi$, and $\triangle\phi$ can be further calculated with Equation 2.22, where χ^M is the metal surface potential induced by dipole.

$$\triangle\phi = e\chi^M \tag{2.22}$$

When the metal is in contact with the solution, there is a small change $\delta\chi^M$ in the surface dipole, resulting in a new surface potential g_{dipole} across the metal | solution interface.

$$g_{dipole} = \chi^M + \delta\chi^M \tag{2.23}$$

This is the change considering the metal side. However, the surface potential g_{dipole} across the metal | solution interface should be also felt on the solution side and experimentally measured as the PZC with some selected reference point. Thus, combining Equations 2.21, 2.22 and 2.23 and assuming electrochemical potential $\bar{\mu}$ is constant, the linear correlation between PZC and work function is expressed in Equation 2.24.

$$PZC = \frac{\Phi}{e} + \delta\chi^M - g_{dipole} + K \tag{2.24}$$

Usually $\delta\chi^M$ is also viewed as a constant, but g_{dipole} is strongly influenced by any event on the solution side, e.g., adsorption. But the linear correlation between PZC and Φ is established in this equation. Since Φ is dependent on the crystal structure of the surface, PZC is inevitably dependent on the crystal structure of the surface. The PZC values for the three low-index crystallographic planes (unreconstructed) of Au listed in Table 2.24 demonstrate this dependence.

On the other hand, if there is a structure change on the surface, electrochemistry should be able to detect the change. Surface reconstruction is one of the examples [136, 138]. Surface reconstruction on Au(111), Au(100) and Au(110) was reviewed in Section 2.1.5. In the electrochemical environment, the surface reconstruction can only survive at potentials that are not very positive. The adsorption of anions at positive potential replenishes the excess amount of

loosely bound electrons on the surfaces and thus reverts the reconstruction back to the (1×1) structure of the surface exposed. The potential of lifting the reconstruction is dependent of the extent of specific adsorption. For example, Cl^- is more specifically adsorbed than ClO_4^-, so a less positive potential is required to lift the reconstructed surface with Cl^- adsorption. The change of surface structure when lifting the reconstruction has been confirmed with in situ elec-troreflectance spectroscopy. The reconstructed surfaces have different atomic roughness as compared to the unreconstructed ones, and consequently, the PZC should be shifted as well. The PZC of an electrode can be measured in dilute and non-adsorbing electrolyte solution. The shift of PZC can be observed when the surface exposed reverts back to the (1×1) structure. Figure 2.21 shows the capacitance curve of a Au(100) electrode measured during the process of lifting the reconstruction [136]. The first cycle (1 and 2) was limited at potential less than 0.4 V, thus the electrode retained the reconstructed (20×5) structure. The PZC of this reconstructed surface is +0.30 V, which is comparable with that of a $(23 \times \sqrt{3})$ reconstructed Au(111) surface. This can rationalized by the structural resemblance of the reconstructed Au(100) surface with the quasi-hexagonal symmetry and the reconstructed Au(111) surface. The positive limit of the second cycle (3) was increased to 0.6 V and thus lifted the reconstructed surface to the (1×1) structure. The PZC of this unreconstructed surface measured at the negative scan of the second cycle (4) is +0.08 V. Lifting the surface reconstruction can be also observed with cyclic voltammetry (CV) measurements [136, 139–142]. A sudden change in surface structure results in additional charging process, shown as a prominent current peak in the voltammogram. The electrochemistry method has been used to determine whether or not one particular crystallographic surface of Au undergoes reconstruction. The results obtained with electrochemical methods are mostly consistent with those measured with in situ STM [44, 45], especially for the frequently studied crystallographic surfaces. Worth mentioning is that no reconstruction has been observed on the two important stepped surfaces, (210) and (311), with either methods. Inconsistent results were obtained with the two methods, even within electrochemistry measurements done by different researchers, for some rarely studied crystallographic surfaces, i.e., (755) and (533) (note that these are surfaces with large (111) terrace), presumable due to different experiment conditions.

Above the relationship between PZC, an important electrochemical parameter and surface
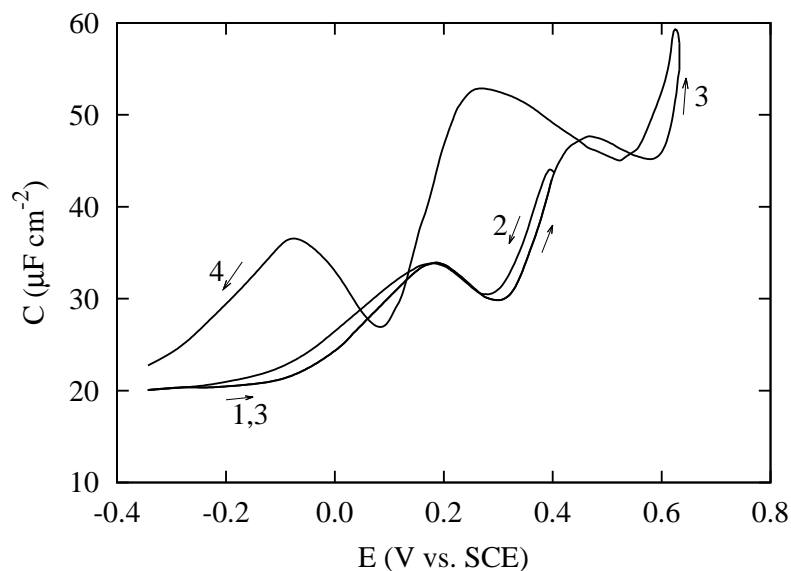
Figure 2.21: Capacitance curve of a Au(100) electrode measured during the process of lifting the (20×5) reconstruction to (1×1) in 0.01 M HClO$_4$ solution, reproduced from [136] with permission from Elsevier.

crystallography has been discussed. However, the concept of atomic roughness of a crystallographic surface is quite empirical. In addition, the experimentally determined PZC values available are limited to those frequently studied planes, namely the three low-index planes and a few stepped planes. Therefore, it would be convenient if there is a numerical parameter which can represent the atomic roughness and surrogate PZC. The density of broken bonds has been proposed as such a parameter [143].

An ideal crystallographic plane (hkl) is the result of perfectly truncating a lattice at a designated direction. The atoms on the surface lose their nearest neighbor atoms above the truncation plane, which is analogous to bond breaking (strictly speaking there is no chemical bond between the atoms). The number of these "broken bonds" per unit surface cell is defined as density of broken bonds (d_{bb}). The higher the d_{bb}, the rougher the crystallographic surface. For a fcc crystal, the density of broken bond of an unreconstructed crystallographic surface (hkl) ($h \geqslant k \geqslant l$) can be calculated with Equation 2.25. Figure 2.22 shows the correlation between d_{bb} and PZC for two metals with fcc crystal structure, Au and Ag. Although some discrepancy exists between the experimentally determined PZC and the numerically calculated d_{bb} for some surfaces, the general correlation is clear and enough for qualitative and semi-quantitative studies.
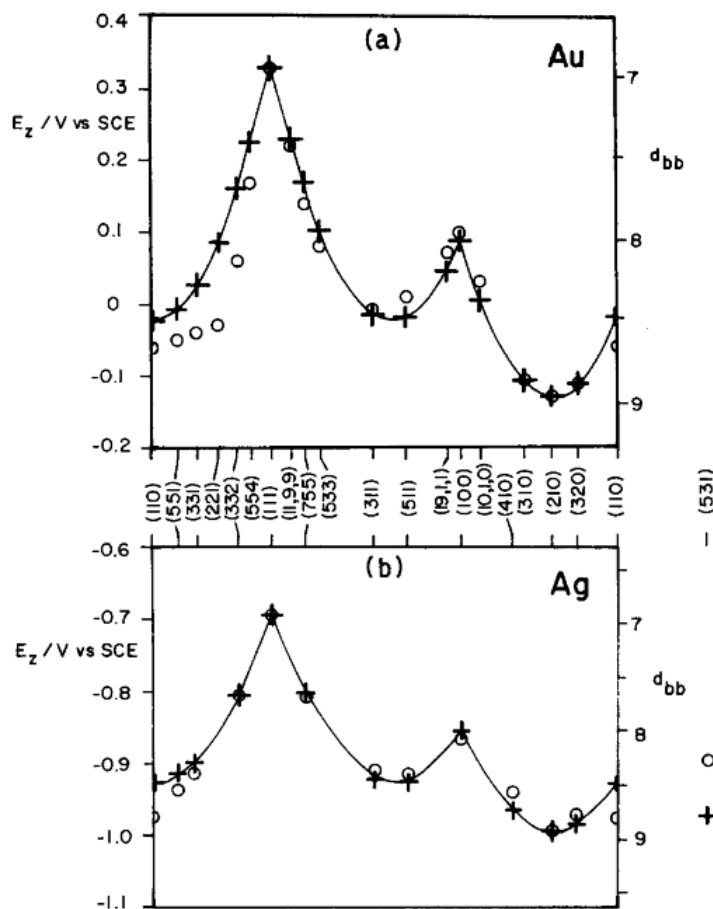
Figure 2.22: Correlation between PZC and density of broken bonds for Au and Ag, where open circles represent the experimentally determined PZC in 0.01 M NaF at 25 °C and pH 5.6 and crosses represent the calculated d_{bb} of the crystallographic surfaces studied. Reprinted from [143] with permission from Elsevier.

$$d_{bb} = \frac{8h + 4k}{\sqrt{h^2 + k^2 + l^2}} \tag{2.25}$$

Also considering the step notation for the stepped surfaces reviewed in Section 2.1.4, some important information about the roughness of the stepped surfaces can be drawn by comparing with d_{bb} and PZC. The (210) surface is the turning point of the (100)-(110) zone, it is also the roughest surface of this zone as well as of all stepped surfaces based on its highest d_{bb} and most negative PZC. The (311) surface is the turning point of the (111)-(100) zone, it is close to the roughest surface of this zone and indeed with the most negative PZC of this zone. The (111)-(110) zone is special because the (110) surface is formed by equal width of (111) terrace

and (111) step. Although the (331) surface is the turning point of this zone, the (110) surface is the roughest surface with the most negative PZC.

2.4 Fluorescence

2.4.1 Overview

SAM-modified surfaces can be described by the electric double layer model, so electrochemical techniques are employed to characterize the SAMs. However, the electrochemical techniques give only the average response of SAMs under the influence of an electric field. In other words, the resolution for the electrochemical techniques is mostly on the scale of the electrode size. In this thesis, the influence of surface crystallography on SAM will be studied, which requires techniques to visualize various crystallographic domains distributed on an electrode surface. Therefore, spectroelectrochemical techniques combining electrochemical methods and fluorescence microscopy are employed to investigate the SAM modified surfaces. Here, the basic principle of fluorescence will be first reviewed. Moreover, fluorescence quenching near a metal surface, the fundamental principle that the in situ fluorescence techniques are relying on, will be discussed. Finally, fluorescence microscopy will be briefly discussed by introducing the instrumental setup.

2.4.2 Basic principles of fluorescence

Fluorescence is a luminescence process when molecules in electronically excited states return to the ground state without change in spin orientation. This process generally starts with the absorption of light to excite a molecule from the lowest vibrational level of electronic ground state (S_0, S denotes the singlet state of spin orientation) to various vibrational levels of an excited state (e.g., S_1). This is followed by internal conversion, in which an excited molecule relaxes to the lowest vibrational level of the excited state. From the lowest vibrational level of the excited state, the excited molecule further returns to various vabrational levels of the ground state accompanied by photon emission. Due to the energy loss in internal conversion, the emitted photon undergoes red shift, called Stokes shift, as compared to the absorbed excitation

light. According to the Franck-Condon principle, the transition time for this process is too short for change in nuclei positions, so the vibrational levels for both the ground state and excited state are similar. Consequently, a mirror image symmetry is observed between the excitation spectrum, representing the probability of the transitions (dependent of the overlap in vibrational wave functions) from the lowest vibrational level of ground state to various vabrational levels of excited state, and the emission spectrum, representing the probability of the transitions from the lowest vibrational level of excited state to various vabrational levels of ground state [144].

Besides returning to ground states accompanied by photon emission, molecules in the excited states can also undergo such processes as collision, complex formation and energy transfer, all of which result in a decreased fluorescence intensity or more precisely, quenching of fluorescence. One important process is fluorescence resonance energy transfer (FRET), also called Förster resonance energy transfer, in which energy transfer occurs between an excited donor molecule to an acceptor molecule through non-radiactive dipole-dipole interaction. Note that non-radiative energy transfer means the donor does not emit a photon and the acceptor does not adsorb a photon, so FRET can be viewed as a quenching process for the donor molecule. The occurrence of the FRET requires a significant overlap between the donor emission spectrum and the acceptor excitation spectrum and favorable relative distance and orientation for the transition dipoles of both molecules. The FRET efficiency (E) has a dependence of the sixth power of the donor-acceptor distance (R) described in Equation 2.26. R_0, referred to as Förster Radius, is defined as the donor-acceptor distance distance at which the efficiency is 50% [145].

$$E = \frac{1}{1 + (R/R_0)^6} \tag{2.26}$$

Other processes that can reduce the excited state population, leading to a decrease of fluorescence intensity include photobleaching and phosphorescence processes. Photobleaching is the process of depleting the excited state through destruction of the excited molecule by intensive exposure to excitation light. This differs to quenching in that the chemically damaged molecule can no longer fluoresce [146]. The occurrence of phosphorescence requires the intersystem crossing in which the excited molecule in the singlet excited state S_1 undergoes spin

conversion, ending up in the triplet excited state T_1. Emission of light upon transition to ground state from triplet excited state is called phosphorescence. However, this transition is forbidden by symmetry, so the emission rate is very low [144].

As discussed, fluorescence is competing with a number of processes such as quenching, so not all the absorbed photons are converted into fluorescence emission. The parameter quantum yield (QY), i.e., the ratio of the number of photons emitted over the number of photons absorbed, describes the efficiency of a fluorescence event or a fluorophore. QY can be calculated with Equation 2.27, where k_r is the emission rate constant and k_{nr} is the non-radiactive decay rate constant.

$$QY = \frac{k_r}{k_r + k_{nr}} \tag{2.27}$$

The reciprocals of the numerator and the denominator, are the intrinsic lifetime of a fluorophore, τ_0 and the measured lifetime under experimental conditions, τ. Substituting these two parameters into Equation 2.27 gives Equation 2.28. This demonstrates the proportionality of QY to measured lifetime. Experimentally, these lifetimes are often measured to study the non-radiactive processes.

$$QY = \frac{\tau}{\tau_0} \tag{2.28}$$

2.4.3 Fluorescence quenching near a metal surface

The fluorescence near a metal surface was first studied experimentally by Drexhage and Kuhn [147–150] with a classic system of an Eu^{3+} complex fluorophore located near a metal surface (Ag or Au) spaced by Langmuir-Blodgett (LB) films of various thicknesses. The experiment of Eu^{3+} complex near Ag surface was reproduced by Amos and Barnes with small modifications [151]. Figure 2.23 shows the lifetime of this classic system of an Eu^{3+} complex as a function of distances from the Ag surface. Note that QY is directly proportional to the measured lifetime, so effectively this result can also be interpreted as the unquenched fluorescence near the metal surface. Two different domains are observed. One is at distance longer than 50 nm, where the lifetime oscillates with distance and the amplitude of oscillation gradually decays with increasing
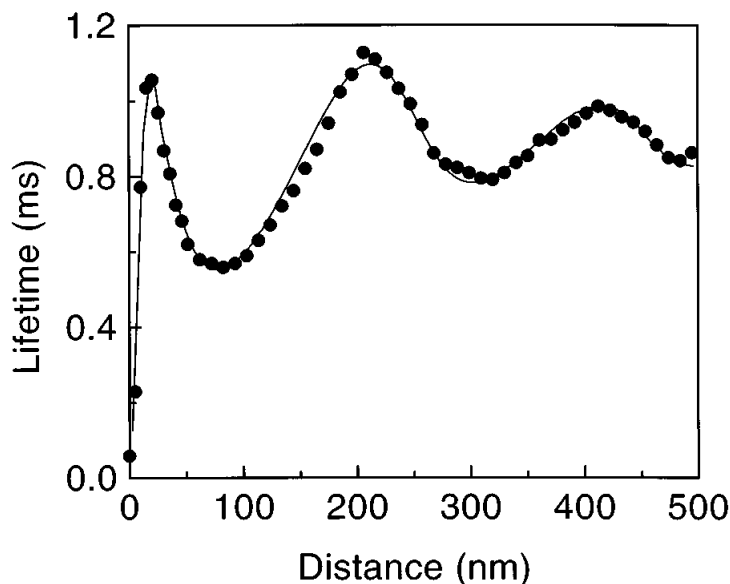
Figure 2.23: Fluorescence life time of the Eu^{3+} complex fluorophore as a function of distance from a Ag surface with the filled circles representing the experimental data points and the solid line representing the theoretical prediction. Reprinted from [151] with permission from American Physical Society.

distance. The other is at distance shorter than 50 nm, where the lifetime decreases sharply with decreasing distance. The phenomenon in the long distance domain has been satisfactorily explained as the alternating constructive and destructive interferences between the emission radiation and the reflected radiation due to the phase change with distance [152–154]. The phenomenon in the short distance domain is usually referred to as the near-field metal-mediated fluorescence quenching.

Theoretical interpretations of the quenching process near a metal surface were detailed by Chance et al. based on classical electromagnetic theory [152, 155] and by Yeung and Gustafson based on quantum theory [156]. While both theories are in good agreement, it is not always easy to understand the physical meanings behind the theory. In simple words, fluorescence is competing with a number of transition pathways with some pathways resulting in radiative decay and some pathways resulting in non-radiative decay, so to calculate QY (Equation 2.27), only the general radiative decay rate and non-radiative decay rate are considered. Therefore the classical electromagnetic approach typically looks for the pathways leading to radiative decay and calculates the rate of radiative decays from these pathways. The emitter

(fluorophore) is typically treated as an electric dipole oscillator because chemically most fluorophores are electric dipoles, required for molecular transitions to produce light [154]. The electromagnetic interpretation is built on the surface plasmons induced by the emitter radiation field. However, the surface plasmons excitation only occurs in near field, i.e., at a distance smaller than wavelength of the emission radiation (depending on the dielectric constant of the metal, this distance can be varied) where the equipotential line density of the emitter radiation field is higher than the intrinsic charge distribution on the metal surface [157]. The calculated decay rate (normalized with the decay rate at an infinite distance) of radiation from the surface plasmons near a 633 nm dipole emitter-Ag interface is shown Figure 2.24 as a function of distance from the Ag surface. The radiation from the surface plasmons only contributes to the measured lifetime of the emitter radiation by changing k_r and k_{nr} in Equation 2.27 at distance less than about half of the wavelength. The contribution from the surface plasmons still does not explain the quenching in the short distance domain shown in Figure 2.23. While the theoretical treatments were solid, a new pathway, the lossy surface waves, was proposed by Ford and Weber in an attempt to explain the quenching [153]. As its name suggests, the emitter radiation decaying into the lossy surface waves result in non-radiative decays, i.e., the fluorescence is "lost". As can be seen from Figure 2.24, the decay rate for the lossy surface waves is dominating in the short distance domain (less than tens of nanometers), explaining the quenching. Unlike the surface plasmons, the nature of the lossy surface waves is nevertheless unclear. Further rationalizations are needed to find the cause for the quenching.

One intuitive interpretation proposed by Lakowicz explains the nature of the lossy surface waves by linking to the surface plasmons [157]. Lakowicz's explanation of the the lossy surface waves starts by considering that emitter radiation field and surface plasmons are in forms of electromagnetic waves. A one-dimensional sine wave propagating in x direction can be expressed in wave equation (Equation 2.29).

$$f(x,t) = A\cos(kx + \omega t + \phi) \tag{2.29}$$

While this basic real form is well-known, the more general form adopts the complex form of Equation 2.30 [14].
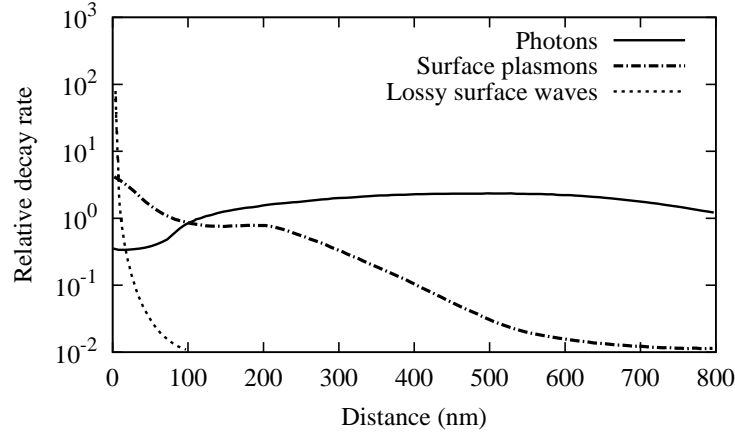
Figure 2.24: The calculated decay rates as a function of distance from the metal surface of the major pathways near a 633 nm dipole emitter-Ag interface: photons, surface plasmons and lossy surface waves. Reproduced from [157] with permission from Elsevier. .

$$f(x, t) = A \exp[\, i(kx + \omega t + \phi)]$$ (2.30)

Strictly speaking, for an electromagnetic field propagating in space, the generalized wave equation for three-dimensional waves should be considered. Nevertheless, for a general understanding, the one-dimensional form is used. The most important parameter in the wave equations used to explain the nature of the lossy surface waves is k, the wavevector (should be written as $\mathbf{k}$ strictly speaking). The amplitude of the wavevector is inversely proportional to the wavelength λ.

$$k = \frac{2\pi}{\lambda}$$ (2.31)

The wavevector is further related to the momentum p of a wave through the de Broglie matter wave relation where h is the Planck constant.

$$p = \frac{h}{\lambda} = \frac{hk}{2\pi} = \hbar k$$ (2.32)

Thus when an electromagnetic wave travels from medium 1 to medium 2 at an angle, based on the momentum conservation, in the interface plane, Equation 2.33 should be fulfilled where θ_1 and θ_2 are the angle of incident and angle of refraction respectively. From a different aspect,

Equation 2.33 suggests that the projection of the wavevectors of the incident wave and the refraction wave equal each other, which is also referred to as wavevector matching.

$$k_1 \sin \theta_1 = k_2 \sin \theta_2 \tag{2.33}$$

Specifically for light, the famous Snell's law describing the refraction phenomenon can be derived from here. The refraction index n of a particular medium is defined as the ratio of speed of light in vacuum over that in the medium.

$$n = \frac{c}{v} = \frac{2\pi c}{\lambda \omega} = \frac{ck}{\omega} \tag{2.34}$$

Snell's law (Equation 2.35) is obtained considering this proportionality of n to k.

$$n_1 \sin \theta_1 = n_2 \sin \theta_2 \tag{2.35}$$

If a beam of light travels from a high refraction index medium 1 to a low refraction index medium 2, then θ_1 is smaller than θ_2. An increase of θ_1 can lead to a critical point where θ_2 equals 90°, i.e., light is traveling in the interface plane. No θ_2 value satisfies Equation 2.35 for even larger θ_1, so in this case all the light is reflected back to medium 2 without traveling into medium 1. This is known as total internal reflection.

The total internal reflection can be further generalized for any form of electromagnetic wave as not being able to satisfy the wavevector matching condition of Equation 2.33. For surface plasmons which stay near the metal surface, only the projection of the incidental wavevector k_1' need to be considered. For a small k_1', an angle of refraction θ_2 is able to satisfy the wavevector matching condition. However, as k_1' increases, θ_2 eventually reaches the critical point of 90°. At even larger k_1', total internal reflection occurs and the surface plasmons are not able to propagate into space as radiation. Considering the magnitude of the wavevector is inversely proportional to wavelength, large k_1' effectively means closely spaced charge distribution on the surface.

The surface plasmons are induced by the emitter radiation field, so the distance between the emitter influences the charge distribution on the surface. In Figure 2.25, the emitter (the

radiation field equipotential lines shown) is placed at different distances from a bulky metal or metal thin film surface. In the case of Figure 2.25a, the emitter is at a distance where surface plasmons can be induced but is still far enough from the surface (typically from tens of nanometers to wavelength). The radiation field equipotential line density is relatively low, resulting in widely spaced charge distribution on the surface where the wavevector matching condition can be satisfied, so the surface plasmons propagate in space as radiation. In the case of Figure 2.25b, the emitter is at a small distance from the surface (typically less than tens of nanometers). The radiation field equipotential line density is high, resulting in closely spaced charge distribution on the surface where the wavevector matching condition cannot be satisfied, so the surface plasmons are not able to propagate in space, ending up as evanescent waves. In other words, this explains the nature of lossy surface waves mentioned above in that the fluorescence is lost because the surface plasmons induced by the emitter can not escape out of the metal as radiation. Worth mentioning is the case of Figure 2.25c, when the substrate is a metal thin film placed on top of a third high refraction index medium (e.g., a glass prism), the wavevector matching can be conditionally accomplished at the second interface and the surface plasmon can be observed as radiation again.

To sum up for the mechanism of the near field metal mediated fluorescence quenching proposed by Lakowicz, because of the inability of achieving the wavevector matching, the surface plasmons induced by an emitter close to the metal surface cannot propagate in space as radiative decays. Thus, the lossy surface waves can be viewed as the trapped evanescent surface plasmons.

One drawback of Lakowicz's interpretation of the near field metal mediated fluorescence quenching is that there is no quantitative estimation of the quenching efficiency near a metal surface. Another intuitive interpretation is present by realizing the resemblance of the metal mediated quenching to FRET. Therefore, the metal surface can be viewed as the acceptor in the energy transfer process. This analogy was used by Kuhn and Chance in the early days [149, 152]. This interpretation still has its own merit since it is relatively easy to understand and semi-quantitative. One important characteristic of FRET is that the energy transfer rate has a R^{-6} dependence on the distance between donor and acceptor R. Analogously, for fluorescence near metal surfaces, the quenching depends on both the distance between the fluorophore
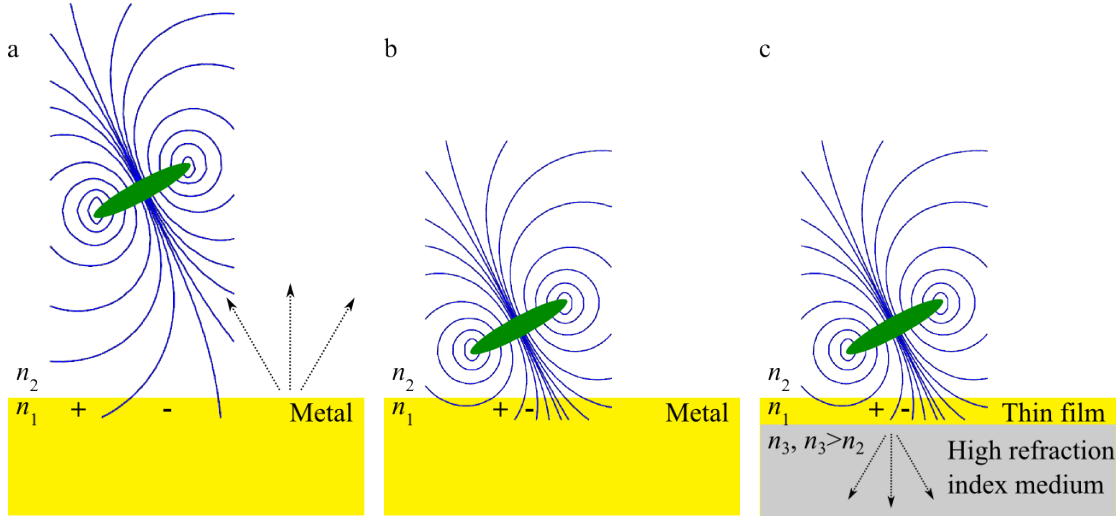
Figure 2.25: The surface plasmons induced by a emitter in the near field: (a) the widely spaced charge distribution induced by the emitter far away enables propagation of the surface plasmons in space as redative decays; (b) the widely spaced charge distribution induced by the emitter nearby leads to non-radiative decays of the surface plasmons; (c) recovery of the non-escaping decays with the substrate of metal thin film placed on top of a high refraction index medium. Adapted from [157] with permission from Elsevier.

and the metal surface d and the metal thickness. For energy transfer to a thick metal film or bulky metal, the rate is a function of d^{-3} and for thin metal films, the rate is a function of d^{-4} [152, 154, 158].

2.4.4 Fluorescence microscopy

The theory of fluorescence near a metal surface was briefly reviewed above. Experimentally, measuring the fluorescence signal from a metal surface can be accomplished by fluorescence microscopy. The fluorescence microscopy is a technique that combines exciting a fluorescence signal from a specimen of interest and employing a microscope to amplify, view and detect the fluorescence signal. The epifluorescence microscope is the most widely used type of fluorescence microscope. The prefix "epi-" represents "episcopic", which means exciting the fluorescence with an incident light and collecting the reflected or scattered light after filtering the excitation light through the same objective [159]. Below, the inverted fluorescence microscope used in this thesis (Olympus IX 70, depicted in Figure 2.26) is taken as an example to demonstrate the epifluorescence microscopy.
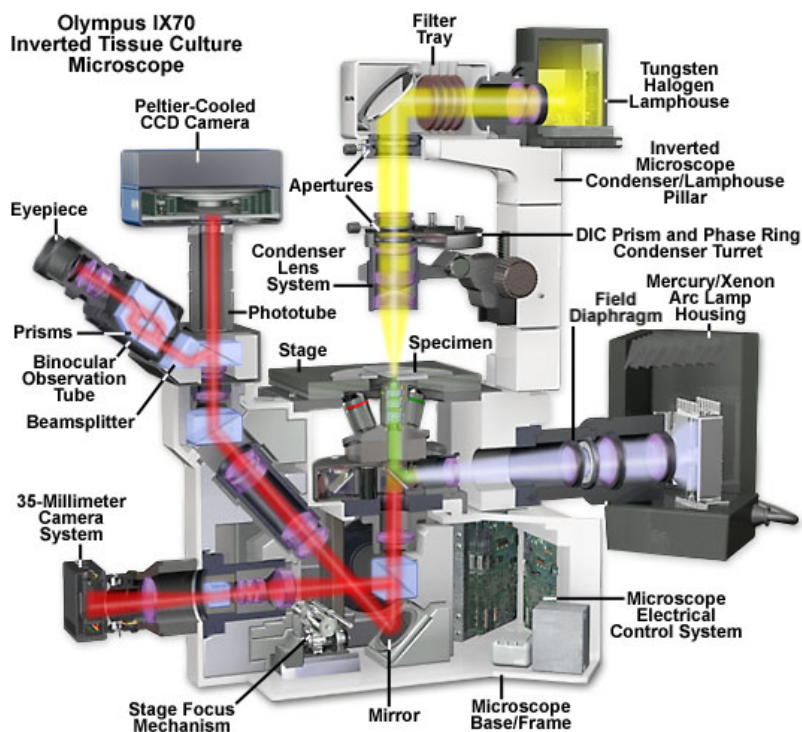
Figure 2.26: Schematic of the inverted epifluorescence microscope used in this thesis. Adapted from [160] with permission from Olympus.

The light source for fluorescence excitation is usually a Hg arc lamp or a Xe arc lamp which covers the entire UV and visible spectrum (a Xe arc lamp even covers the infrared). A Xe arc lamp is probably preferred because of its much more uniform intensity across the visible spectrum as compared to the multiple spikes in the Hg arc lamp spectrum [161] even though a Hg arc lamp is used in this thesis. After collimated with the collector lens and optionally apertured down with a field diaphragm, the excitation light is sent into the filter set. In a fluorescence microscope, a filter set is one of the most important components. Typically, a filter set is a combination of a band-pass excitation filter of a short wavelength, a dichromatic mirror equivalent to a long-pass filter and a band-pass emission filter of a long wavelength. Selection of these filters are based on the fluorophore used. Ideally, the excitation filter allows the maximum excitation peak to pass through, the emission filter allows the maximum emission peak to pass through and the dichromatic mirror reflects the excitation light but allows the emission light to pass through. The light path inside the filter set is presented in Figure 2.27. The light is first filtered with the excitation filter, then reflected by the dichromatic mirror through the objective to the sample surface. While the reflected excitation light from the specimen is again reflected
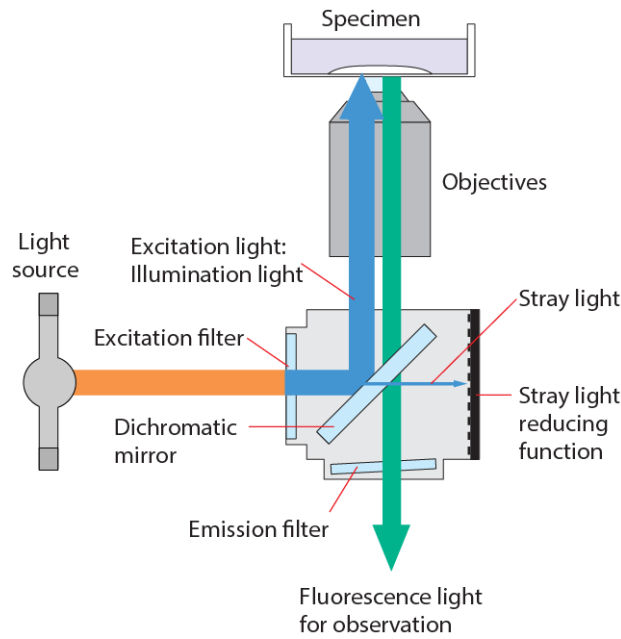
Figure 2.27: Schematic of a filter set for the inverted fluorescence microscope. Reprinted from [162] with permission from Olympus.

by the dichromatic mirror back to the light source, the fluorescence emitted from the surface travels through the objective, passes through the dichromatic mirror and is finally directed in to the eyepieces or the detectors by multiple optical elements, e.g., mirror, lens, prism and beam-splitter. Multiple ports are available for integrating various detectors such as charge-coupled device (CCD) camera and photomultiplier tube (PMT).

It is important to select the proper objective for imaging. The typical parameters taken into accounts are magnifying power and numerical aperture (NA). The magnifying power defines the area of the specimen in view and the ability to observe the subtle details. While it is impossible to achieve both, the actual trade-off made depends on the system studied. NA is another important parameter to consider in that it largely determines the resolution and the depth of focus.

The theoretical resolution of an optical microscopy is diffraction limited. Briefly, the light passing through an aperture (in this case, the aperture of the objective) ends up as a diffuse circular diffraction pattern known as Airy disk. The theoretical minimum resolved distance is given by a sufficient separation of two neighboring Airy disks. Different criteria can be chosen to define the sufficient separation, of which a famous one is the Abbe resolution limit given in

Equation 2.36 (also with the definition of NA) where d_{min} is the minimum resolved distance, λ is the wavelength, n is the refraction index of the medium and α is the angular semi-aperture [14]. As can be seen, increasing NA is one way of improving the resolution. Therefore, water or oil immersion objectives are frequently employed due to the high NA as a result of the high refraction index working medium.

$$d_{min} = \frac{\lambda}{2n\sin\alpha} = \frac{\lambda}{2NA} \tag{2.36}$$

The depth of focus is a parameter to estimate image deterioration compared to the focal plane. Theoretically, the image of an object deviated from the focal plane is blurred. However, if the distance between an image point off the focal plane and an image point on the focal plane is smaller than resolved distance, there will be no significant image deterioration between the two points. Therefore, the depth of focus is also termed the axial resolving power (R_{ax}) [158]. The depth of focus or axial resolving power can be estimated using Equation 2.37 where f is the focal length and D is the aperture diameter [14].

$$R_{ax} \approx \frac{2.4\lambda f^2}{D^2} \tag{2.37}$$

R_{ax} can be further related to NA.

$$NA = n\sin\alpha = n\sin(\arctan(\frac{D}{2f})) \approx n\frac{D}{2f} \tag{2.38}$$

$$R_{ax} \approx \frac{0.6n^2\lambda}{(NA)^2} \tag{2.39}$$

Thus, as is shown in Equation 2.39, a large numerical aperture results in a small depth of focus, i.e., the image becomes out of focus at a small distance away from the focal plane. Very often, the depth of field is interchangeably referred to the depth of field. Strictly speaking, the definition of the depth of field, i.e., the distance between the nearest and farthest objects that are sufficiently sharp in an image, is somewhat arbitrary and not commonly used in optical physics.

Note that in an inverted microscope, the objective is below the specimen, so the fluores-

cence is excited from the bottom of the specimen. It is also possible in the setup to incorporate the transmitted illumination from the top of the specimen. In this case, if the specimen is transparent, the fluorescence (so-called diascopic fluorescence) as well as diffracted and refracted light is transmitted through the objective. This technique is the transmitted-light fluorescence microscopy, developed before the epifluorescence microscopy [159]. However, this transmitted-light fluorescence microscopy is not used in this thesis simply because non-transparent systems are studied.

Chapter 3

Experimental methodology and instrumentation

The general experimental methodology applied in all following chapters is described. This includes the adsorbates studied, general reagents and materials used. Worth highlighting is the fabrications of the single-crystal bead electrode because of its important role in facilitating the investigations of a variety of SAMs throughout the thesis. Additionally, electrochemical and spectroelectrochemical methods are the common techniques employed to characterize the SAMs investigated. Thus, a general overview of the instrumentation is given in this chapter with details presented in the corresponding chapters.

3.1   Adsorbates, reagents and materials

3.1.1   Adsorbates studied

Three main classes of adsorbates will be studied in this thesis: alkanethiol, thiol-modified Aib peptide and thiol-modified DNA. These adsorbates are further labeled with fluorophores to facilitate the spectroelectrochemical measurements. Three types of fluorophores are used: BODIPY, AlexaFluor488 and AlexaFluor647.

BODIPY is the abbreviation of boron-dipyrromethene and the trade name for the series of fluorophores with the core structure of 4,4-difluoro-4-bora-3a,4a-diaza-s-indacene (Figure 3.1a) [163]. The BODIPY fluorophores tend to be UV adsorbing but the excitation and emission wavelengths can be tuned by derivatization. The derivative used to label the adsorbates studied is the BODIPY 493/503 (Figure 3.1b, the bond marked by asterisk will be linked to the adsorbate terminal groups). The BODIPY fluorophore can form two types of dimers: H-dimer
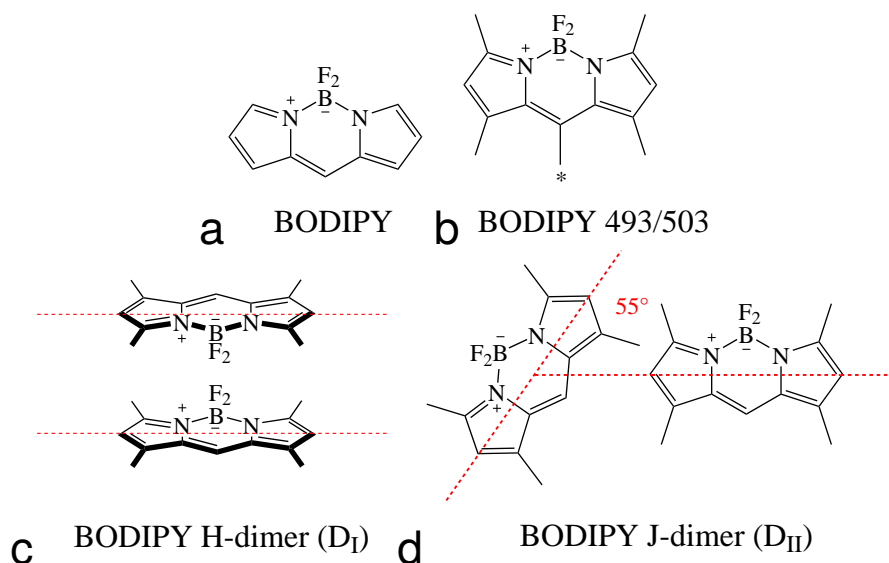
Figure 3.1: (a) Core structure of BODIPY fluorophores; (b) structure of BODIPY 493/503 (the bonds marked by an asterisk will be linked to the adsorbate terminal groups.); structures of (c) BODIPY H-dimer (D_I) and (d) BODIPY J-dimer (D_{II}).

(also called D_I, Figure 3.1c) and J-dimer (also called D_{II}, Figure 3.1d). The H-dimer formed by two monomers in two parallel planes stacking together with a distance of 0.49 nm is non-fluorescent, whereas the J-dimer, formed by two monomers with a distance of 0.38 nm between two mass centers and an angle of 55° between two long diagonal axes in one plane is fluorescent, exhibiting red shifts in both the excitation band and the emission band as compared to the monomer spectra [163–165].

Alexa Fluor® is a family of fluorophores developed by Molecular Probe Inc. featuring high brightness, high photostability and insensitivity to its environment [166, 167]. The structures of the Alexa Fluor® 488 (AlexaFluor488 hereafter) and Alexa Fluor® 647 (AlexaFluor488 hereafter) are shown in Figure 3.2 a & b respectively.

The selected representative of fluorophore labeled alkanethiol is the HS-C10-BODIPY (Figure 3.3a), which is a ten carbon alkyl chain with a thiol group modifying end and a BODIPY 493/503 fluorophore modifying the other end. This adsorbate was custom synthesized by Arnold Kell and Mark S. Workentin at University of Western Ontario as reported in [168].

The α-aminoisobutyric acid (Aib) peptide is a class of synthetic peptide forming the 3_{10}-helix structure (Further discussed in Chapter 5). The selected representative of fluorophore labeled thiolated Aib peptide is the HS-Aib4-BODIPY (Figure 3.3b), which is a four Aib residue peptide
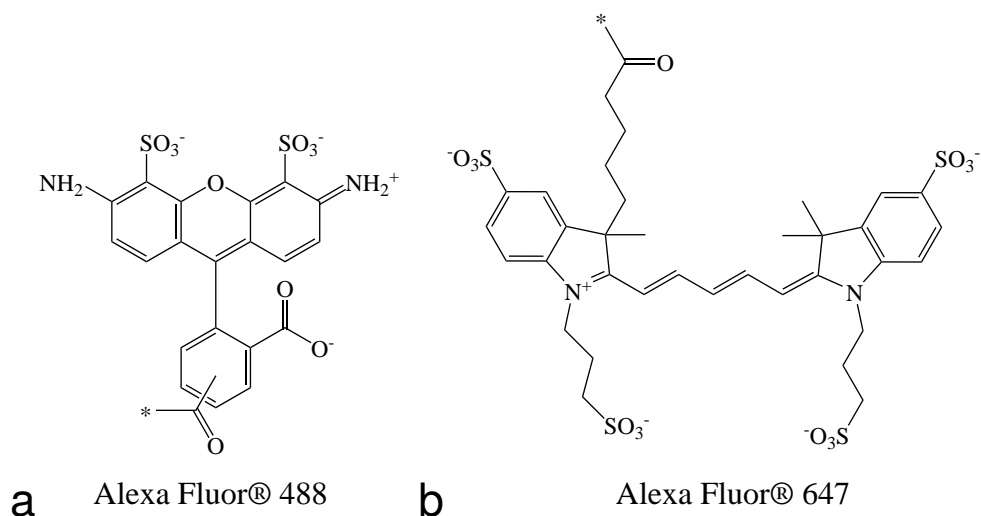
Figure 3.2: Structures of (a) Alexa Fluor® 488 and (b) Alexa Fluor® 647. The bonds marked by asterisks will be linked to the adsorbate terminal groups.

chain with the N-terminus modified by a thiol group spaced with two carbons and the C-terminus modified by a BODIPY 493/503 fluorophore spaced with a benzene ring. This adsorbate was custom synthesized by Ivan Guryanov and Flavio Maran at University of Padova as reported in [8]. Note that HS-Aib4-BODIPY was stored at −20 °C to prevent instant oxidation.

The 30-mer DNA (5'-CTG-TAT-TGA-GTT-GTA-TCG-TGT-GGT-GTA-TTT-3') adsorbates studied were custom synthesized and dual high performance liquid chromatography (HPLC) purified by Eurogentec North America. Few secondary structures are stable at room temperature for this DNA sequence. The 5' end was modified with a thiol group spaced with a six carbon linker and the 5' end was labeled with an Alexa Fluor fluorophore (either AlexaFluor488 or AlexaFluor647). The complementary strand (5'-AAA-TAC-ACC-ACA-CGA-TAC-AAC-TCA-ATA-CAG-3') was also custom synthesized by Eurogentec North America. All DNA stock samples (solid or solution) were store at −20 °C to prevent degradation.

The last adsorbate is the 6-mercaptohexan-1-ol (MCH), which is a hydroxyl-terminated short chain alkanethiol commonly used as the diluent for DNA SAMs [108–110]. This adsorbate was purchased from Aldrich with a purity of ⩾ 99%.
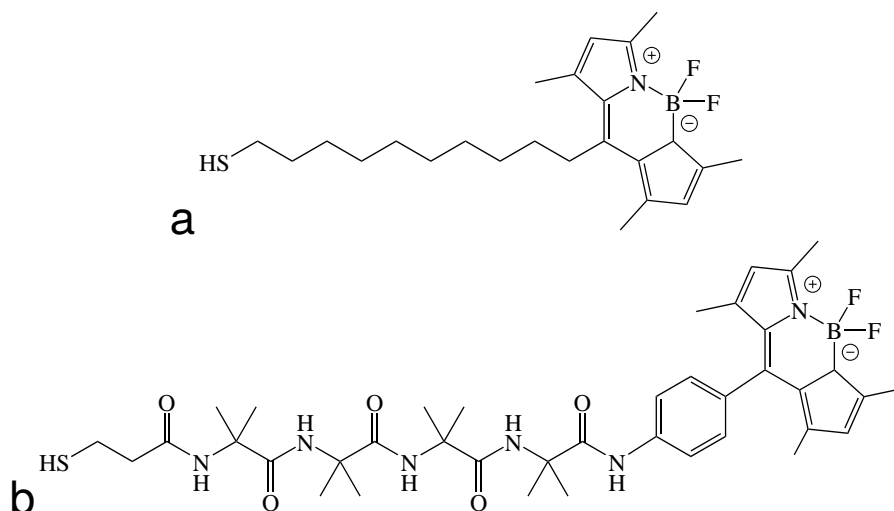
Figure 3.3: Structures of (a) HS-C10-BODIPY and (b) HS-Aib4-BODIPY.

3.1.2 Reagents

Surface chemistry is extremely sensitive to impurities, so the commercial reagents employed were of the highest purity available from major chemical vendors (Sigma-Aldrich, Fisher Scientific, etc.) without further purification. These include the electrolyte salts to prepare the buffer solutions, organic solvents and acids or bases to adjust pH. Besides these directly used commercial reagents, some other important reagents are worth highlighting. The water was purified with a Milli-Q® Integral 5 water purification system to an ultrapure level of > 18 MΩ•cm resistivity and $\leqslant 3$ ppb total organic carbon. $KClO_4$ was doubly recrystallized from the purchased reagent using the ultrapure water prior to making electrolyte solutions. The gold wire used to fabricate the substrate electrodes was purchased from Alfa Aesar with a purity of 99.999%, which is a requirement for forming a single-crystal electrode. The gold wire (Ø = 1.0 mm) was further purified by immersing the part to be melted in aqua regia for 15 min. Ar gas used to deoxygenate the solutions in electrochemical measurements was purchased from Praxair with a purity of $> 99.998\%$.

3.1.3 Materials

The electrochemical and spectroelectrochemical cells were made by Brian Ditchburn, the UBC Chemistry glassblower, of which the procedures are detailed in [169]. All glasswares were

immersed in ~80 °C 1:1 volume of concentrated HNO_3:H_2SO_4bath for 3 h, then rinsed and soaked in ultrapure water for over 12 h prior to use. The pipette tips (from Gibson Diamond) used to measure small volumes of liquid samples were autoclaved at 120 °C for 40 min to remove any contaminants potentially degrading the adsorbates. The siliconized microcentrifuge tubes (Bio Plas G-Tube®) used to store small volumes of sample solutions were certified by the manufacturer to be RNase and DNase free and human DNA free.

3.2 Substrate fabrication and cleaning

3.2.1 Single-crystal Au bead electrode

The fabrication of a single-crystal Au bead electrode was based on the well-known procedures of making Pt single crystal electrodes [170]. Briefly, the ultrahigh purity and further purified gold wire was heated and melted with a butane torch in an area protected from air currents. The bottom part of the gold wire was kept molten until a gold bead formed and grew to approximately 2 mm in diameter. The bead was slowly cooled down and solidified by gently moving the flame away. Typically aqua regia cleaning was followed to further dissolve the superficial layer of Au atoms along with possible impurities. After this cleaning process, the melting and solidifying process was repeated with flame intensity and position well controlled to keep the molten part below the boundary between the uncrystallized wire and the crystallized bead, preventing further growth of the bead. This aqua regia cleaning followed by melting and solidifying was usually repeated 2-3 times to guarantee a high quality single crystal bead electrode. Usually big (111) facets and small (100) facets could be seen on the surface through a microscope following the fcc single crystal pattern, completely or partially. While incompletely formed single crystal (e.g. bi-crystal) with at least one complete stereographic triangle present was acceptable especially under high power magnification, the complete single crystal bead was achieved most of the time in this thesis by carefully and slowly (sometimes repeatedly) melting a small portion of uncrystallized wire so it recrystallizes.

The single-crystal Au bead electrode was typically cleaned following four routines. First, each time after an electrochemical experiment where a SAM was desorbed, the electrode was

cleaned with cyclic voltammetry scans, −1.20 V to +0.85 V (vs. Ag|AgCl), at 200 mV/s in a newly prepared $KClO_4$ solution (pH = ~12 adjusted with KOH) for 20 min. In addition, after this mild electrochemical cleaning, the electrode was heated with butane torch until the bead turned orange (not melted) for approximately 20 s, followed by rinsing in the ultrapure water. This heating and rinsing procedure was typically performed three times before assembling another SAM onto the electrode. Furthermore, a gentle electropolishing (modified from [171]) by polarizing the gold bead at +2.45 V (vs. Au wire) in a 1 M $HClO_4$ solution for 30 s followed by immersion in 1 M HCl solution for 10 s was conducted typically for an electrode with accumulated organic residues left after repeated deposition of SAMs (typically no more than three times) especially less hydrophilic adsorbate (e.g. the thiolated Aib petide). The electropolishing treatment was followed by cyclic voltammetry scans, −1.0 V to +1.0 V (vs. saturated calomel electrode (SCE)), at 200 mV/s in a newly prepared $KClO_4$ solution for 10 min. Lastly, since electropolishing could lead to roughening of the surface, this treatment was at most repeated twice. For an aged or often used electrode, an aqua regia cleaning followed by melting and solidifying was performed to resume a good surface condition, but in order to keep the original surface crystallography, the melting did not exceed the wire - bead boundary.

3.2.2   Polished single-crystal Au(111) electrode

The polished single-crystal Au(111) electrode was prepared from a single-crystal Au bead electrode and used for electrochemical measurements in Chapter 5. This Au bead electrode was fabricated by carefully adjusting the angle of melting so that a (111) facet was formed very close to the bottom of the bead. The orientation of the electrode was aligned to be along the normal direction of the (111) facet with a laser and fixed with a purposely designed holder. Mechanical polishing was conducted first with sandpapers (600 grit and 1200 grit) and then with diamond polishing materials (LECO premium grade aerosol diamond spray 6 μm, 3 μm and 1 μm sequentially) sprayed on polishing felts. After being cleaned by sonication in ethanol and water each for 15 min to remove excess polishing materials embedded on the surface, the resultant polished electrode was annealed at 700 °C for 24 h. The final treatments were the gentle electropolishing followed by cyclic voltammetry scans described above. The area of the planar

surface were measured with two methods. First, an image of the planar surface was taken and analyzed with ImageJ to obtain the geometric area. Second, the electrochemical area was calculated by dividing the capacitance of the planar surface (hanging meniscus configuration, described below) in ClO_4^- solution (acidic or basic) at –0.8 V (vs. SCE) by 20 μF cm^{-2}, the unit area capacitance in the absence of specific adsorption [172, 173]. The similarity of the two results (roughness factor = 1.04) demonstrated the smoothness of the polished electrode.

The polished Au(111) electrode was also cleaned with the same approaches as the single crystal Au bead electrode, except for aqua regia cleaning and remelting.

3.3 Electrochemical instrumentation

3.3.1 Electrochemical setup

The electrochemical measurements without coupling to spectroscopic techniques were only performed for a polished Au(111) electrode in Chapter 5. The schematic of the electrochemical setup is shown in Figure 3.4. The electrode was fit into a holder and placed into the electrochemical cell as the working electrode (WE). The counter electrode (CE) was a Au wire with a coil at the end and the reference electrode (RE) was SCE (Beckman Coulter 511100) connected through the salt bridge. The electrolyte solution was deoxygenated with Ar gas bubbling for 15 min before measurements and the Ar flow was maintained above the solution during measurements. The WE was gently lowered so that the flat surface of the electrode just touches with the supporting electrolyte surface creating a hanging meniscus [169, 174, 175].

All electrochemical experiments were conducted with a HEKA PG590 potentiostat and a Princeton Applied Research Model 175 universal programmer which generated the potential scans. An EG&G Model 5210 lock-in amplifier was also used to generate AC potential perturbation in capacitance measurements. All data were digitized with a National Instruments PCI-6052E data acquisition board (DAQ) and further transferred to a computer interface coordinated by a LabVIEW program.
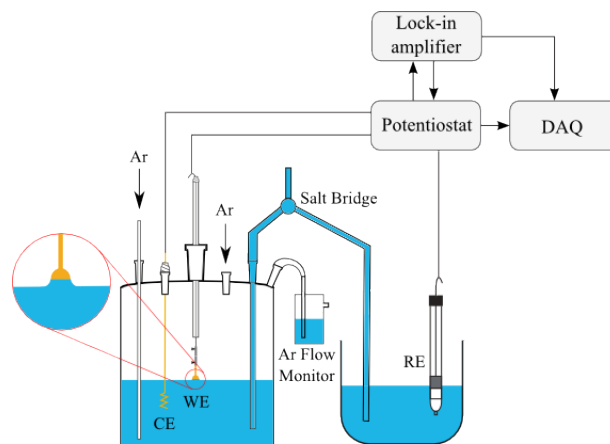
Figure 3.4: Schematic of the electrochemical setup.

3.3.2 Electrochemical techniques

Cyclic voltammetry between two set potentials was the main technique used to study the SAM modified electrode. For a SAM-modified electrode, the scan was limited in the potential range (typically -0.10 V to 0.30 V (vs. SCE)) where the SAM was stable without the occurrence of reductive or oxidative desorption. Usually, more than 20 potential range limited scans were conducted until no significant change was observed. The purpose of repeating scans was to minimize the wetting effect. As a matter of fact, in the cyclic voltammetry and capacitance measurements, charging current and capacitance signals greatly depended on the area of the electrode covered with solution. The hanging meniscus configuration to the utmost guarantees that only the flat surface at the bottom of the electrode was covered, but the electrolyte solution was still able creep up the sides, covering part of the electrode above the edges. Nevertheless, with potential scans, the wetted area gradually decreased as a result of drying. Consequently, the charging current and capacitance decreased as well, approaching a constant level. Therefore, it was necessary to minimize the wetting issue by repeating potential scans until no change of current or capacitance observed.

Differential capacitance was also employed to check the quality of the SAM formed on the electrode surface. The capacitance measurements were conducted by adding an AC sinusoidal potential perturbation (200 Hz and ~5 mV) from the lock-in amplifier to the DC potential applied by the potentiostat. The output AC current was then fed into the lock-in amplifier and

separated into real and imaginary components. Assuming the electrode | solution interface can be modeled as a capacitor (double layer capacitance) and a resistor (solution resistance) in series (see Section 2.3.3), the capacitance was calculated with Equation 3.1 derived from impedance theory [13].

$$C = \frac{i_{Re}^2 + i_{Im}^2}{2\pi f E_{rms} i_{Im}} \tag{3.1}$$

Here C is the capacitance of the interface, i_{Re} is the real component of the AC current, i_{Im} is the imaginary component of the AC current, f is the frequency of the AC perturbation and E_{rms} is the root mean square (rms) amplitude of the AC potential wave. Note that this capacitance calculation is only valid for systems behaving as IPEs. For systems

3.4   Spectroelectrochemical instrumentation

3.4.1   Spectroelectrochemical setup

The schematic of the spectroelectrochemical setup is shown in Figure 3.5. All spectroelectro-chemical measurements were performed in a spectroelectrochemical cell featuring an optical window of 250 μm thickness forming the base. Besides the optical window, the spectroelec-trochemical cell functioned similarly to an electrochemical cell with ports for WE (the polished Au(111) electrode or the single crystal bead electrode), CE (a Pt wire with a coil at the end) and Ar and integrated salt bridge also acting as the RE (BASi® RE-6 Ag|AgCl or CHI150 SCE) housing. The potentiostat (FHI-ELAB 0599 potentiostat or FHI-ELAB G050-0298 potentiostat) and lock-in amplifier (EG&G 5208 lock-in amplifier or SRS SR830 lock-in amplifier) were em-ployed for electrochemical measurements.

The spectroelectrochemical cell was further placed on top of an Olympus IX70 inverted fluorescence microscope. The type of objective was chosen as required for each specific ex-periment. Most of the optical measurements in the spectroelectrochemical experiments were performed with dry objectives. However, some of the experiments in Chapter 6 were performed with water immersion objectives in an attempt to improve the resolution (according to Equation 2.36, d_{min} of ~400 nm can be achieved using a 40× water immersion objective) and image
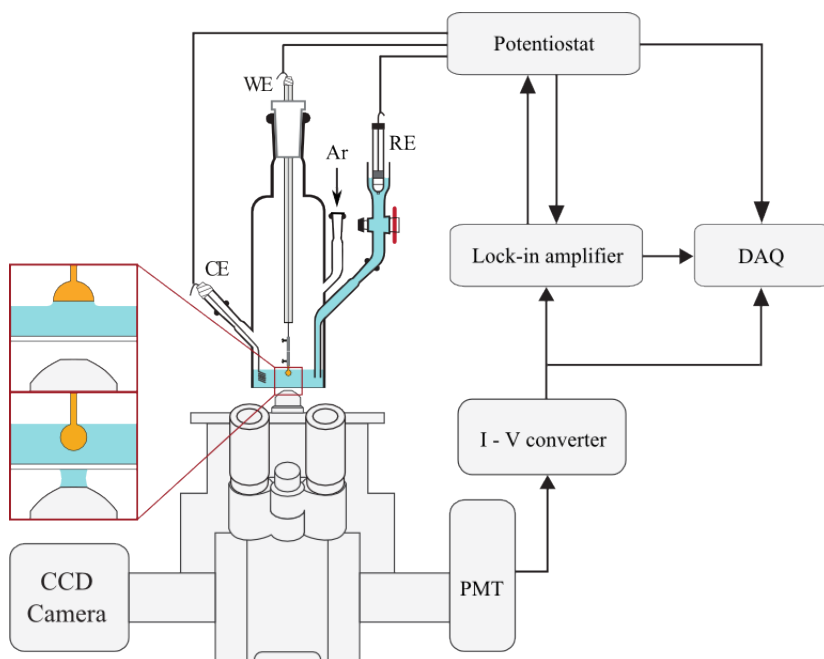
Figure 3.5: Schematic of the spectroelectrochemical setup. Adapted from [169] with permission. Copyright (2017) Springer.

quality. Since most of the surfaces imaged are curved, the depth of focus should also be considered. According to Equation 2.39, the depth of focus is very small (~1 μm) when imaging is performed with an objective with a high numerical aperture (e.g., a 40× water immersion objective). But typically in this type of measurements, a field diaphragm was closed down so that a small region (~96 μm in diameter) was illuminated, so within the illuminated region, the image was mostly in focus.

A fluorescence illuminator equipped with a Hg arc lamp was employed to excite the fluorophores. The light from the fluorescence illuminator came from the back of the microscope (not shown in Figure 3.5) and further traveled through the filter set which directs light for illumination, filtration and collection. Depending on the fluorophore used to label the adsorbate studied, a particular filter set was chosen. The same filter set from Chroma (excitation: ET470/40x, dichromatic: T495LPXR, emission: ET525/50m) was used for both the BODIPY and AlexaFluor488, whereas another filter set from Chroma (excitation: HQ620/60x, dichromatic: Q660LP, emission: HQ700/75m) was used for AlexaFluor647. The spectra of the fluorophores used in this thesis and their corresponding filter sets are shown in Appendix A. The brief specifications for the filter sets are listed in Table 3.1. Worth mentioning is that no prominent spectral spike (from

Table 3.1: Fluorophores and corresponding filter sets

Fluorophore	Excitation filter	Dichromatic mirror	Emission filter
BODIPY (monomer), AlexaFluor488	450-490 nm	495 nm	500-550 nm
AlexaFluor647	590-650 nm	660 nm	662-738 nm

the Hg arc lamp) was present in the two excitation bands listed in Table 3.1 (see Figure A.1 in Appendix A).

The microscope was further equipped with two types of detectors: charge-coupled device (CCD) cameras and photomultiplier tube (PMT). Two CCD cameras were utilized for imaging: Photometrics Evolve® 512 EMCCD camera with the image size of 512×512 pixels and SBIG ST-7XMEI CCD camera with the image size of 765×510. The PMT used was a Newport 77348 model with the active area of 8×24 mm^2 and the signal output from the PMT was further converted into voltage with a Stanford Research SRS570 current preamplifier. Note that the fluorescence images taken with the Photometrics Evolve® 512 EMCCD camera was illuminated with an Excelitas X-Cite® exacte fluorescence illuminator, while the fluorescence images taken with the SBIG ST-7XMEI CCD camera and the fluorescence detected by the PMT were with an Excelitas X-Cite® 120PC fluorescence illuminator.

3.4.2 Spectroelectrochemical techniques and data analysis

The spectroelectrochemical techniques employed were mainly dependent on the detector used. When a camera was the detector, the in situ fluorescence imaging technique was used. Briefly, the WE was stepped to a series of potentials, while at each potential, one or more fluorescence images were taken with the preset conditions (exposure time, illuminator light intensity, electron-multiplying (EM) gain for the Evolve® 512 EMCCD camera) and the capacitance was measured. Two major potential stepping schemes (profiled in Figure 3.6a) were programmed. In the first potential stepping scheme, the potential started from an initial potential (E_i), sequentially stepped to a series of step potentials (E_s) with the same step width (typically a negative value) between two neighboring E_s and completed at a final potential E_f. This potential stepping scheme was used to study the reductive desorption process of a SAM (Chapter 4 and Chapter 5). Compared with the first potential stepping scheme, E_i was also a base potential (E_b) in the second potential stepping scheme and after each E_s, the potential was stepped back to E_b.

The two potential stepping schemes

Events during a potential step
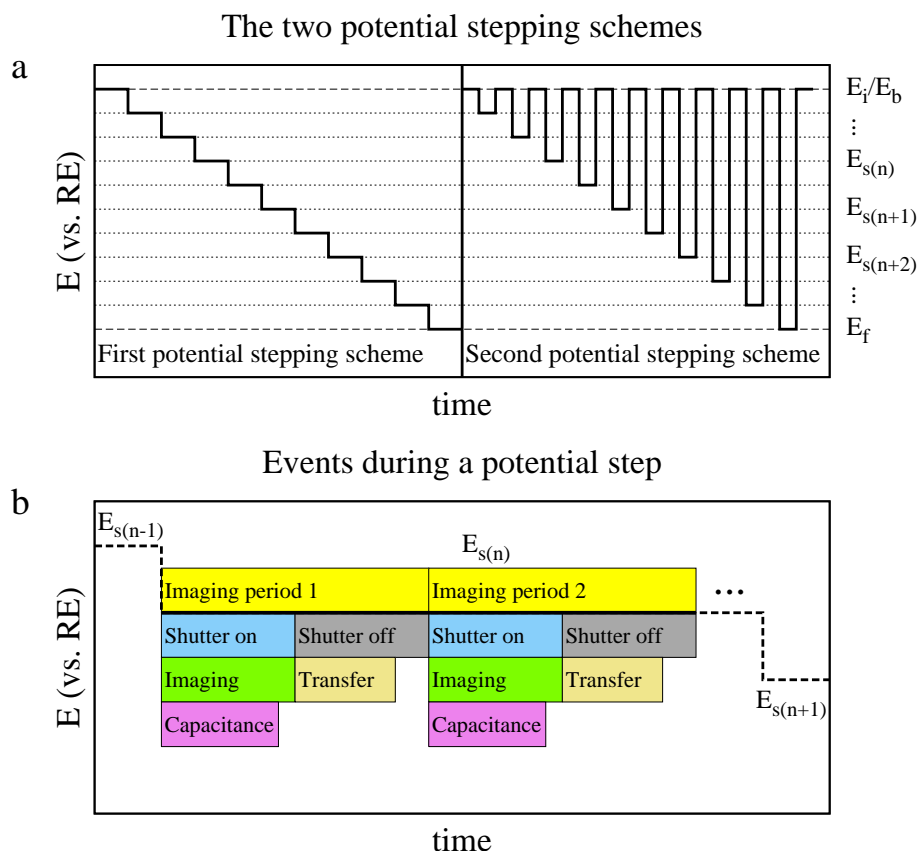
Figure 3.6: (a) Potential profiles of the two potential stepping schemes and (b) events occurring during a potential step.

This potential stepping scheme was used to study the potential modulated response of a SAM (Aib peptide SAM in Chapter 5 and DNA SAM in Chapter 6). All experimental events, including the potential stepping, illuminator shutter triggering, imaging, capacitance measurement and data transfer (illustrated in Figure 3.6b) were coordinated with Labview programs.

After each potential stepping measurement, an image stack was created from the fluorescence images, which was analyzed with ImageJ. The images were first despeckled and smoothed with the built-in function of Accurate Gaussian Blur (standard deviation = 2) [176]. Subtracting the background was also performed for each image. However, the background determination was not always easy. Cameras have dark current noise as part of the measurements [177, 178]. Background resulting from the dark current noise was measured in the absence of illumination and subtracted from each image. Stray light and light reflected from the metal surface that leaked through the filters were also important components of the background.

For a flat substrate (i.e., a Au(111) facet on a single-crystal bead electrode), the background was measured with an unmodified electrode. For a curved substrate (i.e., a bead electrode), measuring the background with an unmodified electrode was not performed because it was difficult to guarantee the same the position and orientation of the electrode. If no fluorescence was emitted at some potentials, the images taken at these potentials could be used as the background. Nevertheless, for most of the studies on bead electrodes in this thesis, the accurate background was not critical, so only the dark current background was subtracted. Important ImageJ functions used for image processing are worth highlighting here [176]. The most commonly used ImageJ function to extract data from an image stack is the z-axis profile function which calculates the average intensity of all pixels inside a selected region of interest (ROI) for all images in the image stack. The z-projection functions look for the maximum or minimum values for each pixel through an image stack and construct the maximum or minimum projection images with the corresponding values.

When a PMT was the detector (further coupled with the current preamplifier), the optical cyclic voltammetry technique for DC optical signal and the harmonic analysis technique with the lock-in amplifier for AC optical signal were used. These techniques will be discussed in-depth in Chapter 6.

Chapter 4

Spectroelectrochemical investigation of the reductive desorption behavior of self-assembled monolayers on a single crystal Au bead electrode due to the influence of surface crystallography

This chapter discusses the influence of the surface crystallography on the reductive desorption behaviors of SAMs deposited on Au single crystal bead electrodes. Two systems are explored: a BODIPY fluorophore-labeled alkanethiol (HS-C10-BODIPY) and a BODIPY fluorophore-labeled thiol-modified α-aminoisobutyric acid (Aib) peptide (HS-Aib4-BODIPY). The single-crystal gold bead electrode has the family of crystallographic surfaces symmetrically distributed following the fcc crystal structure. As the substrate, this type of electrode enables exploration of a SAM deposited on the surfaces representing the full fcc crystallographic triangle simultaneously and under identical conditions. In situ fluorescence imaging is utilized to monitor the fluorescence responses of a SAM during the reductive desorption process on the variety of crystallographic surfaces.

4.1   Reductive desorption of self-assembled monolayers

As was mentioned in Section 2.2.2, thiolate SAMs deposited on Au electrode can be reductively desorbed by applying a sufficiently negative potential. The reductive desorption is an important process that requires further understanding so as to be used for surface modification in a controlled manner. Selective desorption of mixed-component SAMs [179, 180] or SAMs deposited on surfaces with different crystal structures [168, 181, 182] has been widely used in controlled functionalization of the surface, especially on the nanometer scale. Because of the fast-developing nanotechnology, where the surface crystal structures become prominent, selective desorption of SAMs deposited on surfaces with different crystal structures is more and more widely employed, and thus requires an in-depth investigation of the influence of the surface crystallography on the reductive desorption in order to achieve controlled surface functionalization.

The study of the reductive desorption process was pioneered by Porter [118, 183–185], Morrin [10, 186–188] and their co-workers. One advantage of the reductive desorption process is that the reaction follows a stoichiometric route shown in Equation 2.10, so it can be used to quantify the surface density of the monolayers [183]. Typically, a linear scan voltammetry measurement can be performed from a positive potential E_a (at which a SAM is adsorbed) to a negative potential E_d (at which the SAM is desorbed). The total charge of desorption can be calculated by integrating the current of the reductive desorption peak between these two potentials, described in Equation 4.1, where Q is the total charge, i is the cathodic current and v is the scan rate.

$$Q = \int_{E_a}^{E_d} \frac{i}{v} dE \tag{4.1}$$

Then based on the Faraday's Law, the surface packing density can be calculated following Equation 4.2 where Γ is the surface packing density, n is the charge number ($n = 1$ for the Au-S system), F is Faraday constant and A is the electrode area.

$$\Gamma = \left| \frac{Q}{nFA} \right| \tag{4.2}$$

This simple approach fails to take an important point into account [189–192]. The current of the reductive desorption peak consists of not only the desorption current, but also the double layer charging current. This causes an overcalculated charge even if the SAM remains adsorbed on the electrode surface. More importantly, once the Au-S bond is reduced at sufficiently negative potential, water molecules and hydrated cations substitute the monolayer, so the dielectric constant changes with potential. As a result, the charging current and thus the effective charge number n is potential-dependent. Since water has much a higher dielectric constant than the monolayer, the charging contribution increases with the negatively scanning potential. Therefore the packing density calculated based on Equation 4.1 and Equation 4.2 is higher than the actual value. A method to accurately quantify the surface packing density was developed by Lipkowski and co-workers [191, 192]. This method employs chronocoulometry and a LB-deposited thiolate film of known packing density to calculate the effective charge number at various potentials during a desorption process. It was found that the packing density calculated by integration of current in a cyclic voltammetry measurement is overestimated by ~20%. However, while this chronocoulometry method does prove to give more accurate results, it definitely requires complicated steps and does not seem to be applicable to all adsorbates because of the important LB-deposition step. Therefore the simple calculation based on Equation 4.1 and Equation 4.2 by arbitrarily setting a linear capacitive current baseline is still a convenient and conventional way to estimate the packing density of SAMs.

A kinetic model proposed by Mulder et al. [193] describes the mechanism of the reductive desorption of alkanethiolate SAMs. An alkanethiolate SAM modified Au surface inevitably has SAM-covered domains and defective domains. The defective domains can be vacancy islands, crystal grain boundaries or less ordered adsorbates, which are relatively permeable to charged species. The potential on the Au-S interfaces is easily set to a sufficiently negative point to initiate the reduction reaction near these defective domains. Consequently, the vacant domains grow radially as the reduction reaction progresses and the SAM-covered domains shrink as well. Eventually, all the vacant domains merge and the SAM-covered domains disappear.

The factors influencing the reductive desorption process have also been studied in detail with electrochemical methods. Studies of reductive desorption of alkanethiolate SAMs showed that the desorption potential was strongly influenced by the chain length of the alkanethiol [10,

118, 183, 185, 186, 188, 190]. To be specific, the desorption potential shifted to more negative potentials with increasing chain length. This can be rationalized by more well-organized and well-packed SAMs formed with longer chain alkanethiol. It was also found that the adsorbate structure[190], the SAM deposition conditions (e.g., the solvent used [189], the deposition time spent [189] and the electrochemical deposition duration [194]), pH of the solution used for electrochemical measurements [10, 186], and composition of the electrolyte [185, 190] can also influence the desorption potential. All these factors, can actually be generalized as factors which can have an impact on the intermolecular interactions between adsorbates.

While the studies above were primarily performed on a Au(111) surface, either Au films on mica sheets or polished single-crystal electrodes, the influence of surface crystallography on reductive desorption has also been investigated. The voltammetry measurements showed different reductive desorption behaviors for the alkanethiol SAMs deposited on three different Au films substrates: Au on mica, Au on Si and Au on glass [184]. Au on mica had predominant (111) feature, so alkanethiol deposited on it had a sharp desorption peak. For the other two substrates, there existed a large portion of non-(111) steps, so additional desorption peaks appeared at more negative potentials. Compatible results were obtained with polished single-crystal electrodes and polycrystalline electrodes [10–12]. Multiple desorption peaks were observed for an alkanethiol SAM deposited on a polycrystalline electrode which correspond to the desorption peaks observed at the same potentials on polished single crystal electrodes (Figure 4.1). The desorption potentials of SAMs on different crystallographic surfaces have some correlation with the PZC of the surfaces. For alkanethiol SAMs on Au, it is generally true that the desorption potentials for various crystallographic surfaces and PZC for corresponding surfaces follow the same order. Thus the reductive desorption of an alkanethiol SAM on a polycrystalline electrode starts from the (111) surface, followed by the (100) surface, and further followed by (110) and (210) surfaces. Note that as reviewed in Section 2.3.4, the (210) surface is the roughest among all stepped surfaces and with the most negative PZC, so it is also widely investigated.

Combining the two major contributions discussed above: the substrate crystal structure and the intermolecular interactions between adsorbates, an elaborated form of Equation 4.3 is presented to describe the reductive desorption process. The influence of the two contributions
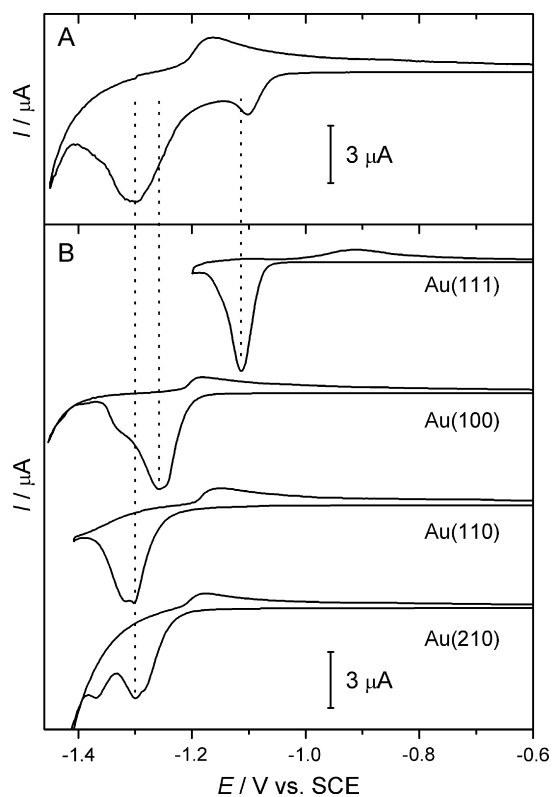
Figure 4.1: Cyclic voltammagrams measured during desorption of decanethiolate SAMs deposited on (A) a polycrystalline Au bead electrode and (B) polished single crystal Au electrodes with the indicated crystallographic orientations. Reprinted from [12] with permission from Elsevier.

on the reductive desorption of SAMs has been detailed by Doneux et al [12] and summarized here. The substrate crystal structure can influence the binding with the adsorbate and the strength of the Au-S interaction. When the adsorbate molecules are reductively removed, the substrate is coated with solvent, so the difference between the applied potential and PZC also acts as a driving force for the desorption process. Even though PZC is shifted negatively upon adsorption of a SAM [192, 195], this driving force is still taking effect. The intermolecular interactions between adsorbates largely determines the stability of a SAM. A SAM stabilized by attractive interactions tends to have a more negative desorption potential and vice versa, a SAM destabilized by repulsive interactions tends to have a less negative desorption potential. Note that the intermolecular interactions can be influenced by a number of factors mentioned above: solvent, electrolyte, etc. and even the substrate crystal structure.

$$\text{RS}(\text{surf}, \text{Au}(hkl)) + x\text{H}_2\text{O}(\text{aq}) + n\text{e}^-(\text{Au}(hkl)) \rightleftharpoons \text{RS}^-(\text{aq}) + x\text{H}_2\text{O}(\text{surf}, \text{Au}(hkl))$$

$$(4.3)$$
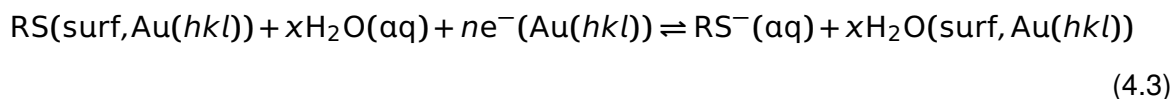
The work reviewed above was performed on electrodes with predominantly one crystallographic orientation (films or polished single-crystal electrodes) or polycrystalline electrodes. Thus to study the influence of surface crystallography on the reductive desorption process, a series of experiments with different electrodes are required. However, it is very important to perform the series of experiments under consistent conditions since the experimental conditions have substantial influence on the intermolecular interaction of the SAMs. Small changes in the SAM assembly conditions (e.g., the assembly time, the solution pH, the temperature, etc.) for each replicate on a particular surface, can result in SAMs that may not represent the designated ones. Small variations in each measurement can also lead to a lack of data reproducibility. Therefore, ideally, all the replicates should be assembled under the same conditions and measured at the same time. In the sections that follow in this chapter, a single crystal bead electrode with the family of crystallographic surfaces symmetrically distributed following the fcc crystal structure is used as the substrate for the SAMs studied. With the single crystal bead electrode, all identifiable crystallographic surfaces are analyzed self-consistently under identical conditions for one single SAM in one single measurement.

4.2 Objectives

In this chapter, the single crystalline Au bead electrode will be used as the substrate for two types of adsorbates: alkanethiol and thiol-modified Aib peptide. The in situ fluorescence imaging method will be used to study the reductive desorption process of the SAMs prepared. With this method, the desorption from all identifiable crystallographic surfaces will be monitored in one single measurement. After detailed analysis, the influence of surface crystallography on reductive desorption will be demonstrated. The alkanethiolate SAMs have been studied intensively, so the comparison with literature reports will verify the feasibility of this method in exploring a fluorophore-labeled SAM on various crystallographic surfaces. This approach will be strengthened by studying the Aib peptide thiolate SAM with vastly different properties, also helping elucidate the influence of intermolecular interactions on reductive desorption.

4.3 Experimental

4.3.1 SAM preparation

The two types of adsorbates studied are: an alkanethiol (HS-C10-BODIPY, Figure 3.3a) and a thiol-modified Aib peptide (AuS-Aib4-BODIPY, Figure 3.3b). Both thiol-modified adsorbates are labeled with the BODIPY fluorophore in order to perform fluorescence imaging measurements. The assembly of these two types of SAMs onto the single crystal Au bead electrode followed the procedures below. Note that the solvents were carefully chosen so that the two adsorbates had appreciable solubility, ensuring high quality SAM formation.

Assembly of the AuS-C10-BODIPY SAMs was performed by immersing a clean substrate electrode in 1 mL of 1 mM HS-C10-BODIPY 1:1 MeOH-CHCl$_3$ solution in a glass vial. Two SAMs were prepared, one for 15 min and the other for 18 h. The modified electrode was then rinsed with the solvent and then water before characterization.

Assembly of the AuS-Aib4-BODIPY SAM was performed by immersing a clean substrate electrode in 50 μL of 1 μM AuS-Aib4-BODIPY ethanolic solution in a sealed microcentrifuge tube (siliconized, from BioPlas) for 2 h. The modified electrode was then rinsed with the solvent and then water before characterization.

4.3.2   In situ fluorescence imaging characterization of the SAMs

The in situ fluorescence imaging performed by applying multiple potential steps to the working electrode and taking the images at each step was discussed in Section 3.4. Specific for this set of experiments, the spectroelectrochemical cell was placed on top the Olympus IX-70 inverted epifluorescence microscope. The modified gold bead electrode was used as a working electrode. The electrochemical measurements were performed with a Pt coil counter electrode and a Ag|AgCl reference electrode connected to the working solution via a salt bridge. The working electrolyte solution was 50 mM $KClO_4$ (pH = 12 (±0.5) adjusted with KOH). The electrolyte solution was deoxygenated with Ar in all experiments. The fluorescence images were acquired with the Evolve® 512 EMCCD camera through an Olympus LMPlanFl 5× objective (NA = 0.13) producing images that represent 1.58 mm × 1.58 mm regions of the surface. The profiles of the potential steps applied were similar for the two types of SAMs in that the potential started at 0.0 V (vs. Ag|AgCl), and was stepped negatively by –20 mV increment. The duration at each step was 2 s for the AuS-C10-BODIPY SAMs and 4 s for the AuS-Aib4-BODIPY SAM. The final potential was –1.4 V (vs. Ag|AgCl) for the AuS-C10-BODIPY SAMs and –1.3 V (vs. Ag|AgCl) for the AuS-Aib4-BODIPY SAM.

4.4   Results and discussion

4.4.1   Reductive desorption of the AuS-C10-BODIPY SAM

The reductive desorption of an alkanethiol SAM occurs at the least negative potential on the Au(111) surface. This behavior has been well studied with electrochemical methods, as reviewed in Section 4.1. In addition, the reductive desorption of fluorophore- labeled alkanethiol SAM on polycrystalline Au bead electrode has also been investigated with in situ fluorescence imaging, further confirming the fact that the desorption occurring at the least negative potential on the identified (111) domain [168]. The fluorescence signal can be observed only when the fluorophore is sufficiently separated from the electrode surface as a consequence of SAM desorption. Thus when the potential was stepped to negative potentials, a detectable fluorescence signal appeared on (111) surface first, with other regions of the surface following at more
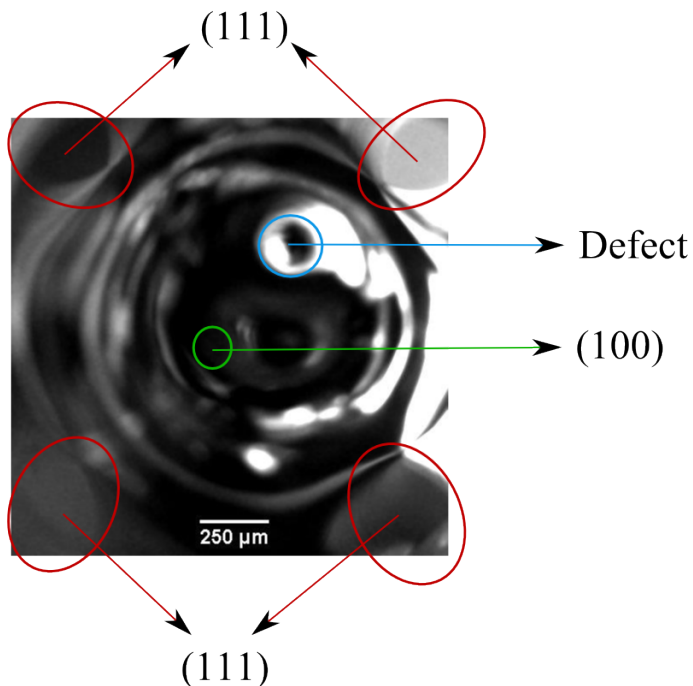
Figure 4.2: Brightfield optical image of the bottom of a gold bead electrode with (111) facets encircled in red, (100) facet encircled in green and defect encircled in blue. Adapted from [8] with permission. Copyright (2014) American Chemical Society.

negative potentials. This fact is relied upon for identifying the surface features on the single crystalline gold bead electrode imaged in the in situ experiments.

A bright field image looking up at the bottom of the Au bead used is shown in Figure 4.2. Four large facets encircled in red are observed in the corners of the image. These facets are the well-known (111) facets which have been employed as the substrates for STM studies [196–200]. In the center of the bright field image, a small facet encircled in green can be vaguely seen (with proper orientation and focal plane, this feature can be clearly seen). Based on the fcc single crystal structure, this small facet is where the (100) surface locates. The crystallographic facets are characteristic of carefully annealed single crystals, particularly prominent in Pt single crystal electrodes [201–203]. The dimple feature encircled in blue is a defect formed during the cooling process of electrode fabrication (seems unavoidable under present conditions). These crystallographic features are more clearly observed in the fluorescence images taken during the reductive desorption of a AuS-C10- BODIPY SAM from the electrode bead surface. Figure 4.3 shows the montage of selected fluorescence images taken from –1.14 V to –1.36 V (vs.

Ag|AgCl) in −20 mV increments during the reductive desorption of the AuS-C10-BODIPY SAM formed with a 15 min immersion time. The fluorescence intensity is false colored (as indicated with the calibration bar). A noticeable amount of fluorescence was observed at −1.14 V (vs. Ag|AgCl) coming from four regions at the four corners of the image, symmetrically oriented with respect to the center of the image. These four regions coincide with the four big (111) facets observed in the bright field image. As the potential was stepped negatively, starting from −1.22 V (vs. Ag|AgCl), fluorescence was observed from the center of the image, revealing a 4-fold symmetric cross with each arm of the cross directed in between two neighboring (111) facets. The center of the cross coincides with the the (100) facet in the bright field image, even though the presence of the defect results in a distortion of the NE portion of the cross. With more negative potential applied, at −1.28 V (vs. Ag|AgCl) the areas between two neighboring arms of the central cross started to fluoresce and further evolved into another cross with the arms pointing towards the (111) factets. At potential more negative than −1.30 V (vs. Ag|AgCl), fluorescence was observed from the rest of the surface, including the identifiable (110) surfaces between two neighboring (111) facets and (210) surfaces between (100) facet and each (110) surface, according to the fcc crystal structure.

The images present a highly symmetric potential-dependent behavior suggesting that the bead is indeed single crystalline in nature. The (111) facets located at the corners of the image are oriented in a 4-fold symmetry around the (100) surface. In addition, between two neighboring (111) facets, the (110) surfaces are present, also oriented in a 4-fold symmetry around the (100) surface, rotated by 45° with respect to the (111) facets. This pattern resembles the stereographic projection of an fcc crystal centered about (100), as reviewed in Section 2.1.4. However, the stereographic projection cannot be used for mapping the images here because the surface features are directly projected onto the image plane. The proper crystallographic projection map was created using a Perl script by assuming the bead was a perfect sphere. Since the (100) facet shown in Figure 4.2 was not exactly at the bottom of the electrode surface, small adjustments of rotating around the x- and y-axes (in plane of the page) and the z-axis (out of the page) had to be made to compensate. The adjustments were properly made by overlaying with a fluorescence image taken at a negative potential with the single crystal pattern clearly present. Figure 4.4a and 4.4b show the fluorescence images of the bead electrode ac-
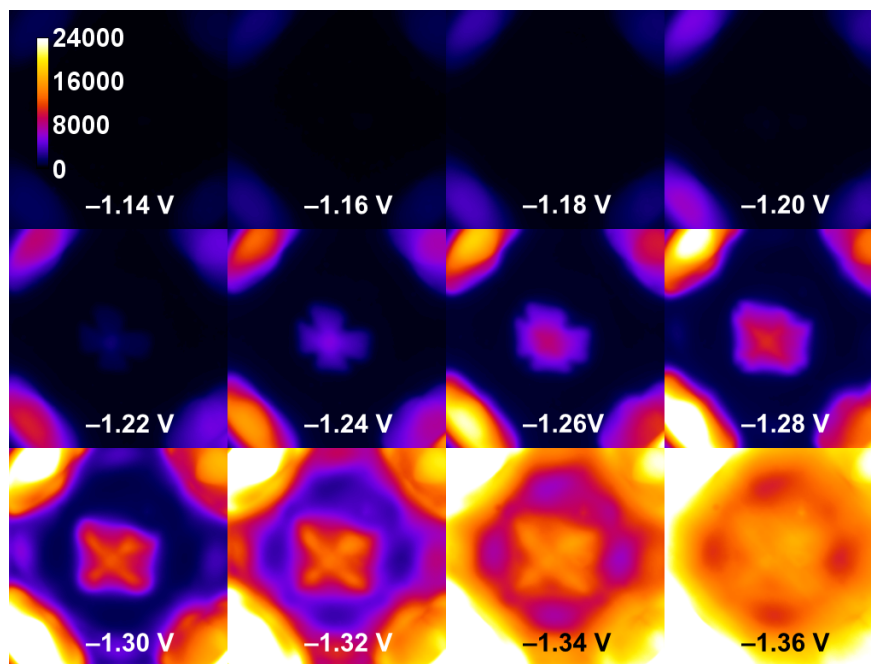
Figure 4.3: Montage of selected fluorescence images taken from −1.14 V to −1.36 V (vs. Ag|AgCl) in −20 mV increments during the reductive desorption of the AuS-C10-BODIPY SAM created with a 15 min immersion time.

quired at −1.24 V (vs. Ag|AgCl) and −1.30 V (vs. Ag|AgCl) with overlay of crystallographic map showing the low-index and stepped surfaces. With easily recognizable features from the (111) facets and the (100) facet, the map was adjusted to the corresponding position and orientation. This also allowed for the other surfaces to be located to subtle features in the fluorescence pattern (e.g., the cross in the center). The almost perfect symmetry of the fluorescence image and the excellent correlation with the crystallographic map for all quadrants on the surface demonstrates the single crystal nature of the Au bead. With this crystallographic map, further analysis of the reductive desorption process can be performed. Note that the assignment of crystallographic surfaces near the (111) facets might not be accurate because of the big size of the facets. Nevertheless, this effect is not expected to be large because these surfaces with large (111) terrace probably behave similarly as the (111) facet. In addition, the defect further distorts the locations of some crystallographic surfaces, but because of the high extent of symmetry, analysis can be conducted in the quadrants with minimum influence from the defect. Another important aspect to consider is the depth of focus because a curved electrode surface was imaged. The depth of focus estimated with Equation 2.39 (using $\lambda = 525\,nm$, $NA = 0.13$

and $n = 1.0$ for simplification) is about 19 μm. In reality, the depth of focus is much larger because of the multi-medium optical aberration [14]. The experimentally estimated depth of focus (strictly speaking, should be called the depth of field in this case) is about ~90 μm in the spectroelectrochemical setup. Assuming the (100) facet is located exactly at the bottom of the bead, the z-distance between the (100) facet and the center of a (111) facet is expected to be ~290 μm, which is three times larger than the apparent depth of field. Therefore, blurring observed in some parts of the image (e.g., the (111) facets) has a negligible influence on the change of fluorescence intensity with potential since the photon collection efficiency for each region is independent of potential.

Based on the crystallographic map, surfaces of interest can be selected to make the plots of fluorescence intensity as a function of potential for surfaces of interest. Figure 4.5a is a collection of the intensity-potential plots for the three low-index and (210) surfaces taken from different quadrants around the Au bead electrode surface for the AuS-C10-BODIPY SAM created with a 15 min immersion time. The intensity is in logarithmic scale due to the large changes. The potential at the start of desorption can be determined by choosing a threshold of the fluorescence intensity (e.g., 1 kcts/sec, indicated with the dotted line). As can be seen, the desorption potential is least negative from (111) surface at ~−1.1 V , followed by (100) at ~−1.2 V and then (110) and (210) both at ~−1.3 V. This order is compatible with those obtained from polished single-crystal electrodes with voltammetry [10–12]. The intensity of the fluorescence also roughly correlates to the surface density of the adsorbates. Therefore, these plots contain comparable information with the standard linear scan voltammogram recorded when reductively desorbing a SAM on a polished single crystal electrode. Worth to mention is that the desorbed molecules diffuse away, both vertically and laterally. Thus, they not only contribute to the fluorescence intensity from the region where they originate, but also contribute to the fluorescence intensity from the neighboring regions [168, 204, 205]. Consequently, it is not easy to use intensity to quantify the density of SAM. However, considering the diffusion coefficient for thiolate is expected to be relatively low (~10^{-6}cm/s) [206], so the lateral drift within the duration of the measurement (estimated to be a few micrometers) should be negligible as compared to the image dimension. In addition, the movement of desorbed molecules is prominent when there is significant H_2 evolution [205] while here the solution was made basic (pH = ~12) to minimize
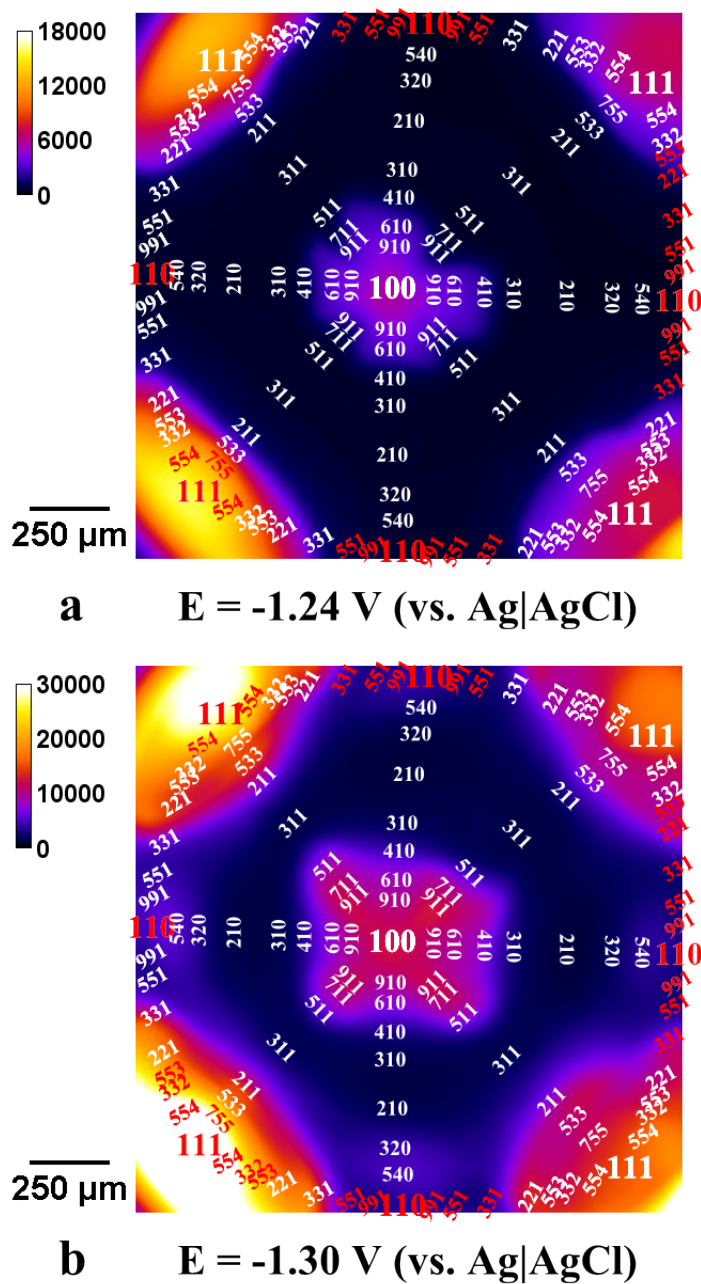
Figure 4.4: Fluorescence images of the AuS-C10-BODIPY SAM (15 min immersion time) modified bead electrode acquired at: (a) −1.24 V (vs. Ag|AgCl) and (b) −1.30 V (vs. Ag|AgCl) with overlay of crystallographic map showing the low-index and stepped surfaces. Adapted from [8] with permission. Copyright (2014) American Chemical Society.

the H_2 evolution. Thus, it is reasonable to use the intensity - potential plot of a region of interest on the image to represent the desorption of adsorbates from the underlying crystallographic surface. For moderately negative potentials before significant lateral drift and H_2 evolution, the fluorescence intensity can be an indication of the density of adsorbates on the surfaces. Further complication comes from the BODIPY fluorophore, because as reviewed in Section 3.1.1, high concentration of BODIPY fluorophore can form a fluorescent J-dimer, which decreases the fluorescence intensity from the monomer [163–165, 204]. The error associated with this contribution is dependent on not only the density of fluorophore, but also the orientation, so it is difficult to compensate. Nevertheless the main purpose here is not to accurately quantify the density of adsorbate on different surfaces, but to compare the differences between surfaces, which are large, so it is not totally invalid to estimate the adsorbate density using the fluorescence intensity. As a rough estimation, the density on a (111) surface is 2-3 times higher than a (100) surface, which is slightly less than a (110) surface but similar to a (210) surface. As a reference, the maximum coverage of a decanethiolate SAM on a (111) surface prepared from solution was reported to be 6.5×10^{14} molecules/cm^2 [207]. The intensity-potential profiles are similar for the same types of crystallographic surfaces from different quadrants, illustrating the single crystal quality of the Au bead electrode used. Similar in situ fluorescence imaging measurement and analysis were performed for the SAM created with an 18 h immersion time. The collection of the intensity-potential plots for this SAM is shown in Figure 4.5b. The intensities measured for the two SAMs are very similar from corresponding crystallographic surfaces. However, the desorption potentials for the SAM created with long immersion time shifted to more negative potentials except for (111) where the shift was not significant. This is compatible with previous reports showing that the adsorption of alkanethiol on Au follows two step: a fast step with more than 80% coverage achieved within a few minutes and a slow step of annealing and organizing the resultant SAM spanning several hours without significant increase of coverage [208, 209]. The annealed and organized SAMs stabilized by higher extent of intermolecular interactions have been observed to have more negative desorption potentials [194]. The rate for annealing and organizing the SAM is probably surface crystallography-dependent and this process was mostly completed on (111) within 15 min.

It is also important to analyze the reductive desorption from the stepped surfaces along the
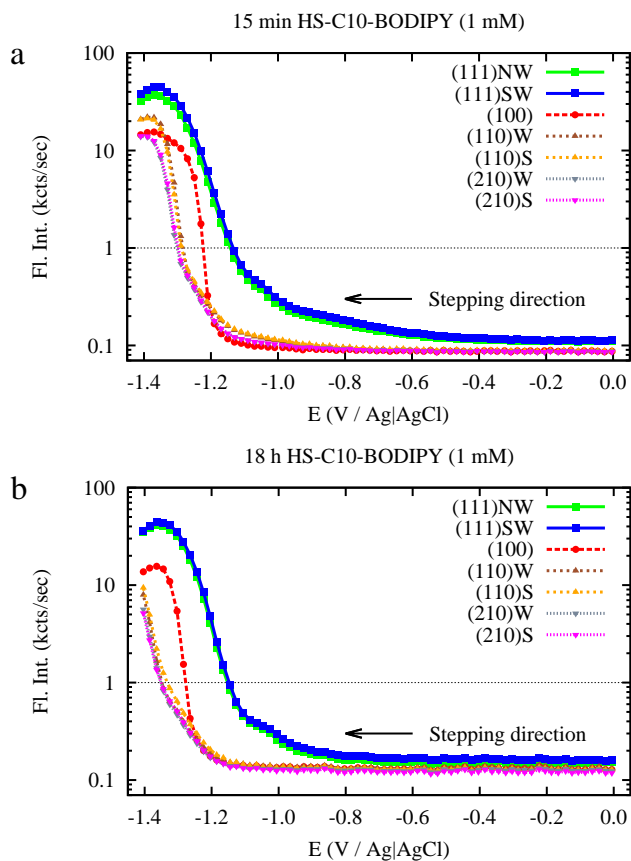
Figure 4.5: Fluorescence intensity - potential for the three low-index and (210) surfaces taken from different quadrants around the Au bead electrode surface: (a) the AuS-C10-BODIPY SAM created with a 15 min immersion time, (b) the AuS-C10-BODIPY SAM created with an 18 h immersion time. Adapted from [8] with permission. Copyright (2014) American Chemical Society.

(100)-(111), (111)-(110) and (110)-(100) zones on the stereographic triangle. According to the step notations for the stepped surfaces reviewed in Section 2.1.4, a stepped surface is formed with terrace of the nearest vertex low-index surface and step of the other vertex low-index surface of the zone. Thus along each zone, the stepped surfaces progress with systematic changes in the step density. Analyzing the reductive desorption from the stepped surfaces along three zones demonstrates the systematic influence of surface crystallography on reductive desorption of the SAM. The one-dimensional analysis of plotting the intensity as a function of potential discussed above can not only be performed on well-studied low-index and stepped (i.e., (210)) crystallographic surfaces, but also on other less-studied stepped or kinked surfaces on the crystallographic map. However, since these surface features are all represented on the electrode surface and a more inclusive two-dimensional analysis can be performed by representing the intensity change as a function of potential along three zones (in the order of (100)-(111)-(110)-(100)) with false color to create the line scan plots. Two types of line scan plots are shown. In Figure 4.6a, the false color represents the raw fluorescence intensity in logarithmic scale while in Figure 4.6b, the false color represents the logarithm of the ratio of the fluorescence intensity to the maximum intensity for each pixel along the zones. The white contour lines are drawn at the intensity of 1 kcts/sec in Figure 4.6a and 10% of the maximum fluorescence intensity in Figure 4.6b (both calculated after subtracting the minimum intensity). The latter is to compensate for the differences in the coverage on different stereographic surfaces. These are used as the thresholds above which the SAM is defined as desorbed. There are multiple complete stereographic triangles realized on the electrode surface in the measurements and shown is the analysis of the one in the west-northwest (WNW) half quadrant. Equivalent results can be obtained from the other complete stereographic triangles due to the symmetry of the single crystal bead electrode. The density of broken bonds (d_{bb}, reviewed in 2.3.4), as the semi-quantitative numerical surrogate for PZC is also calculated and presented for the surfaces indicated in the line scan plots. The line scan plots demonstrate the strong influence of surface crystallography on the reductive desorption potential. It is true that applying two different thresholds yields slightly different desorption potentials for the crystallographic surfaces investigated, but the overall trends are similar. Worth to mention is that- the line scan plots can be generated for any crystallographic zone with systematic terrace-step transition,
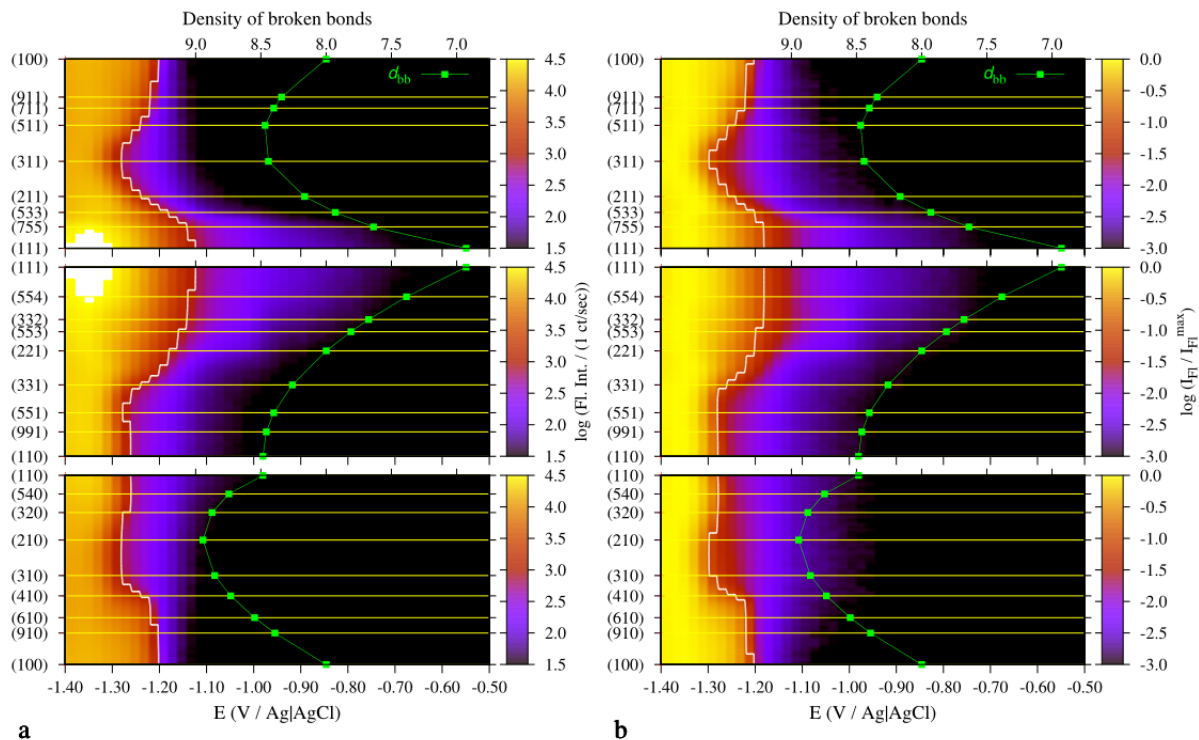
Figure 4.6: Influence of surface crystallography on the fluorescence intensity changes with potential during reductive desorption of the AuS-C10-BODIPY SAM created with a 15 min immersion time, shown for the (100)-(111), (111)-(110) and (110)-(100) zones in the WNW stereographic triangle: (a) raw fluorescence intensity in logarithmic scale false colored, with a white contour line drawn at an intensity of 1 kcts/sec, similar to the dotted line in Figure 4.5; (b) the logarithm of the ratio of the fluorescence intensity to the maximum intensity for each pixel along the zones false colored, with the white contour line drawn at 10% of the maximum intensity. In both figures, the density of broken bonds calculated for each surface on the y-axis is included. Adapted from [8] with permission. Copyright (2014) American Chemical Society.

not restricted to the three sides of the stereographic triangle.

Along the (100)-(111) zone (top panel in Figure 4.6), the desorption potentials for the surfaces in this zone mostly correlate with d_{bb}. The least negative desorption potentials are observed for the two low-index planes (111) and (100) with lowest d_{bb} while the most negative desorption potentials is observed for the (311) surface. The (311) surface can be expressed as $2(100) \times (111)$ or $2(111) \times (100)$ in step notation, which is the turning point of the transition from (100) terrace to (111) terrace in this zone. Although it is not the roughest surface according to its d_{bb}, its PZC is most negative in this zone (see Figure 2.22). The d_{bb} decreases dramatically away from both low-index planes, however, a smooth transition in the desorption potential is observed. Near the (111) surface, this smooth transition can be explained by the

large (111) facet overwhelming a number of crystallographic surfaces in the map. However, the (100) facet is very small, and only slightly more negative desorption potentials are observed from the (911) and (711) surfaces well away from the (100) facet. Therefore, the desorption potential does not always follow the d_{bb}, evidently demonstrate that PZC is only one of the major factors that control the desorption potential, and the intermolecular interactions also plays a crucial role, as reviewed in Section 4.1. The (100) terrace probably provides a favorable structure for alkanethiol adsorption and organization, resulting in the smooth transition in desorption potential near the (100) facet.

Similar correlation between desorption potential and d_{bb} is observed along the (111)-(110) zone. A sharp change in desorption potential near the (111) surface is again not seen presumably because of the large (111) facet. Away from the (111) facet, desorption potential and d_{bb} share comparable trend until (331) which is the turning point of the transition from (111) terrace $(3(111) \times (111)$ or $2(111) \times (110))$ to (110) terrace $(2(110) \times (111))$ in this zone. Near constant desorption potential is observed from (311) to (110) which suggests the (110) terrace dominates the behavior of the alkanethiol adsorption.

Along the (110)-(100) zone, a smooth transition in desorption potential is again observed near the (110) surface and the (100) surface, similar to the other two zones. The most negative desorption potential is observed in (210), which is the the turning point of the transition from (110) terrace $(2(110) \times (100))$ to (100) terrace $2(100) \times (110))$ in this zone. This is not unexpected considering its highest d_{bb} and most negative PZC. However, considering all stepped surfaces in the three zones, although the (210) surface has the highest d_{bb} and the most negative PZC, the desorption potential observed from (210) is not significantly more negative than that from any other stepped surfaces. The smooth transition of desorption potential from (100) surface to neighboring stepped surfaces with large (100) terrace is also observed in this zone, extending to (610).

The line scan plots for the AuS-C10-BODIPY SAM created with an 18 h immersion time are also shown in Figure 4.7 for comparison. The overall influence of surface crystallography on reductive desorption of this SAM created with a longer immersion time is similar to that of the SAM created with short immersion time discussed above. It has been found with the one-dimensional intensity-potential plots that longer immersion time results in similar maximum
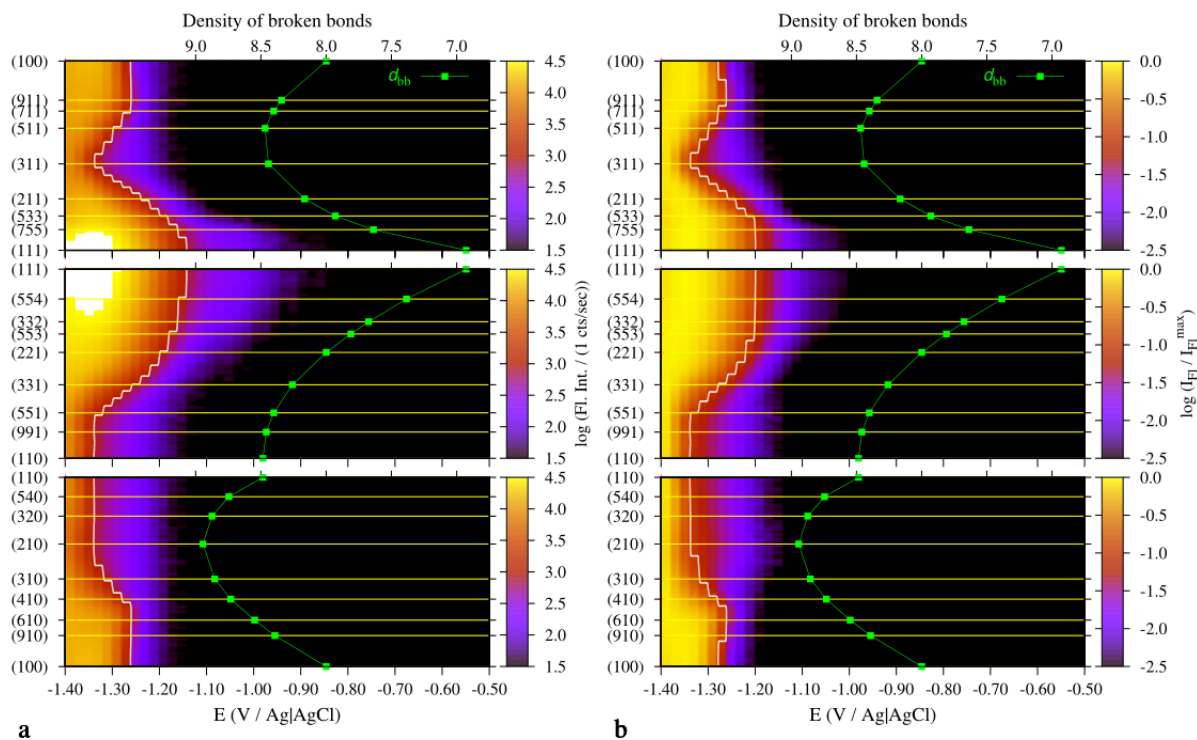
Figure 4.7: Influence of surface crystallography on the fluorescence intensity changes with potential during reductive desorption of the AuS-C10-BODIPY SAM created with an 18 h immersion time, shown for the (100)-(111), (111)-(110) and (110)-(100) zones in the WNW stereographic triangle: (a) raw fluorescence intensity in logarithmic scale false colored, with a white contour line drawn at an intensity of 1 kcts/sec, similar to the dotted line in Figure 4.5; (b) the logarithm of the ratio of the fluorescence intensity to the maximum intensity for each pixel along the zones false colored, with the white contour line drawn at 10% of the maximum intensity.

intensity and more negative desorption potential presumably because of the adsorbate annealing and organizing. This is also observed with the line scan plots for all surfaces investigated. However, the negative shift of desorption potential is not the same for all surfaces. The ~20 mV negative shift is minimal for the (111) surface. The desorption potentials for the stepped surfaces with (111) terrace also do not shift too much. On the contrary, the ~70 mV negative shift for the (100) surface is the maximum shift observed. A large negative shift is also observed on surfaces with (100) terrace. The ~50 mV negative shift for the (110) is also relatively big. This big negative shift also applies to surfaces with (110) terrace. The difference in this shift in the onset of desorption suggests high extent of molecular reorganization and stabilization occurring on the (100) and (110) terraces during the long immersion process.

Analyses performed on the two AuS-C10-BODIPY SAMs with short and long immersion times demonstrate the general correlation of desorption potential with d_{bb} or PZC of the underlying crystallographic surfaces and the progression of the SAM formation on different crystallographic surfaces. However, there are discrepancies between the trends of desorption potential and d_{bb} or PZC, most notably for surfaces with a large (100) terrace or a large (110) terrace. Coincidentally, they are surfaces with the largest negative shift of desorption potential after hours of adsorbate annealing and organizing to achieve a higher extent of intermolecular interaction. These observations from the analyses of the in situ fluorescence imaging might originate from the energetics of the particular adsorption sites on the (100) and (110) terraces. However, as reviewed in Section 2.2.2, even the adsorption site on (111) surface is under constant debate, so further studies are required to elucidate the details of adsorption on the (100) and (110) terraces. Moreover, although it is has been observed that lifting the reconstructed (111) surface is achieved within 15 min upon adsorption of alkanethiol at a slight negative potential (−0.38 V (vs. SCE)) [68], there is a lack of in situ study on lifting the reconstruction of other reconstructed surfaces by alkanethiol adsorption, so the possibility of lifting the reconstructed (100) and (110) (see Section 2.1.5) over long immersion time is not excluded. As a concluding remark for this section, while this in situ fluorescence imaging performed on single crystal bead electrode cannot reveal all details, it provides direction to the in-depth investigation of the interesting surfaces using methods to analyze molecular orientation or structure to understand the adsorbate-surface and adsorbate-adsorbate interactions at the specific adsorption site.

4.4.2 Reductive desorption of the AuS-Aib4-BODIPY SAM

The Aib peptides are a class of synthetic peptides with special structure and potentially useful in biosensing applications [210–212]. They form the 3_{10}-helix induced by the intramolecular hydrogen bonds, which in turn induces a strong dipole moment along peptide backbone. When the Aib peptides are thiol-modified and immobilized on a Au surface, not only does the helical structure retained, but an intermolecular hydrogen bond network is formed as well [210, 211]. The Aib peptides and Aib peptide thiolate SAMs will be further discussed in Chapter 5. Here, a Aib peptide thiolate SAM is studied as a contrast to the alkanethiolate SAM to demonstrate the wide applicability of the influence of surface crystallography and the influence of intermolecular interactions on reductive desorption.

The BODIPY fluorophore-labeled thiol-modified Aib peptide HS-Aib4-BODIPY was used to create a SAM, and with the fluorophore, similar in situ fluorescence imaging measurement was performed to study the reductive desorption process. One difference in the measurement as compared to that for the AuS-C10-BODIPY SAM was that at each potential step, the waiting time was slightly longer. The AuS-C10-BODIPY SAM here was created from a dilute solution of HS-Aib4-BODIPY over a relative short period of immersion time as compared with highly packed SAMs reported in literature [211]. In addition, the low solubility of the HS-Aib4-BODIPY prevented the desorbed molecules from diffusing quickly. These two factors combined resulted in lower fluorescence signal than the AuS-C10-BODIPY SAM. In order to achieve better imaging quality, the waiting time was longer (the camera exposure time was longer as well) at each step to allow for larger separation between the fluorophore and the electrode.

The substrate electrode used for the AuS-Aib4-BODIPY SAM was another single crystal bead electrode with similar orientation to the one used for the AuS-C10-BODIPY SAM (i.e., the (100) facet in the center and the 4 (111) facet close to the four corners). Figure 4.8 shows the montage of selected fluorescence images taken from −1.14 V to −1.36 V (vs. Ag|AgCl) in −20 mV increments during the reductive desorption of the AuS-Aib4-BODIPY SAM. The reductive desorption was observed first from the 4 (111) facets, similar to what was observed for the AuS-C10-BODIPY SAM. The reductive desorption from the (100) facet followed (111) at −1.12 V (vs. Ag|AgCl), but a square shape was seen instead of the cross shape around the
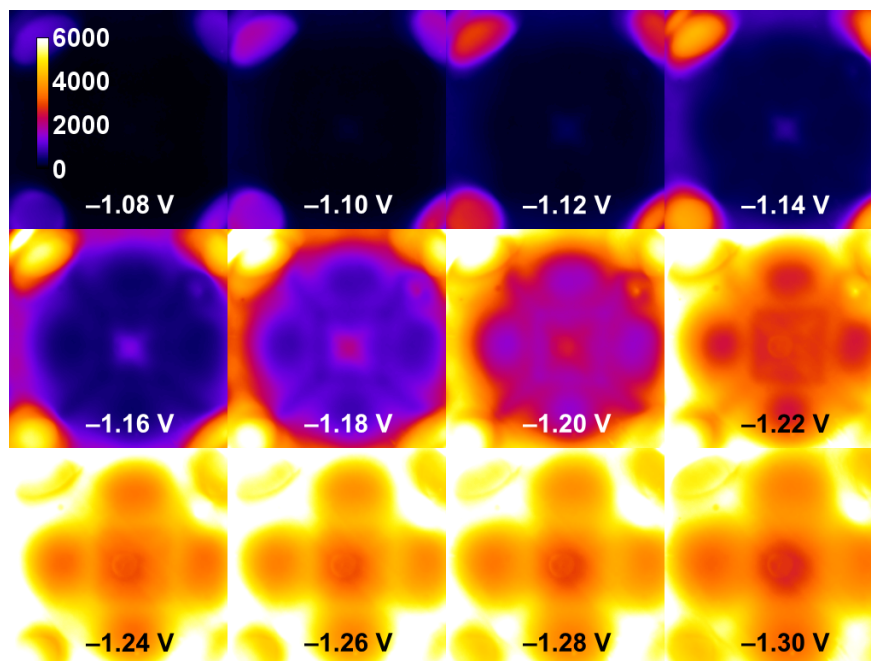
Figure 4.8: Montage of selected fluorescence images taken from −1.08 V to −1.30 V (vs. Ag|AgCl) in −20 mV increments during the reductive desorption of the AuS-Aib4-BODIPY SAM.

(100) facet for the AuS-C10-BODIPY SAM. At −1.16 V (vs. Ag|AgCl), fluorescence intensity started to increase quickly for the rest of the surface. The symmetry of the fluorescence images again demonstrates the single crystal character of the bead electrode surface with the intensity distributed according to the fcc single crystal pattern in the four quadrants equally (except for the northeast quadrant distorted by a defect similar to that observed in Figure 4.2).

Mapping of the electrode surface was performed with the fluorescence image taken at −1.18 V (vs. Ag|AgCl). With the crystallographic map (Figure 4.9), the one-dimensional intensity-potential analysis for selected crystallographic surfaces and two-dimensional line scan analysis for selected zones were also conducted and plotted in Figure 4.10. The desorption of AuS-Aib4-BODIPY from various surfaces follows a similar sequence to that observed for the AuS-C10-BODIPY SAMs except for three major differences. First, reductive desorption occurs at less negative potentials for the AuS-Aib4-BODIPY SAM (applying the 1 kcts/sec threshold probably even overestimate the negative desorption potentials considering the low coverage of the AuS-Aib4-BODIPY SAM). Moreover, a unique two-step desorption is observed from the (111) facets but not from any other surfaces studied. This two-step desorption will be further discussed in Chapter 5. Furthermore, the potential separation from (100) surface and the other

Figure 4.9: Fluorescence images of the AuS-Aib4-BODIPY SAM modified bead electrode acquired at –1.18 V (vs. Ag|AgCl) with overlay of crystallographic map showing the low-index and stepped surfaces. Adapted from [8] with permission. Copyright (2014) American Chemical Society.

two surfaces, (100) and (210) is smaller than that observed for the AuS-C10-BODIPY SAM. The low adsorbate concentration and short immersion time resulted in a layer that may not be as well organized as reported ones on extended gold surfaces [211]. In this low coverage case, it might be assumed that the intermolecular hydrogen bonds may not play such a significant role in influencing the desorption potential. However, the retaining dipole moment (in the case of AuS-Aib4-BODIPY, the positive pole is proximate to the surface while the negative pole is distal from the surface) can still have an impact on the desorption process. The maximum fluorescence intensity, which correlates to the coverage, on the (111) and (110) surface are roughly double that of the (100) and (210) surfaces. Considering the low packing density of the SAM, this surface coverage difference possibly reflects the initial stages of adsorption process as dependent on the coordination with surface.

The line scan plots for the (100)-(111), (111)-(110) and (110)-(100) zones are presented in Figure 4.11, showing the influence of the surface crystallography on the reductive desorption for the AuS-Aib4-BODIPY SAM. Because of the low coverage, the desorption potentials

Figure 4.10: Fluorescence intensity - potential for the three low-index and (210) surfaces taken from different quadrants around the AuS-Aib4-BODIPY SAM modified Au bead electrode surface. Adapted from [8] with permission. Copyright (2014) American Chemical Society.

extracted with the 1 kct/sec threshold (Figure 4.11a) are slightly more negative than those extracted with the 10% of the maximum intensity threshold (Figure 4.11b). However, similar trends are observed with the two thresholds. The comparison of desorption potential as a function of underlying crystallographic surfaces with d_{bb} of corresponding surfaces shows significant correlation between the two. The major discrepancy lies in the (111) surface with two-step desorption. The two-step desorption for the (111) surface is also observed for the (755) surface in the (100)-(111) zone and (553) surface in the (111)-(110) zone, which may be due to inaccurate indexing inside the big (111) facets. However, from the crystallographic map in Figure 4.9, the (553) surface is clearly off the facet, suggesting the two-step desorption also occurs on surfaces with large (111) terrace. Other than the (111) surface, despite the broad similarity between the desorption potential trend and the d_{bb} trend, the Aib peptide SAM reductive desorption potentials determined for various crystallographic surfaces are similar and do not vary too much (largest difference of ~50 mV). To date, only Aib peptide SAMs deposisted on planar (111) surfaces have been systematically studied [211–214], with no reports on any other crystalline surfaces. Considering the big difference in the desorption behaviors between (111) surface and other surfaces for this Aib peptide SAM, it would be valuable to further explore the structures and properties of Aib peptide SAMs on other surfaces to elucidate the difference.

Significant differences have been observed in the influence of surface crystallography on the reductive desorption for the AuS-Aib4-BODIPY SAM and the AuS-C10-BODIPY SAMs.
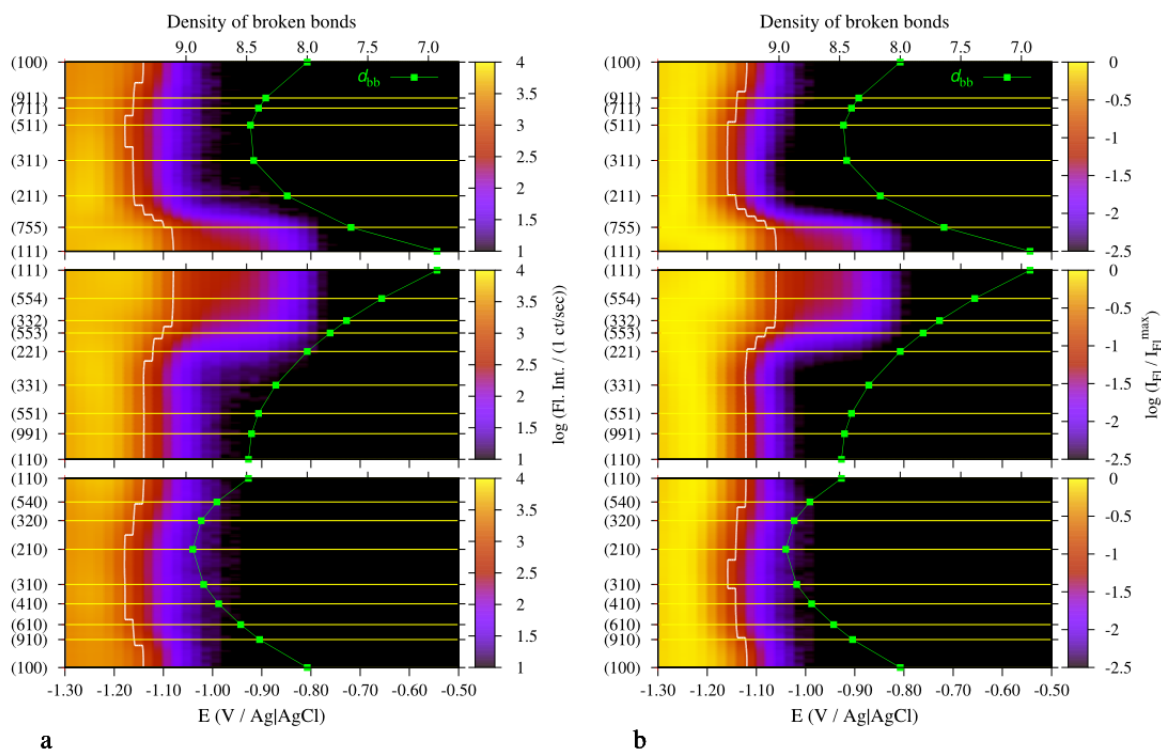
Figure 4.11: Influence of surface crystallography on the fluorescence intensity changes with potential during reductive desorption of the AuS-Aib4-BODIPY SAM, shown for the (100)-(111), (111)-(110) and (110)-(100) zones in the WNW stereographic triangle: (a) raw fluorescence intensity in logarithmic scale false colored, with a white contour line drawn at an intensity of 1 kcts/sec, similar to the dotted line in Figure 4.10; (b) the logarithm of the ratio of the fluorescence intensity to the maximum intensity for each pixel along the zones false colored, with the white contour line drawn at 10% of the maximum intensity. In both figures, the density of broken bonds calculated for each surface on the y-axis is included. Adapted from [8] with permission. Copyright (2014) American Chemical Society.

The reductive desorption potential for the AuS-Aib4-BODIPY SAM seems to follow the d_{bb} or PZC more closely than the AuS-C10-BODIPY SAMs except for the unique (111) surface. The influence of intermolecular interactions on the reductive desorption has been demonstrated by comparing the two AuS-C10-BODIPY SAMs created with different immersion time. While the hydrogen bonds between Aib peptide molecules might not be strong enough to impact the reductive desorption process on the whole bead surface for this low coverage SAM, locally there might be densely-packed adsorbates connected by the hydrogen bonds, or the orientation of the dipole moment might be strongly dependent on surface crystallography via the packing density. Most importantly, comparing these two distinct types of SAMs shows the wide utility of this in situ fluorescence imaging approach on the Au single crystal electrodes in exploring the influence of surface crystallography on various types of SAMs in a self-consistent and comparable fashion.

4.4.3 Mapping the desorption potential for the alkanethiolate and Aib peptide thiolate SAMs on the whole single crystal Au bead surface

The influence of surface crystallography on the reductive desorption potentials for selected two-dimensional zone can be observed with the line scan plots described above. It is also important and convenient to obtain the desorption potentials across the whole surface for one particular SAM. This desorption potential map can be achieved by interpolating the value of the potential at which the fluorescence intensity crosses a threshold going through one reductive desorption image stack (background subtraction was conducted by subtracting the first image taken at 0 V (vs. Ag|AgCl)). The analysis was performed at each pixel in the fluorescence images for all three SAMs (the AuS-C10-BODIPY SAM formed with short deposition time, the AuS-C10-BODIPY SAM formed with long deposition time and the AuS-Aib4-BODIPY SAM) using either 1 kct/sec or 10% of the maximum fluorescence intensity (for that particular pixel) as the threshold. The latter threshold aims at accounting for the difference in coverage on difference surfaces. The maps of the interpolated reductive desorption potential for the AuS-C10-BODIPY SAMs and for the AuS-Aib4-BODIPY SAM are shown in Figure 4.12 and Figure 4.13, respectively. The maps in the left column were generated by applying the 1 kct/sec threshold while the the maps in the right column were generated by applying the 10% of maximum intensity threshold.
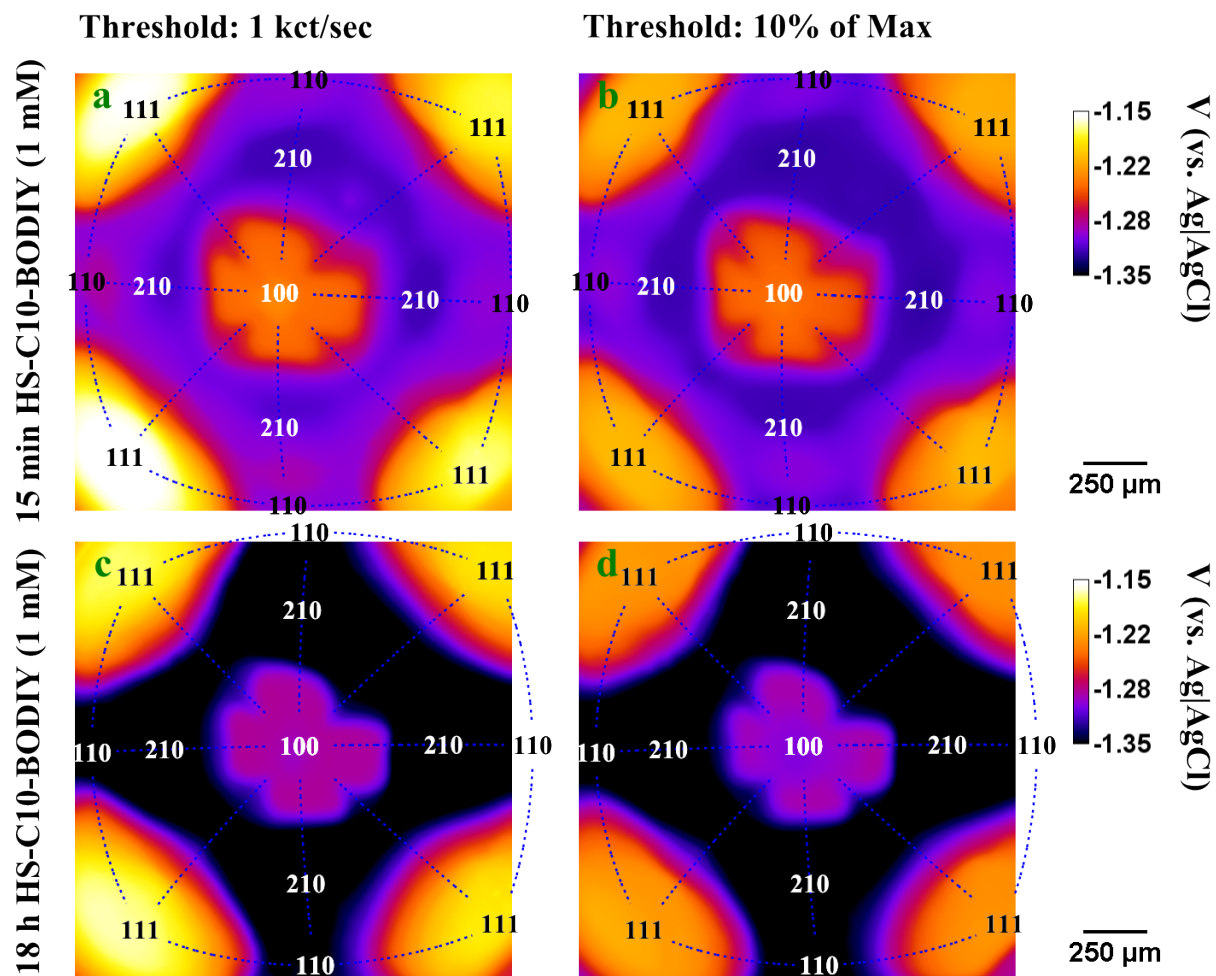
Figure 4.12: Maps of the interpolated reductive desorption potential (V (vs Ag|AgCl)) for the AuS-C10-BODIPY SAMs using a threshold of 1000 kct/sec (left column) or a threshold of 10% of the maximum intensity (right column). First row (a, b) for the AuS-C10-BODIPY SAM created with 15 min immersion time and second row (c, d) for the AuS-C10-BODIPY SAM created with 18 h immersion time. Adapted from [8] with permission. Copyright (2014) American Chemical Society.
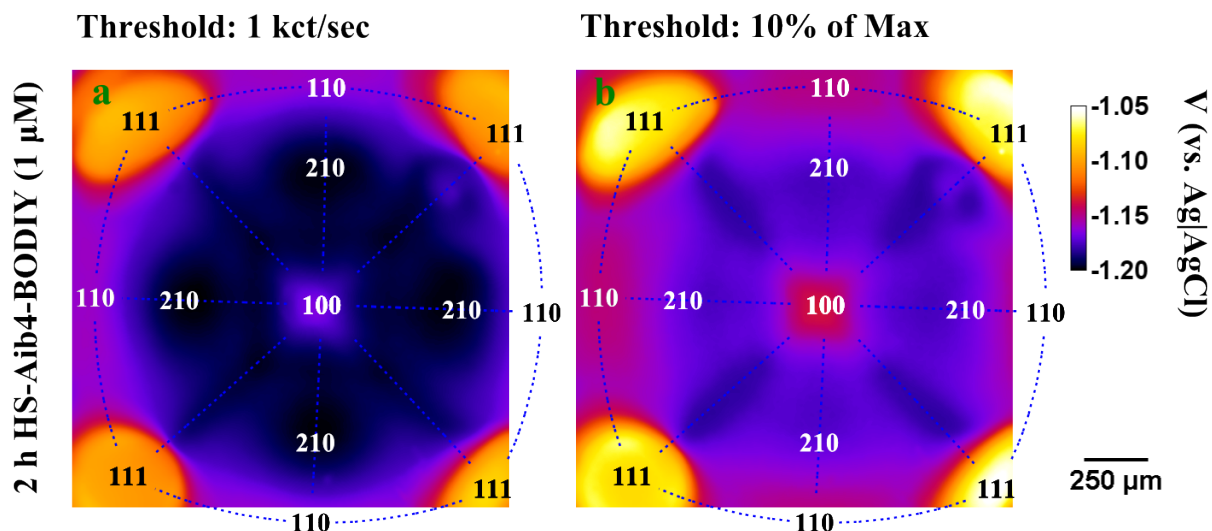
Figure 4.13: Maps of the interpolated reductive desorption potential (V (vs Ag|AgCl)) for the AuS-Aib4-BODIPY SAM using (a) a threshold of 1000 kct/sec or (b) a threshold of 10% of the maximum intensity. Adapted from [8] with permission. Copyright (2014) American Chemical Society.
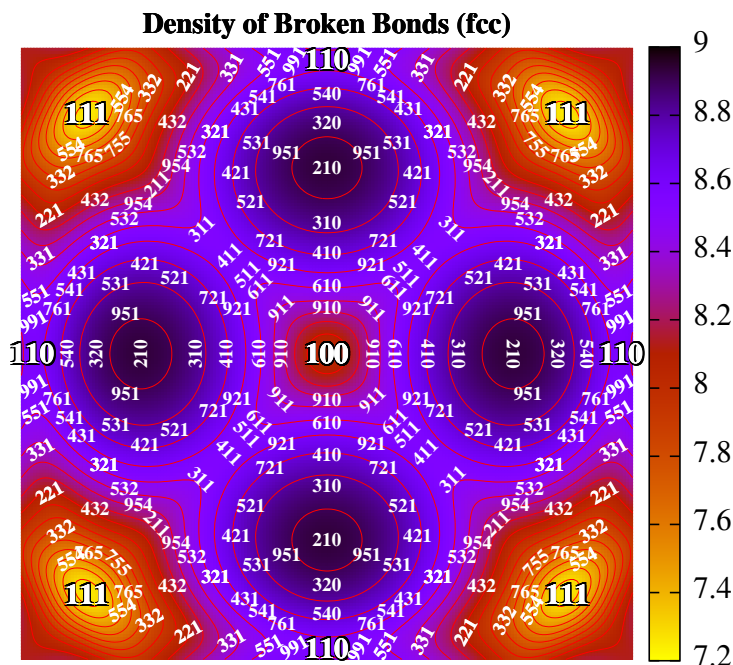
Figure 4.14: The map of calculated density of broken bonds (d_{bb}) for a fcc spherical surface observed from the bottom with the (100) surface in the center. Adapted from [8] with permission. Copyright (2014) American Chemical Society.

The map of calculated d_{bb} for a fcc spherical surface projected to a plane with the (100) surface in the center is plotted in Figure 4.14 with color coding to match the desorption potential trend, facilitating a direct comparison. The (111) has the highest d_{bb} of ~7 (yellow) and the (210) has the lowest d_{bb} of ~9 (dark blue). Note that the one major assumption here is that the reconstructed crystallographic surfaces are reverted back to unreconstructed (1×1) structures upon adsorption of thiol-modified molecules. This has been observed for the three low-index surfaces: (111) [68, 73], (100) [96, 97] and (110) [215] surfaces, even though the kinetics for lifting the reconstruction has been explored only for the (111) surface [68]. It has to be admitted that the possibility of partial lifting of the reconstructed surface exists and has been observed experimentally [74, 99–101]. However, from the fundamental point of view, to complete the de-reconstruction process, the SAM has to be highly-packed and well-organized (typically seen on high density long alkanethiolate SAMs) so that the relatively electronegative thiolate head group can withdraw the excess amount of negative charge on the surface [74]. Therefore, it is not un-reasonable to assume that the AuS-C10-BODIPY SAMs here fall into this category. As for the AuS-Aib4-BODIPY SAM, considering the dipole moment from the Aib peptide with the positive pole proximate to the surface, the assumption of de-reconstruction by the AuS-Aib4-BODIPY SAM, despite its low density, is probably valid. In addition, the highly stepped surfaces, (210), (320), (311) and (511) have been shown not to reconstruct and those reconstructed surfaces appear to be less stepped and have large low-index plane terrace, which might have a large extent of resemblance to the terrace plane [44, 45, 141, 142]. Therefore, all surfaces are as-sumed to retain their prinstine unreconstructed structures and the d_{bb} map for unreconstructed surfaces is used for comparison with the desorption potential maps. The general influence of surface crystallography is similar for the two types of adsorbates compared with the surface d_{bb} map: the lower the d_{bb}, the more negative the desorption potential. However, very sig-nificant differences can be observed between the desorption potential map and the d_{bb} map, which again suggests d_{bb} or PZC is not the only factor that determines the desorption po-tential.Only small differences are observed when comparing the desorption potential maps for each AuS-C10-BODIPY SAM generated with the two different thresholds shown in Figure 4.12. The major discrepancy between the desorption potential maps for these alkanethiol SAMs and the d_{bb} map is the central cross observed in the desorption potential maps instead of a simple

square with 4-fold symmetry. This central cross covers the (100) facet and a series of stepped and kinked surfaces with large (100) terrace. This smooth transition of desorption potential near the (100) facet has been shown with the line scan plots. The line scan plots were created for low-index and stepped surfaces, whereas the desorption potential maps here also show the characteristics of the kinked surfaces. One arm of the cross region around the (100) surface extends to (610) along the (100)-(110) zone and almost (911) along the (100)-(111) zone. The step notations for (610) and (911) are $6(100) \times (110)$ and $5(100) \times (111)$, respectively. This suggests that there might be a boundary between surfaces with 6 atom wide (100) terrace and those with 5 atom wide (100) terrace, beyond which the adsorption environment for alkanethiol is completely different. Adsorption of alkanethiol on Au(100) adopts a $c(2 \times 8)$ structure with (1×4) Au missing row [97, 98]. The (1×4) Au missing row requires at least 6 atom wide (100) terrace, which might explain the two different adsorption environments. The most negative desorption potential is observed from the (210) surface for the AuS-C10-BODIPY SAMs as expected considering the lowest d_{bb} of (210). However, this negative desorption potential is also observed from stepped and kinked surfaces around the central cross, which is not agreeing with the d_{bb} trend. The desorption potential maps for the two AuS-C10-BODIPY SAMs show similar features, but the desorption potential is more negative across the whole surface for the long immersion SAM. After extending the immersion time, a small negative shift (<20 mV) of desorption potential is observed from the four (111) facets, whereas this negative shift is considerably larger (~40-60 mV) from other surfaces.

The desorption potential maps for the AuS-Aib4-BODIPY SAM generated with the two different thresholds are considerably different presumably due to the low packing density and large difference among surfaces of this SAM, so it is reasonable to discuss based on the desorption map generated with the 10% of the maximum fluorescence intensity threshold. The desorption potential map for the Aib peptide thiolate SAM shows closer correspondence to the d_{bb} map. The two-step desorption for the (111) surfaces is hidden here. A square feature is seen in the center around the (100) surface in the desorption map, which is highly similar to the central region in the d_{bb} map. The large (100) terrace in the stepped or kinked surfaces does not seem to provide similar adsorption environment to the (100) surface, presumably because of the larger footprint of the thiol-modified Aib peptide molecules [211]. There is also

a similarity in the regions around the (210) surface, which resembles a round valley, between the desorption potential map and the d_{bb} map. However, the lowest desorption potential is not observed from the (210) surface, but from the (511) to (211) in the (100)-(111) zone featuring 2-3 atoms wide (111) or (100) terrace. The d_{bb} for these surfaces ((511), (311) and (211)) are somewhat comparable to each other but are not at the extreme value of the (210) surface. Thus the highly-stepped surfaces with narrow terrace might be the favorable adsorption sites for the AuS-Aib4-BODIPY molecules where adsorbates of this size might coordinate well between step edges or stable hydrogen bond networks might form on these surfaces.

Large differences can be observed in the reductive desorption behaviors for different SAMs and significant discrepancies can be found between the desorption potential maps and the d_{bb} map. These comparisons represent useful starting points for further in-depth molecular study of adsorbates on these various surfaces to understand these differences. The majority of experimental studies have focused on low-index planes for alkanethiol SAMs which correlate well with the d_{bb} map. There are significant discrepancies between the desorption potential map and the d_{bb} map on the stepped or even kinked surfaces, which are worth exploring to understand these differences. For the Aib peptide thiolate SAM, so far the only crystalline substrate studied is the (111) surface. However, considering the big difference in desorption behaviors between on the (111) surface and on the other surfaces, pursuing the studies of Aib peptide thiolate SAMs on surfaces other than (111) might be rewarding. Therefore, the use of a single-crystal Au bead and the in situ imaging approach can guide the more detailed study of the adsorption onto the unusual and understudied crystallographic surfaces.

4.5 Conclusions

The work discussed in this chapter introduces the single crystalline Au bead electrode with the family of crystallographic surfaces symmetrically distributed following the fcc crystal structure as the substrate electrode for SAMs. With this type of electrode, the influence of surface crystallography on the reductive desorption of SAMs has been investigated with the in situ fluorescence imaging method. The fluorescence images displaying the expected symmetry of the fcc crystal surface enable the indexing of the surface. More importantly, all identifiable crys-

tallographic surfaces have been analyzed self-consistently under identical conditions for one single SAM in one single measurement. This not only reduces the number of experimental replicates, minimizing the error associated with them, but also enables the study of SAMs on a series of crystallographic surfaces in the stereographic triangle with self-consistency.

Three SAMs prepared from two different adsorbates were characterized to demonstrate the wide applicability of this method to a variety of systems and to explore the influence of inter-molecular interaction on reductive desorption: a AuS-C10-BODIPY SAM created with short immersion time, a AuS-C10-BODIPY SAM created with long immersion time, and a AuS-Aib4-BODIPY SAM. Based on the intensity-potential plots generated with one-dimensional analysis on selected crystallographic surfaces, line scan plots generated with two-dimensional analysis on selected crystallographic zones crossing many related surfaces and desorption potential maps for the whole Au bead surface in view, the general correlation between desorption potential and d_{bb} as the surrogate for PZC of the surface studied has been realized. However, there are large discrepancies between the desorption potential and d_{bb} and in the reductive desorption behaviors between the three types of SAMs. Comparison of the two AuS-C10-BODIPY SAMs informs on how the SAM annealing process influences on the reductive desorption process due to different crystallographic surfaces. The differences between the AuS-C10-BODIPY SAMs and AuS-Aib4-BODIPY SAM and the discrepancies between the desorption potential trend and the d_{bb} trend are indicative of the influence of the generalized intermolecular interactions on the reductive desorption process. Thus the results from this method are paving the way for future in-depth explorations of various SAMs, unique interactions, and understudied stepped or kinked surfaces.

Chapter 5

In situ fluorescence imaging characterization of the α-aminoisobutyric acid peptide thiolate self-assembled monolayers on Au(111) surfaces

This chapter discusses the study of fluorophore-tagged α-aminoisobutyric acid (Aib) peptide thiolate SAMs deposited on Au electrodes using in-situ fluorescence imaging. Aib peptides have a restrained conformation and an oriented dipole moment along the peptide backbone resulting from their stiff 3_{10}-helical structure and intermolecular hydrogen bond network. Thus thiol-modified Aib peptide have been used to make SAMs with high uniformity and stability, which are important in sensing applications.

5.1   Aib peptides and Aib peptide SAMs

Devising biosensors based on SAMs has developed into an intense multidisciplinary research field. SAMs are organized surface structures formed when organic compounds are spontaneously adsorbed onto solid substrates. Therefore, SAMs are widely utilized to link the bioreceptor and the transducer together, acting as the platform for biosensors, and most commonly, electrochemical biosensors. For example, a number of DNA sensors, a class of biosensors, have been developed, of which many are based on alkanethiolate SAMs (using alkanethio-

late as the molecular spacer and diluent) [52–54, 108]. Despite the development of a variety of electrochemical biosensors over the past decades, their low sensitivity and specificity still hinders breakthroughs. One major reason for these issues is that the surface organizations are still far from highly ordered [1]. In other words, the SAMs are formed with a considerable number of defects [4, 65, 66].

As reviewed in Section 2.2.2, conventional alkanethiolate SAMs with van der Waals interactions tend to be highly dynamic and defective. Although alkanethiolate SAMs have been intensely investigated and employed as the platform for biosensors, it is questionable whether they are the best candidates [65, 66]. Thus, to form SAMs with high order, one natural consideration is to replace the alkyl chains with other organic chain structures with favorable properties to promote the foundation of a SAM with less defects which result from spacer chains. Typically there are two aspects to improving spacer structure. First, since alkanethiolate SAMs mainly interacts with neighboring molecules through intermolecular van der Waals forces, alkanethiolate SAMs tend to be more flexible. Thus, if additional intermolecular interactions can be involved in the system, the resultant SAMs would not only be more stable, but more densely packed with correspondingly fewer defects. Secondly, alkyl chains bear relatively flexible conformations, which accounts for the observed phase transitions on the surface [106, 107]. Consequently, good candidates for spacers in SAMs require a conformation constrained by intramolecular interactions. Combining these two aspects, Aib peptides, with the 3_{10}-helix secondary structure, becomes a class of attractive candidates for molecular spacers in SAMs [210–212].

The general structure of the thiol-modified Aib$(n+1)$ series is shown in Figure 5.1. The presence of the HS terminal group enables formation of Aib peptide SAMs on Au (as well as other metals that can form a M-S bond), while the other end of the chain can be further functionalized to meet various application requirements. The Aib peptides bear the 3_{10}-helix secondary structure induced by intramolecular C=O$\cdots$H-N hydrogen bonds [216, 217]. The *n* in the Aib$(n+1)$ series denotes the number of hydrogen bonds. In the 3_{10}-helix structure, C=O$\cdots$H-N hydrogen bonds are formed between residues *i* and *i+3*. On average, a single turn of the helix requires 3.24 residues, and the length of the peptide chain increases by 1.94 Å per residue, resulting in a helix pitch of 6.29 Å. The steric structure of 3_{10}-helix is highly constrained at the α-carbon with backbone torsion angles of 3_{10}-helix being $\varphi = 57°$ and $\psi = $

30°. These parameters fall into the same conformational map (Ramachandran plot, or [φ, ψ] plot) as the those of the common α-helix which involves hydrogen bonds between residues *i* and *i*+4. The comparison of the two helices is shown in Table 5.1. The significant difference in bonding schemes of the two helices lead to considerable differences in stability. Generally, 3_{10}-helix is not as stable as α-helix, but their conformational proximity might infer 3_{10}-helix as an intermediate involved in the process of folding α-helical proteins [217]. Although the α-helix is the dominant intramolecular secondary structure in peptides, more than 8 residues are required to form an α-helix. On the contrary, the length of 3_{10}-helix can range from one turn to 7-12 residues, which gives a high degree of control over spacer length [210, 218]. The highly sterically constrained conformation of Aib peptides also induces a strong dipole moment along peptide backbone. Orientation of the dipole moment is maintained with increasing number of Aib residues due to the accompanied increase in the number of hydrogen bonds [210, 218, 219]. As can be seen from Table 5.1, in the 3_{10}-helix structure, the angle of the carbonyl group in the peptide bonds with respect to the helical axis is 28°. The projection of these polar carbonyl groups onto the helical axis result in a dipole moment along the peptide backbone. Orientation of the dipole moment is maintained with increasing number of Aib residues due to the accompanied increase in the number of hydrogen bonds [210, 211, 218, 220]. Here, this HS-Aib(n+1) series is called the "+" series of peptide because the dipole moment orients from the positive pole on the N-terminus to the negative pole on the C-terminus. Likewise, the series of peptides with the HS- group on the other side is called the "−" series. A "+" thiol-modified Aib peptide, HS-Aib4, is chosen here because the dipole moment orienting this way help stabilize the SAM formed by this thiol-modified Aib peptide. The evidence for this is the more negative desorption potential for a SAM form by a "+" thiol-modified Aib peptide than that formed by a "−" thiol-modified Aib peptide of the same number of Aib residues [221]. The maximum apparent packing density of the AuS-Aib4 SAM on planar Au(111) electrode was determined to be $\sim 3 \times 10^{14}$ molecules cm^{-2} (0.33 nm^2/molecule) using the conventional charge integration typically done after linear scan voltammetry measurement [211]. The simple charge integration tends to provide an overestimate of the packing density (see Section 4.1). Even after taking this into account, the footprint calculated based on this measurement is significantly smaller than the ~0.8 nm^2/molecule calculated from X-ray analysis result [222], which can be rationalized by
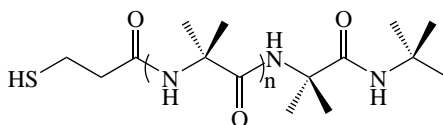
Figure 5.1: The primary structure of the "+" thiol-modified Aib peptide series.

Table 5.1: Comparison of 3_{10}-helix and α-helix. Summarized from [216] and [217].

Parameter	3_{10}-helix	α-helix
Bonding scheme	*i* and *i*+3	*i* and *i*+4
Backbone torsion angles (φ, ψ)	(57°, 30°)	(63°, 42°)
C=O⋯H-N bond angle	128°	156°
Rotation per residue	111°	99°
Axial translation per residue	1.94 Å	1.94 Å
Number of residues per turn	3.24	3.63
Pitch	6.29 Å	5.67 Å
Angle of C=O with respect to helical axis	28°	13°
Dipole moment	4.57 D	5.16 D
Diamter	9.7 Å (Aib) [222]	Dependent on side chains

the influence of the dipole moment on the desorption charge [211]. Interestingly, the calculated footprint for the HS-Aib(n+1) series further exhibits a periodicity based on n, and one period is comprised of three types of peptides where $n = 3k, 3k + 1, 3k + 2$ (k represents integers). A slight increase of calculated footprint within one period was observed, whereas an overall decrease of calculated footprint was observed from period to period with increasing k [221]. This periodicity is probably due to a helical turn of three residues.

SAMs formed by thiol-modified Aib peptide on gold nanoclusters [210, 218, 220] and gold plates [211] have been reported by Maran and co-workers. It was found that the peptide molecules form well packed layers on both substrates. In addition to the intramolecular hydrogen bonds, previous studies also show that a peptide molecule can form hydrogen bonds with adjacent molecules in a SAM, which creates a large hydrogen bond network on the surface. This hydrogen bond network accounts for the well-defined organization of this type of Aib peptide SAMs [210, 211, 218, 220]. In addition, the hydrogen bonds are also dipoles, which could also feel the influence from the electric field, so the conformation of the Aib peptide may also be manipulated by an electric field. Venanzi and coworkers also studied SAMs on gold surfaces using peptides with 3_{10}-helix Aib peptide as the core structure [72, 212–214, 223, 224]. These peptide SAMs were also densely and homogeneously packed. Furthermore, the dipole mo-

ment along the peptide backbone could facilitate the formation of bi-component nano-structure through helix-helix interactions between opposite dipole moments on the surface [214]. These properties have made Aib peptide SAMs promising platforms for bio-sensing [211] and photo-voltaic [223, 224] applications.

As the platform for eletrochemical biosensors, the property of facilitating electron transfer is necessary. Previous studies have shown that the Aib peptides can act as the electron tunneling mediators. The Aib peptides display a special dependence of intramolecular electron transfer rate on the number of Aib units [219, 225]. The intramolecular hydrogen bonds play a critical role in facilitating electron transfer. Thus the electron transfer mechanism through a Aib peptide bridge is believed to be a combination of the superexchange mechanism which greatly depends on the distance between the donor and the acceptor, and the hopping mechanism which greatly depends on the number of intramolecular hydrogen bonds [225].

5.2   Objectives

As an extension of the studies in Chapter 4, the Aib peptide thiolate SAMs will be explored via electrochemistry on a polished Au(111) electrode and spectroelectrochemically using a Au(111) facet on a single crystal Au bead electrode. It was shown in Chapter 4 that the low-packing-density Aib peptide SAM shows a two-step desorption from the (111) surface. In contrast, high-packing-density SAMs similar to those reported in the literature [211] will be prepared and studied, thereby giving insights into Aib peptide SAMs.

Additionally, the thickness of a SAM is not only dependent on the length of the adsorbate, but also the orientation. In the case of Aib peptides, the peptide backbone is featured with an oriented dipole moment induced by polar groups. This dipole moment may be influenced by the electric field, which leads to the change of the orientation or structure. If the adsorbate is further labeled with a fluorophore, the change of SAM thickness can be reported as the change in fluorescence intensity. Therefore, in situ fluorescence measurements will be performed using modulated potential steps to investigate the potential induced orientation / structure change of the low-packing-density Aib peptide SAMs on a Au(111) facet.

5.3 Experimental

5.3.1 The substrates

Two types of substrate electrodes were used in the formation of Aib peptide SAMs. Fabrication of both types involved melting an ultrapure gold wire with a torch and slowly cooling down to form a predominant single crystal bead. The first type of substrate was a planar Au(111) electrode accomplished by polishing a single crystal bead as described in Section 3.2. The second type of substrate was a single crystal bead similar to that used in Chapter 4, except that a (111) facet was formed very close to the bottom of the bead by carefully adjusting the angle of melting. For the second type of electrode, the orientation of the electrode was carefully adjusted by twisting the electrode stem so that the (111) facet was perpendicular to the light path in subsequent spectroelectrochemical measurements.

5.3.2 Preparation of AuS-Aib4-BODIPY SAMs

The thiol-modified Aib peptide is HS-Aib4-BODIPY the same as used in Chapter 4. The general preparation procedure for AuS-Aib4-BODIPY SAM is described as below. A clean substrate electrode was immersed in the thiol-ethanol solution with designated concentration for a predetermined period of deposition time. The modified electrode was then rinsed with and immersed in ethanol for 30 min to remove the non-specifically adsorbed species. The highest concentration of the HS-Aib4-BODIPY solution was 60 μM and all the lower concentration solutions were prepared from this stock. Table 5.2 lists all the AuS-Aib4-BODIPY SAMs prepared for further investigations with the conditions under which they were formed. Besides the categorization based on the substrate, they can be further distinguished based on packing density. The SAMs prepared with 60 μM solution are categorized as high-packing-density SAMs whereas the SAMs prepared with 1-2 μM solutions are categorized as low-packing-density SAMs.

Table 5.2: AuS-Aib4-BODIPY SAMs prepared and their formation conditions

Electrode	Solution concentration	Deposition time
Polished Au(111)	60 μM	1 h
Single crystal Au bead	60 μM	2 h
Single crystal Au bead	1 μM	0.5 h
Single crystal Au bead	1 μM	2 h
Single crystal Au bead	1 μM	18 h
Single crystal Au bead	2 μM	0.5 h

5.3.3 Electrochemical and in situ fluorescence imaging characterization of the SAMs

All electrochemical and in situ fluorescence imaging measurements were conducted in 50 mM KClO$_4$ solution (pH = 12 ($\pm$0.5) adjusted with KOH). The setup for these measurements has been generally described in Section 3.3 and Section 3.4.

A high-packing-density AuS-Aib4-BODIPY SAM deposited on a polished Au(111) electrode was characterized electrochemically. A cyclic voltammetry measurement from 0.10 V to –1.30 V (vs. SCE, converted to vs. Ag|AgCl in the subsequent analysis) at 20 mV/s was performed to study the reductive desorption process from the (111) surface and quantify the packing density of this SAM.

In situ fluorescence imaging measurements were conducted on the high-packing-density AuS-Aib4-BODIPY SAM deposited on a single crystal Au bead electrode with the Evolve® 512 EMCCD camera while capacitance was measured at the same time. A similar spectroelectro-chemical measurement of the reductive desorption process of a AuS-Aib4-BODIPY SAM was discussed in Chapter 4. However, in this chapter, the electrode was oriented so that a Au(111) facet was in view through an Olympus LCPlanFL 20× objective (NA = 0.40).

For the low-packing-density AuS-Aib4-BODIPY SAMs deposited on a single crystal Au bead electrode, besides the potential stepping to study the reductive desorption, modulated potential steps were applied to study the potential induced response of the low-packing-density SAMs over the potential range before the optical onset of reductive desorption. Specifically, the potential was stepped from 0 V (vs. Ag|AgCl) to –0.7 V (vs. Ag|AgCl) with –25 mV intervals but the potential was returned to the base potential (0 V) after each step potential. Five sequential images were taken at each potential step to monitor the gradual change of intensity. Note that

in the reductive desorption measurements, the fluorophore-substrate distance changed drasti-

cally during the desorption process, so all imaging settings (illuminator intensity, exposure time

and EM gain) were set to low sensitivity levels to avoid signal saturation. For the potential step-

ping measurements to study potential modulated response, all imaging settings were adjusted

to high levels to magnify the signal by about ten times because the intensity change is expected

to be small as compared to that caused by desorption. The Evolve® 512 EMCCD Camera with

the desirable sensitivity and EM gain function was employed to study the low-packing-density

AuS-Aib4-BODIPY SAMs.

5.4 Results and discussion

5.4.1 High-packing-density AuS-Aib4-BODIPY SAM deposited on a polished Au(111) electrode

Aib peptide thiolate SAMs deposited on planar Au(111) surfaces have been studied. Reductive

desorption was one of the methods used to characterize the electrochemical stability and park-

ing density of the SAMs. Here the thiol-modified Aib peptide is further tagged with a BODIPY

fluorophore, facilitating the spectroelectrochemical characterizations. However, the presence

of the fluorophore noticeably changes the property of the adsorbate. The most obvious dif-

ference is the solubility of the adsorbate HS-Aib4-BODIPY (60 μM), which is almost ten times

lower than that of the unlabeled HS-Aib4 used in [211]. Therefore, before further in situ flu-

orescence imaging characterization, electrochemical characterization using cyclic voltamme-

try was performed on the HS-Aib4-BODIPY SAM prepared on a polished Au(111) electrode.

Figure 5.2 shows the cyclic voltammogram recorded during the reductive desorption of the

HS-Aib4-BODIPY SAM. Compared with the voltammogram of the AuS-Aib4 SAM shown in

[211], the peak potential of ~0.9 V (vs. Ag|AgCl) is comparable. The major difference is the

broader current peak for this AuS-Aib4-BODIPY SAM with the onset appearing at ~–0.6 V (vs.

Ag|AgCl) which is less negative than the HS-Aib4 SAM. This might be an effect due to the pres-

ence of the big BODIPY fluorophore, which perturbed the packing, considering the influence

of different terminal functional groups (e.g., the carbohydrate group in [211]) on the desorption
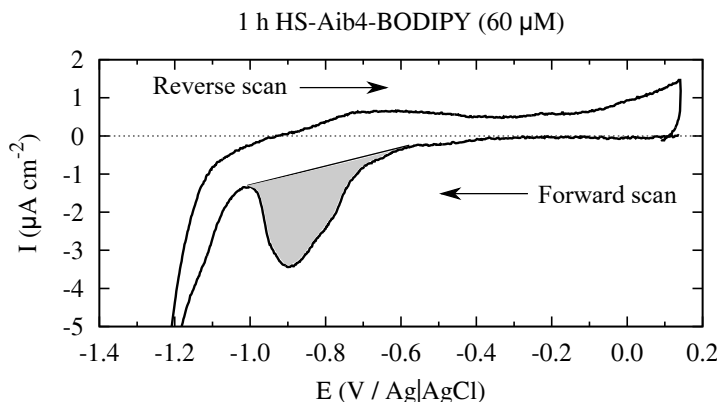
Figure 5.2: Cyclic voltammogram recorded during a reductive desorption measurement of a high-packing-density AuS-Aib4-BODIPY SAM deposited on a polished Au(111) electrode.

potential. The packing density of this AuS-Aib4-BODIPY SAM can be estimated by integrating the desorption current peak (the gray area in Figure 5.2 enclosed with the current peak and the linear capacitive current baseline arbitrarily drawn for a rough estimation), giving ~1.4×10^{14} molecules cm^{-2} (0.71 nm^2/molecule) assuming a one-electron reduction process. Despite the lower solution concentration, shorter deposition time and error associated with the calculation, this packing density is roughly comparable with the ~3×10^{14} molecules·cm^{-2} calculated in the same way for the HS-Aib4 SAM. The approximate packing densities for the labeled and unlabeled SAMs suggest the even the AuS-Aib4-BODIPY SAM formed in this condition might be close to its maximum surface coverage.

5.4.2 High-packing-density AuS-Aib4-BODIPY SAM deposited on an unpolished single crystal Au bead electrode

In Chapter 4, the use of single crystal Au bead electrode with the full stereographic triangle has been discussed. One important characteristic of the single crystal Au bead electrode is that big (111) facets can be observed on the surface and with a proper melting treatment and alignment, one (111) facet can appear at the bottom of the electrode. This can be useful because with the imaging method used, the SAMs deposited on the (111) facet, the most stable and intensely studied surface, can be investigated spectroelectrochemically. There are advantages of employing a facet on a single crystal bead electrode over a polished (111) electrode. First, a facet formed by proper annealing is close to atomically flat [201–203]. Additionally, it is rela-

tively easy to fabricate and clean the single crystal bead electrode compared to the laborious polishing needed to obtain a high quality planar electrode. Therefore, in this section, the AuS-Aib4-BODIPY SAM is prepared on an unpolished single crystal Au bead electrode and one of the (111) facets on the bead electrode is investigated. The high-packing-density AuS-Aib4-BODIPY SAM similar to those on the polished surface discussed above is first investigated to demonstrate the feasibility of this approach.

The bright field image of the Au(111) facet is shown in Figure 5.3a. The facet is only occupying about half of the image and surrounding the facet are step-like features which are narrow (111) terraces. Montage of selected fluorescence images taken at potentials from −0.925 V to −1.3 V (vs. Ag|AgCl) shown in Figure 5.3b verifies the prediction above. At potentials positive of −1.0 V (the fourth image of the first row), the fluorescence is from the facet. Stepping to more negative potentials results in a fast increase of the intensity from the steps around the facet which surpasses that from the facet at −1.175 V (the third image of the third row). It is clear the heterogeneity in intensity observed in the images is mainly due to the different surface characteristics of the facet and the steps. Although the minimum projection of the image stack (Figure 5.3c) shows some bright spots indicative of non-uniformity of the SAM in adsorption state. However, the sources of these bright spots are unknown and they can either leave the surface at negative potentials or stay after the complete potential stepping. The maximum projection of the image stack (Figure 5.3d) demonstrates the two distinctive domains due to two different types of surfaces. More importantly, the packing density within the (111) facet appears to be quite uniform.

The intensity as a function of potential is plotted for a ROI on the facet in Figure 5.4a. From the starting potential 0 V to around −0.7 V, the intensity remains similar to the background level. This suggests that at this potential range, the layer remains adsorbed and the fluorophore is near the substrate, so fluorescence is mostly quenched. The onset of a large intensity increase occurs at around −0.7 V. The intensity reaches a plateau at around −0.9 V but further increases at around −1.1 V until another plateau at around −1.2 V. The two-step desorption feature has been observed for low-packing-density AuS-Aib4-BODIPY SAM from (111) surface and surfaces with large (111) terrace in Chapter 4. A sustained increase in capacitance starts at ~−0.6 V and continues at more negative potentials (Figure 5.4b), suggesting the re-
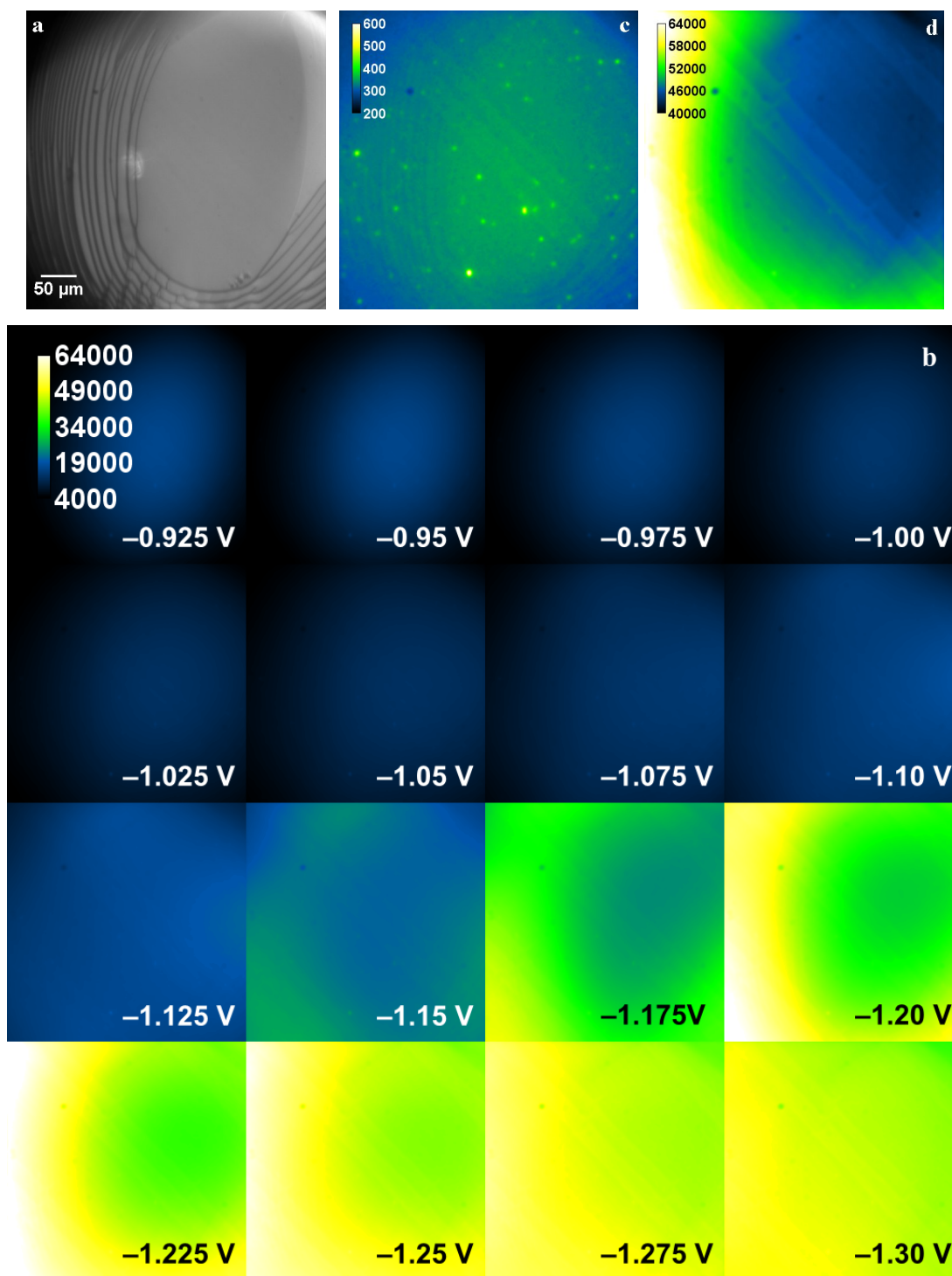
Figure 5.3: (a) Bright field image of a Au(111) facet on a single crystal bead electrode; (b) montage of selected fluorescence images from a high-packing-density AuS-Aib4-BODIPY SAM deposited on a single crystal bead electrode with a Au(111) facet in view, representing the overall fluorescence response of the layer from –0.925 V to –1.3 V (vs. Ag|AgCl); (c) the minimum projection image of the image stack; (d) the maximum projection image of the image stack.

duction of the Au-S bond and the uninterrupted displacement of the desorbed SAM with H_2O and hydrated electrolyte ions. However, the two-plateau profile of the intensity change during desorption suggests that the Aib peptide molecules do not diffuse away immediately after the reduction of the Au-S bond, but stay close to the surface instead. It was reported that desorbed Aib peptide thiolate molecules bound by intermolecular hydrogen bonds stay close to the Hg substrate electrode surface at potential slightly more negative than the desorption potential [222]. The intermolecular hydrogen bond network observed in Aib peptide thiolate SAMs deposited on Au(111) surfaces [211], hypothetically would also be able to the stabilize the desorbed SAM and hold the adsorbate molecules together, explaining the first plateau in the intensity-potential curve. At more negative potential, this intermolecular hydrogen bond network would presumably be destabilized by a large amount of H_2O, hydrated electrolyte ions and possibly the H_2 evolution, leading to fast diffusion of Aib peptide molecules and thus drastic increase of fluorescence intensity to form the second plateau. The two-step desorption applies to both the high-packing-density SAM investigated in this section and the low-packing-density SAM in Chapter 4, which may imply a relatively long active length of the intermolecular hydrogen bonds or tilted orientation of the peptide chains.

The start of reductive desorption according to the capacitance-potential plot (Figure 5.3b) is comparable to that obtained from a cyclic voltammetry measurement for a AuS-Aib4-BODIPY SAM on a polished Au(111) electrode (Figure 5.2). However, the capacitance is representing the average property of the whole surface in the electrolyte solution. An unpolished single crystal bead electrode is featured with a variety of crystallographic surfaces including the (111) facet in view, so strictly speaking the capacitance-potential plot shown in Figure 5.4b and the cyclic voltammogram shown in Figure 5.2 inform on the reductive desorption processes from different types of surfaces.The area of the planar polished Au(111) electrode can be easily determined and used to normalize the capacitance. For an unpolished single crystal bead electrode, due to the complexity of the surface, it is difficult to accurately measure the area of the electrode. Nevertheless, for a rough estimation, at ~−1.0 V (vs. Ag|AgCl), the electrode surface is mostly covered with H_2O molecules and hydrated electrolyte ions, and the H_2 evolution is not significant in such a high pH solution, so the unit area capacitance in the absence of specific adsorption for a number of crystallographic surfaces (~20 $\mu F\ cm^{-2}$ [172, 173]) can be used to

a

2 h HS-Aib4-BODIPY (60 μM)

b
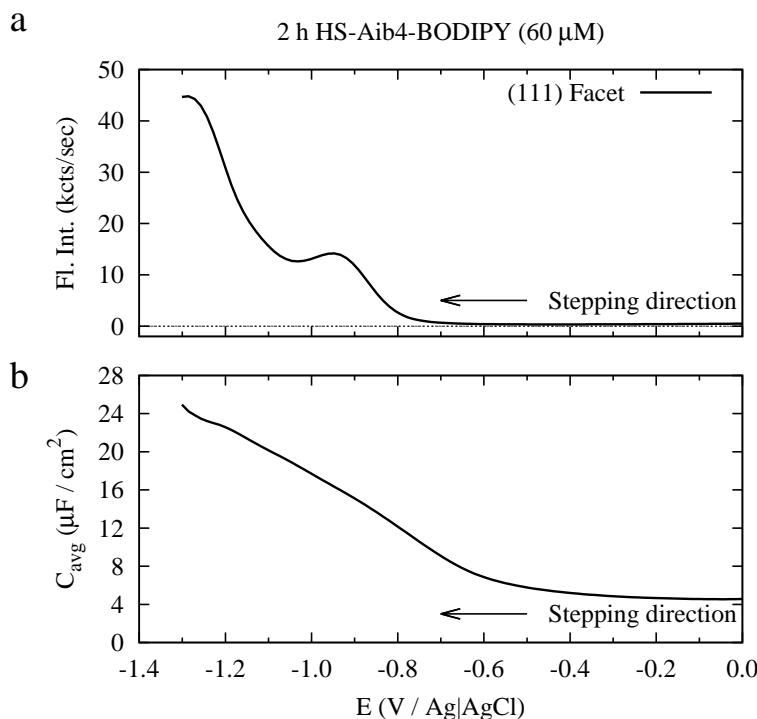
Figure 5.4: (a) In situ fluorescence intensity as a function of potential from a Au(111) facet for the high-packing-density AuS-Aib4-BODIPY SAM deposited on an unpolished single crystal bead electrode; (b) capacitance change per unit area as a function of potential for the AuS-Aib4-BODIPY SAM modified electrode.

calculate the electrode area for the following normalization.

5.4.3 Low-packing-density AuS-Aib4-BODIPY SAMs deposited on unpolished single crystal Au bead electrodes

In the previous section, a high-packing-density AuS-Aib4-BODIPY SAM on a Au(111) facet was investigated with in situ fluorescence imaging technique. Similar approach will be used in this section to investigate the potential modulated response of the low-packing-density AuS-Aib4-BODIPY SAMs. The fluorescence intensity is dependent on the distance between the fluorophore and the substrate, so besides desorption, any orientational or structural change of the peptide layer may result in a change of the fluorescence intensity. The orientational or structural change was not observed on the high-packing-density SAMs presumably because of a lack of space between adsorbate molecules. Here, modulated potential steps were applied to the modified electrode to induce a change in the fluorophore-substrate separation. The

114
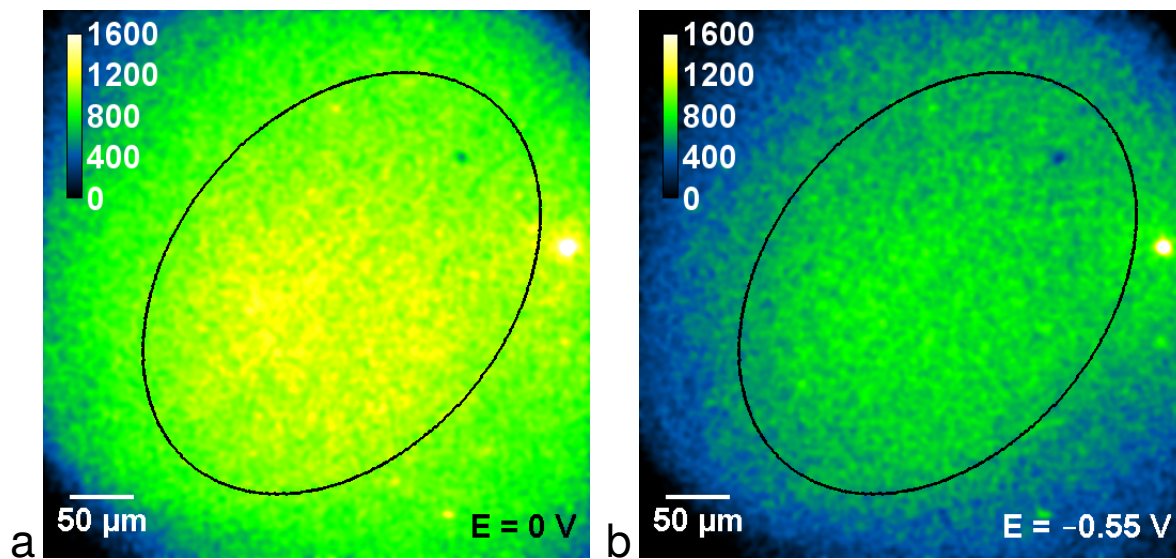
Figure 5.5: Fluorescence images of a low-packing-density AuS-Aib4-BODIPY SAM taken at (a) 0 V (vs. Ag|AgCl) and (b) −0.55 V (vs. Ag|AgCl) with the (111) facet outlined.

potential profile applied is shown in Figure 5.6a, and note that the potentials applied were limited so as to avoid the occurrence of reductive desorption. At each step, images were taken to monitor the fluorescence intensity change.

A typical low-packing-density AuS-Aib4-BODIPY SAM was created by immersing the single crystal bead electrode in 1 μM adsorbate solution for 0.5 h. Figure 5.5 shows the fluorescence images of this low-packing-density AuS-Aib4-BODIPY SAM taken at 0 V (vs. Ag|AgCl) and −0.55 V (vs. Ag|AgCl) with the perimeter of (111) facet drawn. Overall, higher intensity is observed at 0 V than at −0.55 V. The fluorescence intensity in the center of the facet is mostly uniform, so the average intensity of the outlined ROI is used to avoid further complication.

The AuS-Aib4-BODIPY layer exhibits a fluorescence intensity which is modulated by the potential steps (Figure 5.6b & c). A decrease in intensity is observed at a negative step potential while the intensity reverts to the original level when stepping back to the base potential. Note that a slow and gradual change of intensity is observed from the five images taken sequentially at each potential step. This trend continues until about −0.6 V where the fluorescence intensity at the step potentials starts to increase significantly, eventually surpassing that at the base potential. The percent change in fluorescence can be calculated by following the formula below for each step potential: $(F_{Estep} - F_{Ebase})/F_{Ebase}$, where F_{Estep} and F_{Ebase} are the fluorescence intensities extracted from the last images taken at a step potential and the base potential imme-
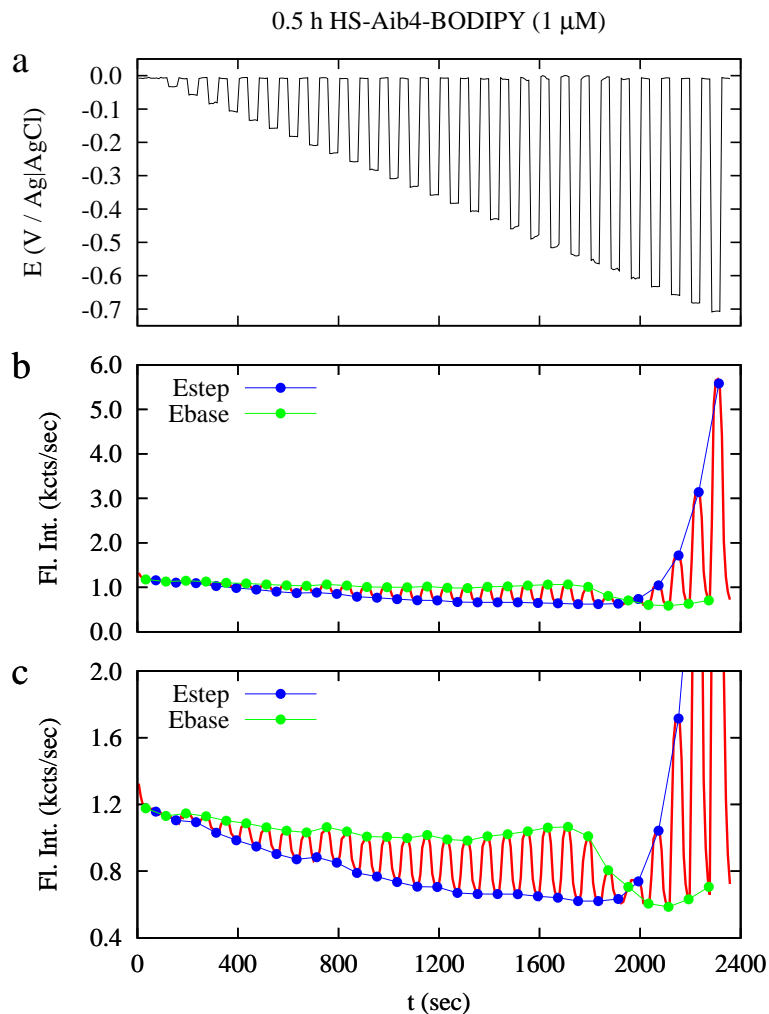
Figure 5.6: (a) Profile of the modulated potential steps; (b) the fluorescence response of a low-packing-density AuS-Aib4-BODIPY SAM; (c) ordinate enlarged fluorescence response. Adapted from [169] with permission. Copyright (2017) Springer.
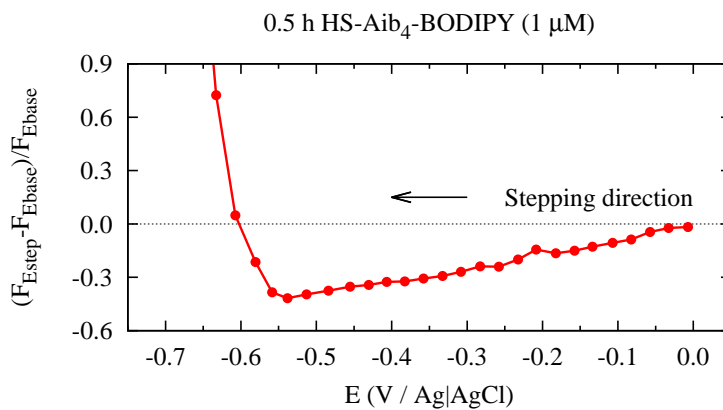
Figure 5.7: Percent fluorescence intensity change (($F_{\text{Estep}} - F_{\text{Ebase}})/F_{\text{Ebase}}$) as a function of step potential of a low-packing-density AuS-Aib4-BODIPY SAM. Adapted from [169] with permission. Copyright (2017) Springer.

diately after the step potential. The fluorescence intensity as a function of the step potential and the percent change as a function of the step potential are presented in Figure 5.7. The negative percent fluorescence change from 0 V to –0.6 V suggests that at this potential range, the fluorescence intensity decreases when stepping to a negative potential. The percent change slowly becomes more negative from almost 0% at 0 V to about –50% at –0.55 V whereafter it inflects to become less negative and eventually changes sign at more negative potentials. The fluorescence intensity at the base potential remains constant before the inflection point except for a slight decrease at the beginning which might be due to photo bleaching. Interestingly, the base potential intensity decreases dramatically at the inflection point potential and stays at this low level..

From the capacitance change shown in Figure 5.4b, it is known that at –0.6 V (vs. Ag|AgCl), reductive desorption starts. However, for the reductive desorption measurement, with low imaging sensitivity, the small fluorescence change at this potential cannot be detected. Here with imaging settings applied to achieve high sensitivity, the fluorescence signal is magnified by about 10 times, so a pronounced increase of fluorescence intensity can be observed at step potentials more negative than –0.6 V. It is reasonable to attribute this intensity increase to reductive desorption which leads to the increasing distance between the fluorophore and the substrate. From the percent fluorescence change as a function of the step potential shown in Figure 5.6c, an inflection point at –0.55 V can be observed which divides the fluorescence response into two regions. This suggests that the actual start of the reductive desorption might be at about –0.55 V (vs. Ag|AgCl). Therefore, at potentials less negative than –0.55 V where the Au-S bond stays intact, there is another orientational or structural change which results in a negative percent fluorescence change. The drastic change of base potential intensity at this inflection potential might be rationalized by the sudden change of SAM organization upon desorption.

Experimentally, the fluorescence modulation for a Aib peptide thiolate SAM was highly reproducible within a limited potential range less negative than the onset of the desorption, or the inflection point potential. Once the SAM experienced a potential negative enough to initiate desorption, the potential modulated behavior was no longer observed. This suggests the Aib peptide SAM responds to the potential modulation without the reduction of the Au-S bond.

Two possible mechanisms can be proposed to explain the potential induced response (Figure 5.8). First of all, the rigid 3_{10}-helix structure of the Aib peptide induces a dipole moment oriented along the backbone [210, 211, 218, 220]. This dipole moment could react to an electric field. To be specific, in the case of AuS-Aib4-BODIPY, the positive pole is at the surface, so presumably the positive pole would respond more dominantly than the negative pole. As a negative potential is applied to the surface, the peptide backbone is more inclined to be attracted because of the dipole moment, thus make the peptide molecule more tilted. As a result, the distance between the fluophore and the surface becomes smaller, which results in a decreased fluorescence intensity. This potential induced response of peptide is analogous to the DNA reorientation reported by Rant et al. [7, 226–228]. However, DNA molecules have negatively charged backbones which strongly respond to electrode potential. The dipole moment along the peptide backbone is the sum of a number of polar carbonyl bonds and may not respond to pottential as promptly. A second proposed mechanism originated from the "peptide spring" reported by Peggion et al. [229]. They showed that the secondary structure of a peptide molecule is dependent on the solvent. The 3_{10}-helix structure conformation is retained in a polar solvent while it converts to the fully extended conformation in a non-polar solvent. This solvent-mediated length change can be as big as 50%. It is hypothesized that the electrical potential applied to the substrate could change the polarity of the environment near the surface, which in turn changes the length of the peptide molecules, resulting in a modulated fluorescence profile. The influence of the electric field on the Aib peptide thiolate SAMs deposited on Hg substrate electrode has been investigated [222]. It was found that applying a potential was able to dramatically change the structure of the Aib peptide thiolate SAM, reversing the dipole moment which originally oriented against the electric field. Admittedly the mobile Hg surface is substantially different from the Au surface, but it is evident that the dipole moment associated with the Aib peptide thiolate SAMs can be impacted by an electric field. However, further in-depth surface characterization techniques are needed to prove whether or not the modulated fluorescence observed here is the consequence of either mechanism.

AuS-Aib4-BODIPY SAMs with higher packing density were also investigated with the potential stepping profiled in Figure 5.6a & b. The packing density was enhanced by either extending the deposition time or increasing the deposition solution concentration. As shown in Figure
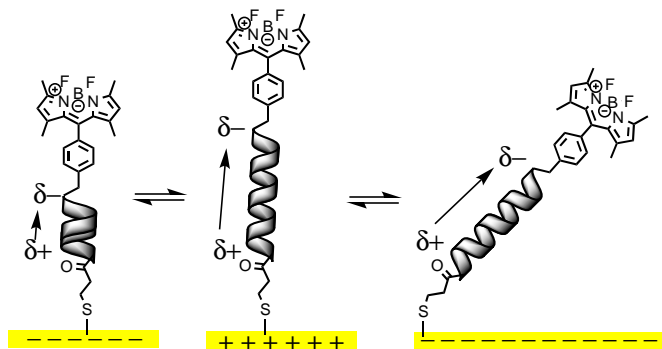
Figure 5.8: Schematic of the hypothesized structure or orientation changes in the Aib peptide thiolate responding to changes in the electrode potential. Adapted from [169] with permission. Copyright (2017) Springer.

5.9a, fluorescence modulation is strongly dependent on the SAM packing density. Extending the immersion time to 2 h significantly reduces the percent fluorescence change per potential step, while further extending the immersion time to 18 h does not substantially change this potential modulated response. Doubling the concentration of the deposition solution to 2 μM completely eliminates the fluorescence modulation at potentials more positive than the start of desorption, and the positive percent change is presumably due to diffusing away of the loosely bound adsorbate molecules. The SAM packing densities are confirmed by the fluorescence intensity during the reductive desorption measurements as shown in Figure 5.9b. As expected, the SAM of lowest packing density, created by immersion in 1 μM deposition solution for 0.5 h, shows the largest percent fluorescence intensity change. The two SAMs with similar percent changes (immersion in 1 μM deposition solution for 2 h and 1 μM deposition solution for 18 h) have similar packing densities, indicative of the highest packing density obtained with this deposition solution concentration. The packing density is significantly higher for the SAM created by immersion in 2 μM deposition solution for 0.5 h, which sets the upper packing density limit for AuS-Aib4-BODIPY SAMs with measurable potential modulated response. As a comparison, a AuS-C10-BODIPY SAM of similar packing density (created with 0.5 h deposition in 0.1 μM HS-C10-BODIPY solution) has been tested in the same way also plotted in Figure 5.9. The AuS-C10-BODIPY SAM exhibits no fluorescence intensity modulation before the start of desorption even though it has a coverage similar to the AuS-Aib4-BODIPY SAMs showing significant intensity modulation. This confirms that the potential modulated fluorescence
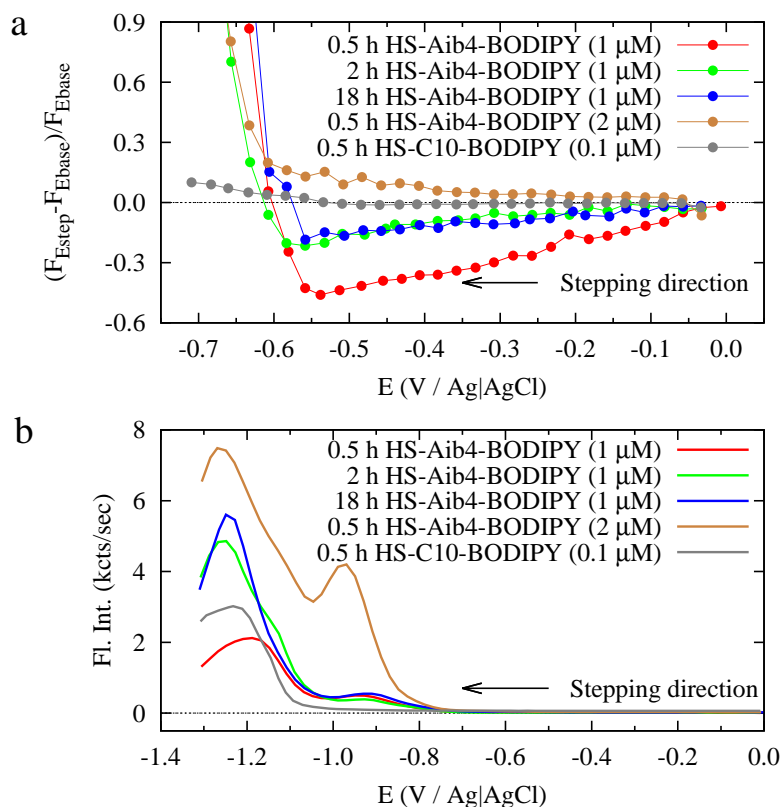
Figure 5.9: (a) Percent fluorescence intensity change (($F_{\text{Estep}} - F_{\text{Ebase}})/F_{\text{Ebase}}$) as a function of step potential and (b) fluorescence intensity as a function of potential recorded during reductive desorption, of the AuS-Aib4-BODIPY SAMs of various packing density and a AuS-C10-BODIPY SAM. Adapted from [169] with permission. Copyright (2017) Springer.

is a characteristic of the Aib peptide SAM. The dependence of potential modulated response on SAM packing density may infer that the orientation change of the Aib peptide molecule, which requires more space, predominantly accounts for the potential mediated fluorescence change. Based on the fluorescence intensity during reductive desorption, the packing density of the AuS-Aib4-BODIPY SAMs with potential modulated response can be roughly estimated by comparing with the high-packing-density SAM (Figure 5.4a). Generally speaking, the potential modulated response requires a packing density that is roughly 10% of that for the high-packing-density SAM. Assuming the high-packing-density SAM on a (111) facet adopts similar packing density to that on a polished (111) surface, 1×10^{13} - 2×10^{13} molecules·cm^{-2} is the estimated packing density required for the potential modulated response.

The potential modulated response is thus a property of low-packing-density Aib peptide thiolate SAMs deposited on Au(111) surface. Typically, high-packing-density Aib peptide SAMs

with well-ordered intermolecular interactions are used in various applications [211, 212, 222], where the property of potential modulated response no longer exists. However, investigation of this property might still be valuable in e.g., the Aib peptide covered Au nano particles, where the substrate surfaces are in the same scale of the adsorbate molecule footprint and the adsorbate molecules without many neighbors might exhibit the potential modulated response.

5.5 Conclusions

In this chapter, Aib peptide thiolate SAMs deposited on Au(111) surfaces have been studied. The high-packing-density AuS-Aib4-BODIPY SAM deposited on a polished planar Au(111) electrode was first characterized electrochemically. Comparable desorption potential and packing density to literature were obtained. In situ fluorescence imaging was employed to investigate the high-packing-density AuS-Aib4-BODIPY SAM deposited on an unpolished single crystal Au bead electrode. A two-step desorption was observed from a (111) facet for this high-packing-density SAM. With the (111) facet as the substrate, the potential modulated response of low pack density AuS-Aib4-BODIPY SAMs was explored at potentials less negative than the desorption potential spectroelectrochemically. The fluorescence intensity from the AuS-Aib4-BODIPY SAM decreased as the potential was stepped negatively, as a result of the change in orientation or structure of the Aib peptide chain in response to an electric field. This potential modulated response is a property of low-packing-density Aib peptide thiolate SAMs deposited on a Au(111) surface and thus increasing the packing density resulted in a decreased or even zero modulated fluorescence.

Chapter 6

Spectroelectrochemical investigation of the potential-driven DNA reorientation on a single crystal Au bead electrode

In the two previous chapters, alkanethiolate SAMs and thiolated Aib peptide SAMs were discussed. These two types of SAMs are mainly used as the molecular spacer and/or diluent to control the position and density of the bio-receptors in a biosensing interface. The DNA SAMs which will be explored in this chapter, are directly related to biosensors capable of capturing specific targets (e.g., nucleic acids, proteins). The negatively-charged DNA strand can respond to the electric potential by changing its orientation, which is an important and useful effect in DNA sensing requiring in-depth investigation. A single-crystal Au bead electrode is also used in this chapter as the substrate to study the influence of surface crystallography on the potential-driven DNA reorientation. Besides the in situ fluorescence imaging technique, a new spectroelectrochemical technique that couples electrochemistry, fluorescence microscopy and harmonic analysis is developed to explore harmonics of the non-linear fluorescence response to an applied AC potential perturbation. Employing this technique aims to achieve a better understanding of the DNA reorientation effect and develop a new sensing mechanism.
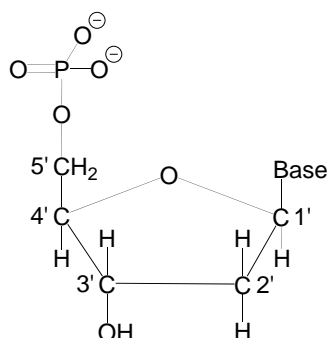
Figure 6.1: Structure of a 5'-nucleotide.

6.1 The chemical and biophysical properties of DNA

DNA (short for deoxyribonucleic acid) is a biological molecule encoding genetic information. The famous double-helix structure proposed by Watson and Crick [230] is one form (the B form) of double-stranded DNA (dsDNA) structure [231, 232]. In this chapter, DNA is an adsorbate system studied without considering its complicated behaviors in a physiological environment, so only the general chemical and biophysical properties of DNA are reviewed here.

6.1.1 Structure of DNA

The structural motif of a nucleic acid chain can be expressed as [231]:

$$-\text{P}-\text{O3}'-\text{sugar}-\text{O5}'-\text{P}-$$
$$\underset{\text{base}}{\mid}$$
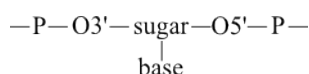
For DNA, the sugar is a deoxyribose. In the sugar ring, the C1' is connected to a base and the C3' and the C5' are both connected to phosphate groups to form the polymeric single-stranded DNA (ssDNA). The monomeric unit, i.e., the nucleotide, is shown in Figure 6.1 (shown is the 5'-nucleotide). The five atoms in the sugar ring are not co-planar and usually one atom is out of the plane. The preferred conformations are C2'-*endo* and C3'-*endo* (*endo* refers to pointing up, similar to the C5') *[231]*. The conformation of the sugar ring has an impact on the dsDNA conformation.

In Figure 6.1, the phosphate group has two "free" deprotonated hydroxyl groups. Indeed, in a ssDNA chain, one hydroxyl group is connected to the C3' of another necleotide through an ether bond, whereas the other hydroxyl is not bonded to any other group. Therefore, because

Table 6.1: Comparison of the three dsDNA conformations: B form, A form and Z form. Summarized from [231] and [232].

Property	B form	A form	Z form
Helix chirality	right-handed	right-handed	left-handed
Sugar conformation	C2'-*endo*	C3'-*endo*	C: C2'-*endo*; G: C3'-*endo*
Repeating unit	1 base pair	1 base pair	2 base pairs
Base pair per turn	10.5	11	12
Diameter	20 Å	23 Å	18 Å [233]
Axial distance between base pairs	3.4 Å	2.6 Å	3.7 Å
Pitch	35.7 Å	28.6 Å	44.6 Å
Torsion angle between base pairs	34.3°	32.7°	CpG: -9°, GpC: -51°
Axial tilt angle	~0°	~20°	-7°

of the low pK_a(~1), at neutral pH, each necleotide is carrying one negative charge except for the terminal ones, making DNA a polyelectrolyte [231, 232].

In DNA, the base can be any of the four types: adenine (A), guanine (G), thymine (T) and cytosine (C). These bases are essential for the dsDNA helical structure where A and T form base pair through two hydrogen bonds and C and G form base pair through three hydrogen bonds (Figure 6.2). The double-helix structure can be formed when these two requirements are fulfilled: one helical chain is from 5'→3' and the other is from 3'→5'; the bases from the first chain find their corresponding complementary bases from the second chain. Two fully complementary segments of DNA strands can further adopt different types of three-dimensional structures depending on the environment and the strand sequence. The most common form *in vivo*, proposed by Watson and Crick, is later termed B form [231] (Figure 6.3). B form DNA can convert into A form DNA in solutions with low H_2O activity [232]. Both B form and A form are right-handed, but a rare Z form is left handed. Z form mainly occurs in alternating poly-(dG-dC) and is adopted in the presence of high electrolyte concentration [233, 234]. The structural properties of the three forms are listed in Table 6.1. Note that all properties listed in Table 6.1 are actually statistical properties. Although there are energetically preferred conformations for each base pair, because of energy fluctuation or perturbation, it is not possible to keep each base pair in the preferred conformation. Therefore, the experimentally determined values are the statistical averages.

There exist other conformations, such as B' form, triple helix, G-quadruplex, etc., but these conformations are rare and require special conditions [232]. Worth mentioning is the hairpin
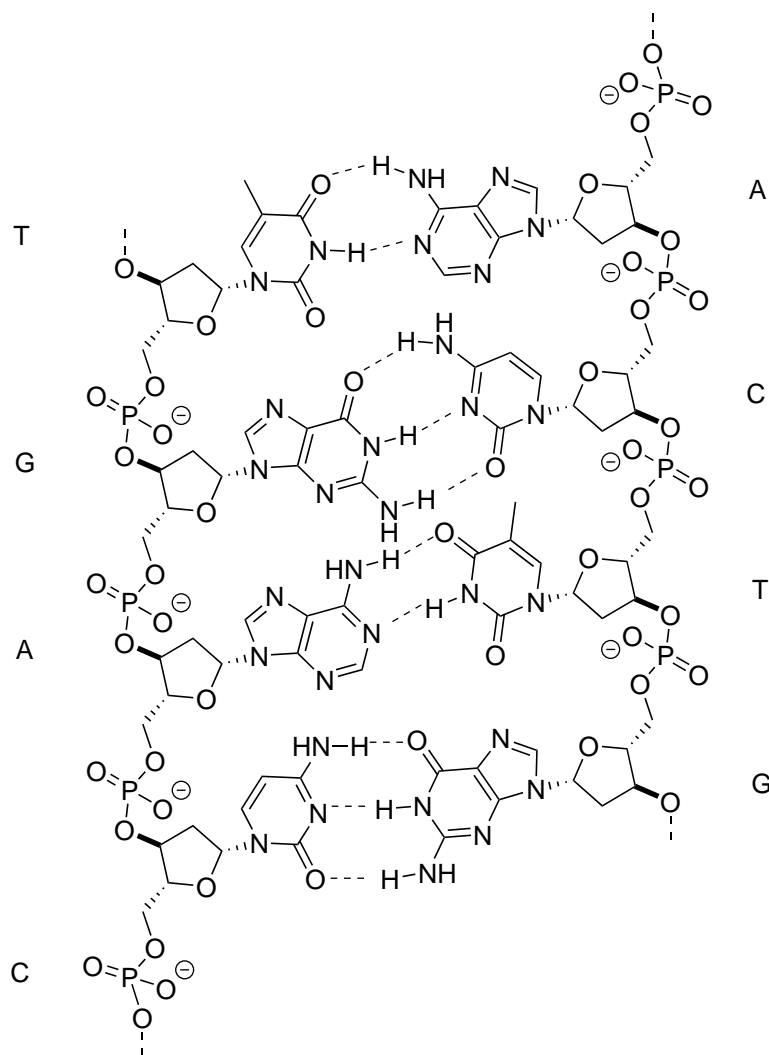
Figure 6.2: Chemical structure of a dsDNA segment showing the complementary base pairs.
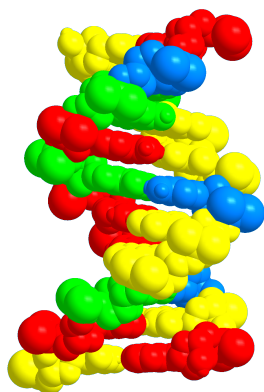
Figure 6.3: Three-dimensional structure of a dsDNA segment with B form configuration. A, G, T, and C are colored in red, green, yellow and blue, respectively.

structure formed within one ssDNA chain with self-complementary segments. This structure has often been exploited in bio-sensing applications [52, 53, 235, 236] in that opening up the hairpin structure with the full complementary strand dramatically changes the apparent length of the DNA chain.

6.1.2 Physical properties

Two important physical properties are reviewed here: the persistence length and the effective diameter. These are important physical properties especially in an electrolyte solution, which is the environment for electrochemical characterization.

The persistence length characterizes the flexibility of a polymer. It can be understood as the maximum length for a polymer chain to behave as a rigid rod [231]. Considering the conformations, dsDNA, with the double-helix structure, is significantly less flexible than ssDNA, so dsDNA has much higher persistence length than ssDNA. The characteristic persistence length for dsDNA is ~50 nm (~147 base pairs for B form DNA) [237] while the characteristic persistence length for ssDNA is < 5 nm (~11 bases) [238]. Moreover, since the DNA backbone is negatively charged, due to charge repulsion, a longer persistence length is expected with an increase in the amount of unshielded charge carried by the DNA chain. Cations, especially multivalent cations, in a electrolyte solution counterbalance the DNA backbone charge and thus DNA has a low persistence length in a solution with high ionic strength[237–239]. This ionic strength dependence is not significant for dsDNA in an solution with [Na^+] of over 1 mM or [Mg^{2+}] of over 0.2 mM, and the ~50 nm persistent length appears to be a minimum under commonly used non-extreme conditions [237].

The effective diameter of DNA characterizes the electrostatic interaction between neighboring DNA chains in an electrolyte solution. Charge repulsion due to the negative charge on the DNA backbone, in addition to the steric hindrance, prevents a DNA chain from approaching the neighboring DNA chains. As expected, at high ionic strength, the backbone charge is mostly shielded, resulting in a small effective diameter and vice versa [240, 241]. The effective diameter of dsDNA as a function of ionic concentration is demonstrated in Figure 6.4. For DNA tethered to a surface, effective diameter is further influenced by the bending of DNA strand. A
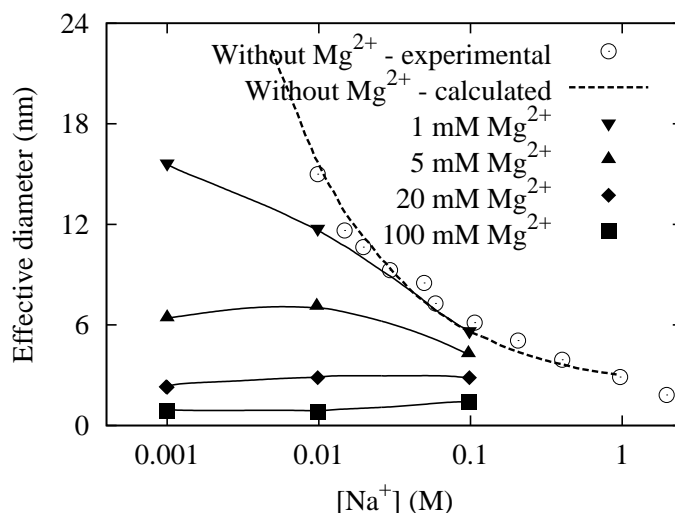
Figure 6.4: Effective diameter of dsDNA as a function of ionic concentration. Reproduced from [241] with permission from Oxford University Press.

DNA strand longer than its persistence length has a larger effective diameter due to bending than a short DNA strand behaving as a rigid rod [242].

6.1.3 DNA hybridization and dehybridization

The process of hybridization between two complementary DNA single-strands is reversible. Traditionally, for experimental convenience, the DNA melting process, i.e., thermal dehybridization of a dsDNA duplex is often discussed. From the thermodynamic point of view, considering $\triangle G° = \triangle H° - T \triangle S°$, for the DNA melting reaction, $\triangle H°$ is positive and $\triangle S°$ is positive as well [243, 244]. Therefore, dsDNA is dehybridized into ssDNA at high temperature and the temperature at which half of the DNA strands are in ssDNA state is defined as the melting temperature T_m. From the microscopic aspect, the entropic change during DNA melting can be described by the facts that one double strand duplex is separated into two single strands and that the separated DNA single strands are structurally much more flexible than the double strand duplex. On the other hand, three factors are contributing to the dsDNA stability: the hydrogen bond and π-stacking interactions formed between complementary bases which stabilize the dsDNA duplex and the repulsion between negatively charged backbones which destabilizes the dsDNA duplex. These three factors are all closely related to the enthalpic change but the entropic change is mostly independent of them [232]. As a consequence, high T_m is expected for long

DNA strands because of a large number of hydrogen bond and π-stacking interactions. DNA strands with a high fraction of GC base pairs is also expected to have high T_m. Additionally, high concentration of electrolyte ions which shield the DNA backbone charges results in high dsDNA T_m [232, 243, 244]. On the contrary, spontaneous dehybridization of dsDNA can occur in a solution with low ionic strength. Experimentally, the dsDNA melting process is usually determined by measuring the UV absorbance (typically at 260 nm) as the temperature increases. An increase of UV absorbance upon dehybridizing the dsDNA duplex (known as hyperchromicity) can be observed due to the breakdown of π-stacked aromatic rings in the dsDNA duplex [245, 246].

Dehybridization of dsDNA can be achieved not only by thermal treatment, but also by chemical treatment. Extreme acidic or basic conditions lead to dehybridization (often termed "denaturation") accompanied by bond break of the DNA chemical structure [245]. Urea treatment, which breaks the hydrogen bonds between complementary bases, exerts a more gentle denaturing mechanism, effective in low ionic strength solutions [247]. Consequently, urea is the commonly used denaturant for DNA polyacrylamide gel electrophoresis (PAGE) [248, 249].

The review given above is based on hybridization in a solution phase. Hybridization on a solution-solid interface is also an important topic because this process is related to biosensing. Thermodynamically, surface hybridization is not as favorable as solution hybridization. Shielding backbone charges is not as effective on a surface because steric hindrance prevents ions from moving into the layer of tethered DNA, so higher ionic strength is required for surface hybridization [244]. One key distinction from solution hybridization is that the density of ssDNA immobilized on a surface (i.e., surface probe) plays a crucial role in the rate and efficiency of the hybridization. Not surprisingly, higher surface probe density results in a lower rate and efficiency of hybridization. Typically, in order to accomplish 100% hybridization, a low surface probe density of no more than 10^{12} molecules/cm^2 is required [250] which is about 1% of the maximum density of thiolated DNA strand (depending on the length) immobilized on a Au substrate [110].
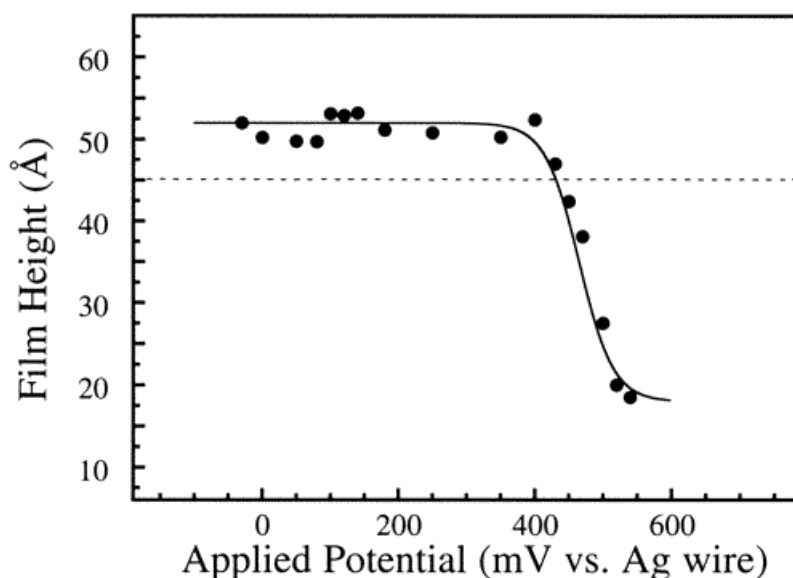
Figure 6.5: The potential-dependent thickness of the DNA SAM immobilized on a Au(111) surface, determined by EC-AFM. The dashed line marks the DNA SAM thickness at open-circuit potential. Reprinted from [251] with permission from American Chemical Society.

6.2 Potential-driven DNA reorientation

The negatively charged backbone of DNA is an interesting and useful feature particularly in DNA SAMs because the orientation of the adsorbed DNA molecules can be controlled by electric potential at the surface. To be specific, at a positive potential, the DNA backbone is attracted to the surface, resulting in a "lying-down" configuration. At a negative potential, the DNA backbone is repelled by the surface, resulting in a "standing-up" configuration.

The potential-driven DNA reorientation effect was first studied with electrochemical atomic force microscopy (EC-AFM) by Kelly et al. [251]. It was observed that the thickness of the DNA SAM immobilized on a Au(111) surface was potential-dependent, as shown in Figure 6.5.

Further if the DNA adsorbate is labeled with a fluorophore, the orientation of a DNA molecule and thus the distance between the fluorophore and the surface is controlled by the potential. Due to the distance-dependent fluorescence quenching near a metal surface (reviewed in Section 2.4.3), the potential-driven DNA reorientation is observed as a potential-controlled fluorescence response represented in Figure 6.6. Rant and co-workers have been investigating the potential-driven DNA reorientation effect using a fluorophore labeled DNA, detailing the mechanisms, kinetics and influencing factors for DNA reorientation [54, 226–228] and applying this
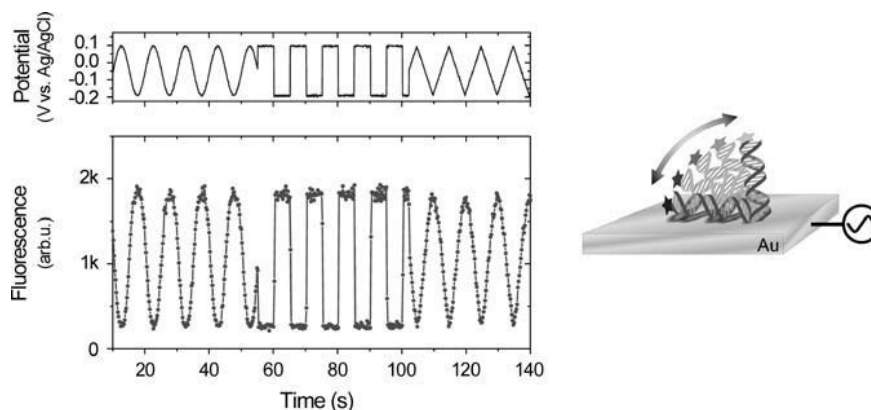
Figure 6.6: The potential-controlled fluorescence response from a fluorophore labelled dsDNA immobilized on a Au surface. Reprinted from [227] with permission from Elsevier.

valuable reorientation effect in biosensing [7, 54, 55, 57]. A few important points are highlighted here. First, the ssDNA and dsDNA have different backbone rigidity, resulting in distinctive reorientation mechanisms. The dsDNA undergoes rigid-body rotation around the anchoring point due to the stiff molecular conformation. On the contrary, the motion of the flexible ssDNA occurs segment by segment. This movement is more prominent when the ssDNA is attracted to the surface by a positive potential, reflected as a short transition time [227]. Moreover, when an alternating potential is applied to drive the reorientation, as expected, above certain threshold frequency, the DNA SAM cannot completely respond to the alternating potential and therefore will not reorient. It was shown that dsDNA can respond to AC potentials of higher frequency than ssDNA of the same length and a short strand can reorient at higher frequencies than a long one [54]. Furthermore, the electrolyte concentration has a profound and critical influence on the DNA reorientation [228]. Theoretically, the electric field across the interface, which drives the DNA reorientation, can only extend to the distance of Debye length (see Section 2.3.3). The Debye length is strongly dependent on the electrolyte concentration. At high electrolyte concentrations (~1 M), the Debye length is only 1-2 nm. Thus, considering the the length of the alkyl linker (~1.3 Å per CH_2 [105]), the electric field is only extended to four base pairs near the alkyl linker, so for a dsDNA with over 20 base pairs (assuming in B form, see Table 6.1), the motion driven by this electric field is small. On the other hand, for ssDNA, the persistence length is on the same order as the Debye length, so the strand adopts a compacted state with little reorientation behavior. In an intermediate electrolyte concentration (~10-100 mM), both

the dsDNA and ssDNA exhibit the reorientation response to potential. As discussed in Section 6.1.3, the dsDNA duplex is stable at a sufficiently high electrolyte concentration. Therefore, at low electrolyte concentrations (~0.1-1 mM), the dsDNA duplex is not formed, but interestingly, the ssDNA strand may adopt an extended conformation (long persistence length) due to a lack of shielding of backbone charge and take up the rigid-body rotation mechanism. Besides the extent of reorientation, the potential at which the DNA changes its orientation between lying down and standing up (termed as the potential of conformation transition, or PCT in [228]) is also dependent on the electrolyte concentration. A decrease of electrolyte concentration results in a negative shift in PCT because of an increase in the amount of unshielded negative charge on the DNA backbone. Lastly, Rant et al. exploited the potential-driven DNA reorientation to create biosensing platforms, mainly based on three motifs: a change in the magnitude of the reorientation response, a shift in the threshold reorientation frequency or a change in the reorientation transition time upon capturing the target (the complementary strand or biological analytes)[7, 54, 55, 57]. Note that for the approach based on the frequency response, it is important to distinguish the charging process from the reorientation response because at high frequencies (> 1 kHz), charging the electrode kinetically limits the DNA reorientation. The actual reorientation rate can be determined by deconvoluting the electrochemical charging time from the measured frequency response [252, 253].

6.3 Harmonic analysis of nonlinear fluorescence response driven by AC potential perturbation

The potential-driven reorientation of a DNA SAM monitored with fluorescence is intriguing in that as shown in Figure 6.6, the shape of the fluorescence response closely resembles the driving potential. Thus, a sinusoidal potential perturbation results in sine-wave like fluorescence response. Therefore, the amplitude and frequency response of the fluorescence were often investigated [7, 54, 55]. However, strictly speaking, the fluorescence signal does not necessarily have the sinusoidal waveform simply because the fluorescence intensity can be non-linearly related to the applied potential.

The alternating potential applied can be described as a complex number:

$$E = E_0 \exp(i(\omega t + \varphi)) \tag{6.1}$$

The fluorescence intensity as a function of potential is generally expressed as:

$$F = f(E) \tag{6.2}$$

If the fluorescence intensity is linearly related to potential, then

$$F = aE + C = aE_0 \exp(i(\omega t + \varphi)) + C \tag{6.3}$$

In this case, the fluorescence response has the same form as the AC potential perturbation. If the fluorescence intensity is quadratically dependent on potential:

$$F = a_1 E + a_2 E^2 + C = a_1 E_0 \exp(i(\omega t + \varphi)) + a_2 E_0^2 \exp(i(2\omega t + 2\varphi)) + C \tag{6.4}$$

Besides an alternating signal with an angular frequency of ω (fundamental frequency), another signal with an angular frequency of 2ω, i.e., the second harmonic, contributes to the AC fluorescence response. The second harmonic is the nonlinear component of the fluorescence response. Equation 6.4 can be generalized for a polynomial function containing m terms:

$$F = \sum_{n=1}^{m} a_n E^n + C = \sum_{n=1}^{m} a_n E_0^n \exp(i(n\omega t + n\varphi) + C \tag{6.5}$$

Equation 6.5 is the sum of a series of signals and that with an angular frequency of $n\omega$ is the nth harmonic term. Therefore, if the fluorescence intensity-potential function F contains an E^n term, this term is transformed into the nth harmonic in the AC fluorescence response. In reality, F can be any non-linear function. A Taylor expansion performed around a DC potential (e.g., 0 V for simplification) gives a polynomial series (only the Maclaurin series is given here):

$$F = \sum_{n=0}^{\infty} \frac{f^{(n)}(0)}{n!} E^n = \sum_{n=0}^{\infty} \frac{f^{(n)}(0)}{n!} E_0^n \exp(i(n\omega t + n\varphi)) \tag{6.6}$$

Equation 6.6 suggests that a general nonlinear fluorescence response can be separated into a series of harmonic terms. The amplitude of the harmonics indicates the extent of the non-linearity of the signal. Harmonic analysis is a method to extract the amplitude of the harmonic components, which can be experimentally achieved using two techniques: Fourier Transform frequency response analysis and phase sensitive detection using a lock-in amplifier. In this chapter, a lock-in amplifier is employed to analyze the harmonic components of the alternating fluorescence response due to its high sensitivity and low noise as compared to the frequency response analysis technique [254, 255].

6.4 Objectives

MCH-DNA SAMs formed by the thiol-exchange mechanism will be studied. The fluorescence image of a typical MCH-DNA SAM so prepared will be compared with the map of crystallographic surfaces to study the influence of the surface crystal structure on DNA SAM formation. In situ fluorescence imaging will be performed to investigate the potential-driven DNA reorientation response as a function of the surface crystallography. Furthermore, a harmonic analysis technique using a lock-in amplifier will be developed to characterize the non-linearity of the fluorescence response to an applied AC potential perturbation. This method will be employed to measure the higher harmonics of the fluorescence response for DNA SAMs of different hybridization states and from different crystallographic surfaces. A new DNA sensing mechanism will be proposed based on the experimental results.

6.5 Experimental

6.5.1 Preparation of MCH-DNA SAMs

Creating a MCH-DNA SAM by partial displacement (i.e., thiol-exchange) of a MCH SAM with thiolated DNA is used to achieve a low density of DNA spaced by MCH on a surface [111, 252, 253, 256]. A variety of MCH-DNA SAMs were prepared for different purposes. In general, a clean single crystal Au bead electrode was first modified with 1 mM MCH solution for 1-2 h, followed by immersion in 0.5-1 μM HS-C6-DNA-AlexaFluor (see Section 3.1.1 for specification)

solution for 16-24 h. The solvent for MCH was either MeOH or a pH = 7.5 buffer solution composed of 10 mM 2-amino-2-(hydroxymethyl)propane-1,3-diol (Tris) and 100 mM NaCl. The solvent for the thiolated DNA was a pH = 7.5 immobilization buffer solution composed of 10 mM Tris, 100 mM NaCl and 50 mM or 500 mM $MgCl_2$. The solvents used did not seem to notably alter the properties of the SAMs, so they are not specified for each individual SAM. The DNA density was mainly controlled by adjusting the deposition time and the adsorbate concentration. Note that the DNA used is a 30-mer strand and the fluorophore at the distal end is positioned sufficiently far away from the Au surface so that fluorescence is not completely quenched. The fluorophore was either AlexaFluor488 or AlexaFluor647 and each has distinctive advantages. AlexaFluor488 has a higher photo-stability. The intensity of AlexaFluor647 is more sensitive to fluorophore-metal separation in the regime of less than 10 nm (the length of a 30-mer dsDNA) away from the metal surface [169], favorable for studying the reorientation response. Overall, the SAMs prepared can be grouped into two categories, listed in Table 6.2.

Table 6.2: The two categories of MCH-DNA SAMs prepared and their formation conditions

Fluorophore	MCH immersion	DNA state	DNA concentration	DNA immersion
AlexaFluor488	1 h	ssDNA	1 μM	24 h
AlexaFluor647	2 h	ssDNA or dsDNA	0.5 μM	16 h

Both ssDNA SAMs and dsDNA SAMs were investigated. The hybridization was performed in solution before assembly on the surface. Hybridization in solution was performed by heating a 1:2 mixture of the HS-C6-DNA-AlexaFluor and the corresponding unlabeled complementary strand in a pH = 7.5 buffer solution of 10 mM Tris, 100 mM NaCl and 50mM $MgCl_2$ to about 90 °C and then slowly cooling it down to room temperature over 1 h. Dehybridization of dsDNA SAM on the surface was achieved by soaking a MCH-dsDNA SAM-modified electrode into 8 M urea solution for 2 min followed by rinsing with H_2O.

6.5.2 Spectroelectrochemical measurements

The setup for spectroelectrochemical measurements was discussed in Section 3.4. All measurements were conducted in a pH = 7.5 buffer solution of 10 mM Tris and 10 mM KNO_3. An electrode modified with a MCH-DNA SAM (except for one after urea treatment) had to be stored

in the immobilization buffer solution for at least 12 h prior to further characterization.

The DNA-AlexaFluor488 SAM was imaged with an Evolve® 512 EMCCD camera through an Olympus LMPlanFl 5× objective at -0.4 V (vs. SCE) for comparison with the map of the crystallographic surfaces. The potential-driven reorientation response was studied on the DNA-AlexaFluor647 SAMs either with a SBIG ST-7XMEI CCD camera or with a Newport 77348 model PMT. In situ fluorescence imaging was performed with an Olympus UMPlanFl 10× (NA = 0.3) water immersion objective. The potential was changed by applying potential steps from an initial/base potential to a final potential with stepping to the base potential (the second scheme described in Figure 3.6a) to induce DNA reorientation and measure the fluorescence response. The initial potential (or base potential) was 0.35 V (vs. SCE), the final potential was -0.40 V (vs. SCE) and the interval was -25 mV.

For measurements with a PMT as the detector, the fluorescence signal was collected with an Olympus LUMPlanFl 40× (NA = 0.8) water immersion objective and a field diaphragm was closed down so that a small region (~96 μm in diameter) was illuminated. Either linear potential scanning or potential stepping with the AC potential perturbation was applied to induce the reorientation response. The linear potential scanning was analogous to the electrochemical cyclic voltammetry scanning between 0.35 V and -0.40 V, except that the fluorescence signal amplified by the PMT (and further converted to voltage with a current preamplifier) was also recorded. For the harmonic analysis measurements, potential stepping was employed (without stepping to the base potential) so that the harmonics at various DC potentials were measured. The modified electrode was held at a step potential applied from the FHI-ELAB G050-0298 potentiostat and perturbed with an AC potential sent from the SRS SR830 lock-in amplifier to induce the alternating fluorescence response detected by the PMT. A Stanford Research SRS570 current preamplifier was used to convert the PMT amplified signal into voltage and further pass it through a 1 kHz low-pass filter. The rms amplitude of this processed signal was measured with a data acquisition board (DAQ) and the harmonic response was analyzed with the lock-in amplifier. The frequency of the AC potential was selected to be 163 Hz for two reasons. First, 163 Hz and its harmonics are not close to the power line frequency of 60 Hz and its harmonics. Second, this frequency is relatively low and the DNA reorientation will not be kinetically impeded by the electrode charging process [253]. The rms amplitude of the

AC potential was typically 50 mV, 100 mV or 150 mV. Care must be taken when choosing the amplitude of the AC potential so that the most positive and negative applied potentials do not exceed the stability limits of the SAMs, e.g., oxidation at positive potentials (i.e., more positive than 0.35 V) or reduction at negative potentials (i.e., more negative than 0.40 V).

6.6 Results and discussion

6.6.1 Influence of surface crystallography on DNA SAM formation

As reviewed in Section 6.2, the potential-driven DNA reorientation is a useful motif in biosensing. One important requirement is to create SAMs with low DNA density ($< 10^{11}$ strands/cm^2), which is necessary for reorientation [54]. The standard approach to make DNA SAMs on a Au surface is to deposit thiolated DNA on the Au surface first, followed by displacing non-specifically adsorbed DNA with MCH [108–110]. Low DNA density SAMs can be achieved either by short exposure to thiolated DNA [226, 227] or partial reductive desorption of DNA in a solution containing MCH at negative potentials [54, 57, 228]. Another approach to form low DNA density SAMs is to deposit MCH first, followed by partial displacing MCH with thiolated DNA [111, 252, 253, 256]. MCH-DNA SAMs formed by this competitive thiol-exchange mechanism have a relatively low DNA density (typically below 5×10^{10} strands/cm^2 [111]), enabling a high extent of DNA reorientation. However, a significant amount of non-uniformity was observed on a MCH-DNA SAM deposited on a polycrystalline electrode with DNA preferentially adsorbed onto various regions [111]. Here, MCH-DNA SAM deposited on a single crystal Au bead electrode is investigated, in an attempt to understand the influence of surface crystallography on DNA SAM formation.

Investigated in this section is the DNA-AlexaFluor488 SAM listed in Table 6.2. A fluorescence image of this MCH-ssDNA SAM on a single crystal Au bead electrode was taken at –0.4 V (vs. SCE) and shown in Figure 6.7. It is assumed that at –0.4 V (vs. SCE), all the DNA molecules are repelled from the surface to the most extended conformation (but not reductively desorbed), so the fluorescence intensity is mainly dependent on the DNA density. The fluorescence image displays a symmetric pattern strongly correlated to the fcc crystal structure,

facilitating proper indexing of surface.

A high fluorescence signal is observed the (100) surface as well as surrounding surfaces with large (100) terrace (wider than 5 atoms), forming a cross-shape feature in the center of the image. This feature is quite familiar, recalling a similar structure in the desorption potential maps of AuS-C10-BODIPY SAMs (Figure 4.12) presented in Chapter 4. Considering the DNA is modified with a hexanthiol linker with a similar structure to MCH, in the linker portion, the coordination to the surface and the intermolecular interaction should be similar to the AuS-C10-BODIPY SAMs. However, in the case MCH-DNA SAM, the fluorescence intensity from a specific region is indicative of the extent of thiol-exchange, which is dependent on the molecular arrangement of the MCH SAM, the availability of defects on the MCH SAM and the intermolecular interaction between DNA strands.

The thiol-exchange process involves competition between an organized SAM and incoming adsorbates, so the molecular arrangement of the SAM has a strong impact on the tendency towards or against adsorbate replacement. The hexanethiol (expected to be similar to MCH) covered (111) and (100) surfaces have been characterized with STM [102, 104]. On a (111) surface, the hexanthiolate SAM is featured with a large fraction of well-ordered domain adopting the widely-observed $(2\sqrt{3} \times 3)$ (also termed $c(4 \times 2)$, see Section 2.2.2) structure and dispersed vacancy defects [104]. As a comparison, the molecular arrangement of a hexanethiolate SAM deposited on a (100) surface is more complicated [101, 102]. Fully lifting a reconstructed (100) surface does not seem to be achievable solely by adsorption of a hexanethiolate SAM. The molecular arrangements on a (1×1) (100) surface and a reconstructed (100) surface are different (termed α phase and β phase respectively) and either one is featured with a significant amount of domain segregation. Therefore, a MCH covered (100) surface is likely to be highly heterogeneous and defective, which is favorable for the thiol-exchange process. Moreover, a compact alkanethiolate SAM is typically formed after a fast adsorption process and a slow annealing process [208, 209]. The number of defects are significantly decreased after the annealing process [209], which lowers the possibility of thiol-exchange. It was shown in Chapter 4 that extending the AuS-C10-BODIPY SAM assembly time from 15 min to 18 h caused a negative shift in desorption potential, which was indicative of the SAM annealing process. The negative shift was more significant on the cross-shape region around (100) (~-70
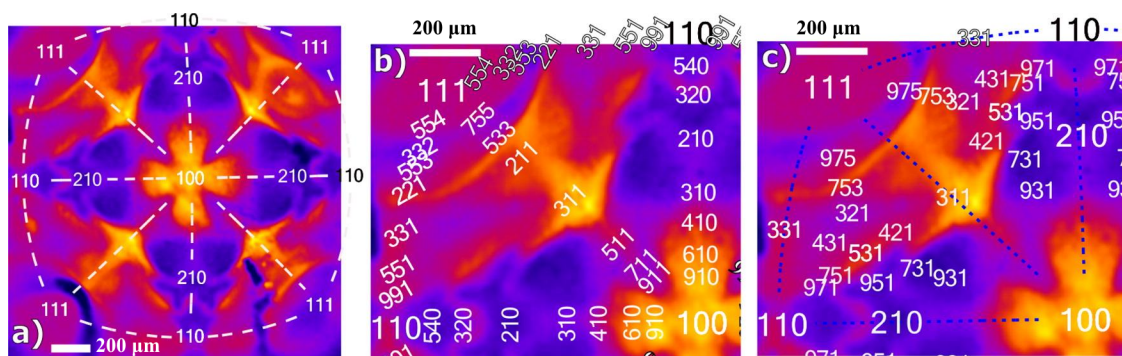
Figure 6.7: Fluorescence image of a MCH-ssDNA-AlexaFluor488 SAM on a single crystal Au bead electrode taken at –0.4 V (vs. SCE) indexed with (a) the low index planes shown for the full image with four quadrants; (b) low-index and stepped surfaces in the NW quadrant; (c) kinked surfaces in the NW quadrant. The scale bar in each image is 200 μm. Adapted from [8] with permission. Copyright (2014) American Chemical Society.

mV) than on a (111) facet (-20 mV), suggesting a difference in the annealing rate. Thus, for a MCH (thiolate) SAM formed after 1 h deposition, a larger number of defects are expected on the cross-shape region, allowing for a higher amount of thiol-exchange. All these factors discussed above combined might be the cause for a higher DNA density in the cross-shape region containing the (100) surface and surfaces with a large (100) terrace than on a (111) facet.

A more detailed correlation between the fluorescence intensity and the surfaces can be observed by plotting the intensity profiles extracted from the WNW portion of Figure 6.7 along the three crystallographic zones which connects the low-index planes (Figure 6.8 a-c). Among numerous subtle features, the fluorescence intensities observed near two highly rough surfaces are worth highlighting. High intensity is observed on a region containing the (311) surface (marked with "*" in Figure 6.8a). The (311) surface is the turning point of the (111)-(100) zone and features equal widths of (111) step and (100) step. In contrast to the (311) surface, fluorescence near the (210) surface (the turning point of the (111)-(100) zone) is the lowest intensity of the three crystallographic zones of (100)-(110)-(111) (marked with "#" in Figure 6.8c). Although these two surfaces are both featured with high density of step edges, the extents of thiol-exchange are vastly distinctive, so the DNA intermolecular interaction might also have an influence, other than simply the atomic arrangement of the surface. The fluorescence intensity stays high from (311) to the region surrounding (111) facet, suggesting the (111) terrace
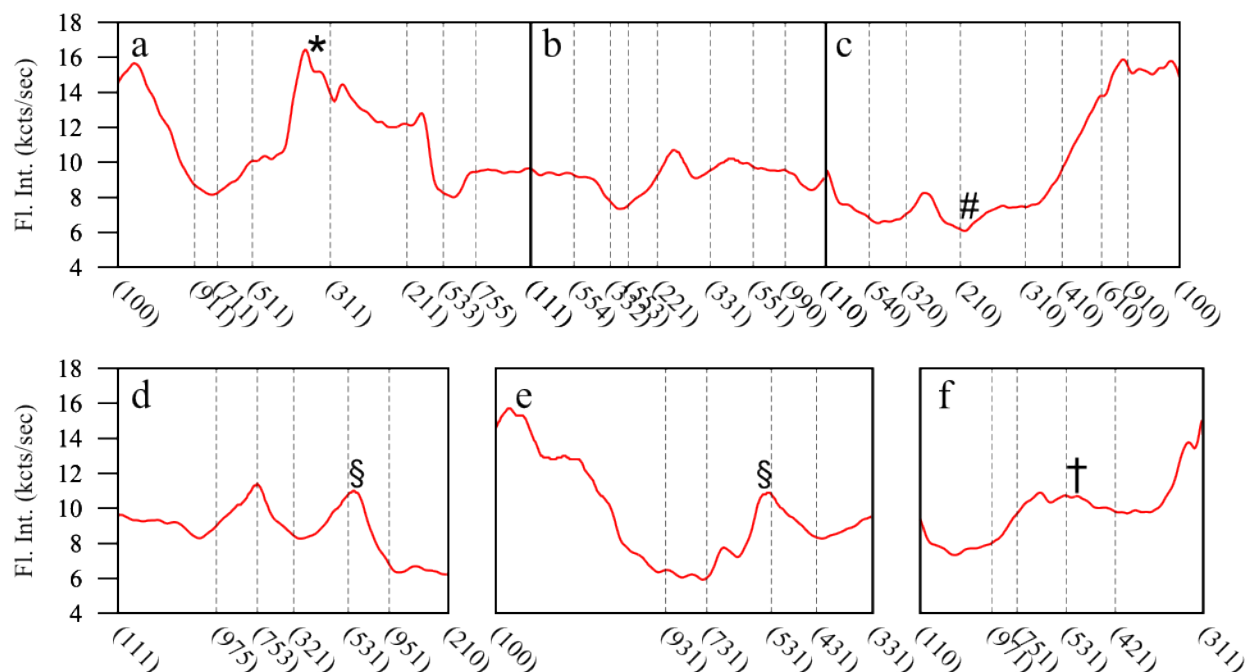
Figure 6.8: Fluorescence intensity profiles extracted from the WNW portion of Figure 6.7 along the three crystallographic zones which connects the low-index planes: (a) (100)–(111), (b) (111)–(110), (c) (110)–(100) and the three zones from the a low-index surface to the turning point stepped surface of the opposite side: (d) (111)–(210), (e) (100)–(331), (f) (110)-(311). Adapted from [8] with permission. Copyright (2014) American Chemical Society.

might be favorable for the intermolecular interaction between adsorbed DNA molecules. On the contrary, the presence of (110) terraces on the stepped surfaces from (210) to (110) might hinder the thiol-exchange. The intensity profiles for the three zones from the a low-index surface to the turning point stepped surface ((210), (311) or (331)) of the opposite side (Figure 6.8 d-f) enables exploring the DNA formation on kinked surfaces. These three zones cross at the (531) surface where (111), (100) and (110) terraces and corresponding (210), (331) and (311) steps coexist (see Figure 2.8 in Section 2.1.4). Locally, a relatively high density of DNA on the (531) surface is observed in the (111)-(210) and (100)-(331) zones (marked with "§" in Figure 6.8d and e), whereas in the (110)-(311) zone, a similar intensity level is observed from (531) (marked with "†" in Figure 6.8f) as well as the neighboring surfaces. This suggests that the presence of (311) characteristic in the (110)-(311) zone might exert an influence in the DNA density on the kinked surfaces.

Besides the major features on the important surfaces mentioned above, there are also a

number of interesting subtle features which cannot be predicted or rationalized by the surface crystal structures. Nevertheless, with this fluorescence imaging technique, the influence of surface crystallography on DNA formation by thiol-exchange for this MCH-DNA SAM was observed. This may be an important factor which causes the non-uniformity in DNA density observed on a MCH-DNA SAM deposited on a polycrystalline electrode. More importantly, the results presented in this section may give insights into energetics of thiol-exchange as a function of surface crystallography.

6.6.2 Investigation of the potential-driven DNA reorientation with in situ fluorescence imaging

In Chapter 5, in situ fluorescence imaging was employed to investigate the potential-controlled behavior of a low packing density Aib peptide SAM. In a similar fashion, potential steps are applied to induce the DNA reorientation, resulting in modulated fluorescence which is detected using a camera. This imaging technique and the use of a single crystal Au bead electrode enables exploration of the potential-driven fluorescence response on various crystallographic surfaces. Two MCH-DNA SAMs are characterized: a MCH-ssDNA-AlexaFluor647 SAM and a MCH-dsDNA-AlexaFluor647 SAM. Note that both SAMs were assembled by direct adsorption from solution, with no hybridization or dehybridization performed on the surface, and the dsDNA was formed in solution before being deposited onto the electrode. In addition, the measurements were conducted for as-prepared SAMs so that the possibility of intensity change due to photo-bleaching or adsorbate degradation is minimized. Thus the hybridization states of the two SAMs investigated in this section are assumed to be pure ssDNA and dsDNA.

Figure 6.9 shows the fluorescence images for the MCH-ssDNA-AlexaFluor647 SAM and the MCH-dsDNA-AlexaFluor647 SAM, both taken at −0.4 V (vs. SCE). The fluorescence pattern which correlates to the crystallographic orientation map is observed in both images, similar to the MCH-ssDNA-AlexaFluor488 SAM shown previously. The lack of some subtle structures in these fluorescence images as compared to Figure 6.7 can be rationalized by the lower DNA density and lower camera sensitivity. However, the major features are easily recognized, notably the three low-index surfaces, the cross-shape feature around (100), the high intensity
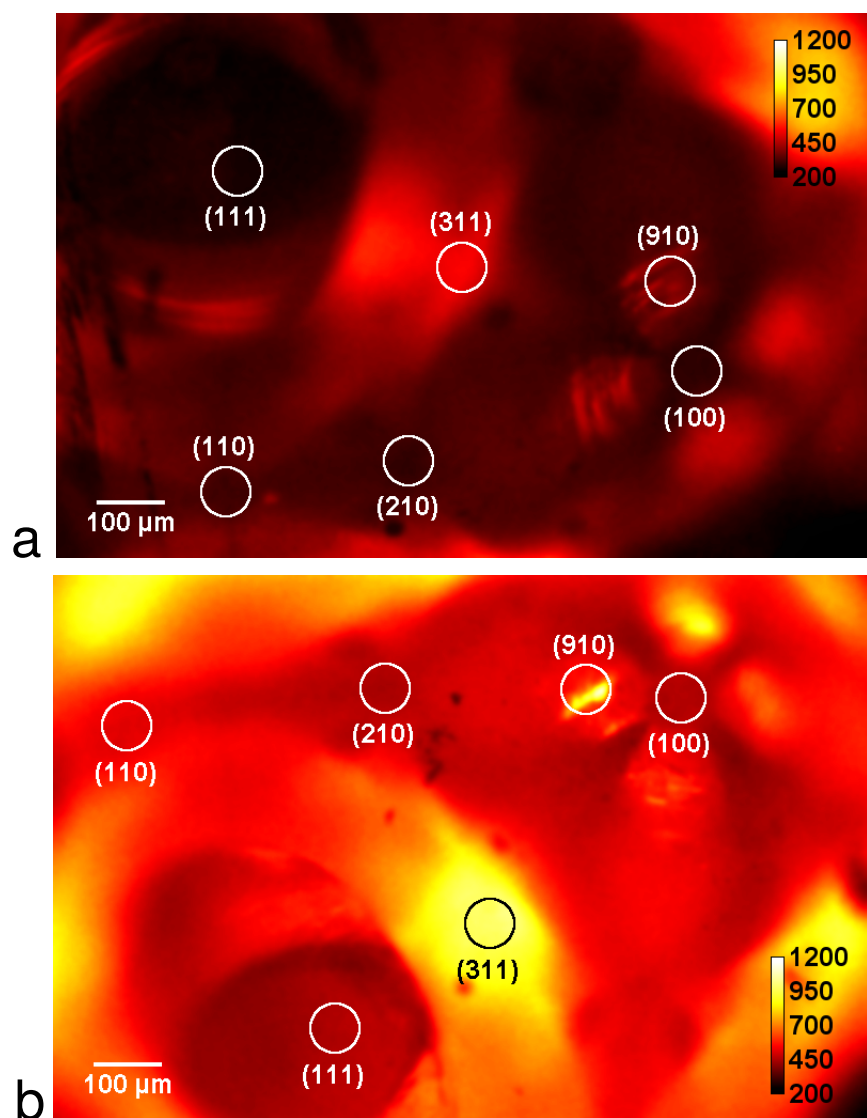
Figure 6.9: Fluorescence images: (a) a MCH-ssDNA-AlexaFluor647 SAM and (b) a MCH-dsDNA-AlexaFluor647 SAM on a single crystal Au bead electrode captured at −0.4 V (vs. SCE). A variety of ROIs with their assigned crystallographic orientations are marked on the images.

(311) surface and the low intensity (210) surface. Several ROIs are selected based on these features for further analysis and marked in both fluorescence images (the (910) surface is generally referring to one arm of the cross-shape around the (100) surface). The overall fluorescence intensities are evidently different for the two SAMs in that the dsDNA SAM has a significantly higher intensity than the ssDNA SAM. This is similar to reported results where an increase of fluorescence intensity was observed when a ssDNA SAM was hybridized with the complementary strand, due to the conversion of the DNA adsorbate from a flexible curly chain to a rigid extended rod [54, 226].

When the potential steps profiled in Figure 6.10a are applied, the fluorescence intensity alternates in response due to DNA reorientation. The average fluorescence change measured from a selected ROI inside a (111) facet (marked in Figure 6.9) is shown for the MCH-ssDNA SAM and the MCH-dsDNA SAM in Figure 6.10b and Figure 6.10c, respectively. These data are also shown as the fluorescence intensity as a function of step potential (Figure 6.11). As expected, the overall intensity of the MCH-ssDNA SAM is lower than that of the MCH-dsDNA SAM. In addition, the MCH-dsDNA SAM has a significantly larger change in fluorescence during a reorientation process. The increase in magnitude of fluorescence response upon hybridization was reported previously and was used in DNA detection [54, 226]. Higher sensitivity was achieved by using longer DNA strand since a much larger change in fluorophore-metal separation is possible for the rigid dsDNA [54]. However, the absolute intensity cannot be used to determine the hybridization state. Different samples of the same hybridization state or even the same sample measured on different days could have different static intensities. Photobleaching is one major reason for intensity variation. Technically, the fluorescence illumination and collection efficiency on a particular ROI and the background intensity (which is not easy to determine for a curved surface covered with a fluorescent SAM) are strongly dependent on the orientation of this curved electrode surface, which also contributes to intensity variation.

The potential-driven fluorescence response measured from selected ROIs ((100), (910) and (311)) highlighted in Figure 6.9 are analyzed and shown in Figure 6.12. On the (111) surface studied above, it is evident that the dsDNA SAM has a larger magnitude of fluorescence reponse than the ssDNA at negative potentials, which is not necessarily observed on the other surfaces. On the (100), (910) and (311) surfaces, the difference in magnitude is insignificant. Considering
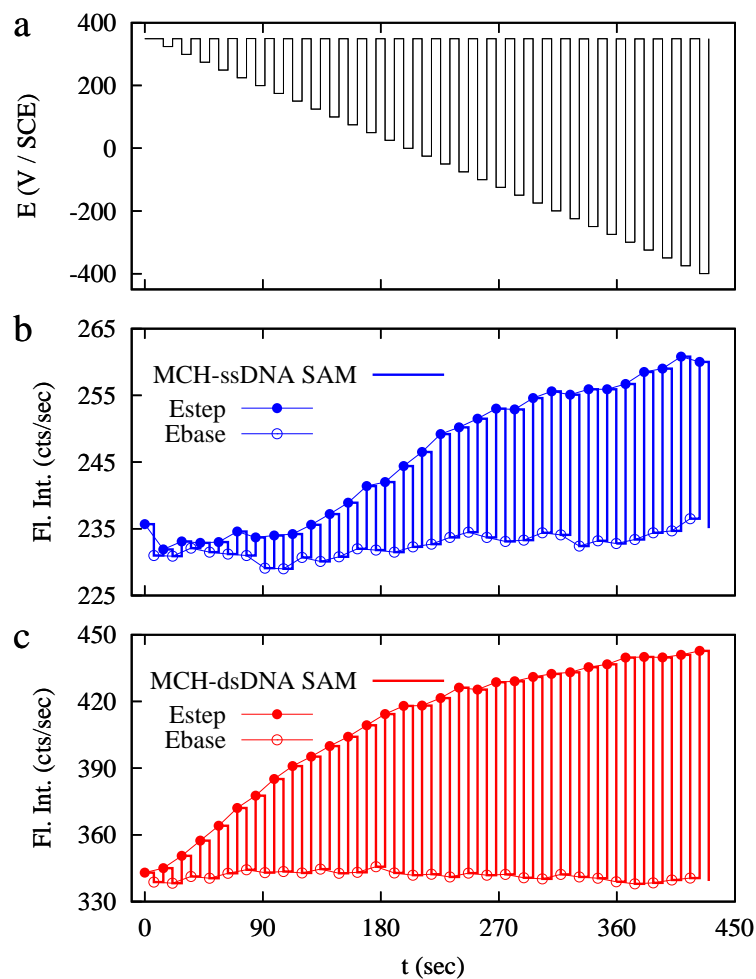
Figure 6.10: The potential-driven fluorescence response of a ROI inside a Au(111) facet (marked in Figure 6.9) for a MCH-ssDNA-AlexaFluor647 SAM and a MCH-dsDNA-AlexaFluor647 SAM: (a) the profile of potential steps applied to drive the DNA reorientation; (b) the fluorescence response of MCH-ssDNA-AlexaFluor647 SAM; (c) the fluorescence response of MCH-ssDNA-AlexaFluor647 SAM. The intensities at the step potentials (Estep) and the based potentials (Ebase) are marked with filled circle and open circles, respectively.
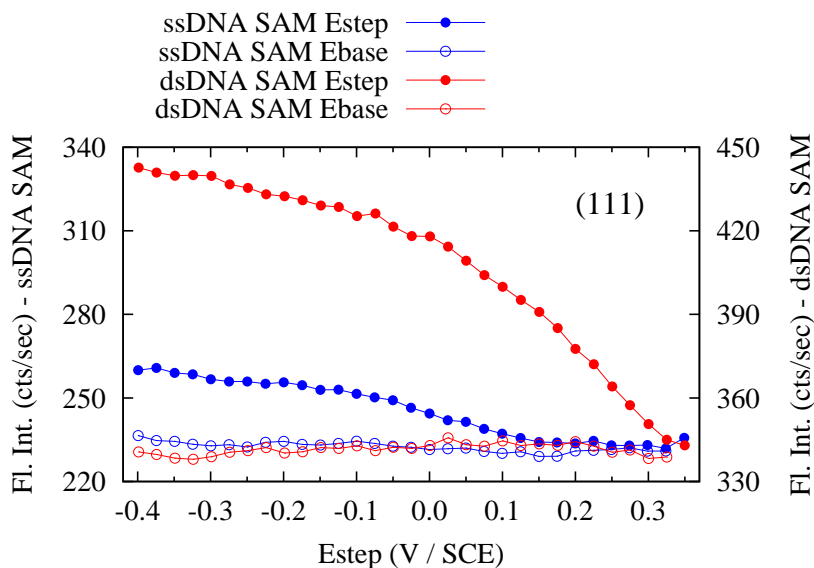
Figure 6.11: The fluorescence intensity as a function of step potential of a ROI inside a Au(111) facet (marked in Figure 6.9) for a MCH-ssDNA-AlexaFluor647 SAM (y-axis on the left) and a MCH-dsDNA-AlexaFluor647 SAM (y-axis on the right). Estep is a particular step potential and Ebase is the base potential 0.35 V (vs. SCE) before stepping to corresponding step potential.

the different reorientation mechanism for ssDNA and dsDNA described in [227] (as reviewed in Section 6.2), it might be reasonable to assume that ssDNA which reorients segment by segment requires less space whereas dsDNA which rotates about the anchor point requires more space. Depending on the DNA density, the dsDNA SAM might not be able to reorient completely.

Therefore, this potential-driven fluorescence response can be influenced by numerous factors, including the density of DNA, the molecular conformation and the surface crystallography. Moreover, inconsistent results have been obtained from newly prepared SAMs and SAMs after measurements presumably due to photo-bleaching of the fluorophore. From the sensing point of view, detection of DNA purely based on the change in fluorescence intensity and magnitude of fluorescence response may not be reliable unless all the conditions are properly controlled.
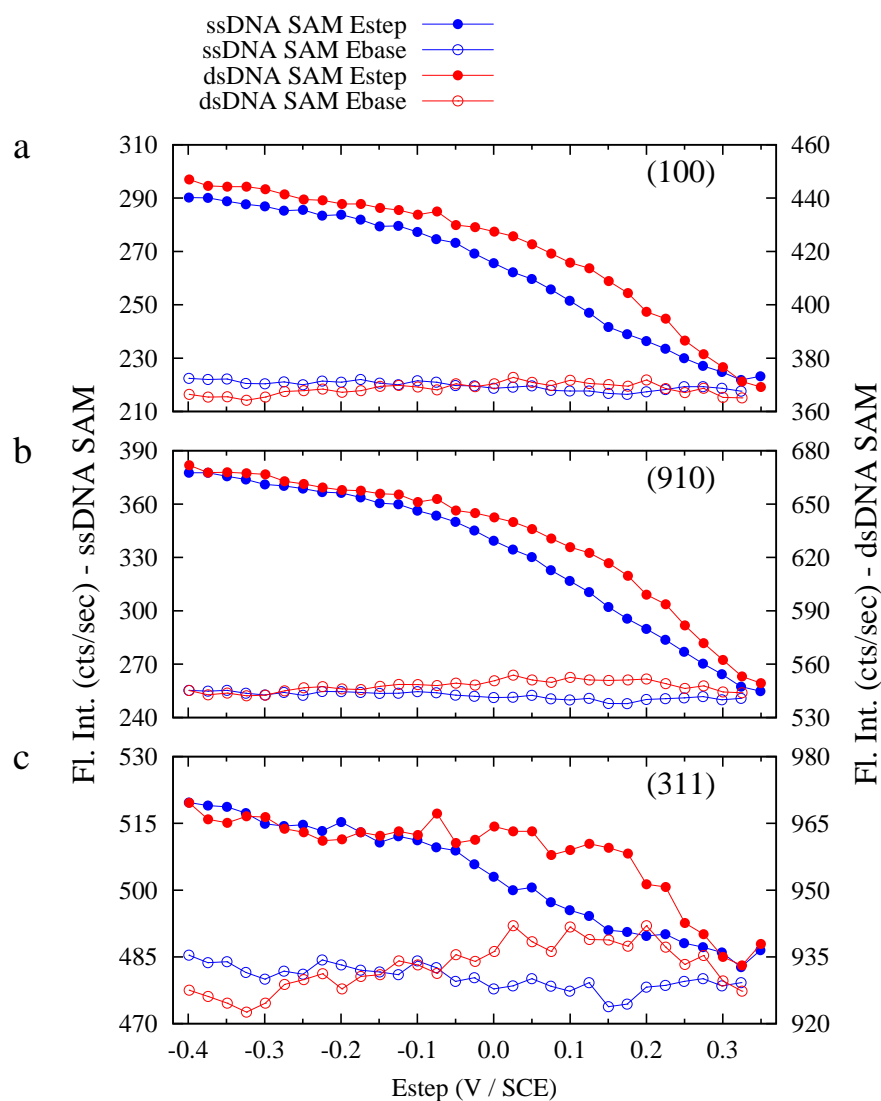
Figure 6.12: The fluorescence intensity as a function of step potential measured on ROIs from (a) (100) surface, (b) (910) surface and (c) (311) surface (marked in Figure 6.9) for a MCH-ssDNA-AlexaFluor647 SAM and a MCH-dsDNA-AlexaFluor647 SAM.

6.6.3 Harmonic analysis of the nonlinear fluorescence response in DNA reorientation

Development of a harmonic analysis technique for measuring the nonlinear fluorescence response driven by an AC potential perturbation

The imaging technique presented has limitations in sensitivity and speed. The fluorescence response driven by the potential steps is a low frequency signal typically accompanied by a large amount of 1/f noise [257]. In order to achieve a higher signal-to-noise ratio, an AC potential perturbation is employed to induce a fluorescence response of higher frequency. The DNA reorientation-based biosensing platforms implemented by Rant et al. are mainly applying the frequency-resolved or the time-resolved AC techniques [7, 54, 55, 57]. These measurements tend to be long and setups can be quite complicated and expensive. In this section, a different approach, namely, the nonlinear fluorescence response of DNA reorientation is analyzed to gain a better understanding and develop a harmonic analysis technique for DNA detection.

The nonlinear fluorescence response expected can be intuitively illustrated with Figure 6.11 where the fluorescence intensity is non-linearly related the step potential. As discussed in Section 6.3, when a sinusoidal potential wave is applied, the nonlinear response function results in harmonics in the fluorescence signal. Moreover, since the ssDNA SAM and the dsDNA SAM each follows a distinctive nonlinear function (in simple words, the shapes of the *F-E* curves are different), the amplitudes of the corresponding harmonics should be different and can be used in distinguishing the hybridization states. Below, the fluorescence response from the (111) surface will be taken as an example to demonstrate the harmonic analysis of the resultant nonlinear fluorescence signal.

The fluorescence intensity from a small ROI inside a (111) facet was first measured with a PMT during a linear potential scan. A $40\times$ water immersion objective was used to increase the optical efficiency. In addition, the field diaphragm was reduced so that a small region was illuminated, excluding signals from other regions. Figure 6.13 shows the current and fluorescence intensity measured during potential scanning for the MCH-ssDNA-AlexaFluor647 SAM and MCH-dsDNA-AlexaFluor647 SAM investigated in last section. The cyclic voltammograms are typical for SAM-solution interfaces devoid of redox reactions that can be modeled as resis-
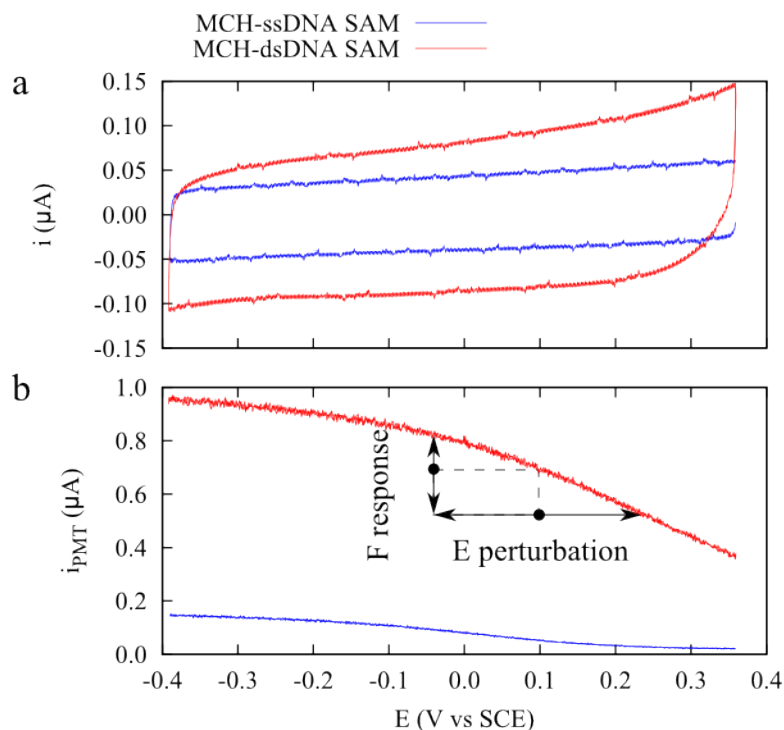
Figure 6.13: (a) Cyclic voltammograms of a MCH-ssDNA-AlexaFluor647 SAM and a MCH-dsDNA-AlexaFluor647 SAM and (b) fluorescence intensity of the two SAMs measured with potential scanning from a ROI inside a (111) facet. The arrows in (b) depict the oscillation directions of the AC potential perturbation and the fluorescence response.

tor–capacitor (RC) circuits. Different magnitudes of capacitive current are observed for the two SAMs because the immersed electrode areas were different. A RC circuit is a linear system [258], so the current response driven by an AC potential potential perturbation only contains the first harmonic of fundamental frequency. However, in the case of DNA SAMs, the optical response is nonlinear within the potential range scanned. As depicted in Figure 6.13b, an AC potential is applied at a constant DC potential. Depending on this DC potential and on the amplitude of the perturbation, the fluorescence response can be linear or nonlinear. Typically, in electrochemical techniques (e.g., AC voltammetry, electrochemical impedance spectroscopy), the amplitude of the AC potential perturbation is small to ensure that the response stays linear and thereby the equivalent circuit analysis of the system is valid [255, 259–261]. Applying a large amplitude potential perturbation to study the nonlinear electrochemical response is being used more often [262–265]. In this section, a large amplitude potential perturbation (e.g., 100 mV rms) is applied to induce the nonlinear fluorescence response. More importantly, for
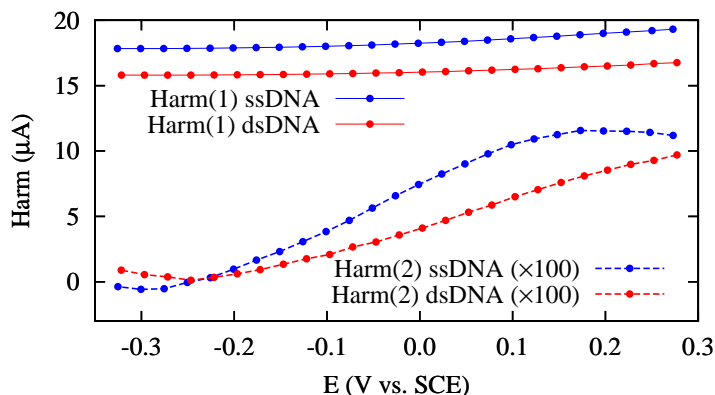
Figure 6.14: Amplitudes of the first harmonic (solid line) and second harmonic (dashed line) signals of the current response driven by 50 mV rms potential perturbation at a series of DC potentials from 0.275 V (vs. SCE) to -0.35 V (vs. SCE) for the MCH-ssDNA SAM and (blue) the MCH-dsDNA SAM (red).

this RC-like system, even with this large amplitude, the current response remains linear. Figure 6.14 shows the amplitude of the first and second harmonics of the electrochemical current driven by 50 mV rms perturbation. The response is essentially linear, with <1% in the second harmonic. Therefore the nonlinear nature of the fluorescence response is driven by a linear electrochemical perturbation.

Figure 6.15 shows the amplitudes of the first (a), second (b) and third (c) harmonics of the fluorescence response driven by 100 mV rms perturbation at a series of DC potentials from 0.2 V (vs. SCE) to -0.25 V (vs. SCE) for the MCH-ssDNA SAM and the MCH-dsDNA SAM. These harmonic measurements were conducted after the potential scanning measurements, on the same (111) ROI as in Figure 6.13. The fluorescence modulation was measured with the PMT and analyzed by the lock-in amplifier.

Clear differences are observed between the ssDNA SAM and the dsDNA SAM in first and second harmonic signals. According to Equation 6.6, the amplitude of the nth harmonic is proportional to the nth derivative of the fluorescence response function. Intuitively, the first harmonic informs on the slope of fluorescence response function at a particular DC potential while the second harmonic is indicative of the curvature at this DC potential. At the negative limit of DC potential, both first and second harmonic amplitudes for the two SAMs converge. This can be explained by a lack of fluorescence intensity oscillation at negative DC potentials because the DNA strands are at the most extended orientation (not necessarily perpendicular to the sur-
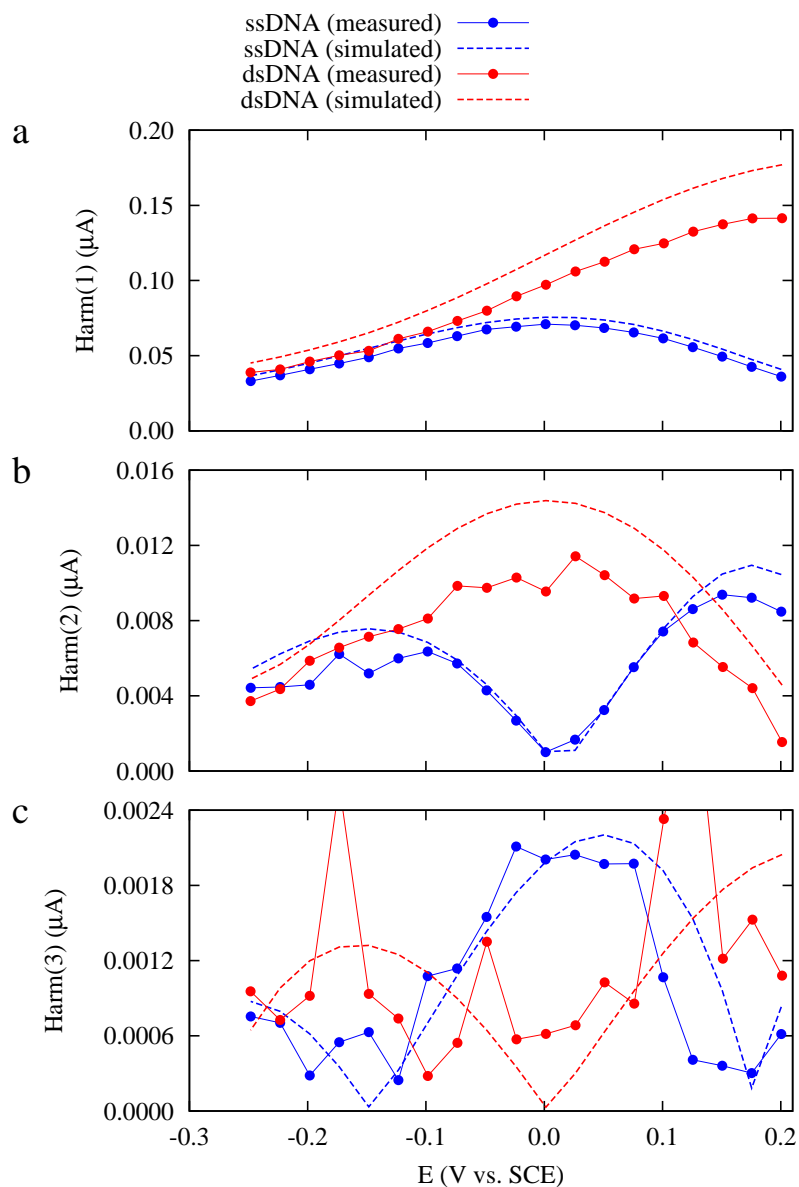
Figure 6.15: Measured and simulated amplitudes of the harmonics of the fluorescence response from a (111) featured ROI driven by 100 mV rms perturbation at a series of DC potentials from 0.2 V (vs. SCE) to -0.25 V (vs. SCE) for the MCH-ssDNA SAM and (blue) the MCH-dsDNA SAM (red): (a) first harmonic, (b) second harmonic and (c) third harmonic.

face). At 0 V (vs. SCE), the first harmonic of the ssDNA SAM reaches a maximum which also corresponds to a minimum in the second harmonic, indicating a drastic change in the shape of the fluorescence response at this potential. The potential where the second harmonic intensity reaches minimum ($E_{\text{H(2)min}}$) has some similarity to the potential of conformation transition (PCT) [228]. However, the definition of PCT is quite ambiguous in that a DNA strand does not change its orientation from lying down to standing up (or vice versa) immediately at a particular potential, but over a range of potentials as observed in Figure 6.13b. A maximum in the first harmonic and a minimum in the second harmonic are observed at a potential slightly more positive than 0.2 V (vs. SCE) for the dsDNA SAM. In other words, the dsDNA SAM has a more positive $E_{\text{H(2)min}}$ than the ssDNA SAM. The difference in $E_{\text{H(2)min}}$ is intriguing because this can be applied in DNA sensing, but measuring the $E_{\text{H(2)min}}$ using harmonic analysis is probably not convenient. Monitoring the change in the amplitude of a harmonic (e.g., the second harmonic) at a constant DC potential (e.g., 0 V (vs. SCE)) upon capturing of a DNA strand might be more practical and feasible.

Since the frequency used is well within the charging time of the interface, the intensity-potential curve (Figure 6.13b) could be used to simulate the AC measurements. An Octave script was used to model the potential scanning fluorescence response as a nonlinear function. The AC fluorescence response was determined based on this nonlinear function for each DC potential. The harmonic responses of these fluorescence signals at different DC potentials were calculated using Fourier transform analysis. The simulated amplitudes of the first, second and third harmonics of the fluorescence response are presented in Figure 6.15 as dashed lines. Overall, the experimental results match the simulated results especially for the ssDNA SAM. The discrepancy shown in the dsDNA results was most likely caused by a change in lamp intensity occurring between the potential scanning measurement and the harmonic measurements. There exists some agreement between the experimental and the simulated results for the third harmonic suggesting that this signal is similar to noise. Increasing the amplitude of the AC potential perturbation (limited by the potential range within which the SAM is stable) may allow detection of the third harmonic more accurately, but higher harmonics may be challenging.

Normalization of the harmonic singal with a reference signal measured simultaneously is needed to account for the intensity variation due to lamp intensity drift, photo-bleaching or a
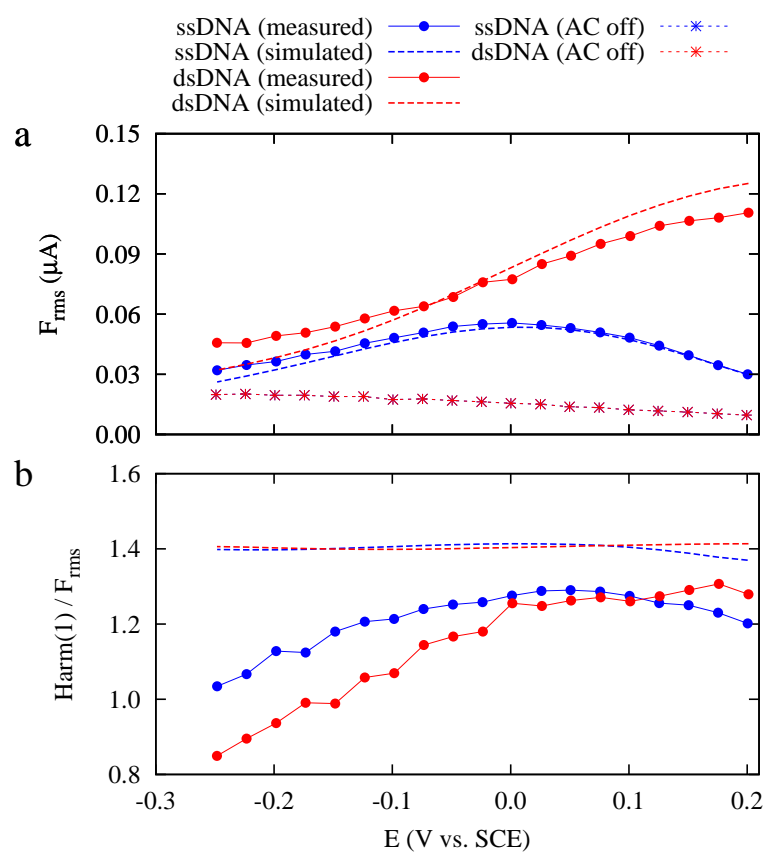
Figure 6.16: Comparison of measured and simulated: (a) rms fluorescence intensity and (b) ratio of the first harmonic amplitude over the rms fluorescence intensity.

change in photon collection efficiency between different samples. For an AC signal, the rms intensity is a plausible reference. However, at the moment, accurate measurements of the rms fluorescence intensity cannot be achieved with the present setup due to undetermined noise limitation. As shown in Figure 6.16a, the rms fluorescence intensity is underestimated at positive positive potentials for the dsDNA SAM and overestimated at negative potentials for both SAMs. The overestimation at the positive potential for the dsDNA SAM was probably due to the lamp intensity drift, similar to difference between the measured and calculated results in the harmonics (Figure 6.15). Besides the lamp intensity drift, an unknown source of noise which is more prominent with increasing intensity is present in the system and clearly observed when the potential perturbation was turned off as shown in Figure 6.16a. According to Figure 6.16b, the simulated ratio of the first harmonic amplitude over the rms fluorescence intensity is a constant (~1.4). This is reasonable considering the fluorescence signal is dominated by the first harmonic and the ratio of center-to-peak amplitude and the rms amplitude for a sine wave is $\sqrt{2}$. Experimentally, at positive potentials the measured ratio is slightly smaller than $\sqrt{2}$ but acceptable. However, a large deviation is observed at negative potentials where the fluorescence oscillation due to DNA orientation is small and contaminated by the noise. Therefore, normalizing the results using the rms fluorescence intensity is not yet reliable. An alternative is to use the first harmonic amplitude for normalization. As a phase-sensitive detector, the lock-in amplifier is only sensitive to a signal with the frequency of interest, so the first harmonic amplitude should be more reliable as it will not be contaminated by the noise which is assumed to be smaller than the measured bandwidth. Strictly speaking, the first harmonic is not an ideal reference simply because different harmonics were measured at different times. Since a harmonic measurement was fast, it is assumed that the first harmonic and the second harmonic were measured under the same conditions.

Measuring the normalized second harmonic response for different crystallographic surfaces

The harmonic analysis of the potential-driven fluorescence response for a MCH-ssDNA SAM and a MCH-dsDNA SAM has been demonstrated. A MCH-DNA SAM prepared by treating a
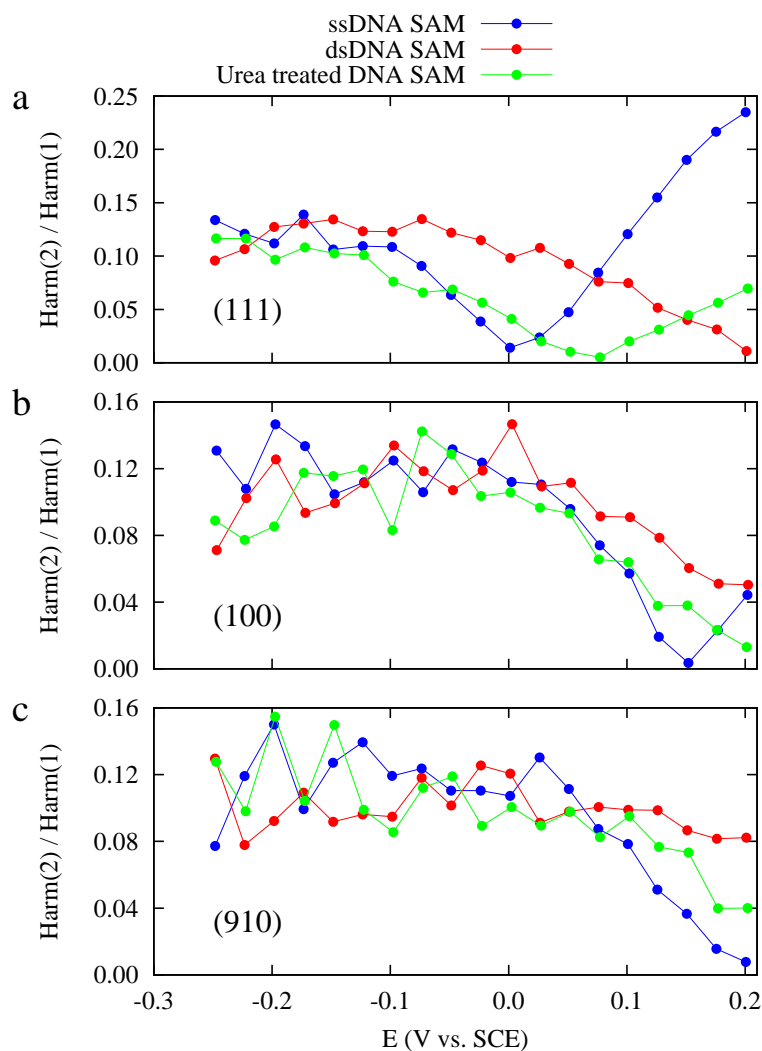
Figure 6.17: Second harmonic amplitude normalized with first harmonic amplitude as a function of DC potential for a MCH-ssDNA SAM SAM, a MCH-dsDNA SAM and a urea treated MCH-DNA SAM measured from three ROIs: (a) a (111) ROI, (b) a (100) ROI and (c) a (910) ROI.

MCH-dsDNA SAM with 8 M urea solution for 2 min was also studied with the harmonic analysis technique. Figure 6.17 shows the normalized second harmonic amplitude as a function of DC potential for the three DNA SAMs. The harmonic analysis technique was performed on three ROIs (a (111) ROI (a), a (100) ROI (b) and a (910) ROI (c)) to study the influence of surface crystallography on the fluorescence response.

The normalized second harmonic intensity for the two SAMs for the (111) surface (Figure 6.17a) not only converge, but also approach a constant at positive potentials, demonstrating the lack of intensity oscillation and reliability of the normalization. The two SAMs started to

show a difference in the normalized second harmonic intensity at ~0.05 V (vs. SCE). A fast decrease is observed for the ssDNA SAM, reaching a minimum of ~0 at ~0 V (vs. SCE). This corresponds to the largest slope and smallest curvature in the fluorescence-potential function. In contrast, the normalized second harmonic intensity for the dsDNA SAM gradually decreases over the potential range with a minimum at ~0.2 V (vs. SCE). As a comparison, the second harmonic response for the urea treated DNA SAM falls between the ssDNA SAM and the ds-DNA SAM. To be specific, the urea treated DNA SAM has the similar response as the other two SAMs at positive potentials and its minimum second harmonic intensity is observed at ~0.08 V (vs. SCE), between those for the other two SAMs. This suggests the short urea treatment at room temperature might result in a surface covered with a mixture of ssDNA and dsDNA. More importantly, it might be possible to detect DNA binding by monitoring the change in normalized second harmonic amplitude at 0 V or at 0.2 V. In addition, a larger amplitude potential perturbation can be applied to increase the sensitivity, but this is only applicable to detection at 0 V. However, a series of DNA SAMs with different hybridization states need to be analyzed to test the feasibility of this DNA sensing mechanism.

The harmonic responses from the (100) surface (Figure 6.17b) and the (910) surface (Figure 6.17c) are similar to each other, but are different from that measured on a (111) surface. The most evident difference is the minimum second harmonic intensity of a SAM, which is observed at more positive potentials on (100) or (910) surfaces as compared to the same SAM on a (111) surface. This difference reflects the different shapes of fluorescence-potential functions on these crystallographic surfaces. Considering the (910) surface is featured with large (100) terraces, DNA strands adsorbed on (100) and (910) surfaces might organize in a similar structure, which explains the similar harmonic responses. On the other hand, the DNA packing structure on (111) surface might be significantly different from that on (100) and (910) surfaces, resulting in the distinctive harmonic response. Different hybridization states (ssDNA, dsDNA and a mixture of ssDNA and dsDNA) can be also distinguished based on the normalized second harmonic amplitude on (100) and (910) surfaces, but only at a potential close to the positive limit of the stable DC potential (e.g., 0.15 V (vs. SCE)), which excludes the possibility of increasing the amplitude of the potential perturbation. Therefore, to develop a DNA sensing platform based on this harmonic analysis technique, substrates with a greater percentage of

(111) surface would be preferred.

6.7 Conclusions

The MCH-DNA-AlexaFluor SAMs were assembled on the single crystal Au bead electrode by thiol-exchange mechanism. The fluorescence image of a typical MCH-DNA SAM showed a high heterogeneity which correlates to the map of crystallographic orientations, demonstrating the influence of the surface crystallography on formation of a DNA SAM via the thiol-exchange mechanism. Moreover, in situ fluorescence imaging was employed to study the potential-driven DNA reorientation for a MCH-ssDNA SAM and a MCH-dsDNA SAM. It was found that potential-driven fluorescence response measured with the imaging technique could be influenced by numerous factors. Thus, the fluorescence intensity and the magnitude of fluorescence response are not reliable criteria in determining the hybridization state of the DNA SAM.

A harmonic analysis technique has been developed to measure the non-linearity of the fluorescence response driven by AC potential perturbation with a lock-in amplifier. There was a minimum intensity observed in the second harmonic response as a function of DC potential. This minimum in the second harmonic intensity for a dsDNA SAM occurred at more positive potentials than that for a ssDNA SAM, which may be useful in distinguishing the hybridization states.DNA binding may be possibly detected by monitoring the change in second harmonic intensity. Different harmonic responses were observed from different crystallographic surfaces. A surface with significant fraction of (111) character would be preferred for developing a DNA sensing platform based on this harmonic analysis technique.

Chapter 7

Concluding remarks

7.1 Summary

Functionalization of a metal surface with self-assembled monolayers has been routinely used in constructing biosensing interfaces with desirable performance [2, 3, 5, 6]. The basic components of a SAM are the substrate and the adsorbate. Naturally, in order to optimize the performance of a SAM-based biosensor, it is necessary to investigate and tune the properties of both the substrate and the adsorbate. In electrochemical biosensors, a metal substrate is used and therefore an important aspect to study is the influence of the surface crystallography on the SAM. Traditionally, research related to this subject involved depositing a number of SAMs on a series of electrodes with one designated crystallographic orientation [9–12]. Two major disadvantages arose in the copious experiments on these electrodes: a lack of reproducibility due to the variation in experimental conditions and a limitation in the crystallographic orientations studied. To overcome these disadvantages, a single crystal electrode was used throughout the experimental works presented in this thesis. With this electrode, identifiable crystallographic orientations were investigated under the same conditions, achieving self-consistent analyses.

Three types of SAMs based on the Au-S interaction were investigated: AuS-C10-BODIPY SAMs, AuS-Aib4-BODIPY SAMs, and MCH-DNA-AlexaFluor SAMs formed by the thiol-exchange mechanism, demonstrating the utility of the single crystal Au bead electrode in the research area of surface modification and characterization. The behavior of the SAMs was manipulated by electrochemical methods. Visualization of the fluorophore-labeled SAMs on different crystallographic domains on the electrode was achieved with fluorescence microscopic techniques. The coupled spectroelectrochemical techniques enables in-depth investigation of the SAMs assembled on the single crystal Au bead electrode in an efficient and effective way useful for

exploring the influence of surface crystallography on the SAMs.

The use of the single crystal Au bead electrode was first demonstrated by characterizing the reductive desorption behavior of AuS-C10-BODIPY SAMs and AuS-Aib4-BODIPY SAMs assembled on this electrode with in situ fluorescence imaging. Reductive desorption maps created by detailed imaging analysis showed a strong correlation to the d_{bb} (as the surrogate for PZC) map of the surface. However, numerous differences were observed between different types of SAMs as well as between the reductive desorption and d_{bb} (or PZC), suggesting the influence of intermolecular interaction on the reductive desorption. The results might inspire in-depth investigation of SAMs on a number of stepped or kinked surfaces showing interesting properties but rarely studied. As an example, the desorption potential on surfaces with a large (100) terrace was similar to that on (100) surface for a AuS-C10-BODIPY SAM but notably different for a AuS-Aib4-BODIPY SAM. This might be an indication of the footprint of the adsorbates or the effective distance of intermolecular interaction, which are important in controlling the packing density of the adsorbate.

AuS-Aib4-BODIPY SAMs were further studied with the single crystal Au bead electrode because of their intriguing properties. The two-step reductive desorption on a (111) surface might result from the intermolecular hydrogen bond network, which helps stabilize and organize the Aib peptide SAMs even when desorbed. Since the conventional alkanethiol SAMs do not have such unique intermolecular interaction, it could be beneficial to create highly robust and ordered SAMs with Aib peptides and further apply them in constructing biosensing platforms. In addition, it was found that the orientation or structure of low packing density AuS-Aib4-BODIPY SAMs on a (111) surface could be manipulated with potential, attributed to response of the helix-induced dipole moment to electric field. Although this property was not observed on high packing density SAMs, it could be potentially applicable in a nano-scale system or useful in developing a potential-controlled molecular switch.

Spectroelectrochemical characterization of MCH-DNA-AlexaFluor SAMs focused on investigating the potential-driven reorientation behavior which is useful in biosensing. A significant amount of heterogeneity was observed on the fluorescence image from a MCH-DNA SAM formed via thiol-exchange mechanism, which strongly correlates to the surface crystallography. This heterogeneity enabled exploring the potential-driven reorientation of the DNA SAM on

identified crystallographic surfaces. However, the changes in fluorescence intensity and magnitude of potential-driven fluorescence response detected by fluorescence imaging were not reliable in distinguishing the hybridization states of a MCH-DNA SAM. In an attempt to deepen the understanding of the DNA reorientation and to develop a new sensing mechanism, a harmonic analysis technique was employed to measure the harmonic response of the alternating fluorescence signal driven by an AC potential perturbation for MCH-DNA SAMs of different hybridization states. A minimum in the second harmonic response was observed at a DC potential which was dependent on the hybridization state of a SAM, so measuring the change in second harmonic response can be used in DNA detection. Compared with other reported DNA detection techniques based on the potential-driven DNA reorientation [7, 54, 55, 57], the sensing mechanism proposed here is probably easy and inexpensive to implement. Different harmonic responses were observed from (111), (100) and (910) surfaces, giving insight into selection of a proper substrate for a biosensing interface. Although it was found that the (111) surface was suitable for such a substrate, there are still a number of identifiable crystallographic surfaces on the single crystal Au bead electrode yet to explore, from which a better one might be found. Typically in actual biosensing, vapor-deposited polycrystalline Au substrates are widely used. On this type Au surface, there should be Au(111) domains which are favorable for sensing and other regions of varied crystallographic structures. More importantly, this flat surface can be easily indexed to identify the crystallographic domains. Thus the results obtained these studies using a single crystal Au bead electrode can be borrowed to optimize the surface preparation for biosensing.

Overall, the single crystal Au bead electrode provides a valuable platform to conduct researches on SAMs. With the spectroelectrochemical techniques discussed, a large number of physical or chemical behaviors dependent on the surface crystallography can be visualized, measured or controlled, guiding future studies on SAMs. As a long-term goal, the findings obtained by employing the single crystal electrode can make contribution to rationally developing biosensing interfaces with desirable performance.

7.2 Future work

A variety of investigations can be conducted as an optimization or an extension of the work presented in this thesis. The general ideas are outlined here without the attempt to demonstrate the feasibility.

7.2.1 Optimization of the single crystal Au bead electrode

The single crystal Au bead electrode used throughout the experimental studies was fabricated simply by flame melting. The conditions (e.g., the temperature, the cooling rate, the angle of heating, etc.) were not well-controlled. Therefore, the size, the crystalline state (complete single crystal or bi-crystal), and orientation (e.g., the locations of the crystallographyc surfaces with respect to the bead growing direction) of the electrode could not be controlled. Fabrication of single crystal bead electrode using electron beam heating or direct current heating was reported [202, 203], which gave better control over the conditions and thus reproducible single crystal bead electrodes with high quality. Thus, it would be rewarding to apply these methods to fabricate single crystal Au bead electrodes for future studies.

7.2.2 Further explorations of the thiolate-terminated Aib peptide SAMs

The length of a Aib peptide adsorbate and the direction of the dipole moment have strong influences on the physical and chemical properties, which in turn affect the electrochemical response of this Aib peptide SAM [210, 211, 218, 222]. To gain a better understanding of the potential-controlled response of the thiolate-terminated Aib peptide SAMs, Aib peptides of various lengths and the opposite dipole moment should be systematically studied. Moreover, it would also be valuable to investigate the influence of surface crystallography on the potential-controlled response. Longer Aib peptides would be preferred, lessening the fluorescence quenching.

7.2.3 Further explorations of the MCH-DNA SAMs

The DNA detection mechanism based on harmonic analysis of the AC potential-driven fluorescence response of a DNA SAM was proposed in Chapter 6. This mechanism requires further tests with MCH-DNA SAMs of a series of hybridization states to determine its feasibility, sensitivity and selectivity. In addition, the DNA length is expected to have a profound influence on the potential-driven fluorescence response. On one hand, a longer DNA strand leads to an increase in intensity, but on the other hand, it might also result in a change in the fluorescence-potential function and the harmonic response. Therefore, it would be necessary to investigate the harmonic responses for SAMs formed with various DNA lengths. Moreover, although the minimum second harmonic intensity can be correlated to the sharpest change in the fluorescence-potential function, it is still not clear about the corresponding orientation or structure of the DNA. Electrochemical atomic force microscopy (EC-AFM) would be useful in providing structural information for a DNA SAM at the DC potential at which the second harmonic intensity is minimum. Furthermore, the sensing target is not necessarily limited to the complementary strand, it would be important to test the applicability of the harmonic analysis technique in detection of other types of bio-molecules such as proteins.

7.2.4 Development of new spectroelectrochemical techniques

The fluorescence microscopic characterization presented in this thesis was mainly based on measuring the intensity of fluorescence, where the density of fluorophore and the fluorophore-metal separation are convoluted. It would be important to develop new techniques to investigate these two factors separately in order to understand different properties on a SAM. Spectroscopic methods based on FRET inform on the distance between a donor fluorophore and an acceptor fluorophore. If a SAM is labeled with an evenly distributed mixture of a FRET pair, the experimentally determined FRET efficiency should indicate the average lateral adsorbate separation. It would be beneficial to investigate the change in FRET efficiency as a function of potential for Aib peptide SAMs or DNA SAMs which might provide information on structural changes driven by an applied potential. Fluorescence-lifetime imaging microscopy (FLIM) is a useful technique to measure the fluorophore-metal separation [169]. Thus characterizing the

potential-driven DNA reorientation using FLIM coupled with electrochemistry would be reward-
ing in fundamentally exploring the change in orientation with potential, especially on different
crystallographic surfaces.

References

[1] Grieshaber, D.; MacKenzie, R.; Voros, J.; Reimhult, E. *Sensors* **2008**, *8*, 1400–1458.

[2] Wink, T.; J. van Zuilen, S.; Bult, A.; P. van Bennekom, W. *Analyst* **1997**, *122*, 43R–50R.

[3] Chaki, N. K.; Vijayamohanan, K. *Biosens. Bioelectron.* **2002**, *17*, 1–12.

[4] Love, J. C.; Estroff, L. A.; Kriebel, J. K.; Nuzzo, R. G.; Whitesides, G. M. *Chem. Rev.* **2005**, *105*, 1103–1170.

[5] North, S. H.; Lock, E. H.; Taitt, C. R.; Walton, S. G. *Anal. Bioanal.Chem.* **2010**, *397*, 925–933.

[6] Gooding, J. J.; Darwish, N. *Chem. Rec.* **2012**, *12*, 92–105.

[7] Rant, U. *Bioanal. Rev* **2012**, *4*, 97–114.

[8] Yu, Z. L.; Casanova-Moreno, J.; Guryanov, I.; Maran, F.; Bizzotto, D. *J. Am. Chem. Soc.* **2015**, *137*, 276–288.

[9] Lipkowski, J.; Stolberg, L.; Yang, D.-F.; Pettinger, B.; Mirwald, S.; Henglein, F.; Kolb, D. *Electrochim. Acta* **1994**, *39*, 1045–1056.

[10] Yang, D.-F.; Wilde, C. P.; ; Morin, M. *Langmuir* **1996**, *12*, 6570–6577.

[11] Zhong, C.-J.; Zak, J.; Porter, M. D. *J. Electroanal. Chem.* **1997**, *421*, 9–13.

[12] Doneux, T.; Steichen, M.; Rache, A. D.; Buess-Herman, C. *J. Electroanal. Chem.* **2010**, *649*, 164–170.

[13] Bard, A. J.; Faulkner, L. R. *Electrochemical methods: fundamentals and applications*; John Wiley & Sons, Inc., 2001.

[14] Lipson, A.; S. G. Lipson, H.; Lipson, *Optical Physics - Fourth Edition*; Cambridge University Press, 2011.

[15] Hermann, K. *Crystallography and Surface Structure: An Introduction for Surface Scientists and Nanoscientists*; Wiley-VCH Verlag GmbH & Co. KGaA, 2011.

[16] Schwarzenbach, D. *Crystallography*; John Wiley & Sons, Inc., 1996.

[17] Borchardt-Ott, W. *Crystallography: An Introduction*; Springer Berlin Heidelberg, 2011.

[18] Hazen, R. M.; Sholl, D. S. *Nat. Mater.* **2003**, *2*, 367–374.

[19] Gellman, A. J.; Horvath, J. D.; Buelow, M. T. *J. Mol. Catal. A: Chem.* **2001**, *167*, 3–11.

[20] Gellman, A. J. *ACS Nano* **2010**, *4*, 5–10.

[21] Lang, B.; Joyner, R.; Somorjai, G. *Surf. Sci.* **1972**, *30*, 454–474.

[22] Van Hove, M.; Somorjai, G. *Surf. Sci.* **1980**, *92*, 489–518.

[23] Cunningham, S. L.; Chan, C. M.; Weinberg, W. H. *Phys. Rev. B* **1978**, *18*, 1537–1549.

[24] Kirschner, J.; Feder, R. *Surf. Sci.* **1979**, *79*, 176–188.

[25] Feder, R.; Kirschner, J. *Surf. Sci.* **1981**, *103*, 75–102.

[26] Noonan, J. R.; Davis, H. L. *Phys. Rev. B* **1984**, *29*, 4349–4355.

[27] Xu, M. L.; Tong, S. Y. *Phys. Rev. B* **1985**, *31*, 6332–6336.

[28] Noonan, J. R.; Davis, H. L. *J. Vac. Sci. Technol., A* **1990**, *8*, 2671–2676.

[29] Methfessel, M.; Hennig, D.; Scheffler, M. *Phys. Rev. B* **1992**, *46*, 4816–4829.

[30] Barrett, S. D.; Dhesi, S. S.; Evans, M. P.; White, R. G. *Meas. Sci. Technol.* **1993**, *4*, 114–119.

[31] Wan, J.; Fan, Y. L.; Gong, D. W.; Shen, S. G.; Fan, X. Q. *Modell. Simul. Mater. Sci. Eng.* **1999**, *7*, 189–206.

[32] Singh-Miller, N. E.; Marzari, N. *Phys. Rev. B* **2009**, *80*, 235407.

[33] Perdereau, J.; Biberian, J. P.; Rhead, G. E. *J. Phys. F: Met. Phys.* **1974**, *4*, 798–806.

[34] Van Hove, M.; Koestner, R.; Stair, P.; Bibérian, J.; Kesmodel, L.; Bartoš, I.; Somorjai, G. *Surf. Sci.* **1981**, *103*, 189–217.

[35] Robinson, I. K. *Phys. Rev. Lett.* **1983**, *50*, 1145–1148.

[36] Ercolessi, F.; Tosatti, E.; Parrinello, M. *Phys. Rev. Lett.* **1986**, *57*, 719–722.

[37] Wöll, C.; Chiang, S.; Wilson, R. J.; Lippel, P. H. *Phys. Rev. B* **1989**, *39*, 7988–7991.

[38] Barth, J. V.; Brune, H.; Ertl, G.; Behm, R. J. *Phys. Rev. B* **1990**, *42*, 9307–9318.

[39] Vlieg, E.; Robinson, I.; Kern, K. *Surf. Sci.* **1990**, *233*, 248–254.

[40] Wang, X.-Q. *Phys. Rev. Lett.* **1991**, *67*, 3547–3550.

[41] Koch, R.; Borbonus, M.; Haase, O.; Rieder, K. H. *Appl. Phys. A* **1992**, *55*, 417–429.

[42] dos Reis, D.; Negreiros, F.; de Carvalho, V.; Soares, E. *Surf. Sci.* **2010**, *604*, 568–573.

[43] Bengió, S.; Navarro, V.; González-Barrio, M. A.; Cortés, R.; Vobornik, I.; Michel, E. G.; Mascaraque, A. *Phys. Rev. B* **2012**, *86*, 045426.

[44] Gao, X.; Hamelin, A.; Weaver, M. J. *Surf. Sci.* **1992**, *274*, L588–L592.

[45] Gao, X.; Edens, G. J.; Hamelin, A.; Weaver, M. J. *Surf. Sci.* **1994**, *318*, 1–20.

[46] Van Hove, M. A.; Weinberg, W. H.; Chan, C.-M. *Low-Energy Electron Diffraction: Experiment, Theory and Surface Structure Determination*; Springer Berlin Heidelberg, 1986.

[47] Jiang, L.; McNeil, C. J.; Cooper, J. M. *J. Chem. Soc., Chem. Commun.* **1995**, 1293–1295.

[48] Willner, I.; Heleg-Shabtai, V.; Blonder, R.; Katz, E.; Tao, G.; Buckmann, A. F.; Heller, A. *J. Am. Chem. Soc.* **1996**, *118*, 10321–10322.

[49] Katz, E.; Bückmann, A. F.; Willner, I. *J. Am. Chem. Soc.* **2001**, *123*, 10752–10753.

[50] Patel, J. N.; Kaminska, B.; Gray, B.; Gates, B. D. Effect of self-assembled monolayers (SAMs) in binding glucose oxidase for electro-enzymatic glucose sensor with gold electrodes. 29th Annual International Conference of the IEEE Engineering in Medicine and Biology Society. 2007; pp 2677–2680.

[51] Anandan, V.; Gangadharan, R.; Zhang, G. *Sensors* **2009**, *9*, 1295–1305.

[52] Fan, C.; Plaxco, K. W.; Heeger, A. J. *Proc. Natl. Acad. Sci. U.S.A.* **2003**, *100*, 9134–9137.

[53] Xiao, Y.; Lai, R. Y.; Plaxco, K. W. *Nat. Protoc.* **2007**, *2*, 2705–2780.

[54] Rant, U.; Arinaga, K.; Scherer, S.; Pringsheim, E.; Fujita, S.; Yokoyama, N.; Tornow, M.; Abstreiter, G. *Proc. Natl. Acad. Sci. U.S.A.* **2007**, *104*, 17364–17369.

[55] Rant, U.; Pringsheim, E.; Kaiser, W.; Arinaga, K.; Knezevic, J.; Tornow, M.; Fujita, S.; Yokoyama, N.; Abstreiter, G. *Nano Lett.* **2009**, *9*, 1290–1295.

[56] Xia, F.; White, R. J.; Zuo, X.; Patterson, A.; Xiao, Y.; Kang, D.; Gong, X.; Plaxco, K. W.; Heeger, A. J. *J. Am. Chem. Soc.* **2010**, *132*, 14346–14348.

[57] Langer, A.; Hampel, P. A.; Kaiser, W.; Knezevic, J.; Welte, T.; Villa, V.; Maruyama, M.; Svejda, M.; Jähner, S.; Fischer, F.; Strasser, R.; Rant, U. *Nat. Commun.* **2013**, *4*, 2099–2106.

[58] Spinke, J.; Liley, M.; Guder, H. J.; Angermaier, L.; Knoll, W. *Langmuir* **1993**, *9*, 1821–1825.

[59] Mirsky, V. M.; Riepl, M.; Wolfbeis, O. S. *Biosens. Bioelectron.* **1997**, *12*, 977–989.

[60] Briand, E.; Salmain, M.; Compère, C.; Pradier, C.-M. *Colloids Surf., B* **2006**, *53*, 215–224.

[61] Mantzila, A. G.; Maipa, V.; Prodromidis, M. I. *Anal. Chem.* **2008**, *80*, 1169–1175.

[62] Takoh, K.; Horie, M.; Someya, H.; Ishida, M.; Kamijo, K. Label-free immunosensor using a gold electrode covered with conductive self-assembled monolayer. IEEE Sensors 2010 Conference. 2010; pp 411–414.

[63] Ahmad, A.; Moore, E. *Analyst* **2012**, *137*, 5839–5844.

[64] Wan, J.; Ai, J.; Zhang, Y.; Geng, X.; Gao, Q.; Cheng, Z. *Sci. Rep.* **2016**, *6*, 19806–19811, Article.

[65] Vericat, C.; Vela, M. E.; Salvarezza, R. C. *Phys. Chem. Chem. Phys.* **2005**, *7*, 3258–3268.

[66] Vericat, C.; Vela, M. E.; Benitez, G.; Carro, P.; Salvarezza, R. C. *Chem. Soc. Rev.* **2010**, *39*, 1805–1834.

[67] Torrelles, X.; Vericat, C.; Vela, M. E.; Fonticelli, M. H.; Millone, M. A. D.; Felici, R.; Lee, T.-L.; Zegenhagen, J.; Muñoz, G.; Martín-Gago, J. A.; Salvarezza, R. C. *J. Phys. Chem. B* **2006**, *110*, 5586–5594.

[68] Zhang, J.; Chi, Q.; Ulstrup, J. *Langmuir* **2006**, *22*, 6203–6213.

[69] Nuzzo, R. G.; Zegarski, B. R.; Dubois, L. H. *J. Am. Chem. Soc.* **1987**, *109*, 733–740.

[70] Kondoh, H.; Kodama, C.; Sumida, H.; Nozoye, H. *J. Chem. Phys.* **1999**, *111*, 1175–1184.

[71] Hasan, M.; Bethell, D.; Brust, M. *J. Am. Chem. Soc.* **2002**, *124*, 1132–1133.

[72] Pace, G.; Venanzi, M.; Castrucci, P.; Scarselli, M.; Crescenzi, M. D.; Palleschi, A.; Stella, L.; Formaggio, F.; Toniolo, C.; Marletta, G. *Mater. Sci. Eng., C* **2006**, *26*, 918–923.

[73] Yeganeh, M. S.; Dougal, S. M.; Polizzotti, R. S.; Rabinowitz, P. *Phys. Rev. Lett.* **1995**, *74*, 1811–1814.

[74] Darling, S. B.; Rosenbaum, A. W.; Wang, Y.; Sibener, S. J. *Langmuir* **2002**, *18*, 7462–7468.

[75] Poirier, G. E. *Langmuir* **1997**, *13*, 2019–2026.

[76] Schreiber, F. *Prog. Surf. Sci.* **2000**, *65*, 151–257.

[77] Dubois, L. H.; Zegarski, B. R.; Nuzzo, R. G. *J. Chem. Phys.* **1993**, *98*, 678–688.

[78] Fenter, P.; Eberhardt, A.; Liang, K. S.; Eisenberger, P. *J. Chem. Phys.* **1997**, *106*, 1600–1608.

[79] Chidsey, C. E. D.; Loiacono, D. N. *Langmuir* **1990**, *6*, 682–691.

[80] Sun, L.; Crooks, R. M. *Langmuir* **1993**, *9*, 1951–1954.

[81] Grönbeck, H.; Curioni, A.; Andreoni, W. *J. Am. Chem. Soc.* **2000**, *122*, 3839–3842.

[82] Yourdshahyan, Y.; Zhang, H. K.; Rappe, A. M. *Phys. Rev. B* **2001**, *63*, 081405.

[83] Masens, C.; Ford, M.; Cortie, M. *Surf. Sci.* **2005**, *580*, 19–29.

[84] Hayashi, T.; Morikawa, Y.; Nozoye, H. *J. Chem. Phys.* **2001**, *114*, 7615–7621.

[85] Vargas, M. C.; Giannozzi, P.; Selloni, A.; Scoles, G. *J. Phys. Chem. B* **2001**, *105*, 9509–9513.

[86] Gottschalck, J.; Hammer, B. *J. Chem. Phys.* **2002**, *116*, 784–790.

[87] Barmparis, G. D.; Honkala, K.; Remediakis, I. N. *J. Chem. Phys.* **2013**, *138*, 064702.

[88] Kondoh, H.; Iwasaki, M.; Shimada, T.; Amemiya, K.; Yokoyama, T.; Ohta, T.; Shimomura, M.; Kono, S. *Phys. Rev. Lett.* **2003**, *90*, 066102.

[89] Roper, M.; Skegg, M.; Fisher, C.; Lee, J.; Dhanak, V.; Woodruff, D.; Jones, R. G. *Chem. Phys. Lett.* **2004**, *389*, 87–91.

[90] Chaudhuri, A.; Odelius, M.; Jones, R. G.; Lee, T.-L.; Detlefs, B.; Woodruff, D. P. *J. Chem. Phys.* **2009**, *130*, 124708.

[91] P. Fenter, P. E., A. Eberhardt *Science* **1994**, *266*, 1216–1218.

[92] Cossaro, A.; Mazzarello, R.; Rousseau, R.; Casalis, L.; Verdini, A.; Kohlmeyer, A.; Floreano, L.; Scandolo, S.; Morgante, A.; Klein, M. L.; Scoles, G. *Science* **2008**, *321*, 943–946.

[93] Camillone, N.; Chidsey, C. E. D.; Liu, G.; Scoles, G. *J. Chem. Phys.* **1993**, *98*, 3503–3511.

[94] Fenter, P.; Eisenberger, P.; Liang, K. S. *Phys. Rev. Lett.* **1993**, *70*, 2447–2450.

[95] Poirier, G. E. *Chem. Rev.* **1997**, *97*, 1117–1128.

[96] Li, J.; Liang, K. S.; Camillone, N.; Leung, T. Y. B.; Scoles, G. *J. Chem. Phys.* **1995**, *102*, 5012–5028.

[97] Poirier, G. E. *J. Vac. Sci. Technol., B* **1996**, *14*, 1453–1460.

[98] Yamada, R.; Uosaki, K. *Langmuir* **2001**, *17*, 4148–4150.

[99] Schweizer, M.; Hagenström, H.; Kolb, D. *Surf. Sci.* **2001**, *490*, L627–L636.

[100] Loglio, F.; Schweizer, M.; Kolb, D. M. *Langmuir* **2003**, *19*, 830–834.

[101] Schweizer, M.; Manolova, M.; Kolb, D. *Surf. Sci.* **2008**, *602*, 3303–3307.

[102] Grumelli, D.; Cristina, L. J.; Maza, F. L.; Carro, P.; Ferrón, J.; Kern, K.; Salvarezza, R. C. *J. Phys. Chem. C* **2015**, *119*, 14248–14254.

[103] Hagenström, H.; Schneeweiss, M. A.; Kolb, D. M. *Langmuir* **1999**, *15*, 2435–2443.

[104] Benítez, G.; Vericat, C.; Tanco, S.; Lenicov, F. R.; Castez, M. F.; Vela, M. E.; Salvarezza, R. C. *Langmuir* **2004**, *20*, 5030–5037.

[105] Porter, M. D.; Bright, T. B.; Allara, D. L.; Chidsey, C. E. D. *J. Am. Chem. Soc.* **1987**, *109*, 3559–3568.

[106] Badia, A.; Lennox, R. B.; Reven, L. *Acc. Chem. Res.* **2000**, *33*, 475–481.

[107] Poirier, G. E. *Langmuir* **1999**, *15*, 1167–1175.

[108] Herne, T. M.; Tarlov, M. J. *J. Am. Chem. Soc.* **1997**, *119*, 8916–8920.

[109] Levicky, R.; Herne, T. M.; Tarlov, M. J.; Satija, S. K. *J. Am. Chem. Soc.* **1998**, *120*, 9787–9792.

[110] Steel, A.; Levicky, R.; Herne, T.; Tarlov, M. *Biophys. J.* **2000**, *79*, 975–981.

[111] Murphy, J. N.; Cheng, A. K. H.; Yu, H.-Z.; Bizzotto, D. *J. Am. Chem. Soc.* **2009**, *131*, 4042–4050.

[112] Chidsey, C. E. D.; Bertozzi, C. R.; Putvinski, T. M.; Mujsce, A. M. *J. Am. Chem. Soc.* **1990**, *112*, 4301–4306.

[113] Collard, D. M.; Fox, M. A. *Langmuir* **1991**, *7*, 1192–1197.

[114] Hostetler, M. J.; Templeton, A. C.; Murray, R. W. *Langmuir* **1999**, *15*, 3782–3789.

[115] Yang, G.; Amro, N. A.; Starkewolfe, Z. B.; Liu, G.-y. *Langmuir* **2004**, *20*, 3995–4003.

[116] Laibinis, P. E.; Fox, M. A.; Folkers, J. P.; Whitesides, G. M. *Langmuir* **1991**, *7*, 3167–3173.

[117] Huang, J.; Hemminger, J. C. *J. Am. Chem. Soc.* **1993**, *115*, 3342–3343.

[118] Widrig, C. A.; Chung, C.; Porter, M. D. *J. Electroanal. Chem. Interfacial Electrochem.* **1991**, *310*, 335–359.

[119] Gorman, C. B.; Biebuyck, H. A.; Whitesides, G. M. *Langmuir* **1995**, *11*, 2242–2246.

[120] Grahame, D. C. *Chem. Rev.* **1947**, *41*, 441–501.

[121] Grahame, D. C.; Whitney, R. B. *J. Am. Chem. Soc.* **1942**, *64*, 1548–1552.

[122] Sato, N. *Electrochemistry at metal and semiconductor electrodes*; Elsevier B.V., 1998.

[123] Brown, M. A.; Goel, A.; Abbas, Z. *Angew. Chem. Int. Ed.* **2016**, *55*, 3790–3794.

[124] Daikhin, L. I.; Kornyshev, A. A.; Urbakh, M. *Phys. Rev. E* **1996**, *53*, 6192–6199.

[125] Daikhin, L.; Kornyshev, A.; Urbakh, M. *Electrochim. Acta* **1997**, *42*, 2853–2860.

[126] Mott, N.; Watts-Tobin, R. *Electrochim. Acta* **1961**, *4*, 79–107.

[127] Bockris, J. O.; Devanathan, M. A. V.; Muller, K. *Proc. R. Soc. London, Ser. A* **1963**, *274*, 55–79.

[128] Trasatti, S. In *Modern Aspects of Electrochemistry: No. 13*; Conway, B. E., Bockris, J. O., Eds.; Springer US: Boston, MA, 1979; pp 81–206.

[129] *Handbook of Chemistry and Physics, the 96nd Edition*; CRC Press, 2015-2016.

[130] Laitinen, H. A.; Mosier, B. *J. Am. Chem. Soc.* **1958**, *80*, 2363–2366.

[131] Sabatani, E.; Rubinstein, I.; Maoz, R.; Sagiv, J. *J. Electroanal. Chem. Interfacial Electrochem.* **1987**, *219*, 365–371.

[132] Lang, N. D.; Kohn, W. *Phys. Rev. B* **1970**, *1*, 4555–4568.

[133] Lang, N. D.; Kohn, W. *Phys. Rev. B* **1971**, *3*, 1215–1223.

[134] Smoluchowski, R. *Phys. Rev.* **1941**, *60*, 661–674.

[135] Hansson, G. V.; Flodström, S. A. *Phys. Rev. B* **1978**, *18*, 1572–1585.

[136] Kolb, D.; Schneider, J. *Electrochim. Acta* **1986**, *31*, 929–936.

[137] Trasatti, S. *J. Electroanal. Chem.* **1971**, *33*, 351–378.

[138] Kolb, D.; Schneider, J. *Surf. Sci.* **1985**, *162*, 764–775.

[139] Hamelin, A.; Sottomayor, M.; Silva, F.; Chang, S.-C.; Weaver, M. J. *J. Electroanal. Chem.* **1990**, *295*, 291–300.

[140] Hamelin, A. *J. Electroanal. Chem.* **1996**, *407*, 1–11.

[141] Hamelin, A.; Martins, A. *J. Electroanal. Chem.* **1996**, *407*, 13–21.

[142] Silva, A. F.; Martins, A. In *Interfacial Electrochemistry: Theory: Experiment, and Applications*; Wieckowski, A., Ed.; Marcel Dekker, Inc, 1999; pp 449–461.

[143] de Levie, R. *J. Electroanal. Chem. Interfacial Electrochem.* **1990**, *280*, 179–183.

[144] Lakowicz, J. R. *Principles of fluorescence spectroscopy - Third Edition*; Springer Science+Business Media, LLC, 2006.

[145] Clegg, R. M. *Curr. Opin. Biotechnol.* **1995**, *6*, 103–110.

[146] Song, L.; Hennink, E. J.; Young, I. T.; Tanke, H. J. *Biophys. J.* **1995**, *68*, 2588–2600.

[147] Drexhage, K. H. *Sci. Amer.* **1970**, *222*, 108–119.

[148] Drexhage, K. *J. Lumin.* **1970**, *1*, 693–701.

[149] Kuhn, H. *J. Chem. Phys.* **1970**, *53*, 101–108.

[150] Kuhn, H.; Möbius, D. *Angew. Chem. Int. Ed. Engl.* **1971**, *10*, 620–637.

[151] Amos, R. M.; Barnes, W. L. *Phys. Rev. B* **1997**, *55*, 7249–7254.

[152] Chance, R. R.; Prock, A.; Silbey, R. In *Advances in Chemical Physics*; Prigogine, I., Rice, S. A., Eds.; John Wiley & Sons, Inc., 1978; pp 1–65.

[153] Ford, G.; Weber, W. *Phys. Rep.* **1984**, *113*, 195–287.

[154] Barnes, W. L. *J. Mod. Opt.* **1998**, *45*, 661–699.

[155] Chance, R. R.; Prock, A.; Silbey, R. *J. Chem. Phys.* **1974**, *60*, 2744–2748.

[156] Yeung, M. S.; Gustafson, T. K. *Phys. Rev. A* **1996**, *54*, 5227–5242.

[157] Lakowicz, J. R. *Anal. Biochem.* **2005**, *337*, 171–194.

[158] Bizzotto, D.; Shepherd, J. L. In *Advances in Electrochemical Science and Engineering: Diffraction and Spectroscopic Methods in Electrochemistry*; Alkire, R. C., Kolb, D. M., Lipkowski, J., Ross, P. N., Eds.; Advances in Electrochemical Sciences and Engineering; Wiley-VCH Verlag GmbH, 2008; Vol. 9; pp 97–126.

[159] Reichman, J. Handbook of Optical Filters for Fluorescence Microscopy. Chroma Technology Corp, 2012.

[160] Fester, W. K.; Abramowitz, M.; Davidson, M. W. Olympus IX70 Fluorescence Microscope Cutaway Diagram. `http://www.olympusmicro.com/primer/techniques/fluorescence/anatomy/ix70fluorescence.html`.

[161] Aswani, K.; Jinadasa, T.; Brown, C. M. *Microscopy Today* **2012**, *20*, 22–28.

[162] Olympus IX71/IX81 Brochure.

[163] Loudet, A.; Burgess, K. *Chem. Rev.* **2007**, *107*, 4891–4932.

[164] Bergström, F.; Mikhalyov, I.; Hägglöf, P.; Wortmann, R.; Ny, T.; Johansson, L. B.-A. *J. Am. Chem. Soc.* **2002**, *124*, 196–204.

[165] Mikhalyov, I.; Gretskaya, N.; Bergstrom, F.; Johansson, L. B.-A. *Phys. Chem. Chem. Phys.* **2002**, *4*, 5663–5670.

[166] Panchuk-Voloshina, N.; Haugland, R. P.; Bishop-Stewart, J.; Bhalgat, M. K.; Millard, P. J.; Mao, F.; Leung, W.-Y.; Haugland, R. P. *J. Histochem. Cytochem.* **1999**, *47*, 1179–1188.

[167] The Molecular Probe Handbook: A Guide to Fluorescent Probes and Labeling Technologies. 2010.

[168] Shepherd, J. L.; Kell, A.; Chung, E.; Sinclar, C. W.; Workentin, M. S.; Bizzotto, D. *J. Am. Chem. Soc.* **2004**, *126*, 8329–8335.

[169] Casanova-Moreno, J.; Yu, Z. L.; Massey-Allard, J.; Ditchburn, B.; Young, J. F.; Bizzotto, D. In *Luminescence in Electrochemistry: Applications in Analytical Chemistry, Physics and Biology*; Miomandre, F., Audebert, P., Eds.; Springer International Publishing, 2017.

[170] Clavilier, J.; Faure, R.; Guinet, G.; Durand, R. *J. Electroanal. Chem. Interfacial Electrochem.* **1979**, *107*, 205–209.

[171] Verlinden, J.; Celis, J.; Roos, J. In *Passivity of Metals and Semiconductors*; Froment, M., Ed.; Elsevier, 1983; pp 341 – 346.

[172] Hamelin, A. *J. Electroanal. Chem. Interfacial Electrochem.* **1982**, *142*, 299–316.

[173] Hamelin, A.; Vitanov, T.; Sevastyanov, E.; Popov, A. *J. Electroanal. Chem. Interfacial Electrochem.* **1983**, *145*, 225–264.

[174] Shepherd, J. L. Electro-fluorescence characterization of insoluble surfactants adsorbed on solid electrodes. Ph.D. thesis, The University of British Columbia, 2005.

[175] Casanova Moreno, J. R. Spectroelectrochemical characterization of ultrathin organic films deposited on electrode surfaces. Ph.D. thesis, University of British Columbia, 2014.

[176] Ferreira, T.; Rasband, W. ImageJ User Guide - IJ 1.46r. 2012.

[177] User Manual for Evolve 512.

[178] Operating Manual for CCD Camera Models ST-7XE/XME, ST-8XE, ST-9XE, ST-10XE/XME, and ST-2000XM/XCM with High Speed USB Interface.

[179] Imabayashi, S.-i.; Hobara, D.; Kakiuchi, T.; Knoll, W. *Langmuir* **1997**, *13*, 4502–4504.

[180] Satjapipat, M.; Sanedrin, R.; Zhou, F. *Langmuir* **2001**, *17*, 7637–7644.

[181] Strutwolf, J.; O'Sullivan, C. K. *Electroanalysis* **2007**, *19*, 1467–1475.

[182] Henry, O.; Maliszewska, A.; O'Sullivan, C. *Electrochem. Commun.* **2009**, *11*, 664–667.

[183] Walczak, M. M.; Popenoe, D. D.; Deinhammer, R. S.; Lamp, B. D.; Chung, C.; Porter, M. D. *Langmuir* **1991**, *7*, 2687–2693.

[184] Walczak, M. M.; Alves, C. A.; Lamp, B. D.; Porter, M. D. *J. Electroanal. Chem.* **1995**, *396*, 103–114.

[185] Zhong, C.-J.; Porter, M. D. *J. Electroanal. Chem.* **1997**, *425*, 147–153.

[186] Yang, D.-F.; Wilde, C. P.; ; Morin, M. *Langmuir* **1997**, *13*, 243–249.

[187] Yang, D.-F.; Morin, M. *J. Electroanal. Chem.* **1997**, *429*, 1–5.

[188] Yang, D.-F.; Morin, M. *J. Electroanal. Chem.* **1998**, *441*, 173–181.

[189] Schneider, T. W.; Buttry, D. A. *J. Am. Chem. Soc.* **1993**, *115*, 12391–12397.

[190] Kawaguchi, T.; Yasuda, H.; Shimazu, K.; Porter, M. D. *Langmuir* **2000**, *16*, 9830–9840.

[191] Kunze, J.; Leitch, J.; Schwan, A. L.; Faragher, R. J.; Naumann, R.; Schiller, S.; Knoll, W.; Dutcher, J. R.; Lipkowski, J. *Langmuir* **2006**, *22*, 5509–5519.

[192] Laredo, T.; Leitch, J.; Chen, M.; Burgess, I. J.; Dutcher, J. R.; Lipkowski, J. *Langmuir* **2007**, *23*, 6205–6211.

[193] Mulder, W. H.; Calvente, J. J.; Andreu, R. *Langmuir* **2001**, *17*, 3273–3280.

[194] Doneux, T.; Nichols, R.; Buess-Herman, C. *J. Electroanal. Chem.* **2008**, *621*, 267–276.

[195] Ramírez, P.; Andreu, R.; Cuesta, Á.; Calzado, C. J.; Calvente, J. J. *Anal. Chem.* **2007**, *79*, 6473–6479.

[196] Kunitake, M.; Batina, N.; ; Itaya, K. *Langmuir* **1995**, *11*, 2337–2340.

[197] Sawaguchi, T.; Mizutani, F.; Taniguchi, I. *Langmuir* **1998**, *14*, 3565–3569.

[198] Ohira, A.; Ishizaki, T.; Sakata, M.; Taniguchi, I.; Hirayama, C.; Kunitake, M. *Colloids Surf., A* **2000**, *169*, 27–33.

[199] He, Y.; Borguet, E. *Angew. Chem. Int. Ed.* **2007**, *46*, 6098–6101.

[200] Wen, R.; Yan, C.-J.; Yan, H.-J.; Pan, G.-B.; Wan, L.-J. *Chem. Commun.* **2011**, *47*, 6915–6917.

[201] Komanicky, V.; Fawcett, W. *Electrochim. Acta* **2004**, *49*, 1185–1194.

[202] Voigtländer, B.; Linke, U.; Stollwerk, H.; Brona, J. *J. Vac. Sci. Technol., A* **2005**, *23*, 1535–1537.

[203] Voigtländer, B.; Cherepanov, V.; Elsaesser, C.; Linke, U. *Rev. Sci. Instrum.* **2008**, *79*, 033911.

[204] Musgrove, A.; Kell, A.; Bizzotto, D. *Langmuir* **2008**, *24*, 7881–7888.

[205] Casanova-Moreno, J. R.; Bizzotto, D. *Langmuir* **2013**, *29*, 2065–2074.

[206] Jung, L. S.; ; Campbell, C. T. *J. Phys. Chem. B* **2000**, *104*, 11168–11178.

[207] Sumi, T.; Uosaki, K. *J. Phys. Chem. B* **2004**, *108*, 6422–6428.

[208] Debono, R. F.; Loucks, G. D.; Manna, D. D.; Krull, U. J. *Can. J. Chem.* **1996**, *74*, 677–688.

[209] Forouzan, F.; Bard, A. J.; Mirkin, M. V. *Isr. J. Chem.* **1997**, *37*, 155–163.

[210] Fabris, L.; Antonello, S.; Armelao, L.; Donkers, R. L.; Polo, F.; Toniolo, C.; Maran, F. *J. Am. Chem. Soc.* **2006**, *128*, 326–336.

[211] Kaplan, J. M.; Shang, J.; Gobbo, P.; Antonello, S.; Armelao, L.; Chatare, V.; Ratner, D. M.; Andrade, R. B.; Maran, F. *Langmuir* **2013**, *29*, 8187–8192.

[212] Gatto, E.; Venanzi, M. *Polym. J.* **2013**, *45*, 468–480.

[213] Venanzi, M.; Pace, G.; Palleschi, A.; Stella, L.; Castrucci, P.; Scarselli, M.; Crescenzi, M. D.; Formaggio, F.; Toniolo, C.; Marletta, G. *Surf. Sci.* **2006**, *600*, 409–416.

[214] Gatto, E.; Porchetta, A.; Scarselli, M.; Crescenzi, M. D.; Formaggio, F.; Toniolo, C.; Venanzi, M. *Langmuir* **2012**, *28*, 2817–2826.

[215] Hauptmann, N.; Robles, R.; Abufager, P.; Lorente, N.; Berndt, R. *J. Phys. Chem. Lett.* **2016**, *7*, 1984–1990.

[216] Shin, Y.-g. K.; Newton, M. D.; Isied, S. S. *J. Am. Chem. Soc.* **2003**, *125*, 3722–3732.

[217] Toniolo, C.; Crisma, M.; Formaggio, F.; Peggion, C.; Broxterman, Q. B.; Kaptein, B. *Pept. Sci.* **2004**, *76*, 162–176.

[218] Holm, A. H.; Ceccato, M.; Donkers, R. L.; Fabris, L.; Pace, G.; Maran, F. *Langmuir* **2006**, *22*, 10584–10589.

[219] Antonello, S.; Formaggio, F.; Moretto, A.; Toniolo, C.; Maran, F. *J. Am. Chem. Soc.* **2003**, *125*, 2874–2875.

[220] Perera, N. V.; Isley, W.; Maran, F.; Gascon, J. A. *J. Phys. Chem. C* **2010**, *114*, 16043–16050.

[221] Gobbo, P. Stability of and Electron Transfer through Self-Assembled Monolayers of Conformationally Constrained Peptides. M.Sc. thesis, University of Padova, 2010.

[222] Becucci, L.; Guryanov, I.; Maran, F.; Guidelli, R. *J. Am. Chem. Soc.* **2010**, *132*, 6194–6204.

[223] Gatto, E.; Venanzi, M.; Palleschi, A.; Stella, L.; Pispisa, B.; Lorenzelli, L.; Toniolo, C.; Formaggio, F.; Marletta, G. *Mater. Sci. Eng., C* **2007**, *27*, 1309–1312.

[224] Gatto, E.; Stella, L.; Formaggio, F.; Toniolo, C.; Lorenzelli, L.; Venanzi, M. *J. Pept. Sci.* **2008**, *14*, 184–191.

[225] Polo, F.; Antonello, S.; Formaggio, F.; Toniolo, C.; Maran, F. *J. Am. Chem. Soc.* **2005**, *127*, 492–493.

[226] Rant, U.; Arinaga, K.; Fujita, S.; Yokoyama, N.; Abstreiter, G.; Tornow, M. *Nano Lett.* **2004**, *4*, 2441–2445.

[227] Rant, U.; Arinaga, K.; Tornow, M.; Kim, Y. W.; Netz, R. R.; Fujita, S.; Yokoyama, N.; Abstreiter, G. *Biophys. J.* **2006**, *90*, 3666–3671.

[228] Kaiser, W.; Rant, U. *J. Am. Chem. Soc.* **2010**, *132*, 7935–7945.

[229] Peggion, C.; Crisma, M.; Toniolo, C.; Formaggio, F. *Tetrahedron* **2012**, *68*, 4429–4433.

[230] Watson, J. D.; Crick, F. H. C. *Nature* **1953**, *171*, 737–738.

[231] Daune, M. *Molecular biophysics: structures in motion*; Oxford University Press, 1999.

[232] Vologodskii, A. *Biophysics of DNA*; Cambridge University Press, 2015.

[233] Wang, A. H.-J.; Quigley, G. J.; Kolpak, F. J.; Crawford, J. L.; van Boom, J. H.; van der Marel, G.; Rich, A. *Nature* **1979**, *282*, 680–686.

[234] Thamann, T. J.; Lord, R. C.; Wang, A. H.; Rich, A. *Nucleic Acids Res.* **1981**, *9*, 5443–5457.

[235] Jonstrup, A. T.; Fredsøe, J.; Andersen, A. H. *Sensors* **2013**, *13*, 5937–5944.

[236] Wang, Q.; Gao, F.; Ni, J.; Liao, X.; Zhang, X.; Lin, Z. *Sci. Rep.* **2016**, *6*, 22441–22410.

[237] Hagerman, P. J. *Biopolymers* **1981**, *20*, 1503–1535.

[238] Tinland, B.; Pluen, A.; Sturm, J.; Weill, G. *Macromolecules* **1997**, *30*, 5763–5765.

[239] Baumann, C. G.; Smith, S. B.; Bloomfield, V. A.; Bustamante, C. *Proc. Natl. Acad. Sci. U.S.A.* **1997**, *94*, 6185–6190.

[240] Rybenkov, V. V.; Cozzarelli, N. R.; Vologodskii, A. V. *Proc. Natl. Acad. Sci. U.S.A.* **1993**, *90*, 5307–5311.

[241] Rybenkov, V. V.; Vologodskii, A. V.; Cozzarelli, N. R. *Nucleic Acids Res.* **1997**, *25*, 1412–1418.

[242] Tsortos, A.; Papadakis, G.; Mitsakakis, K.; Melzak, K. A.; Gizeli, E. *Biophys. J.* **2008**, *94*, 2706–2715.

[243] Petruska, J.; Goodman, M. F. *J. Biol. Chem.* **1995**, *270*, 746–750.

[244] Qiao, W.; Chiang, H.-C.; Xie, H.; Levicky, R. *Chem. Commun.* **2015**, *51*, 17245–17248.

[245] Laland, S.; Lee, W.; Overend, W.; Peacocke, A. *Biochim. Biophys. Acta* **1954**, *14*, 356–365.

[246] DeVoe, H.; Tinoco, I. *J. Mol. Biol.* **1962**, *4*, 518–527.

[247] Herskovits, T. T. *Biochemistry* **1963**, *2*, 335–340.

[248] Maniatis, T.; Jeffrey, A.; deSande, H. V. *Biochemistry* **1975**, *14*, 3787–3794.

[249] Summer, H.; Grämer, R.; Dräge, P. *J. Vis. Exp.* **2009**, e1485.

[250] Peterson, A. W.; Heaton, R. J.; Georgiadis, R. M. *Nucleic Acids Res.* **2001**, *29*, 5163–5168.

[251] Kelley, S. O.; Barton, J. K.; Jackson, N. M.; McPherson, L. D.; Potter, A. B.; Spain, E. M.; Allen, M. J.; ; Hill, M. G. *Langmuir* **1998**, *14*, 6781–6784.

[252] Casanova-Moreno, J.; Bizzotto, D. *Electrochim. Acta* **2015**, *162*, 62–71.

[253] Casanova-Moreno, J.; Bizzotto, D. *Anal. Chem.* **2015**, *87*, 2255–2263.

[254] About Lock-In Amplifiers. Stanford Research Systems.

[255] Lasia, A. *Electrochemical Impedance Spectroscopy and its Applications*; Springer New York: New York, NY, 2014; pp 67–84.

[256] Josephs, E. A.; Ye, T. *J. Am. Chem. Soc.* **2012**, *134*, 10021–10030.

[257] Malmstadt, H. V.; Enke, C. G.; Crouch, S. R. *Electronics and instrumentation for scientists*; The Benjamin/Cummings Publishing Company, Inc., 1981.

[258] Moura, L.; Darwazeh, I. *Introduction to Linear Circuit Analysis and Modelling : From DC to RF*; Newnes, 2005.

[259] Sluyters-Rehbach, M.; Sluyters, J. In *Electroanalytical Chemistry: A Series of Advances*; Bard, A., Ed.; Marcel Dekker, New York, 1970; Vol. 4; Chapter 1, pp 1–127.

[260] Macdonald, D. D. *Transient Techniques in Electrochemistry*; Springer US: Boston, MA, 1977; pp 229–272.

[261] Sluyters-Rehbach, M.; Sluyters, J. In *Comprehensive Treatise of Electrochemistry*; Yeager, E., Bockris, J., Conway, B., Sarangapani, S., Eds.; Plenum Press, 1984; Vol. 9; Chapter 4, pp 177–289.

[262] Engblom, S. O.; Myland, J. C.; Oldham, K. B. *J. Electroanal. Chem.* **2000**, *480*, 120–132.

[263] Engblom, S. O.; Myland, J. C.; Oldham, K. B.; Taylor, A. L. *Electroanalysis* **2001**, *13*, 626–630.

[264] Kiel, M.; Bohlen, O.; Sauer, D. *Electrochim. Acta* **2008**, *53*, 7367–7374.

[265] McDonald, T. J.; Adler, S. *ECS Trans.* **2012**, *45*, 429–439.

[266] X-Cite exacte USER'S GUIDE.

[267] Chroma Spectra Viewer. `https://www.chroma.com/spectra-viewer`.

[268] Thermo Fisher Fluorescence Spectra Viewer. `https://www.thermofisher.com/ca/en/home/life-science/cell-analysis/labeling-chemistry/fluorescence-spectraviewer.html`.

Appendix A

Spectra

A.1 Hg arc lamp spectrum and excitation filter bands
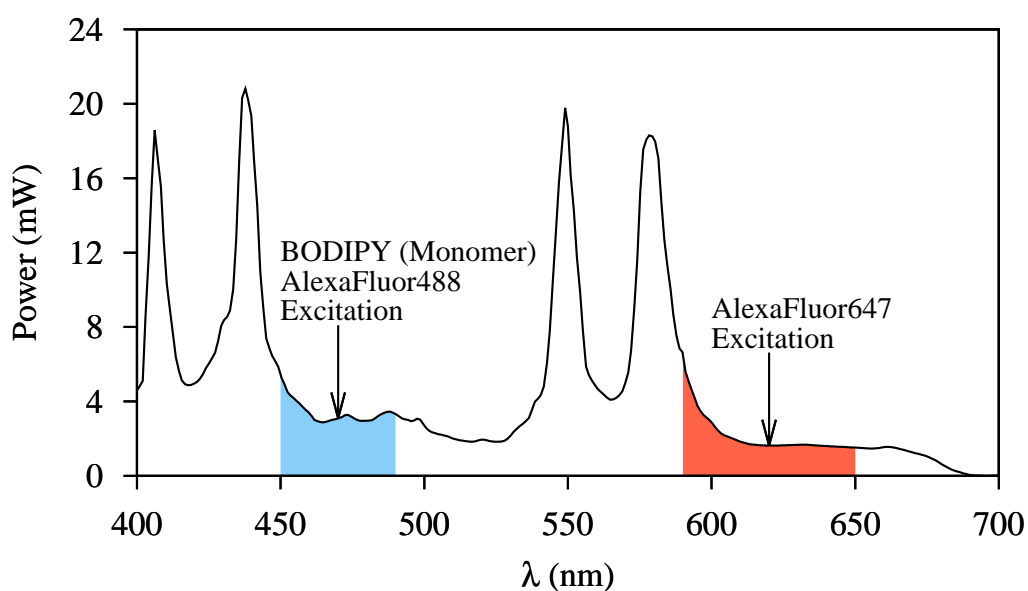

Figure A.1: Hg arc lamp spectrum of an Excelitas X-Cite® exacte fluorescence illuminator (data obtained from user's guide provided by Excelitas [266]). The two excitation filter bands correspond to the ones listed in Table 3.1: Chroma ET470/40x and Chroma HQ620/60x.

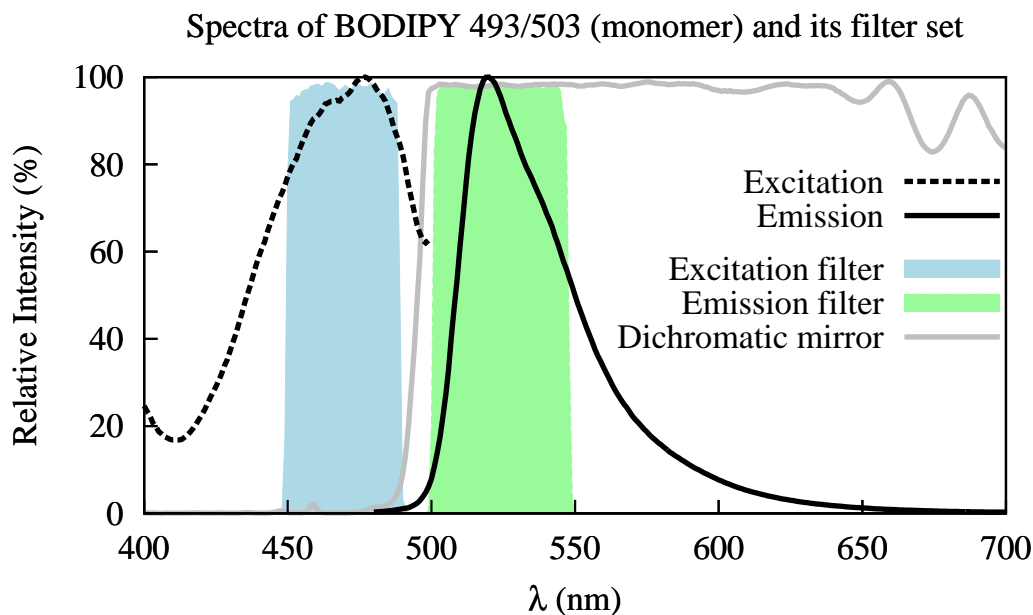## A.2 Spectra of the used fluorophores and their corresponding filter sets

Figure A.2: Spectra of BODIPY 493/503 (monomer) and its corresponding filter set (excitation: ET470/40x, dichromatic: T495LPXR, emission: ET525/50m). The BODIPY 493/503 (monomer) spectra were measured with an Agilent Cary Eclipse Fluorescence Spectrophotometer. The filter set spectral data were obtained from Chroma's spectra viewer website [267].
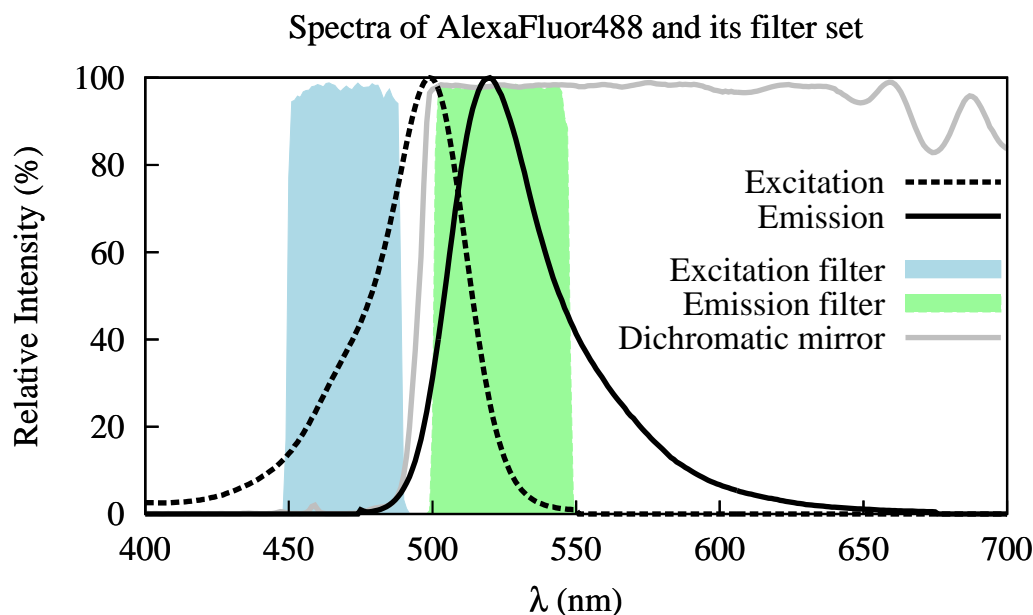

Figure A.3: Spectra of AlexaFluor488 and its corresponding filter set (excitation: ET470/40x, dichromatic: T495LPXR, emission: ET525/50m). The AlexaFluor488 spectral data were obtained from Thermo Fisher's fluorescence spectra viewer website [268]. The filter set spectral data were obtained from Chroma's spectra viewer website [267].
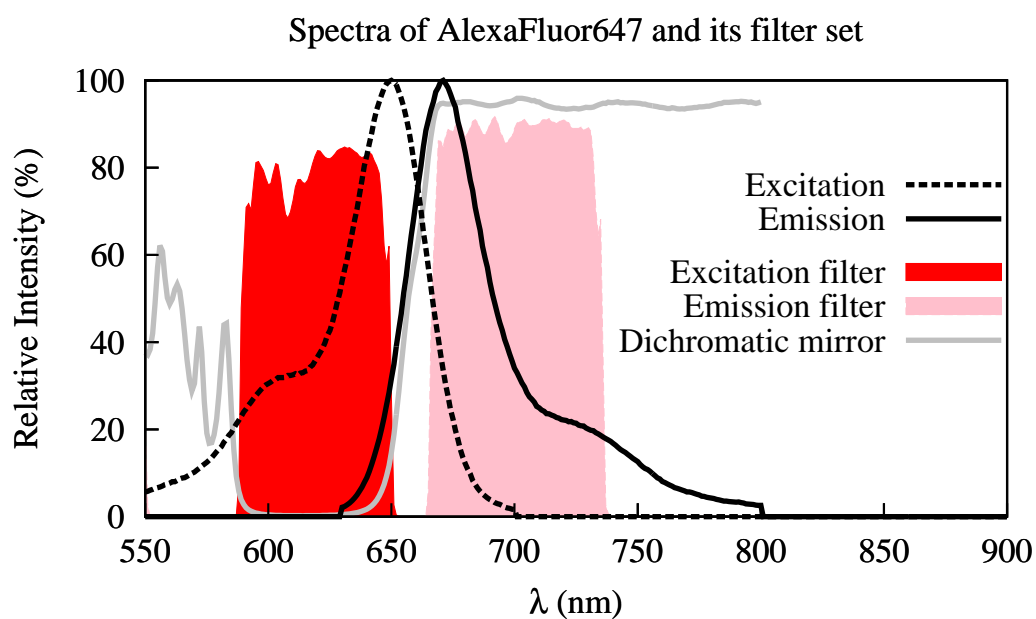
Spectra of AlexaFluor647 and its filter set

Figure A.4: Spectra of AlexaFluor647 and its corresponding filter set (excitation: HQ620/60x, dichromatic: Q660LP, emission: HQ700/75m). The AlexaFluor488 spectral data were obtained from Thermo Fisher's fluorescence spectra viewer website [268]. The filter set spectral data were obtained from Chroma's spectra viewer website [267].